Insertion Devices for the MAX IV 3 GeV Storage Ring

Erik Wallén*

2009-09-22

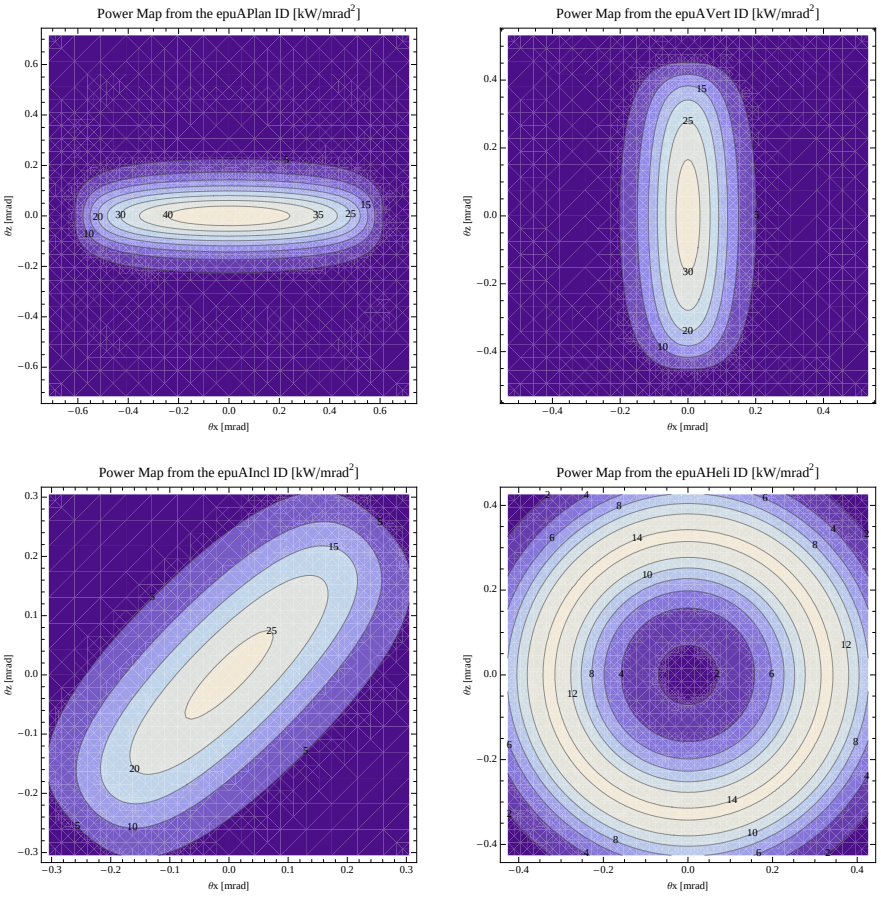

*Email: erik.wallen@maxlab.lu.se, Telephone +46 46 222 33 56, Address: Erik Wallén, MAX-lab, Box 118, SE-22100 Lund, Sweden

Contents

List of Tables

List of Figures

1 Introduction

The synchrotron radiation used at the experimental stations at MAX IV is created in insertion devices on the straight sections. The insertion devices could be either of undulator or wiggler type. Both wigglers and undulators consist of a periodic arrangement of magnet poles that forces the stored electron beam to oscillate transversely to the direction of motion of the beam and synchrotron radiation is emitted as illustrated in Figure 1.

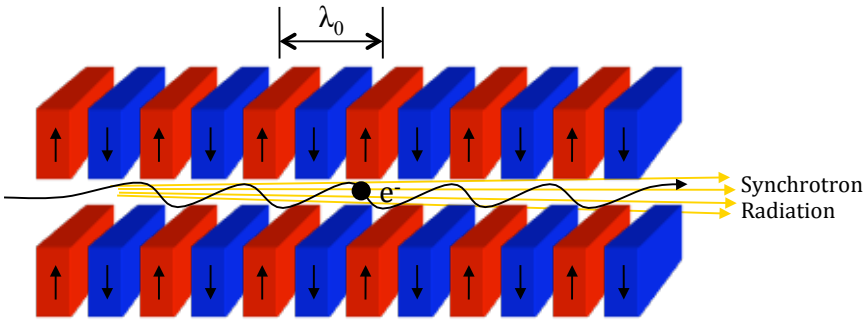

Figure 1: Illustration of the emission of synchrotron radiation in a periodic insertion device.

A wiggler has stronger magnetic fields than an undulator and the synchrotron radiation from a wiggler is in principle a superposition of the bending magnet radiation of the poles in the wiggler. In an undulator the emitted light from the consecutive undulator poles is added up to a Fourier sum, which results in an amplification of the light at certain resonance wavelengths in the radiation spectrum. The basic resonance wavelength and the wavelength of the higher harmonics at odd multiples of the basic wavelength are determined by the undulator period length λ_0, the undulator peak field B_0, and the relativistic factor γ of the stored electron beam in the storage ring.

The wavelength λ_n of the n:th harmonic of the radiation emitted on axis from the undulator is

$$\lambda_n = \frac{\lambda_0}{2n\gamma^2}\left(1 + \frac{K^2}{2}\right) \tag{1}$$

K is the amplitude of oscillation for the transverse velocity of the stored beam when passing through the undulator in units of $1/\gamma$. Instead of wavelength it may be of interest to know the energy of the emitted photons, which is given by the relation $E_n[\text{keV}] = 12.4/\lambda_n$ [Å]. For the special case of a sinusoidal field in the undulator the K-value is given by

$$K = 0.934\lambda_0[\text{cm}]B_0[\text{T}] \tag{2}$$

By varying the peak field B_0 in the undulator it is possible to change the resonance wavelengths. The variation of the peak field in a permanent magnet undulator or wiggler

is done by varying the magnetic gap and in a superconducting undulator or wiggler, the peak field is varied by varying the current in the superconducting coils. To have an overlap between the first and third harmonic in the emission spectrum from an undulator, the maximum K-value has to be larger than 2. If a lower limit of the K-value of 0.5 is assumed, the maximum K-value that should be obtained in the undulator must be 2.18 in order to get overlapping between the first and third harmonics. If there is no need of an overlap between the first and third harmonic it is sufficient to obtain a maximum K-value of 1.5. A wiggler has a K-value considerably larger than 1.

There is a general interest in the synchrotron radiation community in producing undulator radiation with a short a wavelength as possible, also using the higher harmonics of the fundamental wavelength. The period length of the undulator should hence be as small as possible. A small period length in combination with a high peak field requires that the magnetic gap of the undulator is small. Small gaps require in turn that the stored electron beam in the accelerator has small dimensions at the position of the insertion device. The search for high brilliance also requires that the beam has a low emittance, i.e. that the beam is well collimated with the electrons in the beam travelling as parallel as possible. The development of the insertion device technology has together with the development of low emittance storage rings designed for the production of synchrotron radiation been the key to the enormous increase in brilliance of the synchrotron light sources over the past decades. The brilliance of an undulator increases with the square of the number of periods in the undulator but the always existing energy spread in storage rings of about 0.1 % has a broadening effect on the peaks in the undulator spectrum and there is no gain in brilliance by increasing the number of periods to more than about 250 periods. Long straight sections on the expense of having a large minimum vertical aperture are hence not beneficial for the performance of the light source.

1.1 Physical limits for the insertion devices

The straight section length available for insertion devices at the 3 GeV MAX IV storage ring is 4.8 m and the minimum vertical beam stay clear aperture in the middle of the straight sections is 4 mm.

In-vacuum undulators are assumed to have a minimum magnetic gap of 4.2 mm and the magnetic length can be up to 3.8 m since approximately 500 mm are needed at the entrance and exit of the vacuum tank of the undulator for valves, absorbers, flanges and tapers.

Elliptically polarising undulators and out of vacuum undulators are assumed to have a minimum magnetic gap of 9 mm and a maximum length of 4 m. The outer vertical aperture of the NEG coated Al vacuum chamber is assumed to be 7 mm. Current strips to compensate for dynamic multipoles will occupy 1.2 mm of aperture and an additional 0.8 mm is needed for clearance.

Wigglers are assumed to have a minimum magnetic gap of 9 mm and a maximum length

of 4 m. The gap may be decreased to 7.8 mm if the same vacuum chamber as for the elliptically polarising undulators is used.

1.2 Undulators

The undulators for high energy photons will by necessity be in-vacuum insertion devices since a small magnetic gap is needed in order to obtain a high undulator peak field in combination with a short period length. The first set of beam lines will use todays state of the art technology with in-vacuum undulators of hybrid type. Cryogenically cooled in-vacuum undulators may also be considered for installation at some of the initial beam lines at the MAX IV 3 GeV ring. The promising but not yet mature technique with superconducting undulators is however not considered for the initial set of beam lines since the fundamental problems with large phase error and field integrals as well as the heat load problems not yet have been solved for this technique. The 3 GeV MAX IV ring is however well suited for the installation of superconducting undulators since the soft end bending magnets flanking the straight sections and the long bunch length in the stored beam will give a moderate heat load to the cold mass of the superconducting undulator.

The three different techniques in-vacuum undulators (PMU), cryogenically cooled in-vacuum undulators (CPMU), and superconducting undulators (SCU) have been compared for the same boundary condition of 4 mm vertical stay clear aperture and the result in the form of a plot of the minimum required period length for a given K-value is shown in Figure 2.

The in-vacuum undulators used for the comparison are of hybrid type with Sm_2Co_{17} (B_r = 1.05 T) as the magnetic material and pure iron as pole material. The peak field is found by magnetic model calculations with the geometry of the iron poles and magnet material in the undulator using the computer code Radia [2]. The vertical physical aperture is 4 mm and there is a 0.1 mm thick sheet covering the pole faces, which results in magnetic aperture of 4.2 mm. The magnetic material Sm_2Co_{17} is used as the permanent magnet material and iron is used as the pole material. The transverse dimensions of the magnet material are 50×30 mm^2 and the pole material 32×24 mm^2. The longitudinal length, or thickness, of the iron pole disk is 13.6 % of the period length and the longitudinal length, or thickness, of the magnet material disk is 36.4 % of the period length.

The peak field in the cryogenically cooled in-vacuum undulator operating at a temperature of 140 K in the comparison is found by carrying out an identical calculation as for the in-vacuum undulator except for that the magnetic material has been changed to NdFeB (B_r = 1.35 T at 140 K, B_r = 1.18 T at 293 K), the pole longitudinal length has been increased to 15 % of the period length, and the longitudinal length of the magnet material has been decreased to 35 % of the period length.

The peak field B_0 of the superconducting undulator with the magnetic gap g[mm] equal

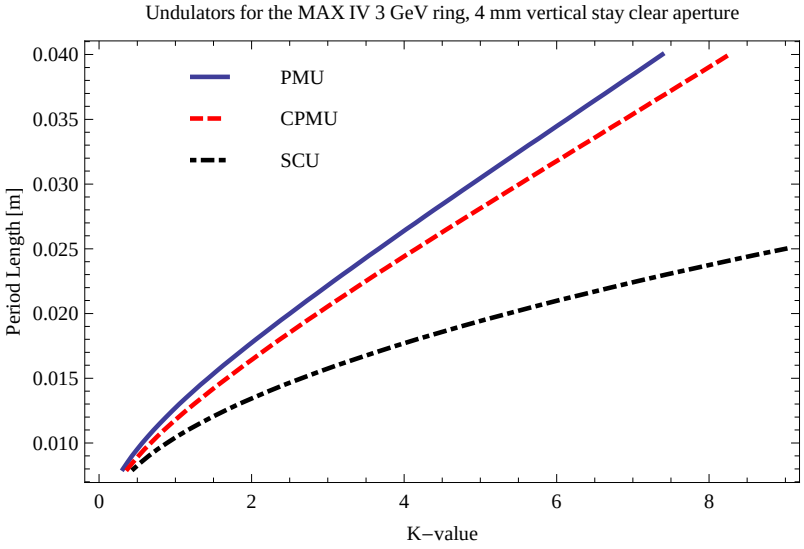

Figure 2: Minimum required period length for a given K-value for the undulator techniques in-vacuum undulators (PMU), cryogenically cooled in-vacuum undulators (CPMU), and superconducting undulators (SCU).

to 4.4 mm and period length λ_0 mm] in the comparison is found by using a generalised expression [1] of the peak field in a superconducting undulator using NbTi coils and iron poles

$$B_0[\mathrm{T}] = (1.85 + 0.194\lambda_0)\, e^{-\frac{\pi g}{\lambda_0}} \tag{3}$$

The brilliance limit for the 3 GeV MAX IV has been calculated from the performance limit of the different undulator techniques shown in Figure 2 and assuming an undulator length of 3 m. The result is shown in Figure 3 and the corresponding spectral flux density is shown in Figure 4. The value shown in Figure 3 represents the limit of the brilliance at peak energy that can be obtained for a given photon energy. The brilliance plotted in Figure 3 is the brilliance at peak energy and not the maximum brilliance which is found at slightly lower photon energy than the peak energy. It is believed that for a low emittance light source like the 3 GeV MAX IV ring, it is more interesting to use the point like cone of the synchrotron radiation produced at the peak energy than the circular cone of radiation which gives a slightly higher brilliance. The undulator period length, peak field strength, and harmonic has been optimised for each given photon energy value in the plot shown in Figure 3. A real undulator that will be used over a larger photon energy range by changing the peak field will be slightly lower than brilliance limit shown in Figure 3 except for the point where the undulator reaches the brilliance limit of the undulator technique. The beam parameters in the middle of the straight sections the 3 GeV MAX-IV storage ring used for the calculation of the brilliance are given below in Table 1.

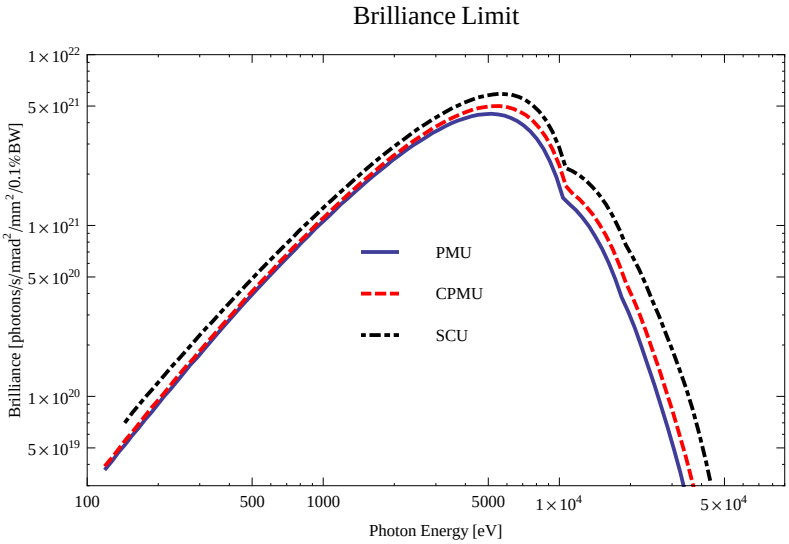

Figure 3: Brilliance limit for the 3 GeV MAX IV for the undulator techniques in-vacuum undulators (PMU), cryogenically cooled in-vacuum undulators (CPMU), and superconducting undulators (SCU). The undulators are assumed to be 3 m long.

Table 1: Beam parameters used for the brilliance calculations

Beam Energy	3.0	GeV
Beam Current	500	mA
Energy Spread (rms)	0.0010	
Horizontal Beta Function	9.00	m
Horizontal Emittance	0.263	nmrad
Vertical Beta Function	4.80	m
Vertical Emittance	0.008	nmrad

1.3 Elliptically polarizing undulators

The MAX IV 3 GeV storage ring will be an excellent storage ring for the installation of elliptically polarizing undulators since the vertical outer dimension of the vacuum tube is as small as 9 mm. It will be possible to reach as high as 2 keV photon energy with 100 % circularly polarized light using an elliptically polarizing undulator with 38 mm period length.

1.4 Wigglers

The function of the wigglers at the 3 GeV storage ring is twofold, to act as damping wigglers to decrease the emittance of the stored beam and to be photon sources for

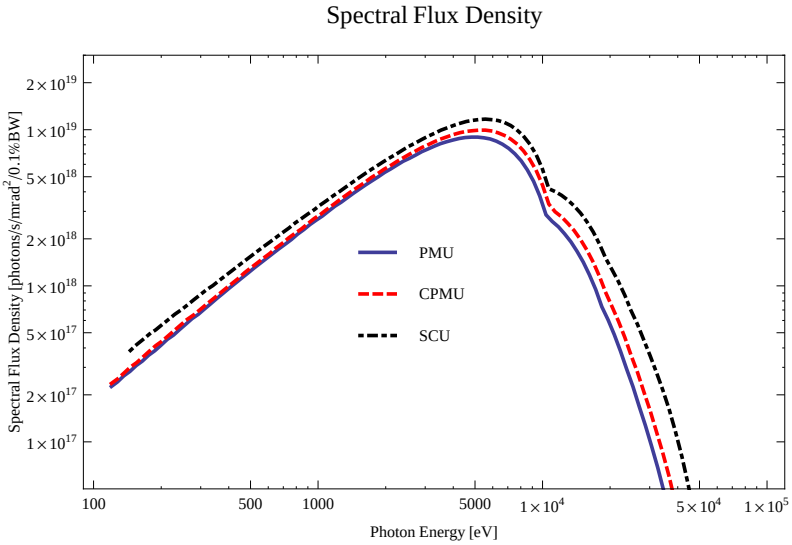

Figure 4: Spectral flux density for the 3 GeV MAX IV for the undulator techniques in-vacuum undulators (PMU), cryogenically cooled in-vacuum undulators (CPMU), and superconducting undulators (SCU). The undulators are assumed to be 3 m long.

experimental stations. The wigglers will also increase the energy spread of the stored beam.

The foreseen wigglers are of hybrid type using permanent magnet material since they have lower running costs than superconducting wigglers.

2 Proposed beamlines at the MAX IV 3 GeV storage ring

At present no decision exists on the priorities for the different beamline projects on the MAX IV facility and the below list should be regarded as examples of beamlines that are being considered. It has been produced to give a possible scenario on what insertion devices that are being considered to be placed around the 3 GeV ring for the Detailed Design Report (DDR) of the machine. All of these 15 beamlines will not be possible to incorporate in Phase 1, also they are not listed in a priority order. The beamlines are shortly described in Table 2 and in the sub-sections below.

Table 2: Proposed beamlines at the MAX IV 3 GeV ring

	Activity	Photon Energy	Source	Polarisation
PX1	Protein Crystallography	5 - 17 keV	Undulator	Horizontal
PX2	Protein Crystallography	7 - 17 keV	Undulator	Horizontal
MSC	Material Science	15 - 100 keV	Wiggler	Horizontal
TOM	Tomography	15 - 100 keV	Wiggler	Horizontal
ENV	Environmental Science	1 - 25 keV [a]	Undulator	Horizontal
NF1	Nanofocus beam line	5 - 30 keV	Undulator	Horizontal
NF2	Nanofocus beam line	5 - 30 keV	Undulator	Horizontal
SXM	Small angle scattering	6 - 17 keV	Undulator	Horizontal
SXB	Small angle scattering biology	≈10 keV fixed	Wiggler	Horizontal
BXF	Bulk EXAFS (811)	2.3 - 20 keV	Wiggler	Horizontal
MUS	Microspectroscopy	2 - 30 keV	Undulator	Horizontal
HRS	High resolution soft x-ray	0.6 - 2 keV	Undulator	All
MAG	Magnetism	0.6 - 2 keV	Undulator	All
HIK	Photoemission HIKE	2 - 30 keV	Undulator	Horizontal
NUC	Compton backscattering	400 - 500 MeV	Laser	From laser

[a] Lower energies, 1- 5 KeV, have priority

2.1 PX1

An undulator based beamline for macromolecular (protein) crystallography with an energy range between 5 and 17 keV. The main focus of the beamline is high-throughput and highly automated structural investigations of protein crystals. The high energy resolution and rapidly tunable wavelength over the complete energy region will also permit optimized phasing experiments.

2.2 PX2

An undulator based beamline for macromolecular (protein) crystallography with an energy range between 7 and 17 keV. It will be possible to focus the beam down 1 micrometer to enable data collection on micro crystals. The same requirements as on PX1 for phasing experiments.

2.3 MSC

A wiggler based beamline for material science and extreme conditions experiments (single crystal/ powder diffraction and EXAFS) with an energy range from 15 to 100 keV. The wide horizontal beam from the wiggler will enable splitting up the beam onto two experimental set-ups.

2.4 TOM

A wiggler beamline for tomography and (medical) imaging experiments with an energy range between 15 and 100 keV. The wide wiggler fan will enable imaging of also larger objects. It could be of interest to use a wider fan than 1 mrad.

2.5 ENV

An undulator beamline focused on Environmental Science (primary EXAFS) in the energy range between 1 and 25 keV but with priorities on the experimentally challenging but for Environmental Science interesting energy region 1 to 5 keV which will cover absorption edges like Ca, Mg and Al.

2.6 NF1

An undulator beamline for nanofocus applications with an energy range between 5 and 30 keV. The design is based on modular optics to permit a variable focus down to beam sizes of 10 nm in the vertical direction and 200 nm in the horizontal without sacrificing the flux. The beamline will focus on microscopy and spectroscopy applications.

2.7 NF2

An undulator beamline for nanofocus applications with an energy range between 5 and 30 keV. The design is based on modular optics to permit a variable focus down to beam sizes of 10 nm in the vertical direction and 200 nm in the horizontal without

sacrificing the flux. The beamline will focus on diffraction, imaging and - tomography applications.

2.8 SXM

An undulator beamline for general purpose small angle X-ray scattering (SAXS) experiments with simultaneous WAXS capacity. The optical design will enable beam sizes down to 50 m with a very small divergence permitting sample to detector distances up to 10 m. The energy range will be between 6 and 17 keV.

2.9 SXB

A wiggler beamline specialized on bio-SAXS experiments. Fixed energy around 10 keV and a short (1 m, 1.86 T) wiggler could be considered as insertion device.

2.10 BXF

A wiggler based bulk EXAFS beamline where most of the optical components can be taken from the existing beamline I811. The energy range will be between 2.3 and 20 keV and a short (1m, 1.86 T) wiggler could be considered as insertion device.

2.11 MUS

An undulator beamline for -spectroscopy applications in the energy range between 2 and 30 keV. The beamline will host a number of spectroscopic and fluorescence techniques. It will be possible to focus the beam down to 1 m and the energy resolution will be selectable from 10^{-2} (pink beam) down to 4×10^{-6}.

2.12 HRS

A high resolution soft X-ray beamline for the energy range between 0.6 and 2 keV. The insertion device is an EPU.

2.13 MAG

A beamline focused on magnetic studies in the energy range between 0.6 and 2 keV. The insertion device is an EPU and most of the beamline parts can be taken from the existing beamline I1011.

2.14 HIK

An undulator beamline focused on HIKE (High Energy Photo Emission) experiments in the energy range between 2 and 30 KeV

2.15 NUC

In addition to the synchrotron radiation beamlines there is a proposal for a Compton backscattering (laser induced) beamline for nuclear physics experiments with an energy range between 400 and 500 MeV.

To summarise, of the 15 beamlines, 8 will use planar field undulators, 2 will use elliptically polarizing undulators, 2 will use wigglers on the long straight section, 2 will use less powerful wigglers which could either be placed on the long or the short straight sections, and one will use backscattered light from laser light hitting the beam.

3 Insertion devices at the MAX IV light source

The beam lines described in Table 2 will use the insertion devices shortly described in Table 3.

Table 3: Insertion devices at the MAX IV 3 GeV storage ring

ID	Beamline	Type	Length	Period
wigS	SXB, MAG	Hybride type wiggler	1.0 m	80 mm
wigD	MSC, TOM	Hybride type wiggler	4.0 m	80 mm
pmuA	PX1, NF1, NF2	In-vacuum undulator	3.8 m	18.5 mm
pmuB	MUS, HIK	In-vacuum undulator	3.8 m	20.0 mm
pmuC	ENV	In-vacuum undulato	3.8 m	22.0 mm
cpmuA	PX2	Cryo-cooled in-vacuum undulator	3.8 m	15.6 mm
cpmuA	SXM	Cryo-cooled in-vacuum undator	3.8 m	16.4 mm
epuA	HRS, MAG	Elliptically polarising undator	4.0 m	38.0 mm

The insertion devices in Table 3 have been modelled in Radia [2] and in the following section details of the magnet models, magnetic fields, photon energy ranges, emitted power, kick maps and tune shifts are described.

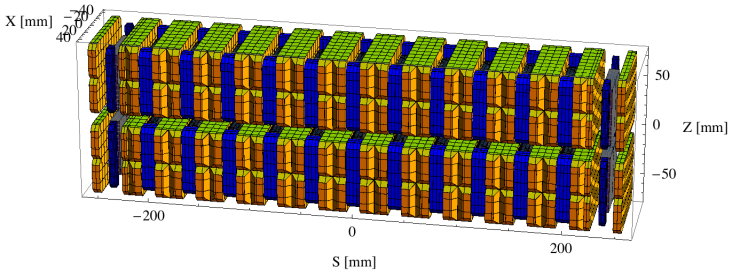

Figure 5: Magnetic model of the wigS ID

4 Magnet model calculations

4.1 The wigS ID

4.1.1 Magnet model of the wigS ID

The wigS is a wiggler of hybrid type and the magnetic model of the wigS is shown in Figure 5. the total length of the magnet model is 510.7 mm. The magnet model is built from three basic building blocks, which are the main blocks, the side blocks, and the poles. The main blocks, which are yellow in Figure 5, are made of an NdFeB material with a remanence of 1.25 T and an intrinsic coercivity of 25 kOerstedt. The main block material is similar to the material Vac863tp from Vacuumschmelze. The side blocks, which are blue in Figure 5, are made of an NdFeB material with a remanence of 1.28 T and an intrinsic coercivity of 21 kOerstedt The side block material is similar to the material Vac776tp from Vacuumschmelze. The poles, which are grey in Figure 5, are made a Vanadium Permendur type material from MetalImphy (Fe : 49%, Co: 49%, V: 2%), a material similar to Vacoflux50 from VacuumSchmelze.

4.1.2 Analysis of the magnetic field of the wigS ID

The vertical magnetic field in a central pole of the wigS ID along the ID axis, X = Z = 0 is shown in Figure 6. The vertical magnetic field in a central pole of the wigS ID in the horizontally transverse direction to the ID axis, S = Z = 0, is shown in Figure 7.

A Fourier anlysis of the magnetic field along the axis of the ID gives the higher harmonic contents in the magnetic field. A non-sinusoidal magnetic field profile along the ID would give a large higher harmonics contribution and it would no longer be possible to calculate the K-value of the ID from the peak field only. Also the higher harmonic contribution must be included to get the correct efficient magnetic field and efficient K-value. The higher harmonic contribution to the magnetic field is given in in Table 4.

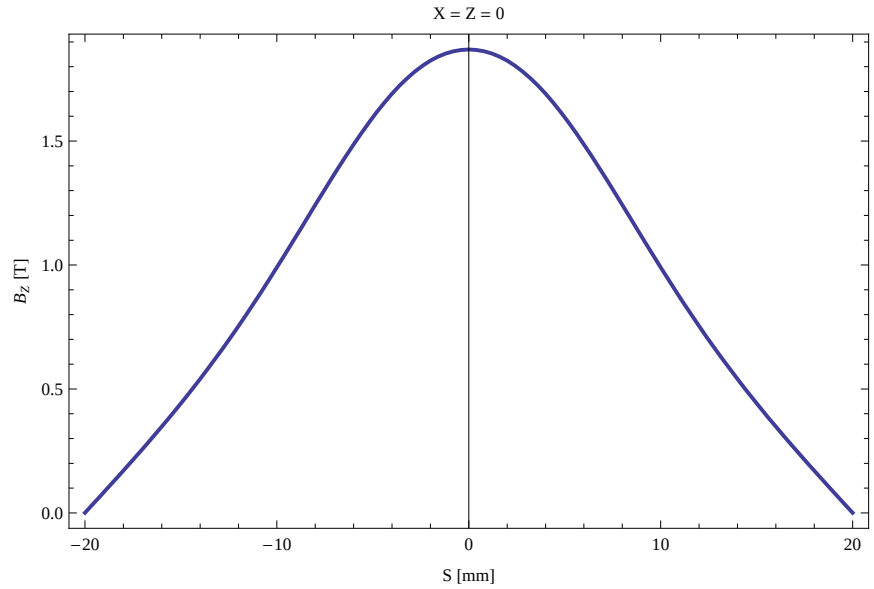

Figure 6: Vertical magnetic field in a central pole of the wigS ID along the ID axis, X = Z = 0

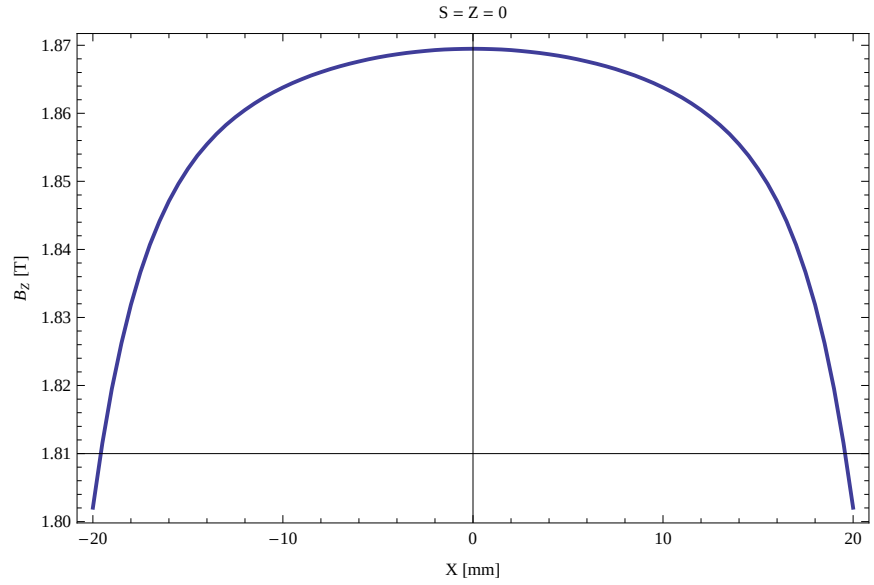

Figure 7: Vertical magnetic field in a central pole of the wigS ID along the horizontally transverse direction to the ID axis, S = Z = 0

Table 4: Fourier Analysis of the magnetic field of the wigS ID

Term	Strength
Harm. Nr. 1	1.639 T
Harm. Nr. 3	0.219 T
Harm. Nr. 5	0.016 T
Harm. Nr. 7	-0.003 T
Harm. Nr. 9	-0.001 T
Harm. Nr. 11	-0.000 T

A tranverse field roll-off may pose a problem to the storage ring since it gives a horizontal tune shift. The transverse field roll-off for the wigS for different horizontal positions out from the ID axis is shown in Figure 7 and numbers are given in Table 5.

Table 5: Transverse field roll-off for the wigS ID

X-Position	B_Z Field	Roll-off
± 0 mm	1.869 T	
± 5 mm	1.868 T	0.07 %
± 10 mm	1.864 T	0.30 %
± 15 mm	1.852 T	0.94 %
± 20 mm	1.802 T	3.61 %

The paremeters of the wigS are summarised in Table 6.

4.1.3 Synchrotron radiation from the wigS ID

The power map of the emitted synchrotron radiation by the wigS ID, assuming a 0.5 A filament beam with an energy of 3. GeV and bending magnet properties of the synchrotrn radiation, is shown in Figure 8.The on-axis power density is 8.933 kW/mrad^2. The spectral flux density on axis is shown in Figure 9. Deatiled calculations of the emitted synchrotron radiation is better carried out with dedicated software packages.

4.1.4 Influence from the wigS ID on the optics of the stored beam

Figure 10 shows the focusing potential from the wigS over the beam stay clear aperture of the ring aparture.

Figure 11 shows the kick map in the beam energy independant unit T^{2}m^2 of the kicks induced by the wigS ID over the beam stay clear aparture.

Table 6: Summary of the wigS ID parameters

Period	80.0	mm
Gap	12.0	mm
Peak Field	1.869	T
Effective Field	1.640	T
Peak k-value	13.969	
Effective k-value	12.258	
Higher Order Contr.	13.38	%
Maximum e-beam deflection	2.00	mrad
Electron Beam Energy	3.0	GeV
Electron Beam Current	500	mA
Max Critical Energy	11.189	keV
Emitted Power	7.284	kW
Photon Energy, n = 1	0.014	keV
Total Length	950.7	mm

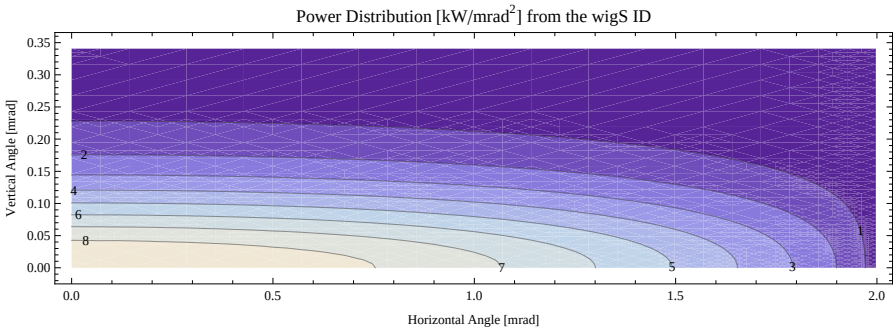

Figure 8: Map of the emitted power in the wigS ID

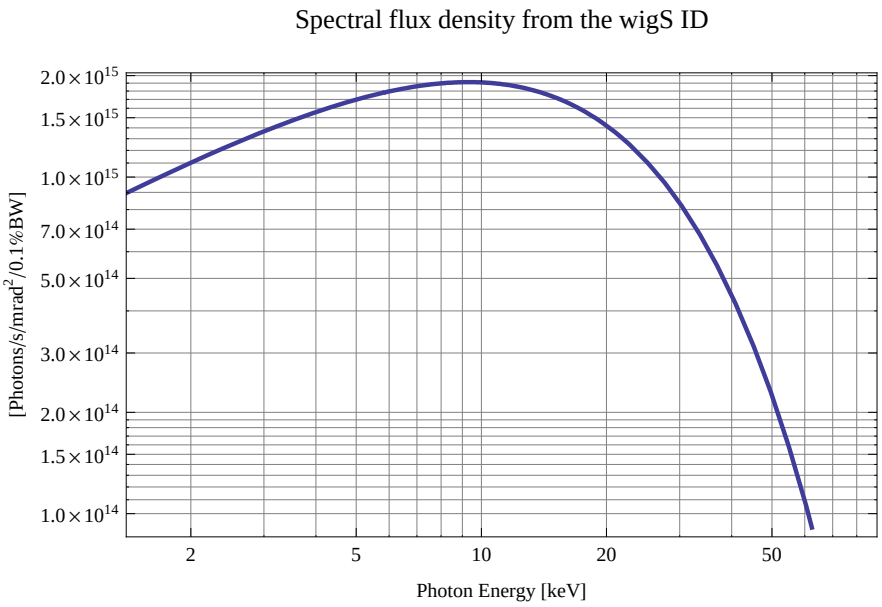

Figure 9: Spectral flux density of the wigS ID

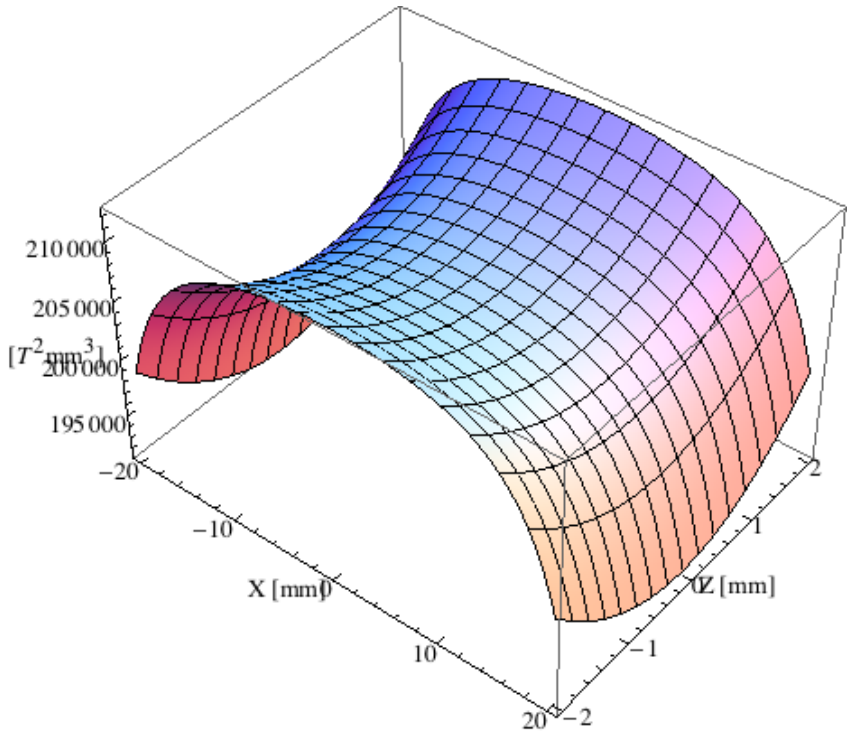

Figure 10: Focusing potential from the wigS ID over the beam stay clear aparture.

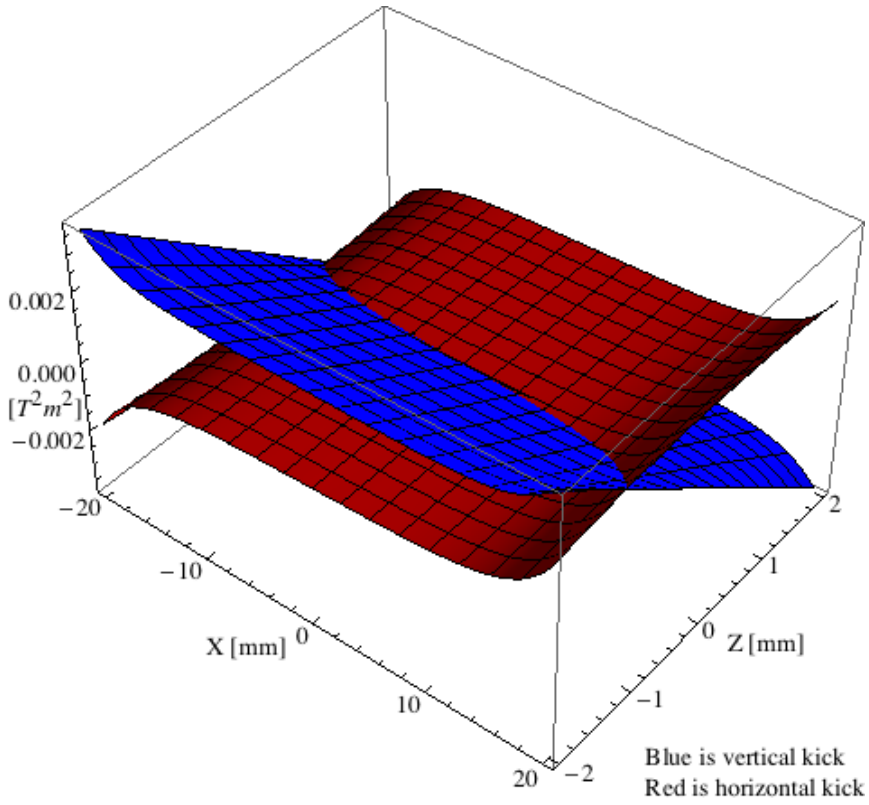

Figure 11: Kick map in the beam energy independant unit T^2m^2 of the kicks induced by the wigS ID over the beam stay clear aparture.

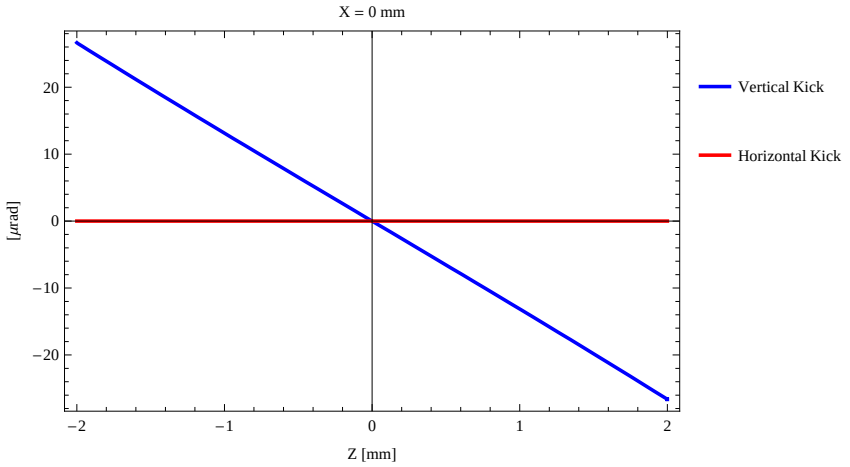

Figure 12: Induced angular kick on the stored beam from the wigS ID as a function of the vertical distance to the ID axis.

Figure 12 shows the induced angular kick on the stored beam from the wigS ID as a function of the vertical distance to the axis of the ID.

Figure 13 shows the induced angular kick on the stored beam from the wigS ID as a function of the horizontal distance to the axis of the ID.

Figure 14 shows tune shift induced by the wigS ID over the beam stay clear aparture. Note that the tune shift depends on the beam size at the ID.

Figure 15 shows the induced tune shift from the wigS ID as a function of the vertical distance to the axis of the ID.

Figure 16 shows the induced tune shift from the wigS ID as a function of the horizontal distance to the axis of the ID.

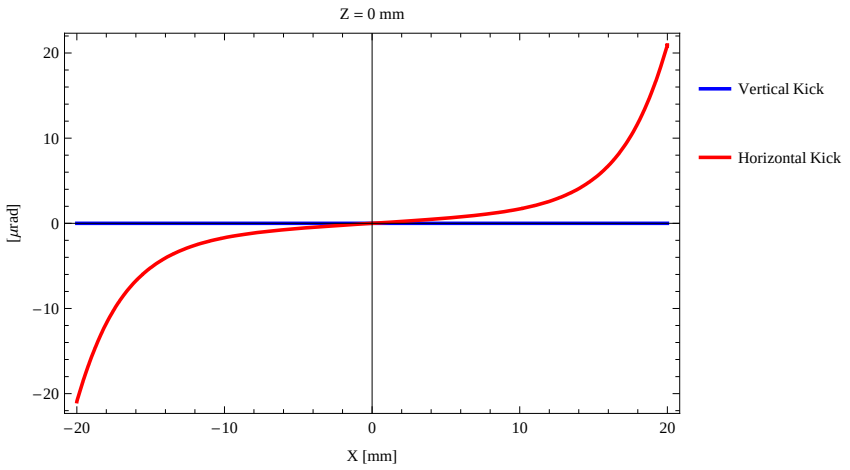

Figure 13: Induced angular kick on the stored beam from the wigS ID as a function of the horizontal distance to the ID axis.

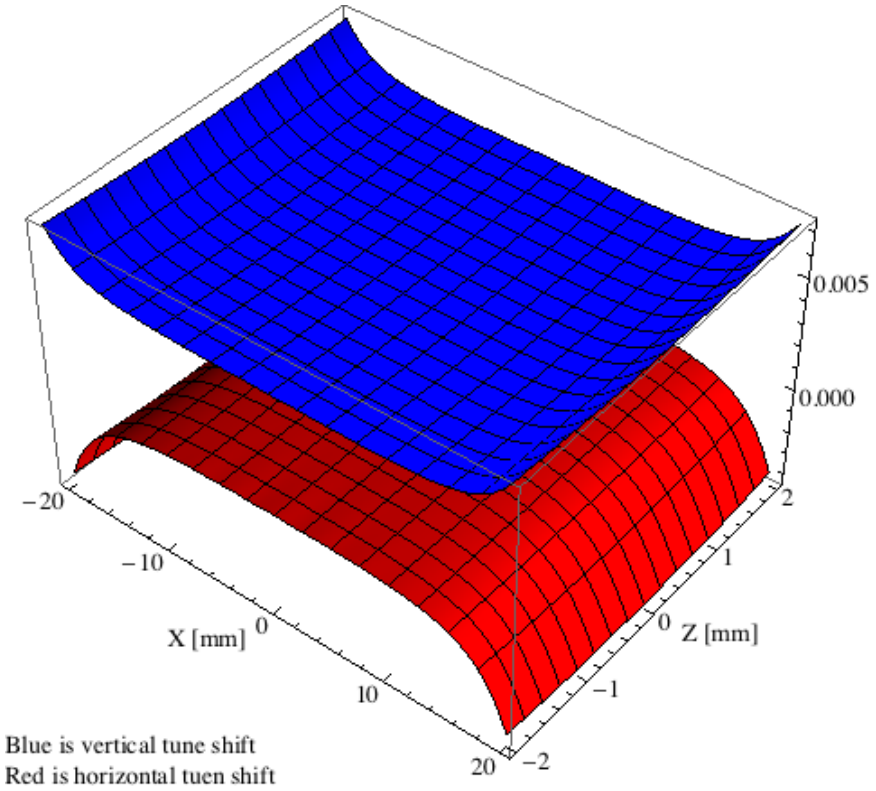

Figure 14: Tune shift induced by the wigS ID over the beam stay clear aparture.

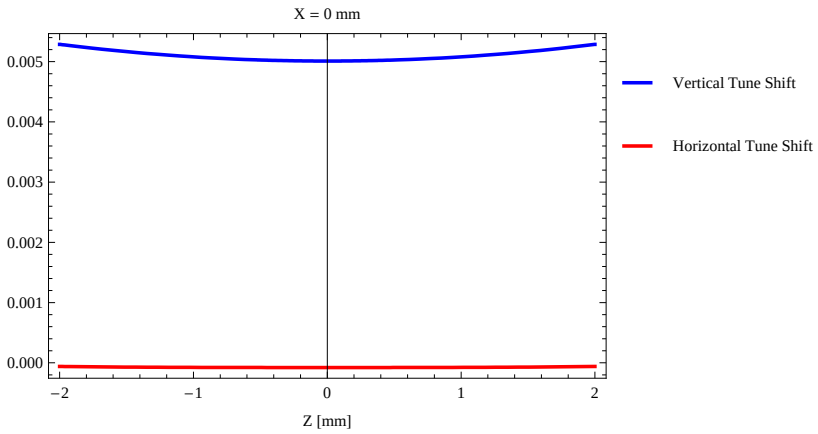

Figure 15: Induced tune shift from the wigS ID as a function of the vertical distance to the axis of the ID.

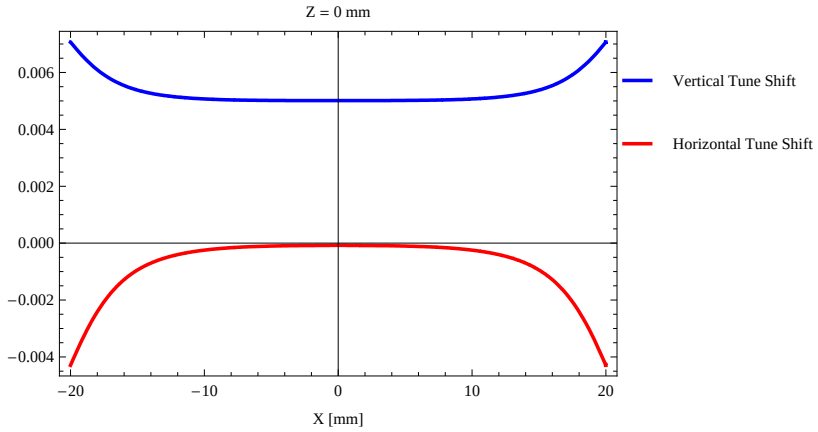

Figure 16: Induced tune shift from the wigS ID on the stored beam from the ID as a function of the horizontal distance to the axis of the ID.

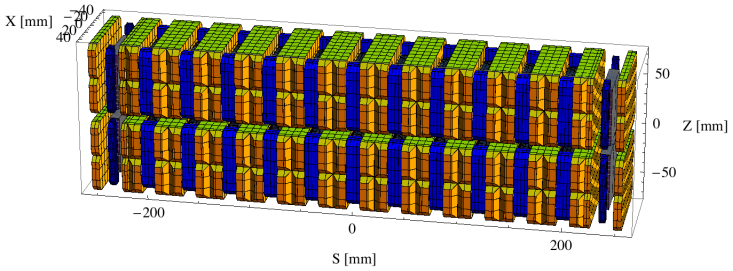

Figure 17: Magnetic model of the wigD ID

4.2 The wigD ID

4.2.1 Magnet model of the wigD ID

The wigD is a wiggler of hybrid type and the magnetic model of the wigD is shown in Figure 17. the total length of the magnet model is 510.7 mm. The magnet model is built from three basic building blocks, which are the main blocks, the side blocks, and the poles. The main blocks, which are yellow in Figure 17, are made of an NdFeB material with a remanence of 1.25 T and an intrinsic coercivity of 25 kOerstedt. The main block material is similar to the material Vac863tp from Vacuumschmelze. The side blocks, which are blue in Figure 17, are made of an NdFeB material with a remanence of 1.28 T and an intrinsic coercivity of 21 kOerstedt The side block material is similar to the material Vac776tp from Vacuumschmelze. The poles, which are grey in Figure 17, are made a Vanadium Permendur type material from MetalImphy (Fe : 49%, Co: 49%, V: 2%), a material similar to Vacoflux50 from VacuumSchmelze.

4.2.2 Analysis of the magnetic field of the wigD ID

The vertical magnetic field in a central pole of the wigD ID along the ID axis, X = Z = 0 is shown in Figure 18. The vertical magnetic field in a central pole of the wigD ID in the horizontally transverse direction to the ID axis, S = Z = 0, is shown in Figure 19.

A Fourier anlysis of the magnetic field along the axis of the ID gives the higher harmonic contents in the magnetic field. A non-sinusoidal magnetic field profile along the ID would give a large higher harmonics contribution and it would no longer be possible to calculate the K-value of the ID from the peak field only. Also the higher harmonic contribution must be included to get the correct efficient magnetic field and efficient K-value. The higher harmonic contribution to the magnetic field is given in in Table 7.

A tranverse field roll-off may pose a problem to the storage ring since it gives a horizontal tune shift. The transverse field roll-off for the wigD for different horizontal positions out

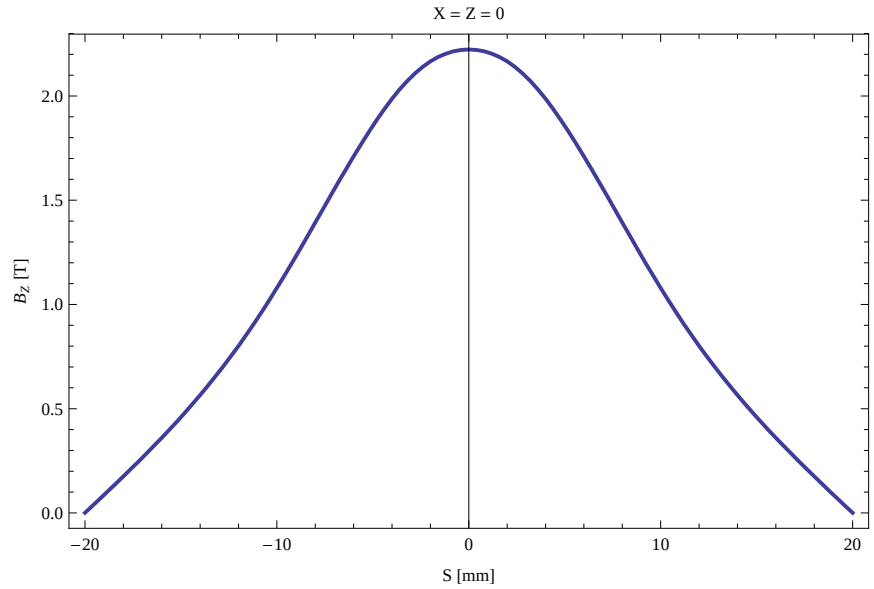

Figure 18: Vertical magnetic field in a central pole of the wigD ID along the ID axis, X = Z = 0

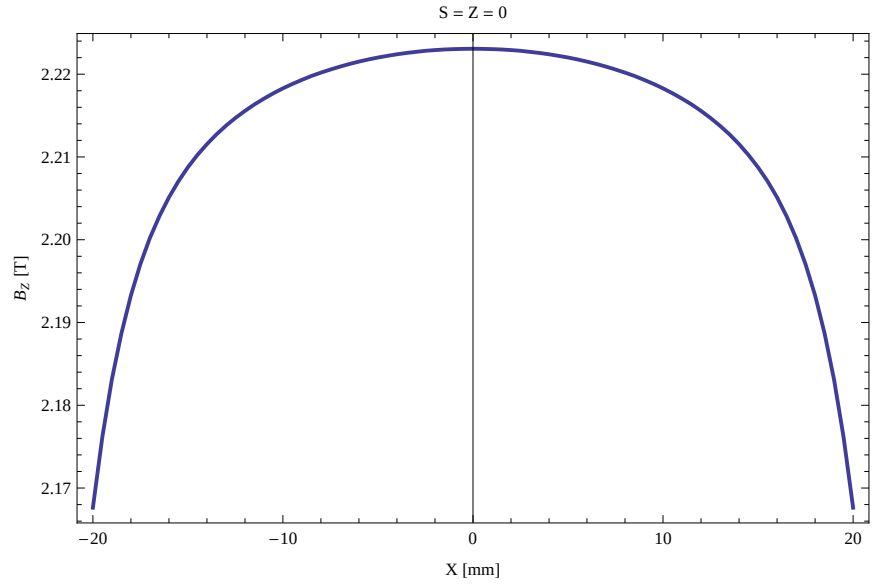

Figure 19: Vertical magnetic field in a central pole of the wigD ID along the horizontally transverse direction to the ID axis, S = Z = 0

Table 7: Fourier Analysis of the magnetic field of the wigD ID

Term	Strength
Harm. Nr. 1	1.883 T
Harm. Nr. 3	0.318 T
Harm. Nr. 5	0.032 T
Harm. Nr. 7	-0.005 T
Harm. Nr. 9	-0.003 T
Harm. Nr. 11	-0.001 T

from the ID axis is shown in Figure 19 and numbers are given in Table 8.

Table 8: Transverse field roll-off for the wigD ID

X-Position	B_Z Field	Roll-off
± 0 mm	2.223 T	
± 5 mm	2.222 T	0.05 %
± 10 mm	2.218 T	0.22 %
± 15 mm	2.209 T	0.64 %
± 20 mm	2.168 T	2.49 %

The paremeters of the wigD are summarised in Table 9.

Table 9: Summary of the wigD ID parameters

Period	80.0	mm
Gap	9.0	mm
Peak Field	2.223	T
Effective Field	1.886	T
Peak k-value	16.611	
Effective k-value	14.096	
Higher Order Contr.	17.00	%
Maximum e-beam deflection	2.27	mrad
Electron Beam Energy	3.0	GeV
Electron Beam Current	500	mA
Max Critical Energy	13.305	keV
Emitted Power	40.434	kW
Photon Energy, n = 1	0.011	keV
Total Length	3990.7	mm

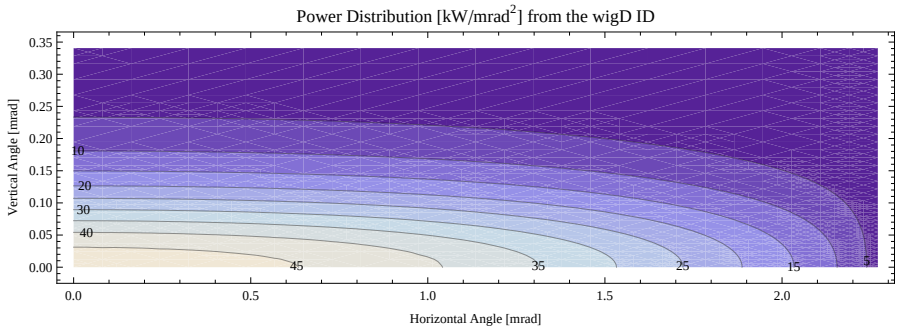

Figure 20: Map of the emitted power in the wigD ID

4.2.3 Synchrotron radiation from the wigD ID

The power map of the emitted synchrotron radiation by the wigD ID, assuming a 0.5 A filament beam with an energy of 3. GeV and bending magnet properties of the synchrotrn radiation, is shown in Figure 20.The on-axis power density is 47.751 kW/mrad^2. The spectral flux density on axis is shown in Figure 21. Deatiled calculations of the emitted synchrotron radiation is better carried out with dedicated software packages.

4.2.4 Influence from the wigD ID on the optics of the stored beam

Figure 22 shows the focusing potential from the wigD over the beam stay clear aperture of the ring aparture.

Figure 23 shows the kick map in the beam energy independant unit T^{2}m^2 of the kicks induced by the wigD ID over the beam stay clear aparture.

Figure 24 shows the induced angular kick on the stored beam from the wigD ID as a function of the vertical distance to the axis of the ID.

Figure 25 shows the induced angular kick on the stored beam from the wigD ID as a function of the horizontal distance to the axis of the ID.

Figure 26 shows tune shift induced by the wigD ID over the beam stay clear aparture. Note that the tune shift depends on the beam size at the ID.

Figure 27 shows the induced tune shift from the wigD ID as a function of the vertical distance to the axis of the ID.

Figure 28 shows the induced tune shift from the wigD ID as a function of the horizontal distance to the axis of the ID.

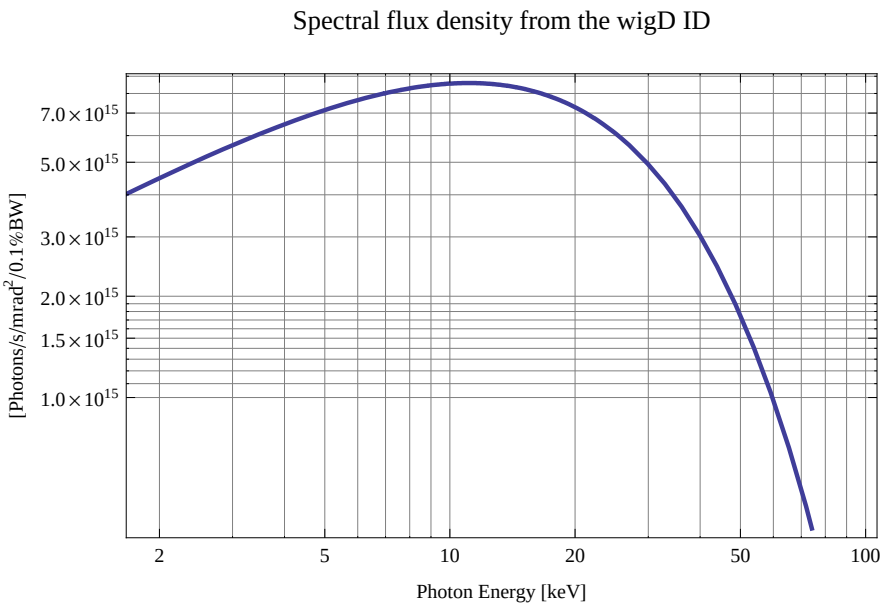

Figure 21: Spectral flux density of the wigD ID

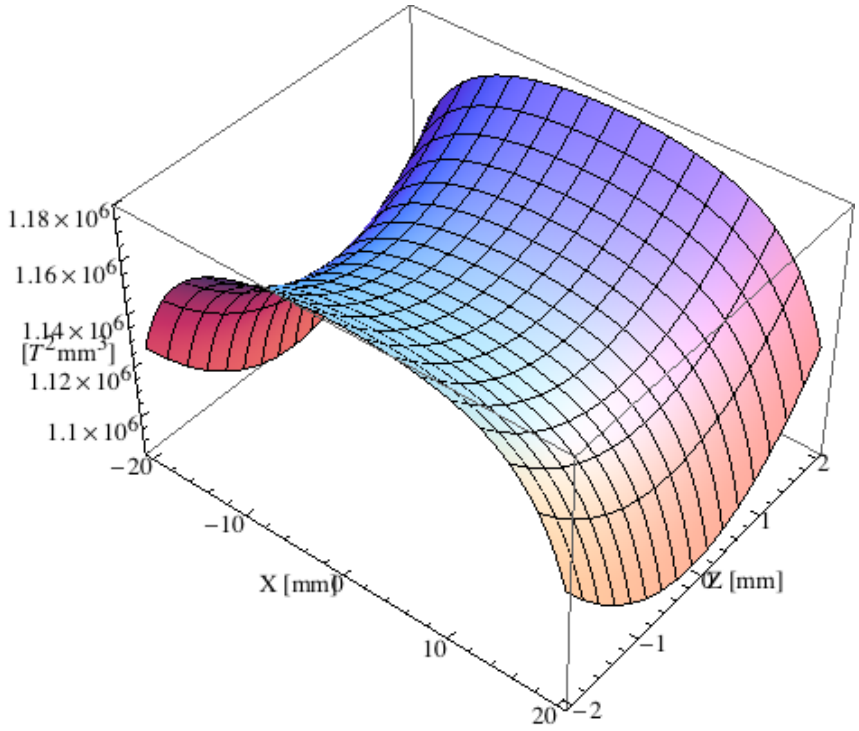

Figure 22: Focusing potential from the wigD ID over the beam stay clear aparture.

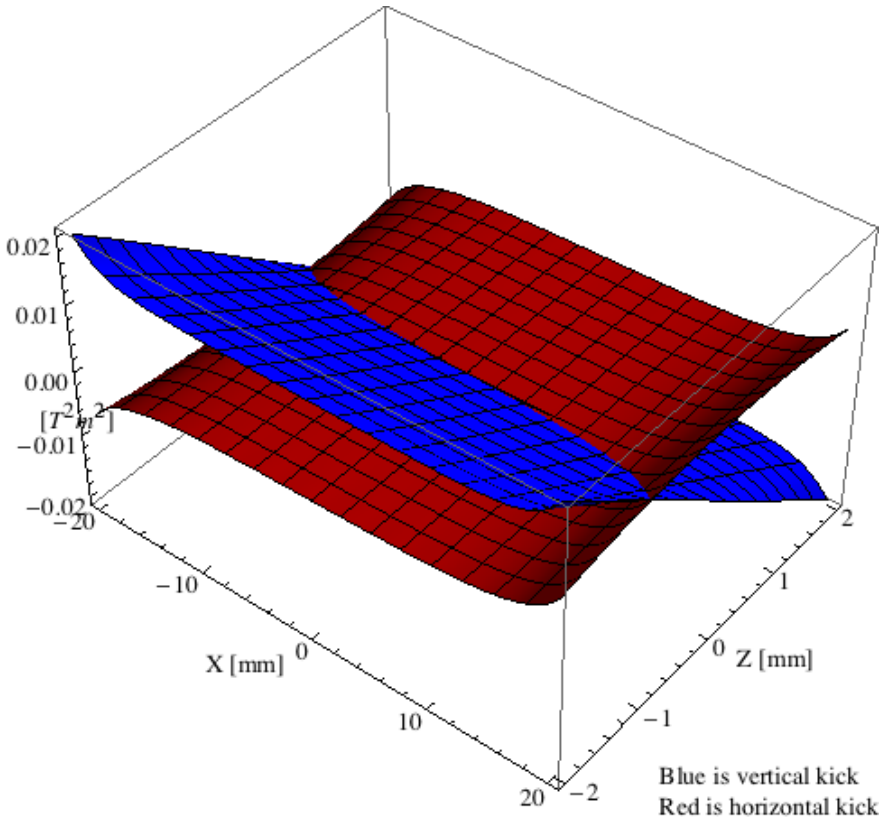

Figure 23: Kick map in the beam energy independant unit T^2m^2 of the kicks induced by the wigD ID over the beam stay clear aparture.

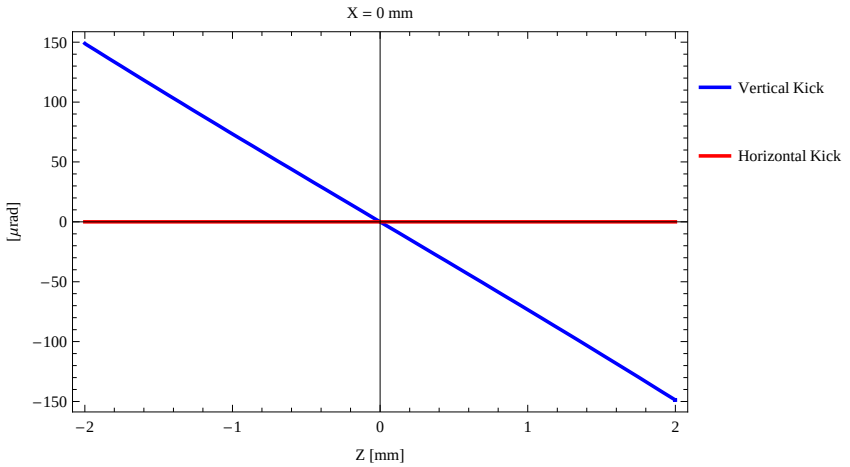

Figure 24: Induced angular kick on the stored beam from the wigD ID as a function of the vertical distance to the ID axis.

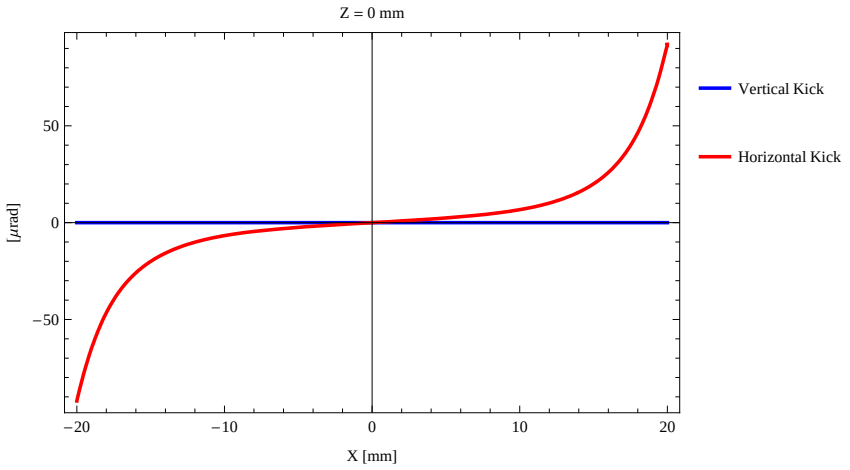

Figure 25: Induced angular kick on the stored beam from the wigD ID as a function of the horizontal distance to the ID axis.

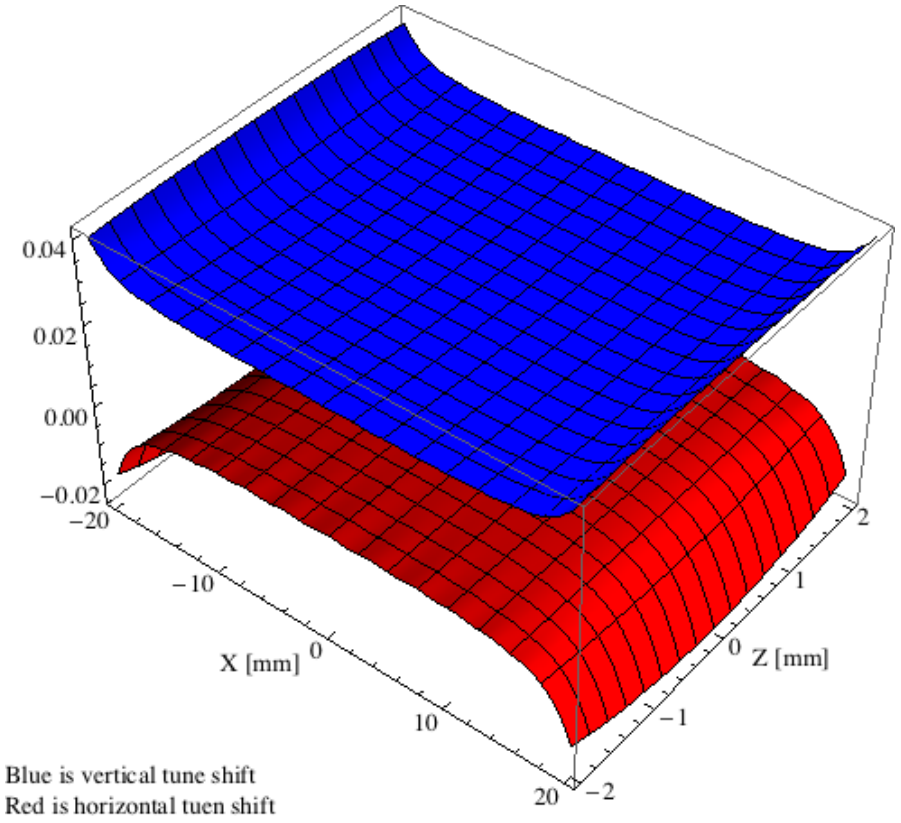

Figure 26: Tune shift induced by the wigD ID over the beam stay clear aparture.

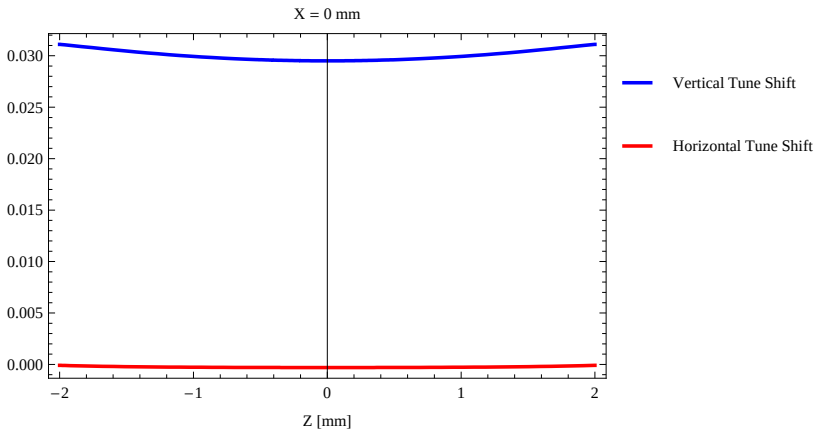

Figure 27: Induced tune shift from the wigD ID as a function of the vertical distance to the axis of the ID.

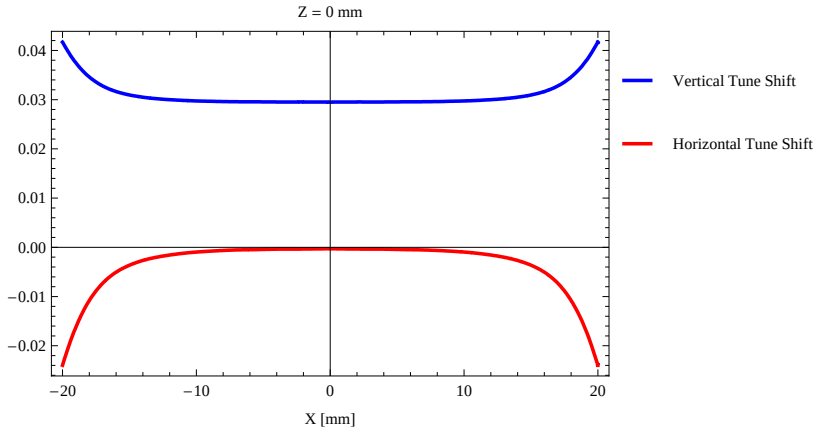

Figure 28: Induced tune shift from the wigD ID on the stored beam from the ID as a function of the horizontal distance to the axis of the ID.

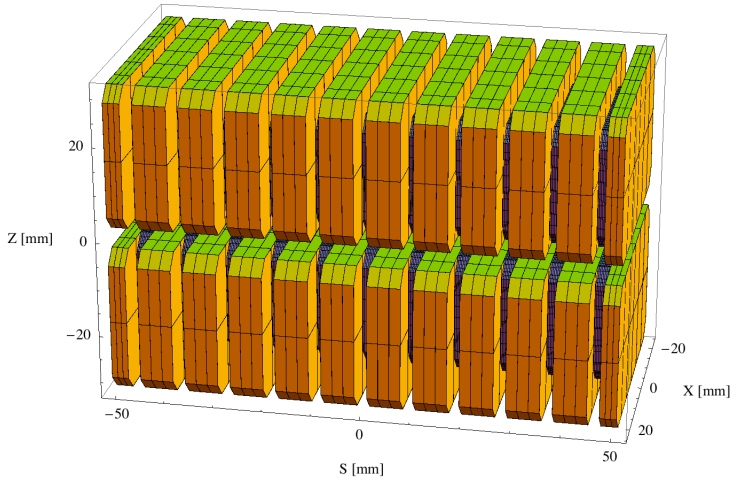

Figure 29: Magnetic model of the pmuA ID

4.3 The pmuA ID

4.3.1 Magnet model of the pmuA ID

The pmuA is an in-vacuum undulator of hybrid type and the magnetic model of the pmuA is shown in Figure 29. The magnet blocks, which are yellow in Figure 29, are made of the magnetic material Sm_2Co_17 with a magnetic remanence of 1.05 T at ambient temperature. The dimensions of the magnet blocks are 50.00x6.73x30.00x mm^3 and there is a 4 mm chamfer at the corners of the magnet blocks. The poles, which are grey in Figure 29, are made of pure iron. The dimensions of the poles are 32.00x2.52x24.00x mm^3 and there is a 3 mm chamfer at the corners of the poles.

4.3.2 Analysis of the magnetic field of the pmuA ID

The vertical magnetic field in a central pole of the pmuA ID along the ID axis, X = Z = 0 is shown in Figure 30. The vertical magnetic field in a central pole of the pmuA ID in the horizontally transverse direction to the ID axis, S = Z = 0, is shown in Figure 31.

A Fourier anlysis of the magnetic field along the axis of the ID gives the higher harmonic contents in the magnetic field. A non-sinusoidal magnetic field profile along the ID would give a large higher harmonics contribution and it would no longer be possible to calculate the K-value of the ID from the peak field only. Also the higher harmonic contribution must be included to get the correct efficient magnetic field and efficient K-value. The higher harmonic contribution to the magnetic field is given in in Table 10.

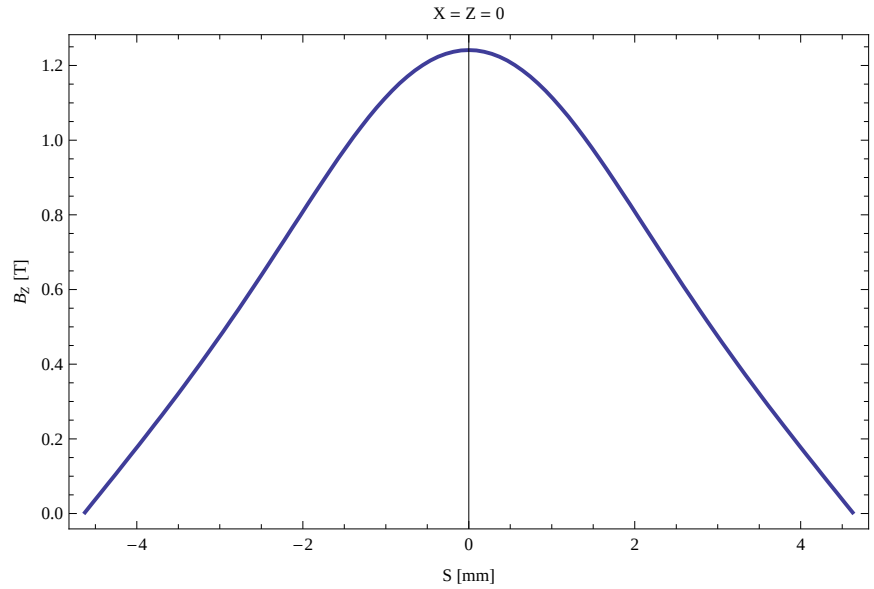

Figure 30: Vertical magnetic field in a central pole of the pmuA ID along the ID axis, X = Z = 0

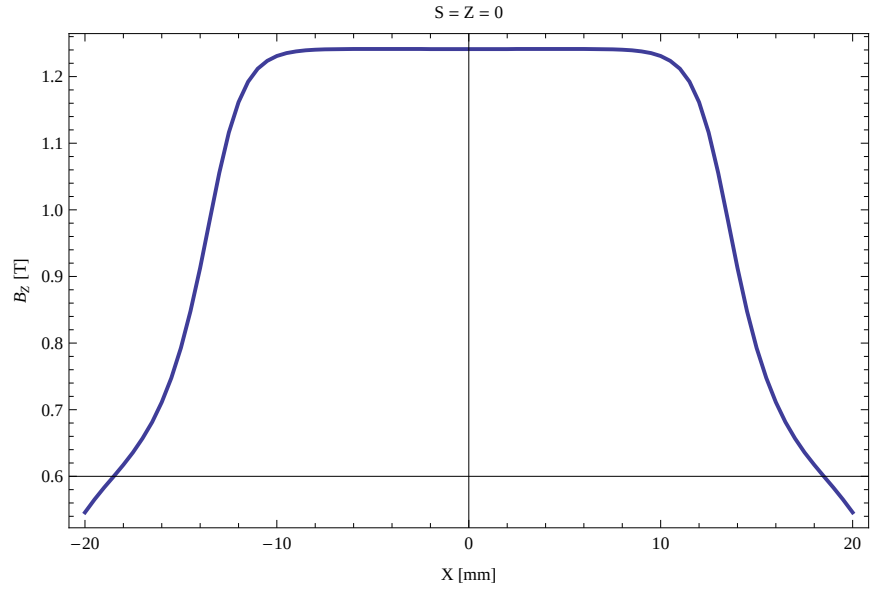

Figure 31: Vertical magnetic field in a central pole of the pmuA ID along the horizontally transverse direction to the ID axis, S = Z = 0

Table 10: Fourier Analysis of the magnetic field of the pmuA ID

Term	Strength
Harm. Nr. 1	1.111 T
Harm. Nr. 3	0.114 T
Harm. Nr. 5	0.008 T
Harm. Nr. 7	-0.001 T
Harm. Nr. 9	-0.001 T
Harm. Nr. 11	-0.000 T

A tranverse field roll-off may pose a problem to the storage ring since it gives a horizontal tune shift. The transverse field roll-off for the pmuA for different horizontal positions out from the ID axis is shown in Figure 31 and numbers are given in Table 11.

Table 11: Transverse field roll-off for the pmuA ID

X-Position	B_Z Field	Roll-off
± 0 mm	1.241 T	
± 5 mm	1.241 T	-0.01 %
± 10 mm	1.231 T	0.84 %
± 15 mm	0.793 T	36.14 %
± 20 mm	0.546 T	56.03 %

The paremeters of the pmuA are summarised in Table 12.

4.3.3 Synchrotron radiation from the pmuA ID

The power map of the emitted synchrotron radiation by the pmuA ID, assuming a 0.5 A filament beam with an energy of 3. GeV and undulator properties of the synchrotron radiation, is shown in Figure 32. The on-axis power density is 97.108 kW/mrad^2

A map of the degree of linear polarisation of the fundamental harmonic of the synchotron radiation emitted by the pmuA ID over the angle of obsevation is shown in Figure 33.

A map of the degree of 45 degree polarisation of the fundamental harmonic of the synchotron radiation emitted by the pmuA ID over the angle of obsevation is shown in Figure 34.

A map of the degree of circular polarisation of the fundamental harmonic of the synchotron radiation emitted by the pmuA ID over the angle of obsevation is shown in Figure 35.

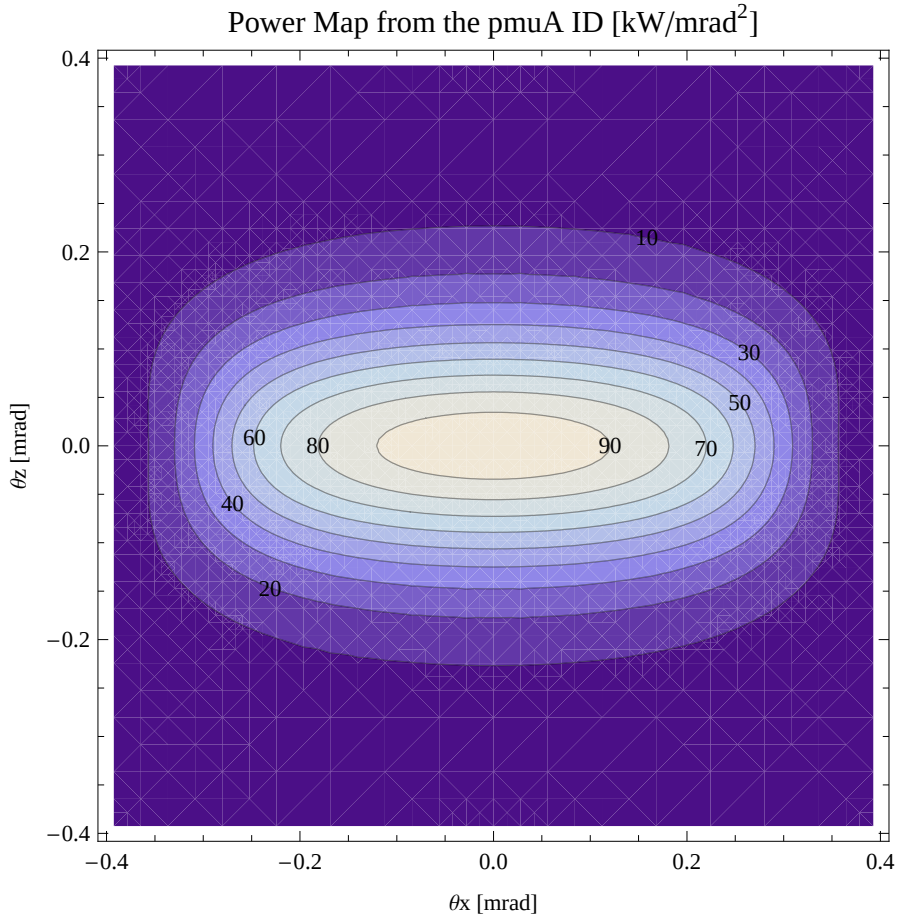

Figure 32: Map of the power distribution of the emitted synchrotron radiation by the pmuA ID

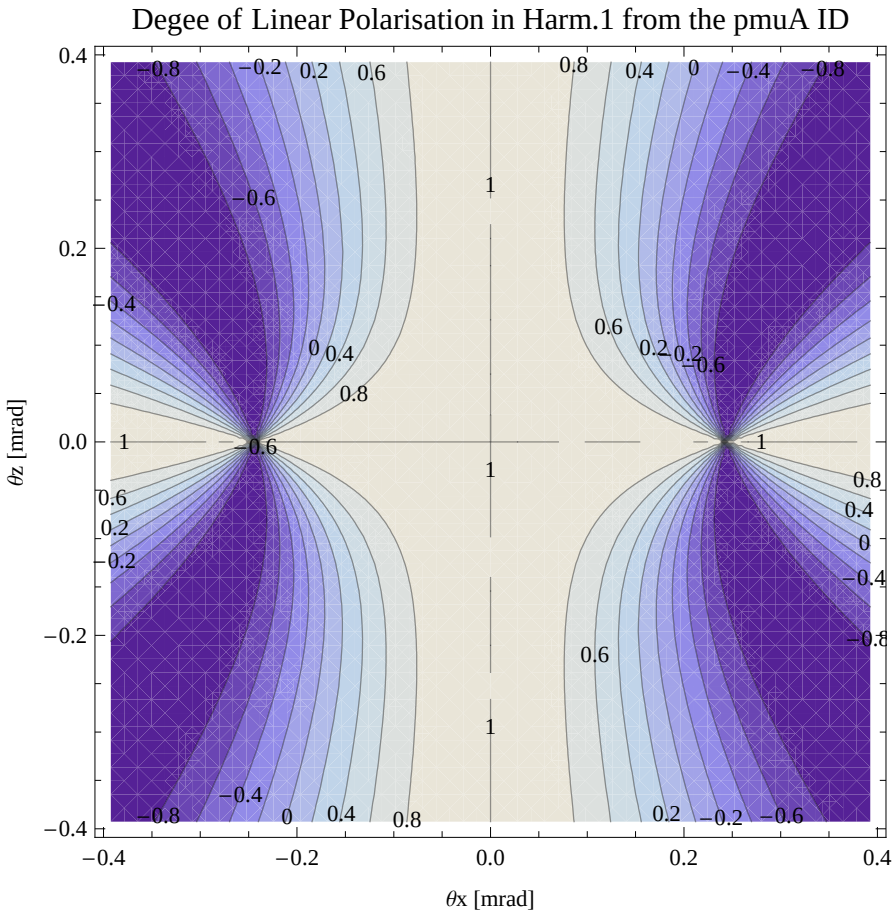

Figure 33: Map of linear polarisation in the fundamental harmonic of the synchotron radiation emitted by the pmuA ID

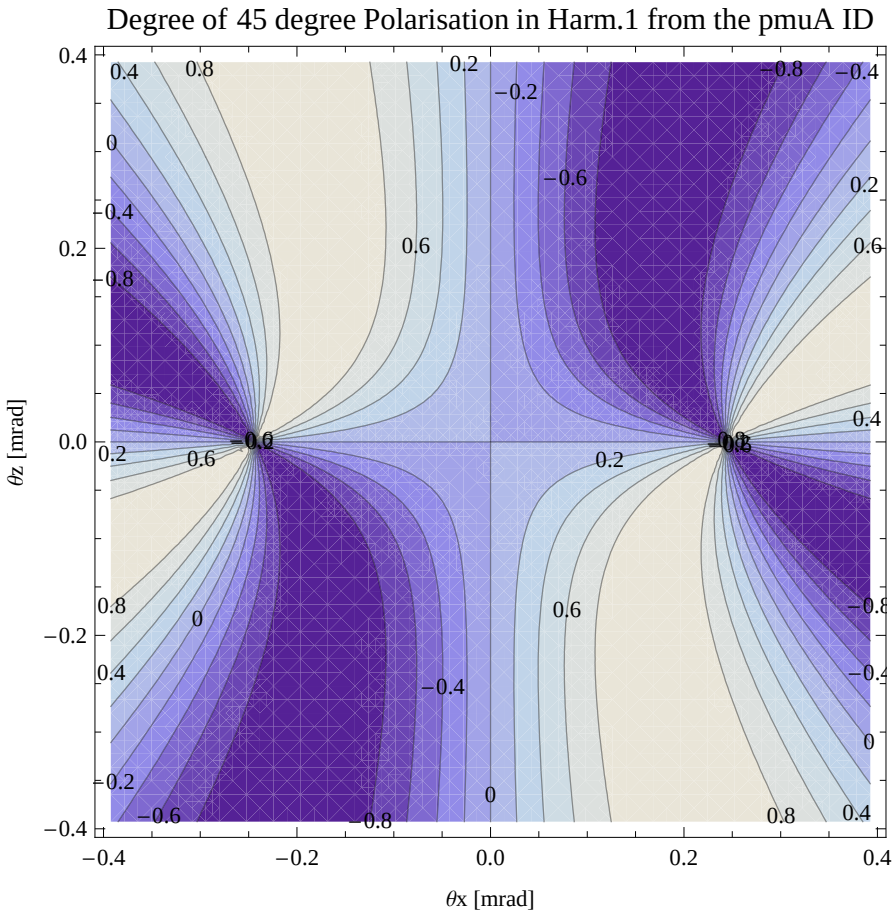

Figure 34: Map of 45 degree polarisation in the fundamental harmonic of the synchotron radiation emitted by the pmuA ID

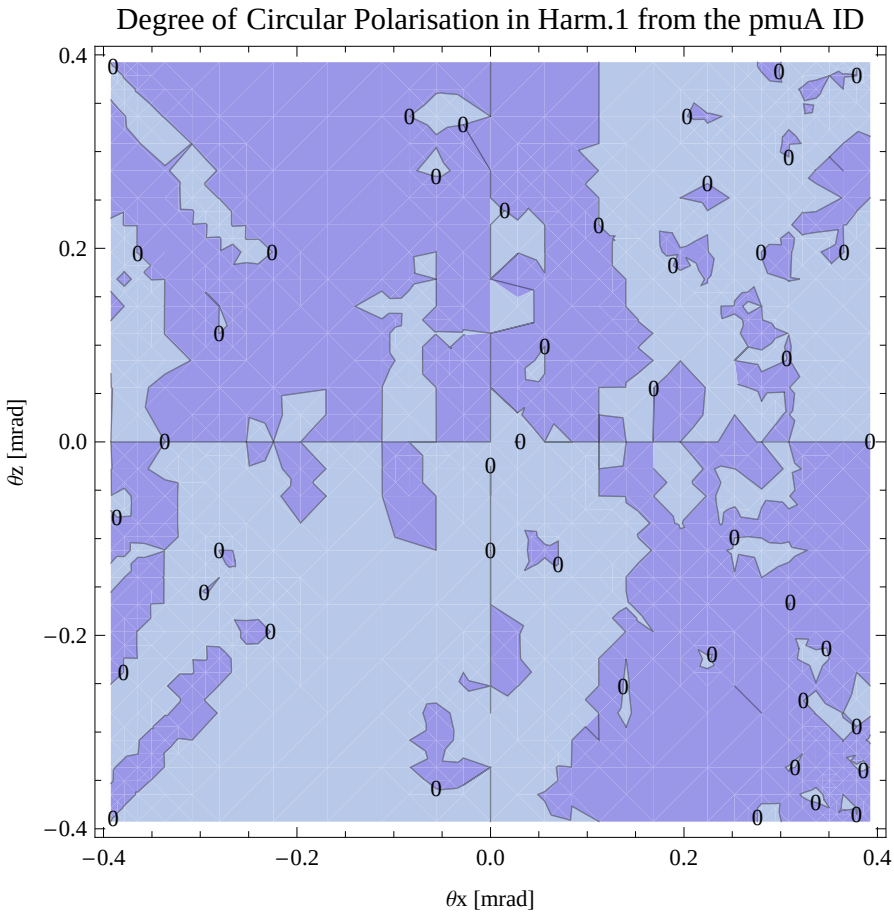

Figure 35: Map of circular polarisation in the fundamental harmonic of the synchotron radiation emitted by the pmuA ID

Table 12: Summary of the pmuA ID parameters

Period	18.5	mm
Gap	4.2	mm
Peak Field	1.241	T
Effective Field	1.111	T
Peak k-value	2.145	
Effective k-value	1.920	
Higher Order Contr.	10.33	%
Maximum e-beam deflection	0.32	mrad
Electron Beam Energy	3.0	GeV
Electron Beam Current	500	mA
Max Critical Energy	7.429	keV
Emitted Power	13.306	kW
Photon Energy, n = 1	1.625	keV
Total Length	3783.3	mm

The on axis brilliance at peak energy the and spectral flux density, also often called angular spectral flux, from the pmuA ID has been calculated with the given beam parameters, which are 0.5 A of stored current, $\beta_H = 9.$ m, $\varepsilon_H = 0.263$ nmrad, $\beta_V = 4.8$ m, $\varepsilon_V = 8.$ pmrad, and an energy spread of 0.001. Figure 36 shows the brilliance at peak energy and Figure 37 shows the the spectral flux density.

The brilliance at peak energy the and the spectral flux density from the pmuA ID for different harmonics at maximum K-value (1.920) are given in Table 13 and for minimum K-value (0.400) these values are given in Table 14.

Table 13: The brilliance at peak energy the and the spectral flux density from the pmuA ID for different harmonics at maximum K-value (1.920)

Harmonic	Photon Energy [keV]	Brilliance [Ph./s/mrad^2/mrad^2/0.1%BW]	Spectral Flux Density [Ph./s/mrad^2/0.1%BW]
1	1.62435	2.23×10^{21}	5.6×10^{18}
3	4.87304	1.6×10^{21}	3.41×10^{18}
5	8.12174	9.72×10^{20}	$2. \times 10^{18}$
7	11.3704	5.91×10^{20}	1.2×10^{18}
9	14.6191	3.61×10^{20}	7.24×10^{17}
11	17.8678	2.22×10^{20}	4.42×10^{17}

The brilliance at peak energy the and the spectral flux density from the pmuA ID for different harmonics at maximum K-value (1.920) are given in Table 13 and for minimum

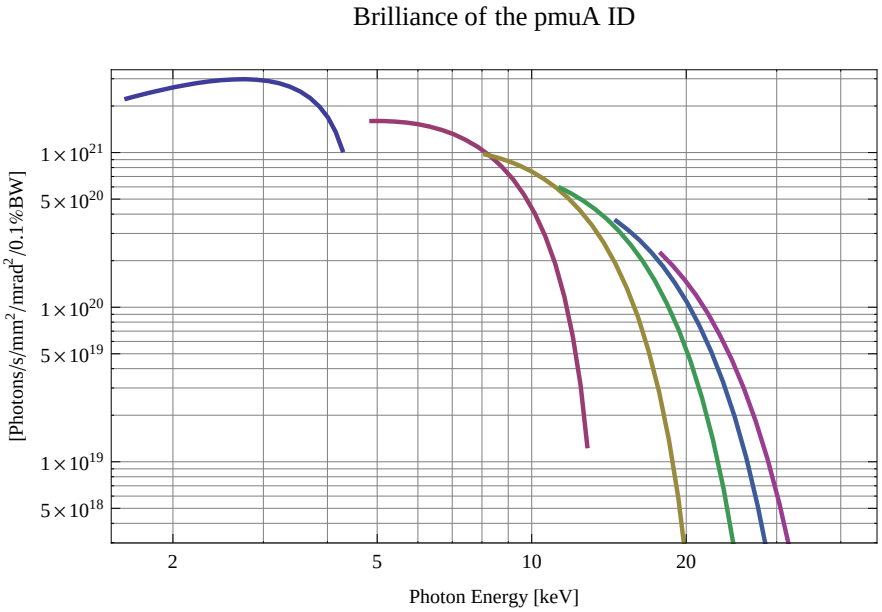

Figure 36: The brilliance at peak energy of the synchotron radiation emitted by the pmuA ID

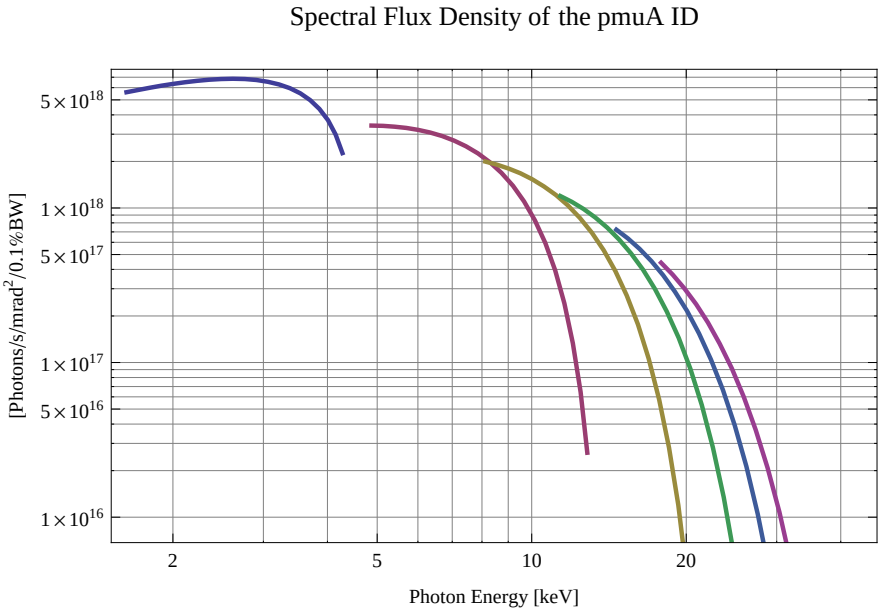

Figure 37: The spectral flux density of the synchotron radiation emitted by the pmuA ID

K-value (0.400) these values are given in Table 14.

Table 14: The brilliance at peak energy the and the spectral flux density from the pmuA ID for different harmonics at minimum K-value (0.4)

Harmonic	Photon Energy [keV]	Brilliance [Ph./s/mrad^2/mrad^2/0.1%BW]	Spectral Flux Density [Ph./s/mrad^2/0.1%BW]
1	4.27766	1.04×10^{21}	2.26×10^{18}
3	12.833	1.26×10^{19}	2.61×10^{16}
5	21.3883	1.3×10^{17}	2.66×10^{14}
7	29.9436	1.31×10^{15}	2.69×10^{12}
9	38.4989	1.33×10^{13}	2.72×10^{10}
11	47.0542	1.34×10^{11}	2.75×10^{8}

4.3.4 Influence from the pmuA ID on the optics of the stored beam

Figure 38 shows the focusing potential from the pmuA over the beam stay clear aperture of the ring aparture.

Figure 39 shows the kick map in the beam energy independant unit T^2m^2 of the kicks induced by the pmuA ID over the beam stay clear aparture.

Figure 40 shows the induced angular kick on the stored beam from the pmuA ID as a function of the vertical distance to the axis of the ID.

Figure 41 shows the induced angular kick on the stored beam from the pmuA ID as a function of the horizontal distance to the axis of the ID.

Figure 42 shows tune shift induced by the pmuA ID over the beam stay clear aparture. Note that the tune shift depends on the beam size at the ID.

Figure 43 shows the induced tune shift from the pmuA ID as a function of the vertical distance to the axis of the ID.

Figure 44 shows the induced tune shift from the pmuA ID as a function of the horizontal distance to the axis of the ID.

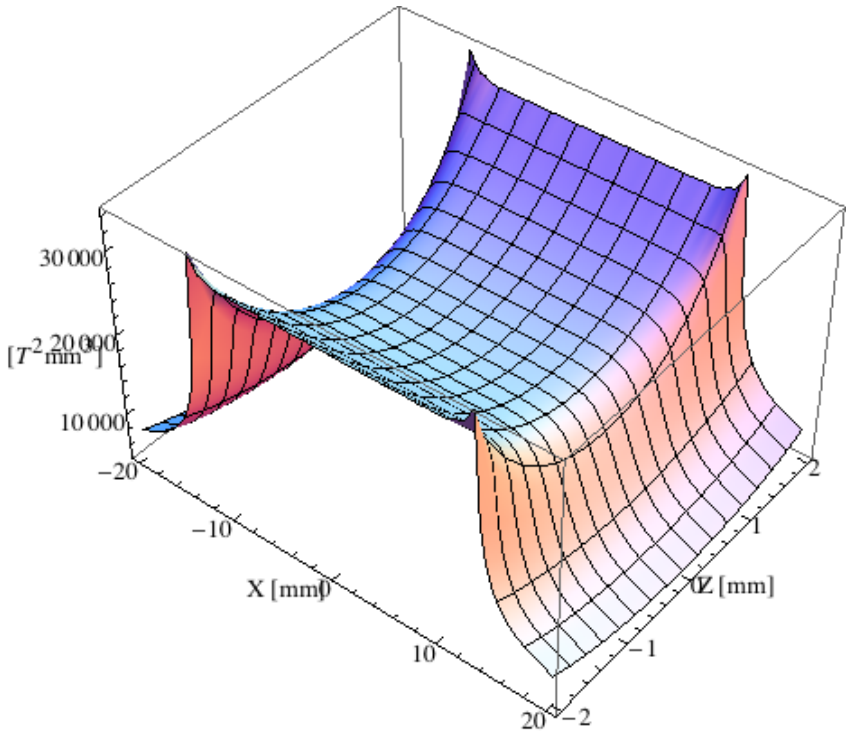

Figure 38: Focusing potential from the pmuA ID over the beam stay clear aparture.

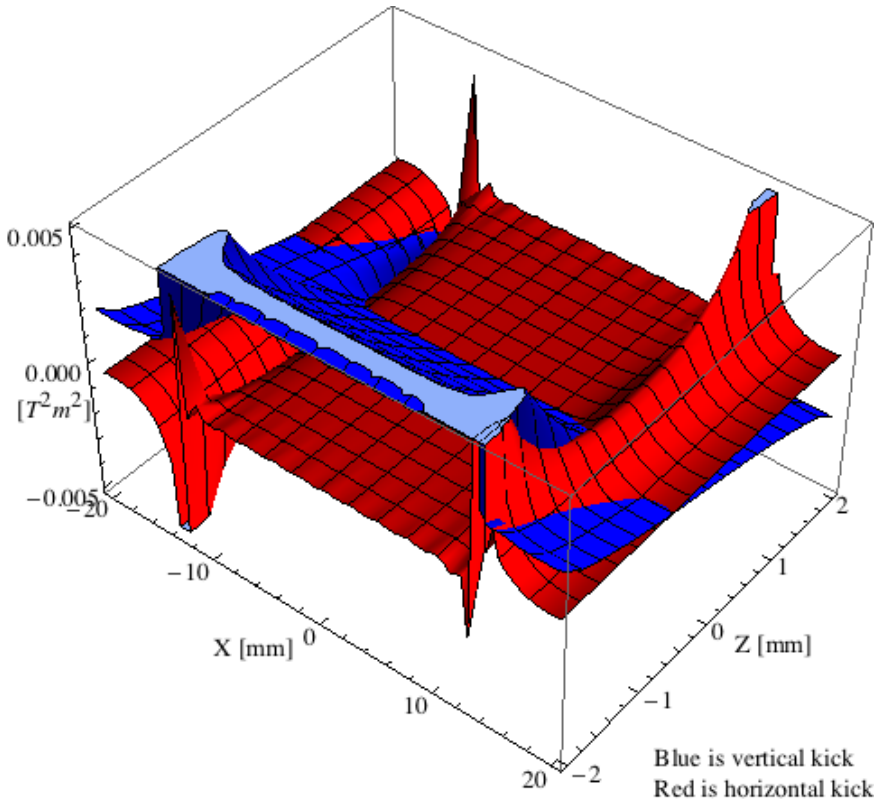

Figure 39: Kick map in the beam energy independant unit T^2m^2 of the kicks induced by the pmuA ID over the beam stay clear aparture.

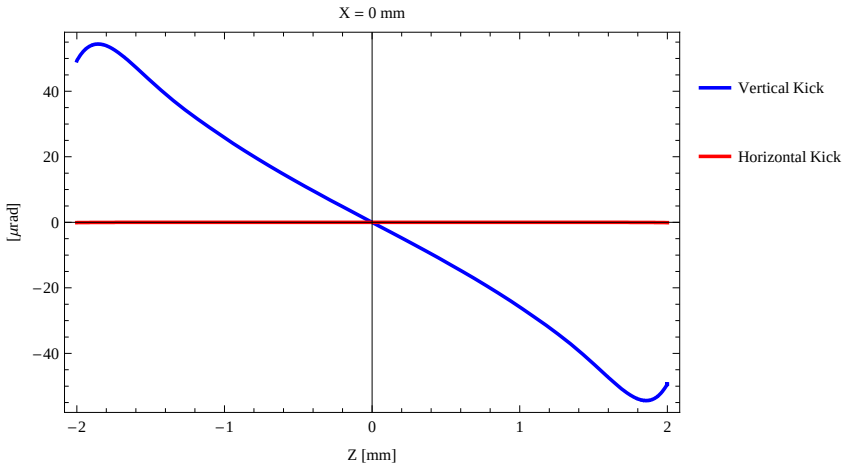

Figure 40: Induced angular kick on the stored beam from the pmuA ID as a function of the vertical distance to the ID axis.

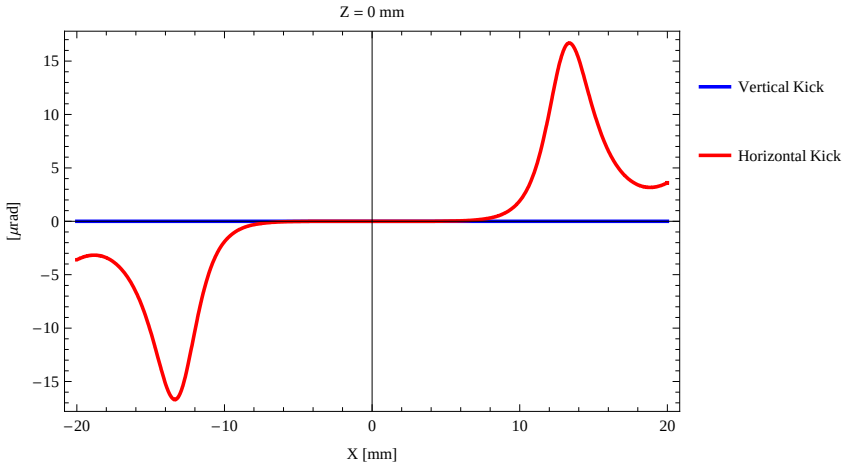

Figure 41: Induced angular kick on the stored beam from the pmuA ID as a function of the horizontal distance to the ID axis.

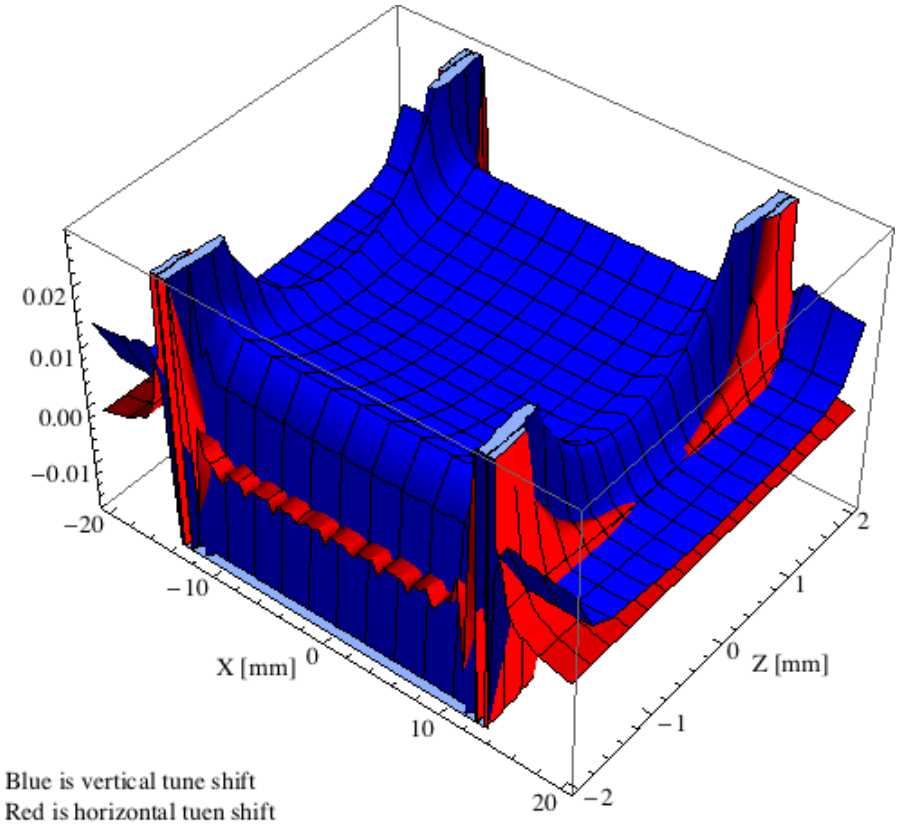

Figure 42: Tune shift induced by the pmuA ID over the beam stay clear aparture.

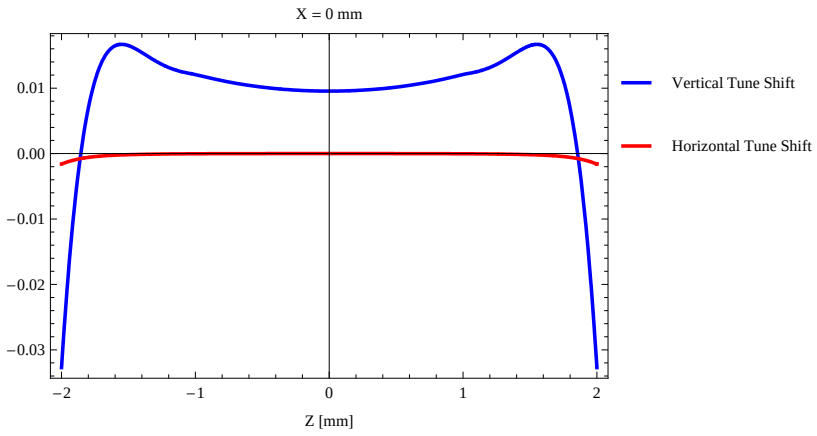

Figure 43: Induced tune shift from the pmuA ID as a function of the vertical distance to the axis of the ID.

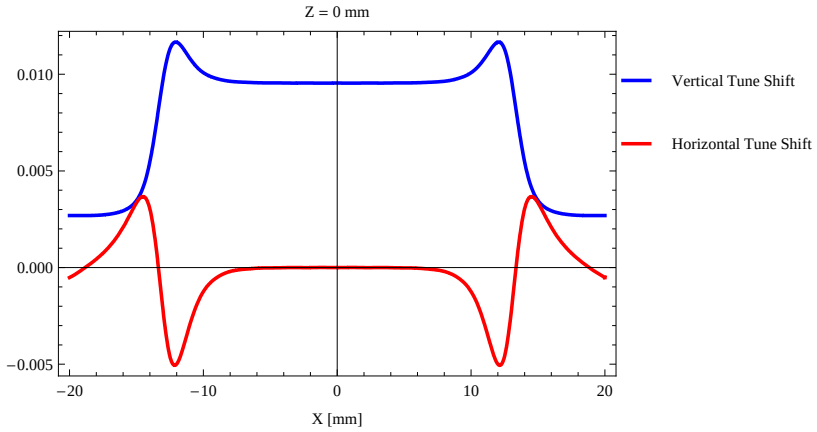

Figure 44: Induced tune shift from the pmuA ID on the stored beam from the ID as a function of the horizontal distance to the axis of the ID.

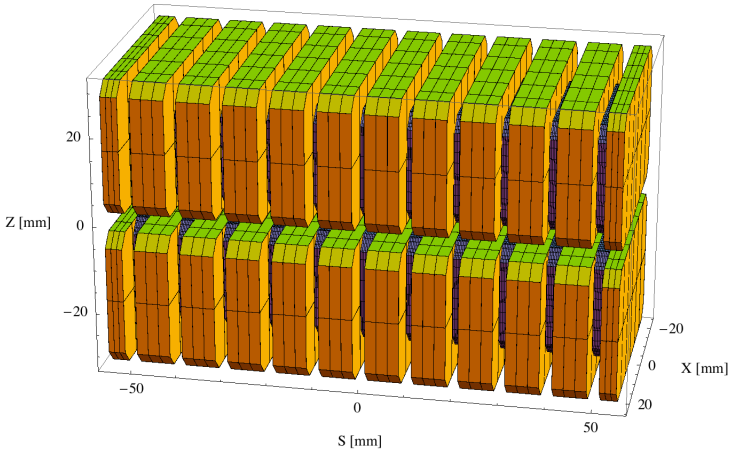

Figure 45: Magnetic model of the pmuB ID

4.4 The pmuB ID

4.4.1 Magnet model of the pmuB ID

The pmuB is an in-vacuum undulator of hybrid type and the magnetic model of the pmuB is shown in Figure 45. The magnet blocks, which are yellow in Figure 45, are made of the magnetic material Sm_2Co_17 with a magnetic remanence of 1.05 T at ambient temperature. The dimensions of the magnet blocks are 50.00x7.28x30.00x mm^3 and there is a 4 mm chamfer at the corners of the magnet blocks. The poles, which are grey in Figure 45, are made of pure iron. The dimensions of the poles are 32.00x2.72x24.00x mm^3 and there is a 3 mm chamfer at the corners of the poles.

4.4.2 Analysis of the magnetic field of the pmuB ID

The vertical magnetic field in a central pole of the pmuB ID along the ID axis, X = Z = 0 is shown in Figure 46. The vertical magnetic field in a central pole of the pmuB ID in the horizontally transverse direction to the ID axis, S = Z = 0, is shown in Figure 47.

A Fourier anlysis of the magnetic field along the axis of the ID gives the higher harmonic contents in the magnetic field. A non-sinusoidal magnetic field profile along the ID would give a large higher harmonics contribution and it would no longer be possible to calculate the K-value of the ID from the peak field only. Also the higher harmonic contribution must be included to get the correct efficient magnetic field and efficient K-value. The higher harmonic contribution to the magnetic field is given in in Table 15.

A tranverse field roll-off may pose a problem to the storage ring since it gives a horizontal

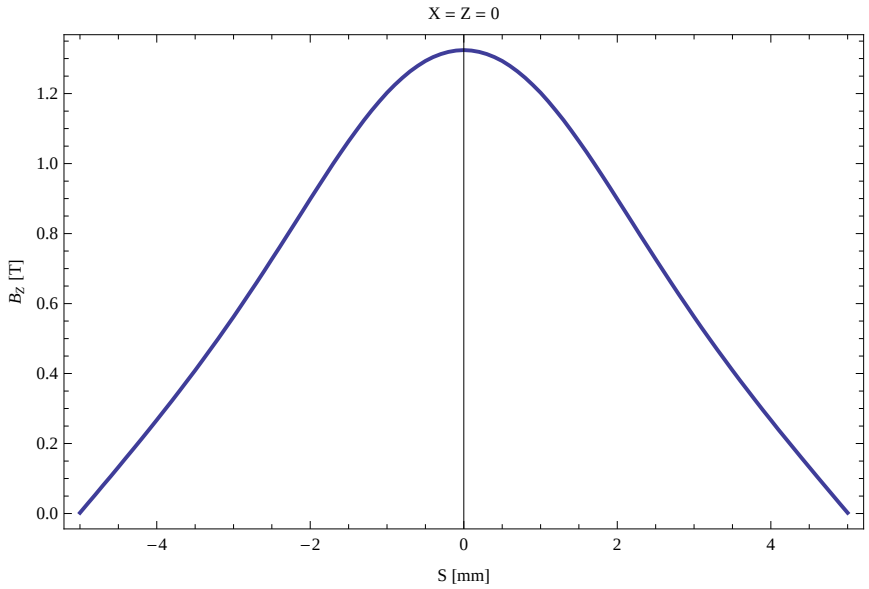

Figure 46: Vertical magnetic field in a central pole of the pmuB ID along the ID axis, X = Z = 0

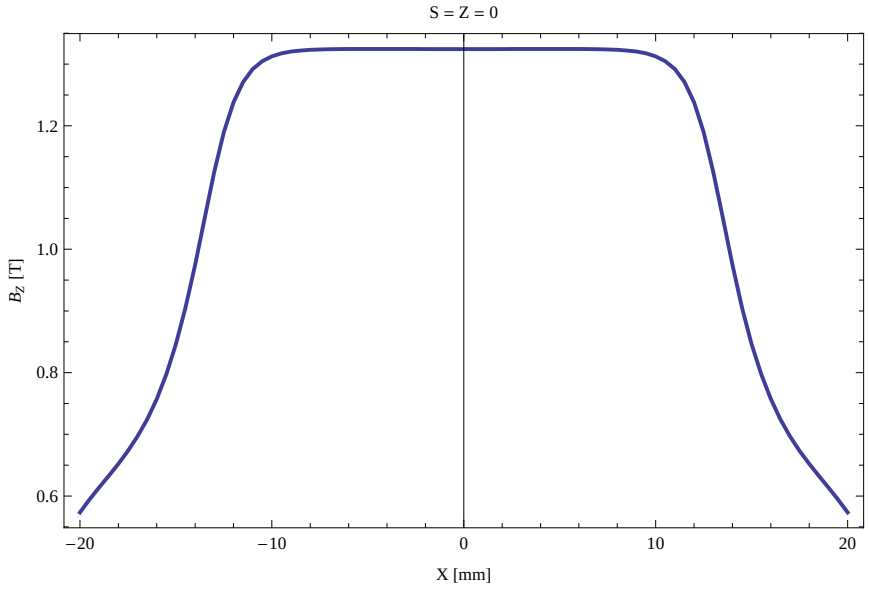

Figure 47: Vertical magnetic field in a central pole of the pmuB ID along the horizontally transverse direction to the ID axis, S = Z = 0

Table 15: Fourier Analysis of the magnetic field of the pmuB ID

Term	Strength
Harm. Nr. 1	1.172 T
Harm. Nr. 3	0.135 T
Harm. Nr. 5	0.011 T
Harm. Nr. 7	-0.001 T
Harm. Nr. 9	-0.001 T
Harm. Nr. 11	-0.000 T

tune shift. The transverse field roll-off for the pmuB for different horizontal positions out from the ID axis is shown in Figure 47 and numbers are given in Table 16.

Table 16: Transverse field roll-off for the pmuB ID

X-Position	B_Z Field	Roll-off
± 0 mm	1.324 T	
± 5 mm	1.325 T	-0.01 %
± 10 mm	1.313 T	0.89 %
± 15 mm	0.846 T	36.11 %
± 20 mm	0.573 T	56.70 %

The paremeters of the pmuB are summarised in Table 17.

Table 17: Summary of the pmuB ID parameters

Period	20.0	mm
Gap	4.2	mm
Peak Field	1.324	T
Effective Field	1.173	T
Peak k-value	2.474	
Effective k-value	2.191	
Higher Order Contr.	11.56	%
Maximum e-beam deflection	0.36	mrad
Electron Beam Energy	3.0	GeV
Electron Beam Current	500	mA
Max Critical Energy	7.927	keV
Emitted Power	14.845	kW
Photon Energy, n = 1	1.257	keV
Total Length	3790.0	mm

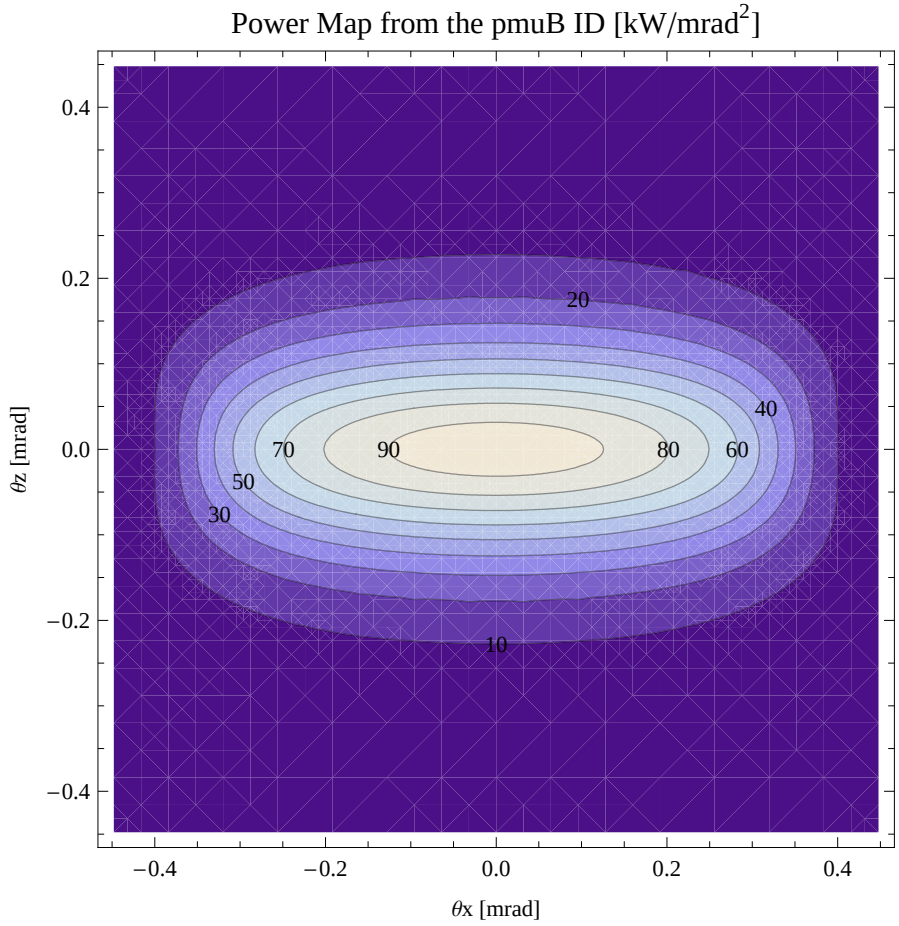

Figure 48: Map of the power distribution of the emitted synchrotron radiation by the pmuB ID

4.4.3 Synchrotron radiation from the pmuB ID

The power map of the emitted synchrotron radiation by the pmuB ID, assuming a 0.5 A filament beam with an energy of 3. GeV and undulator properties of the synchrotron radiation, is shown in Figure 48. The on-axis power density is 95.818 kW/mrad^2

A map of the degree of linear polarisation of the fundamental harmonic of the synchotron radiation emitted by the pmuB ID over the angle of obsevation is shown in Figure 49.

A map of the degree of 45 degree polarisation of the fundamental harmonic of the synchotron radiation emitted by the pmuB ID over the angle of obsevation is shown in Figure 50.

A map of the degree of circular polarisation of the fundamental harmonic of the syn-

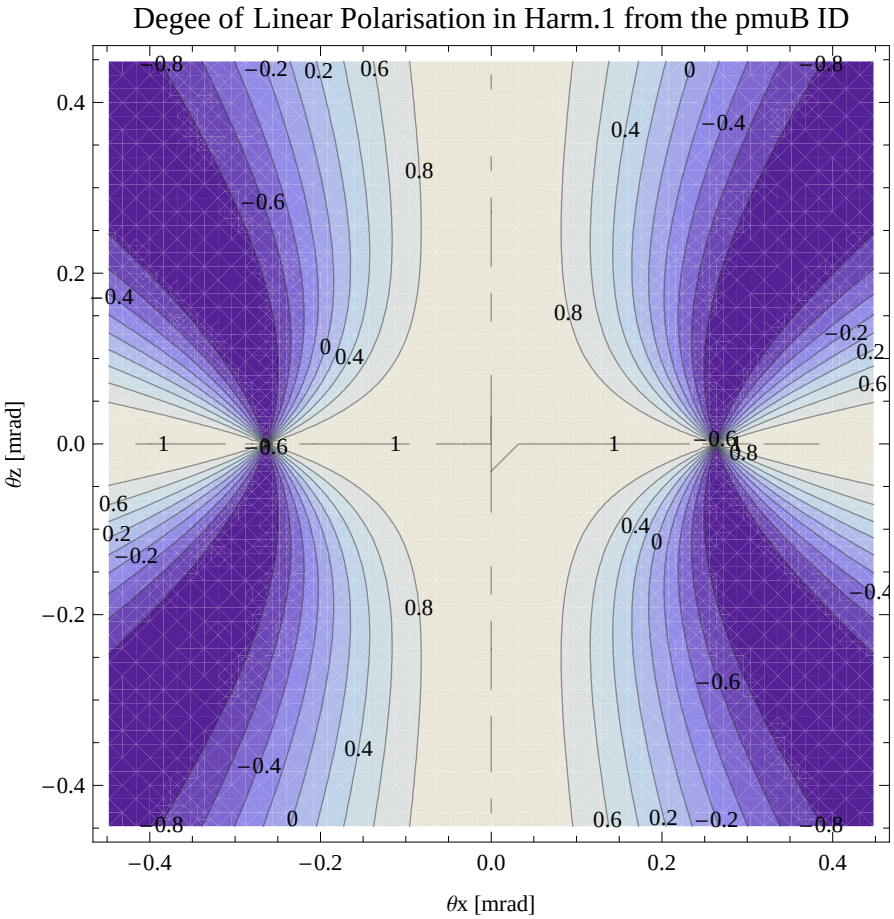

Figure 49: Map of linear polarisation in the fundamental harmonic of the synchotron radiation emitted by the pmuB ID

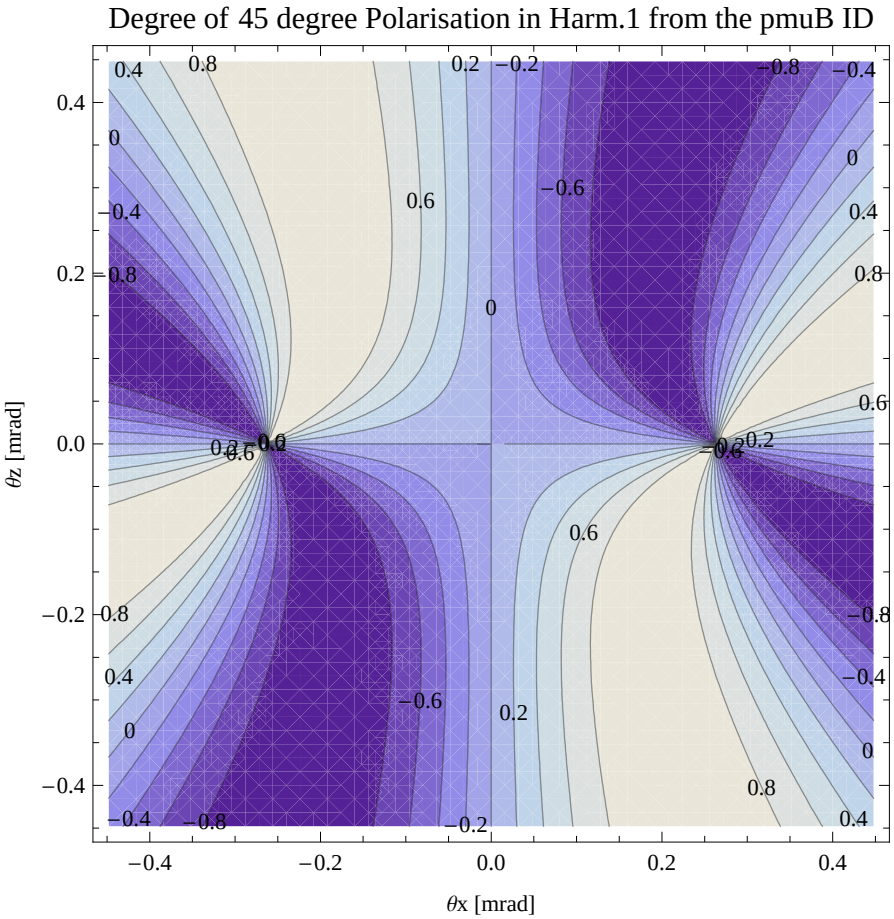

Figure 50: Map of 45 degree polarisation in the fundamental harmonic of the synchotron radiation emitted by the pmuB ID

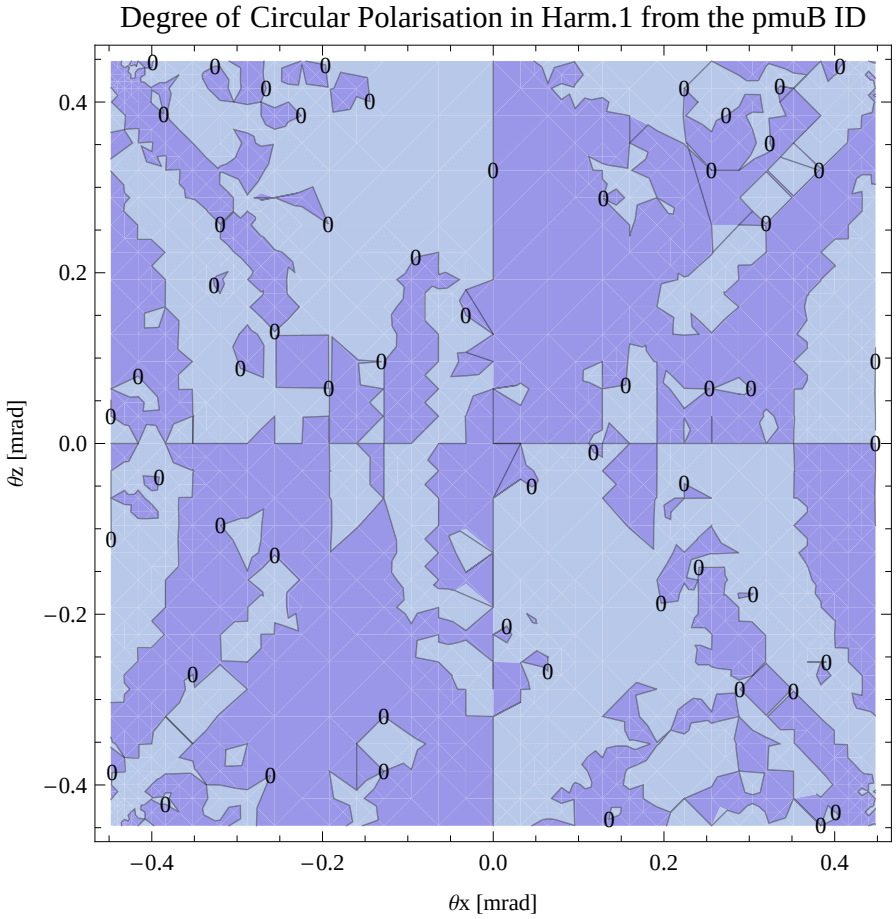

Figure 51: Map of circular polarisation in the fundamental harmonic of the synchotron radiation emitted by the pmuB ID

chotron radiation emitted by the pmuB ID over the angle of obsevation is shown in Figure 51.

The on axis brilliance at peak energy the and spectral flux density, also often called angular spectral flux, from the pmuB ID has been calculated with the given beam parameters, which are 0.5 A of stored current, $\beta_H = 9.$ m, $\varepsilon_H = 0.263$ nmrad, $\beta_V = 4.8$ m, $\varepsilon_V = 8.$ pmrad, and an energy spread of 0.001. Figure 52 shows the brilliance at peak energy and Figure 53 shows the the spectral flux density.

The brilliance at peak energy the and the spectral flux density from the pmuB ID for different harmonics at maximum K-value (2.191) are given in Table 18 and for minimum K-value (0.400) these values are given in Table 19.

The brilliance at peak energy the and the spectral flux density from the pmuB ID for different harmonics at maximum K-value (2.191) are given in Table 18 and for minimum

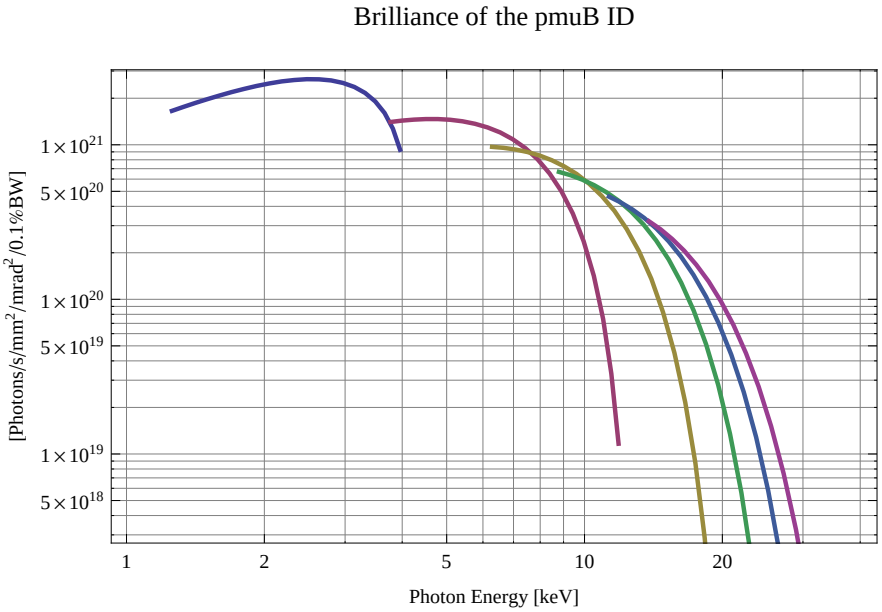

Figure 52: The brilliance at peak energy of the synchotron radiation emitted by the pmuB ID

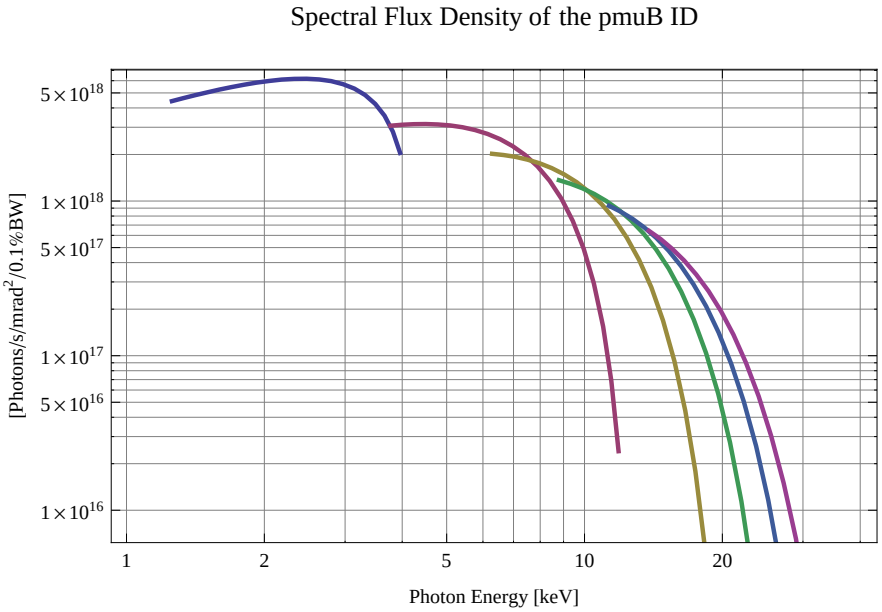

Figure 53: The spectral flux density of the synchotron radiation emitted by the pmuB ID

Table 18: The brilliance at peak energy the and the spectral flux density from the pmuB ID for different harmonics at maximum K-value (2.191)

Harmonic	Photon Energy [keV]	Brilliance [Ph./s/mrad^2/mrad^2/0.1%BW]	Spectral Flux Density [Ph./s/mrad^2/0.1%BW]
1	1.25675	1.66×10^{21}	4.43×10^{18}
3	3.77025	1.4×10^{21}	3.07×10^{18}
5	6.28374	9.69×10^{20}	2.02×10^{18}
7	8.79724	6.67×10^{20}	1.36×10^{18}
9	11.3107	4.62×10^{20}	9.32×10^{17}
11	13.8242	3.21×10^{20}	6.42×10^{17}

K-value (0.400) these values are given in Table 19.

Table 19: The brilliance at peak energy the and the spectral flux density from the pmuB ID for different harmonics at minimum K-value (0.4)

Harmonic	Photon Energy [keV]	Brilliance [Ph./s/mrad^2/mrad^2/0.1%BW]	Spectral Flux Density [Ph./s/mrad^2/0.1%BW]
1	3.95683	9.28×10^{20}	2.05×10^{18}
3	11.8705	1.17×10^{19}	2.41×10^{16}
5	19.7842	1.2×10^{17}	2.47×10^{14}
7	27.6978	1.22×10^{15}	2.5×10^{12}
9	35.6115	1.24×10^{13}	2.53×10^{10}
11	43.5252	1.25×10^{11}	2.56×10^{8}

4.4.4 Influence from the pmuB ID on the optics of the stored beam

Figure 54 shows the focusing potential from the pmuB over the beam stay clear aperture of the ring aparture.

Figure 55 shows the kick map in the beam energy independant unit T^2m^2 of the kicks induced by the pmuB ID over the beam stay clear aparture.

Figure 56 shows the induced angular kick on the stored beam from the pmuB ID as a function of the vertical distance to the axis of the ID.

Figure 57 shows the induced angular kick on the stored beam from the pmuB ID as a function of the horizontal distance to the axis of the ID.

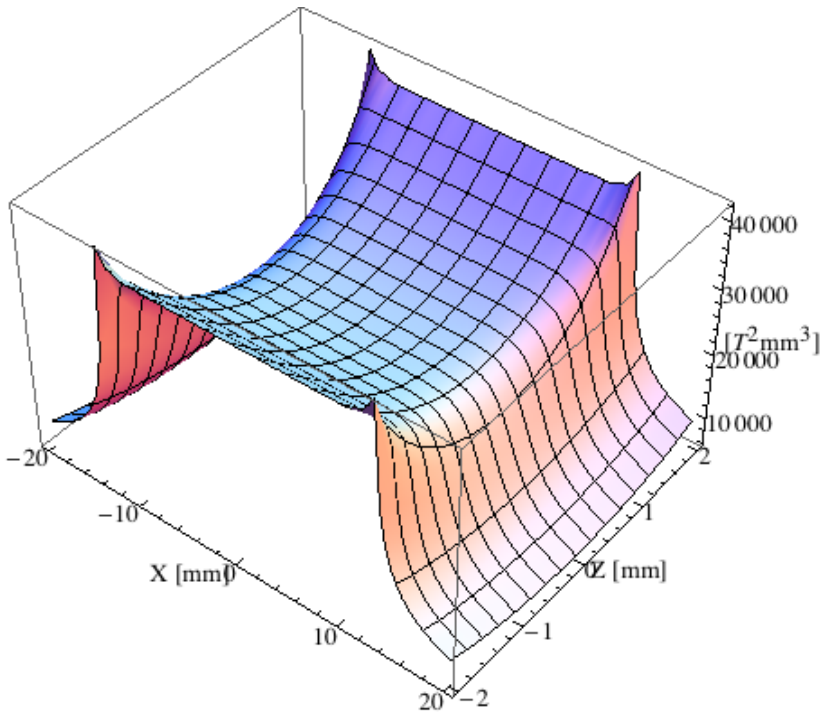

Figure 54: Focusing potential from the pmuB ID over the beam stay clear aparture.

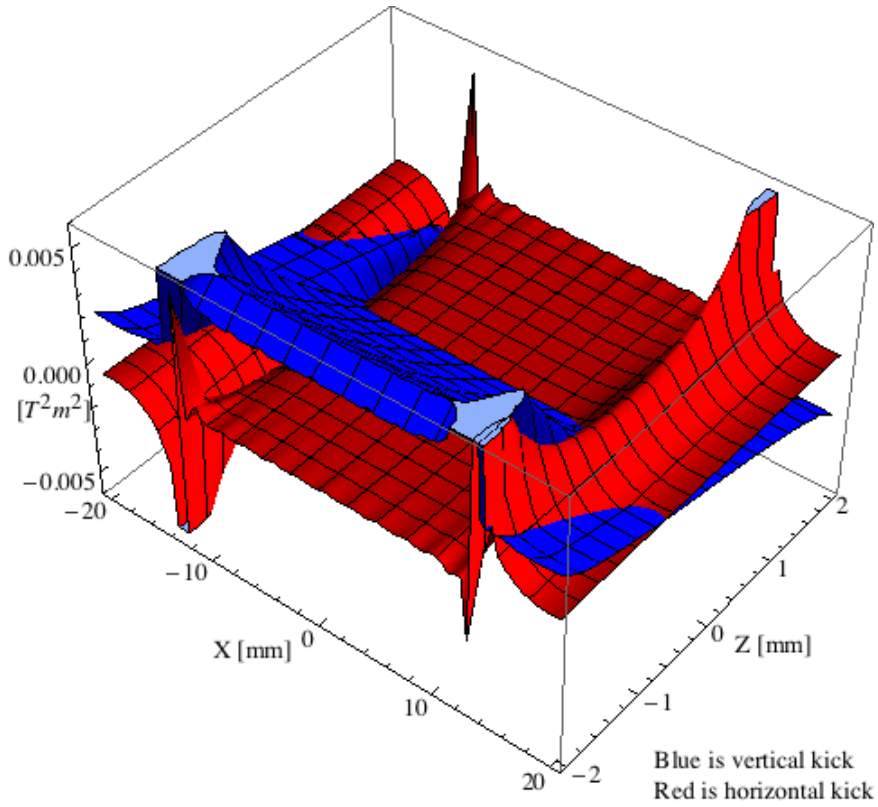

Figure 55: Kick map in the beam energy independant unit T^2m^2 of the kicks induced by the pmuB ID over the beam stay clear aparture.

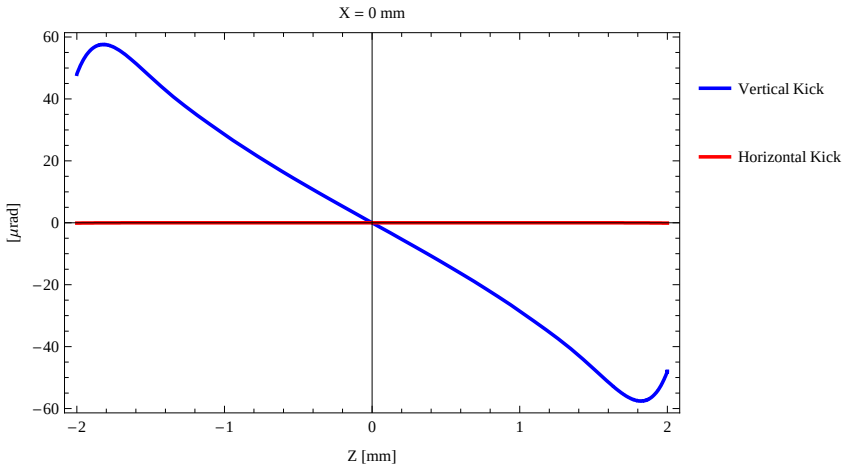

Figure 56: Induced angular kick on the stored beam from the pmuB ID as a function of the vertical distance to the ID axis.

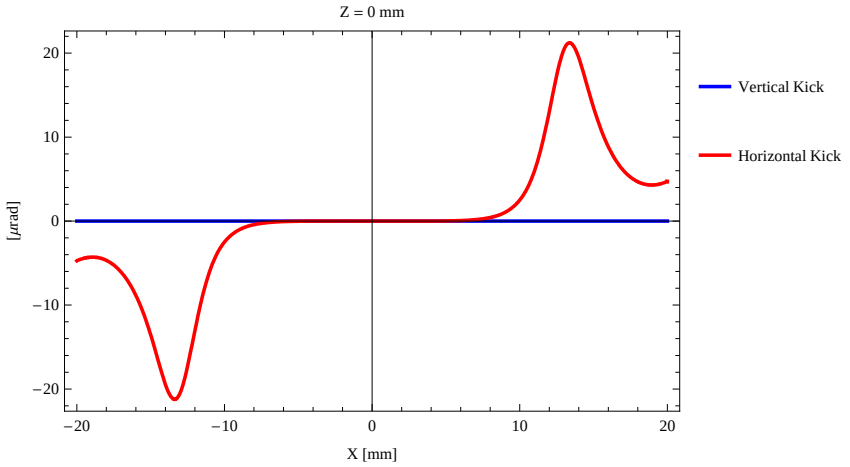

Figure 57: Induced angular kick on the stored beam from the pmuB ID as a function of the horizontal distance to the ID axis.

Figure 58 shows tune shift induced by the pmuB ID over the beam stay clear aparture. Note that the tune shift depends on the beam size at the ID.

Figure 59 shows the induced tune shift from the pmuB ID as a function of the vertical distance to the axis of the ID.

Figure 60 shows the induced tune shift from the pmuB ID as a function of the horizontal distance to the axis of the ID.

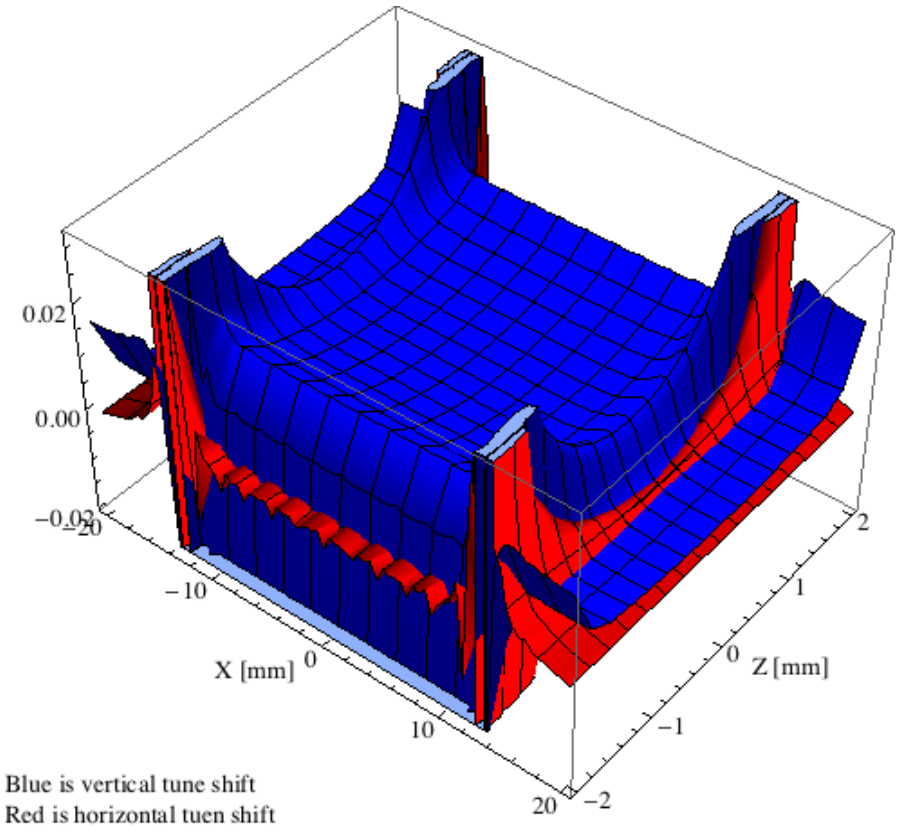

Figure 58: Tune shift induced by the pmuB ID over the beam stay clear aparture.

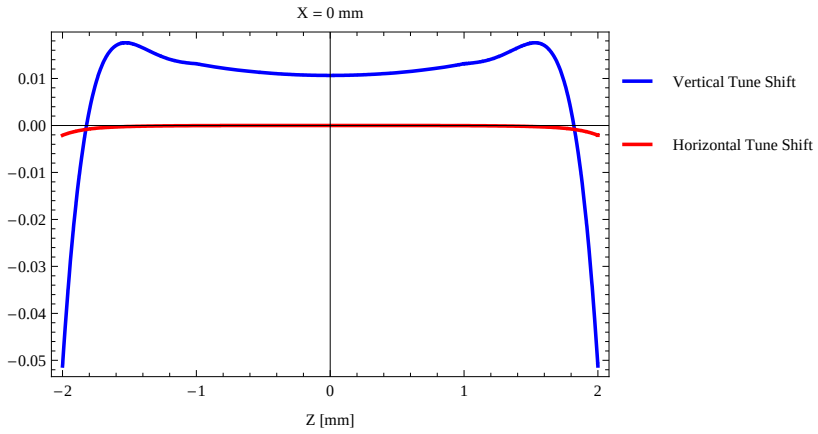

Figure 59: Induced tune shift from the pmuB ID as a function of the vertical distance to the axis of the ID.

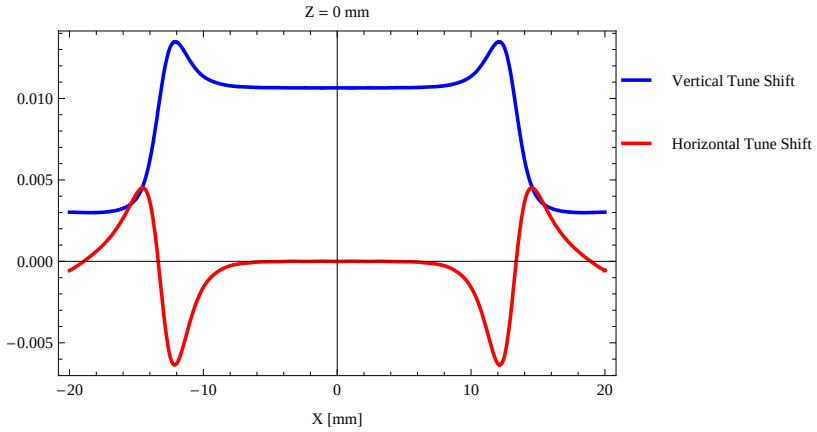

Figure 60: Induced tune shift from the pmuB ID on the stored beam from the ID as a function of the horizontal distance to the axis of the ID.

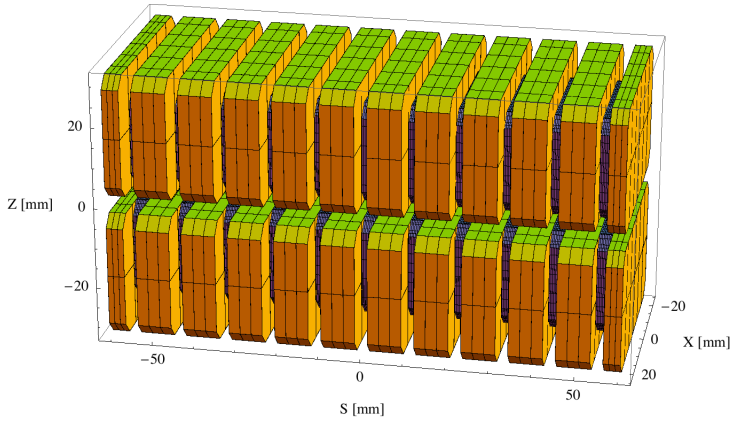

Figure 61: Magnetic model of the pmuC ID

4.5 The pmuC ID

4.5.1 Magnet model of the pmuC ID

The pmuC is an in-vacuum undulator of hybrid type and the magnetic model of the pmuC is shown in Figure 61. The magnet blocks, which are yellow in Figure 61, are made of the magnetic material Sm_2Co_17 with a magnetic remanence of 1.05 T at ambient temperature. The dimensions of the magnet blocks are 50.00x8.01x30.00x mm^3 and there is a 4 mm chamfer at the corners of the magnet blocks. The poles, which are grey in Figure 61, are made of pure iron. The dimensions of the poles are 32.00x2.99x24.00x mm^3 and there is a 3 mm chamfer at the corners of the poles.

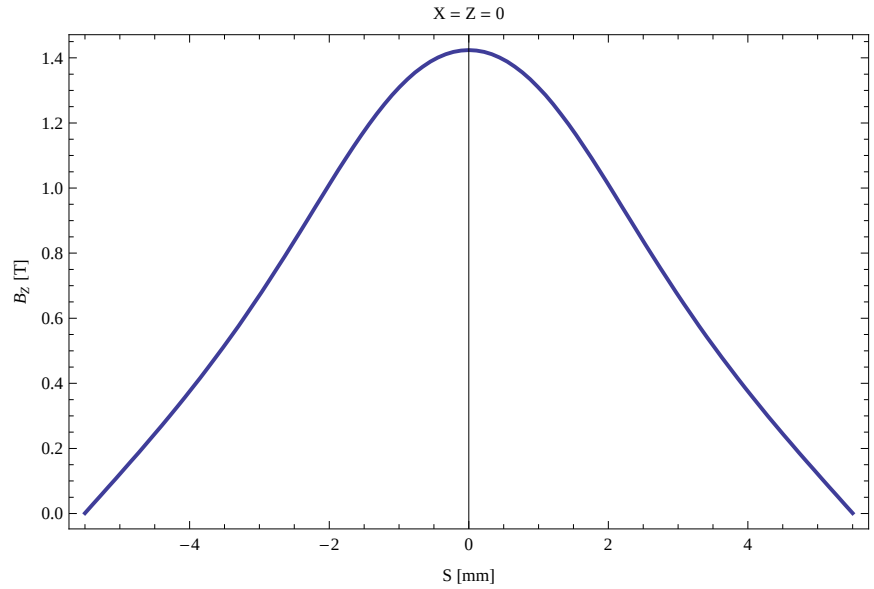

Figure 62: Vertical magnetic field in a central pole of the pmuC ID along the ID axis, X = Z = 0

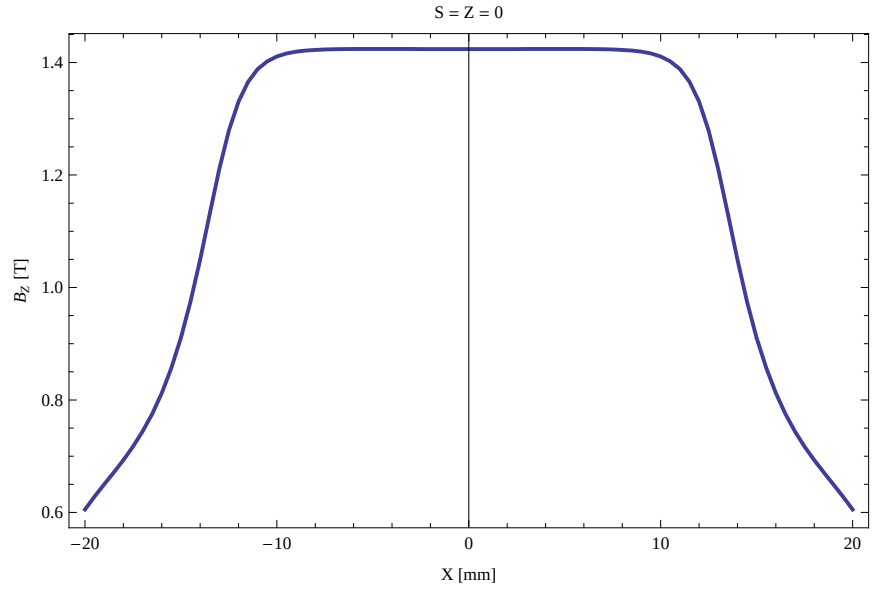

Figure 63: Vertical magnetic field in a central pole of the pmuC ID along the horizontally transverse direction to the ID axis, S = Z = 0

4.5.2 Analysis of the magnetic field of the pmuC ID

The vertical magnetic field in a central pole of the pmuC ID along the ID axis, X = Z = 0 is shown in Figure 62. The vertical magnetic field in a central pole of the pmuC ID in the horizontally transverse direction to the ID axis, S = Z = 0, is shown in Figure 63.

A Fourier anlysis of the magnetic field along the axis of the ID gives the higher harmonic contents in the magnetic field. A non-sinusoidal magnetic field profile along the ID would give a large higher harmonics contribution and it would no longer be possible to calculate the K-value of the ID from the peak field only. Also the higher harmonic contribution must be included to get the correct efficient magnetic field and efficient K-value. The higher harmonic contribution to the magnetic field is given in in Table 20.

Table 20: Fourier Analysis of the magnetic field of the pmuC ID

Term	Strength
Harm. Nr. 1	1.243 T
Harm. Nr. 3	0.162 T
Harm. Nr. 5	0.015 T
Harm. Nr. 7	-0.002 T
Harm. Nr. 9	-0.001 T
Harm. Nr. 11	-0.000 T

A tranverse field roll-off may pose a problem to the storage ring since it gives a horizontal tune shift. The transverse field roll-off for the pmuC for different horizontal positions out from the ID axis is shown in Figure 63 and numbers are given in Table 21.

Table 21: Transverse field roll-off for the pmuC ID

X-Position	B_Z Field	Roll-off
± 0 mm	1.424 T	
± 5 mm	1.424 T	-0.01 %
± 10 mm	1.411 T	0.92 %
± 15 mm	0.910 T	36.06 %
± 20 mm	0.605 T	57.49 %

The paremeters of the pmuC are summarised in Table 22.

Table 22: Summary of the pmuC ID parameters

Period	22.0	mm
Gap	4.2	mm
Peak Field	1.424	T
Effective Field	1.244	T
Peak k-value	2.926	
Effective k-value	2.556	
Higher Order Contr.	13.10	%
Maximum e-beam deflection	0.42	mrad
Electron Beam Energy	3.0	GeV
Electron Beam Current	500	mA
Max Critical Energy	8.522	keV
Emitted Power	16.717	kW
Photon Energy, n = 1	0.911	keV
Total Length	3795.0	mm

4.5.3 Synchrotron radiation from the pmuC ID

The power map of the emitted synchrotron radiation by the pmuC ID, assuming a 0.5 A filament beam with an energy of 3. GeV and undulator properties of the synchrotron radiation, is shown in Figure 64. The on-axis power density is 92.308 kW/mrad^2

A map of the degree of linear polarisation of the fundamental harmonic of the synchotron radiation emitted by the pmuC ID over the angle of obsevation is shown in Figure 65.

A map of the degree of 45 degree polarisation of the fundamental harmonic of the synchotron radiation emitted by the pmuC ID over the angle of obsevation is shown in Figure 66.

A map of the degree of circular polarisation of the fundamental harmonic of the synchotron radiation emitted by the pmuC ID over the angle of obsevation is shown in Figure 67.

The on axis brilliance at peak energy the and spectral flux density, also often called angular spectral flux, from the pmuC ID has been calculated with the given beam parameters, which are 0.5 A of stored current, $\beta_H = 9.$ m, $\varepsilon_H = 0.263$ nmrad, $\beta_V = 4.8$ m, $\varepsilon_V = 8.$ pmrad, and an energy spread of 0.001. Figure 68 shows the brilliance at peak energy and Figure 69 shows the the spectral flux density.

The brilliance at peak energy the and the spectral flux density from the pmuC ID for different harmonics at maximum K-value (2.556) are given in Table 23 and for minimum K-value (0.400) these values are given in Table 24.

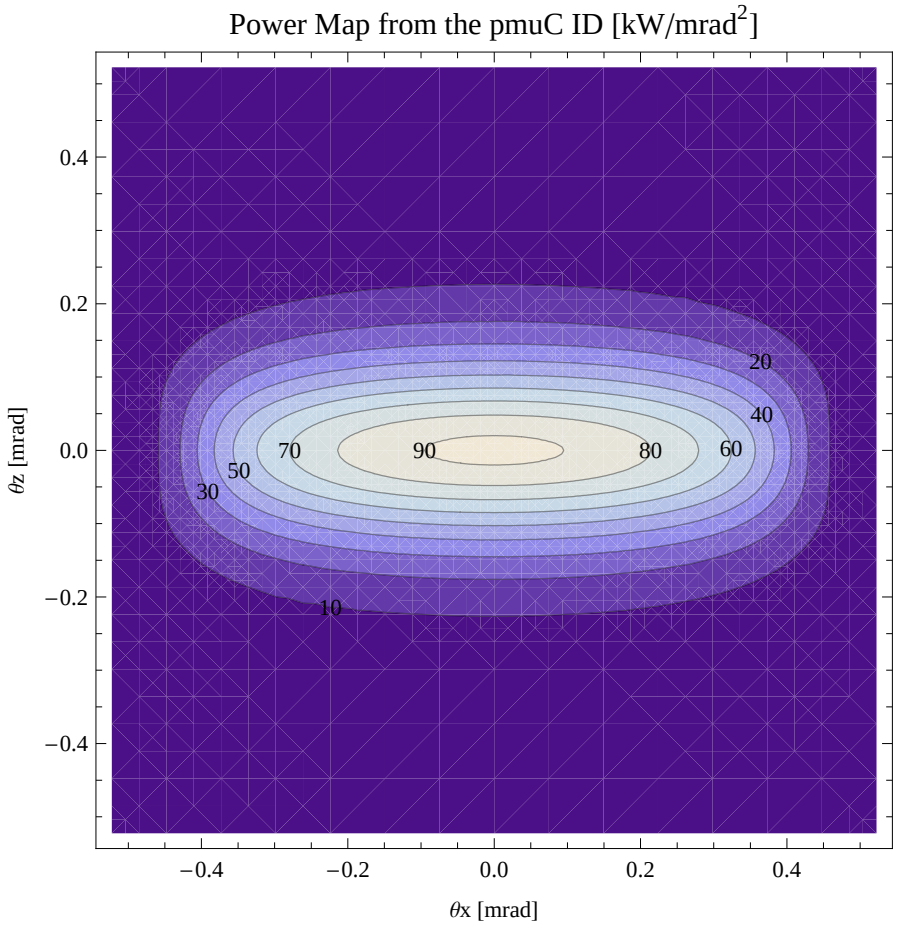

Figure 64: Map of the power distribution of the emitted synchrotron radiation by the pmuC ID

Table 23: The brilliance at peak energy the and the spectral flux density from the pmuC ID for different harmonics at maximum K-value (2.556)

Harmonic	Photon Energy [keV]	Brilliance [Ph./s/mrad^2/mrad^2/0.1%BW]	Spectral Flux Density [Ph./s/mrad^2/0.1%BW]
1	0.910624	1.08×10^{21}	3.17×10^{18}
3	2.73187	1.09×10^{21}	2.49×10^{18}
5	4.55312	8.48×10^{20}	1.82×10^{18}
7	6.37437	6.52×10^{20}	1.36×10^{18}
9	8.19561	5.03×10^{20}	1.03×10^{18}
11	10.0169	3.89×10^{20}	7.87×10^{17}

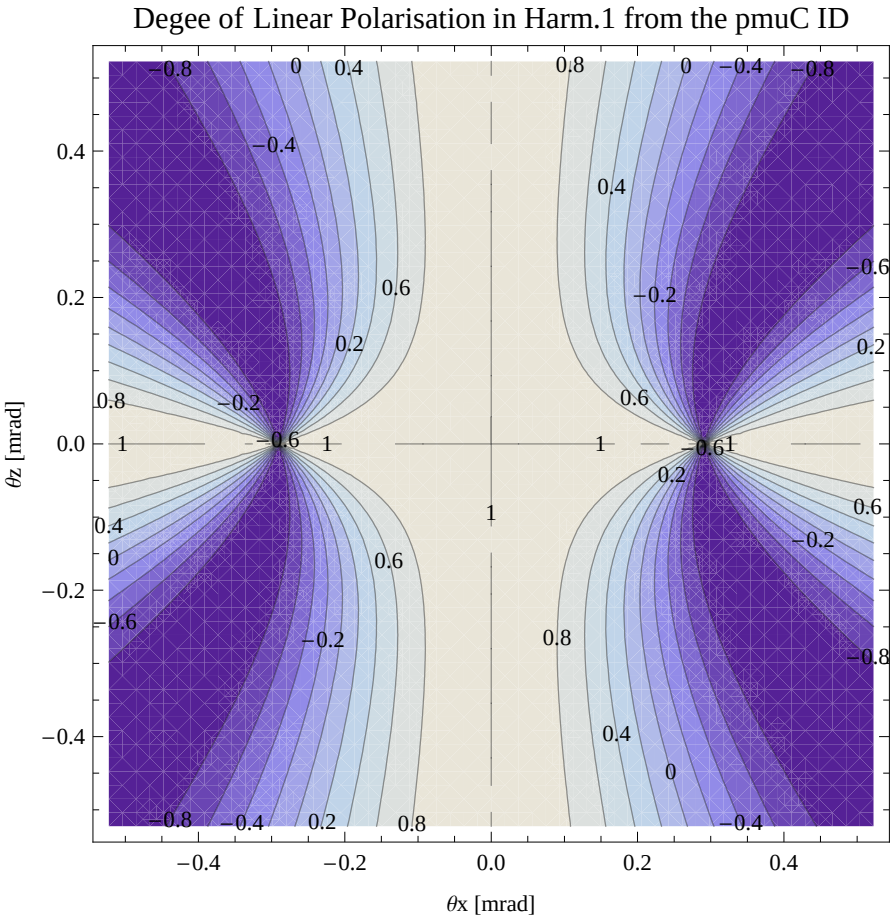

Figure 65: Map of linear polarisation in the fundamental harmonic of the synchotron radiation emitted by the pmuC ID

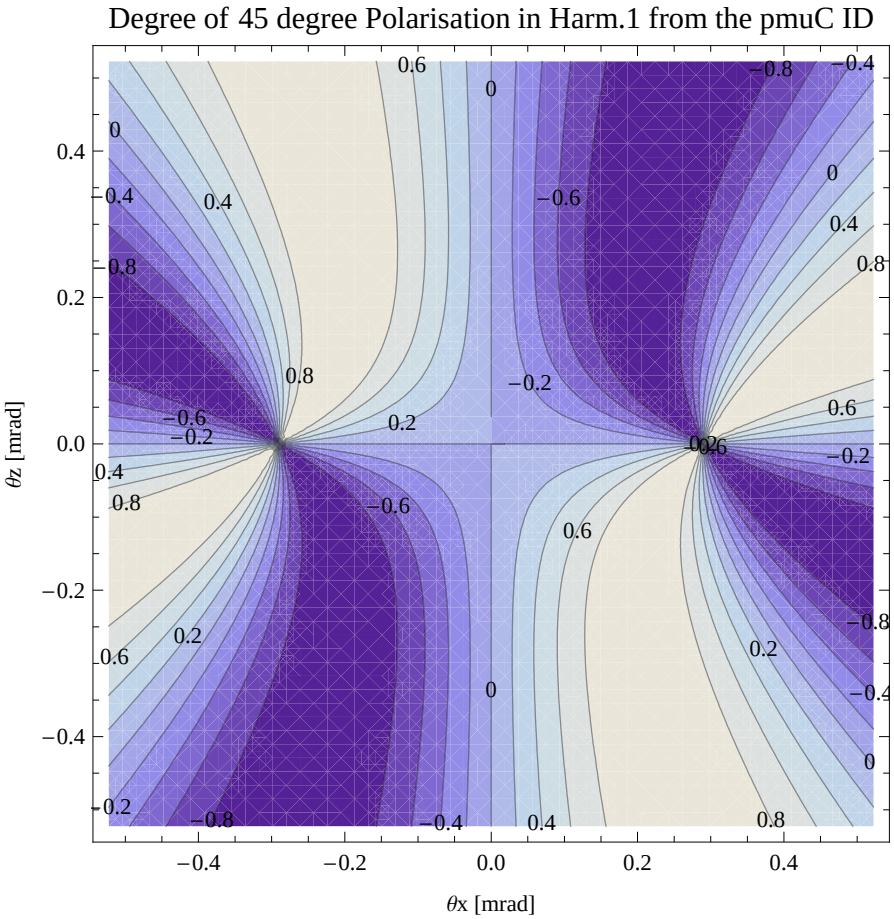

Figure 66: Map of 45 degree polarisation in the fundamental harmonic of the synchotron radiation emitted by the pmuC ID

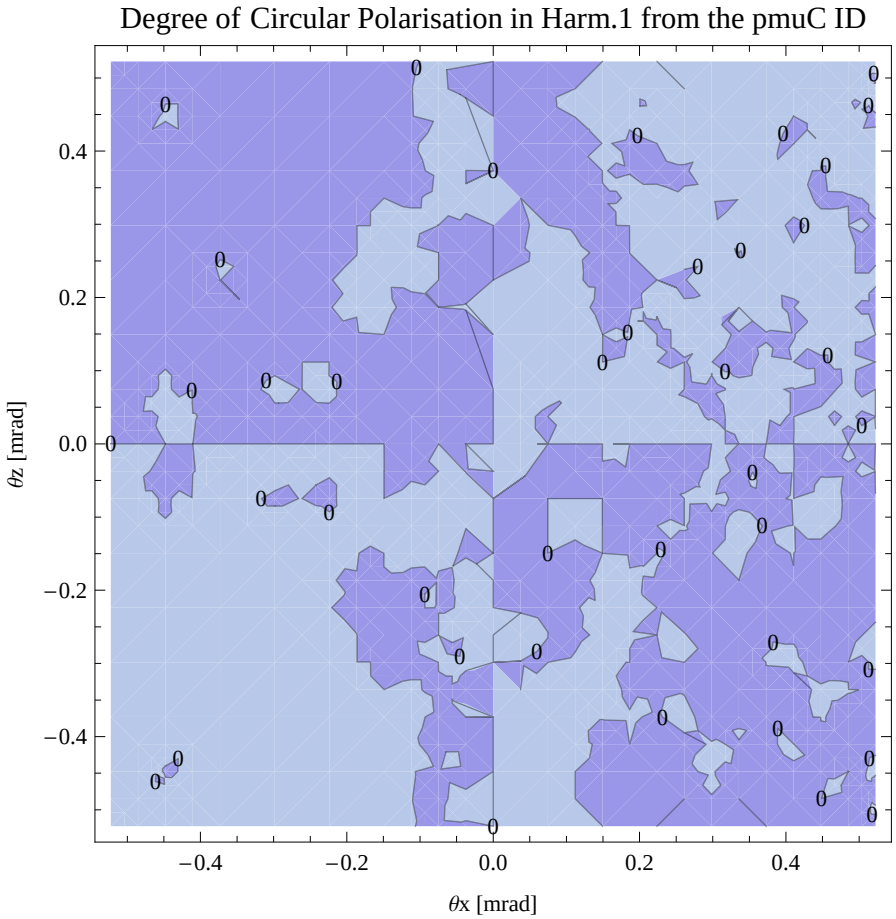

Figure 67: Map of circular polarisation in the fundamental harmonic of the synchotron radiation emitted by the pmuC ID

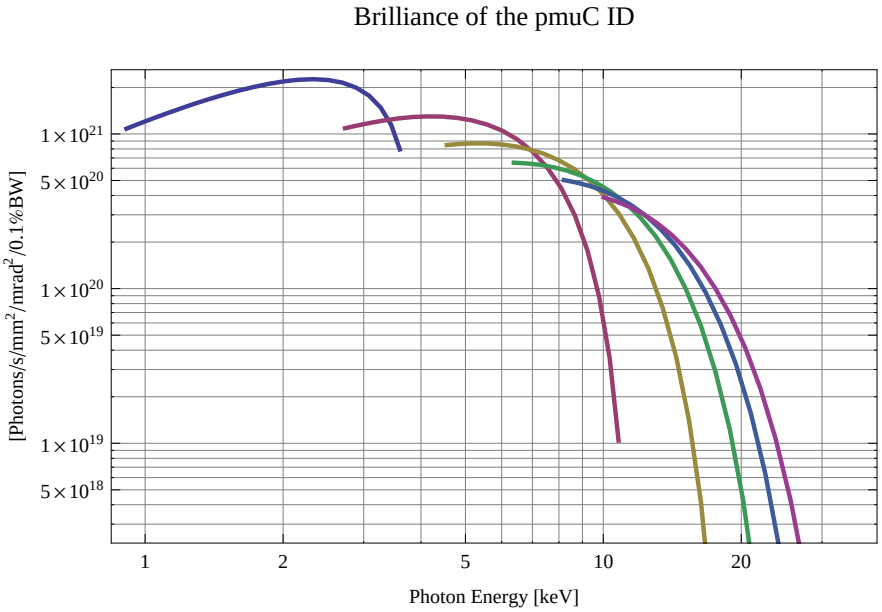

Figure 68: The brilliance at peak energy of the synchotron radiation emitted by the pmuC ID

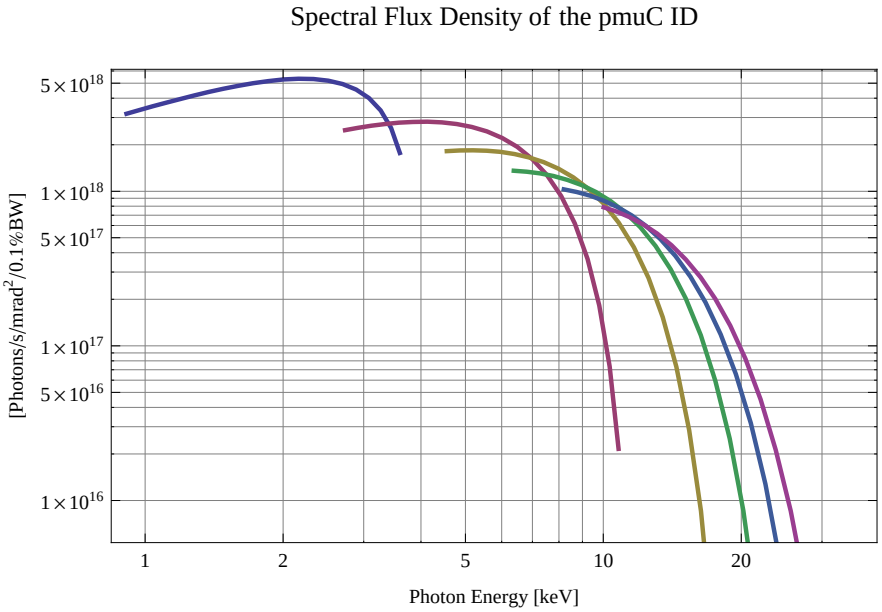

Figure 69: The spectral flux density of the synchotron radiation emitted by the pmuC ID

The brilliance at peak energy the and the spectral flux density from the pmuC ID for different harmonics at maximum K-value (2.556) are given in Table 23 and for minimum K-value (0.400) these values are given in Table 24.

Table 24: The brilliance at peak energy the and the spectral flux density from the pmuC ID for different harmonics at minimum K-value (0.4)

Harmonic	Photon Energy [keV]	Brilliance [Ph./s/mrad^2/mrad^2/0.1%BW]	Spectral Flux Density [Ph./s/mrad^2/0.1%BW]
1	3.59712	7.96×10^{20}	1.77×10^{18}
3	10.7914	1.04×10^{19}	2.16×10^{16}
5	17.9856	1.08×10^{17}	2.22×10^{14}
7	25.1798	1.1×10^{15}	2.26×10^{12}
9	32.3741	1.12×10^{13}	2.29×10^{10}
11	39.5683	1.13×10^{11}	2.31×10^{8}

4.5.4 Influence from the pmuC ID on the optics of the stored beam

Figure 70 shows the focusing potential from the pmuC over the beam stay clear aperture of the ring aparture.

Figure 71 shows the kick map in the beam energy independant unit T^2m^2 of the kicks induced by the pmuC ID over the beam stay clear aparture.

Figure 72 shows the induced angular kick on the stored beam from the pmuC ID as a function of the vertical distance to the axis of the ID.

Figure 73 shows the induced angular kick on the stored beam from the pmuC ID as a function of the horizontal distance to the axis of the ID.

Figure 74 shows tune shift induced by the pmuC ID over the beam stay clear aparture. Note that the tune shift depends on the beam size at the ID.

Figure 75 shows the induced tune shift from the pmuC ID as a function of the vertical distance to the axis of the ID.

Figure 76 shows the induced tune shift from the pmuC ID as a function of the horizontal distance to the axis of the ID.

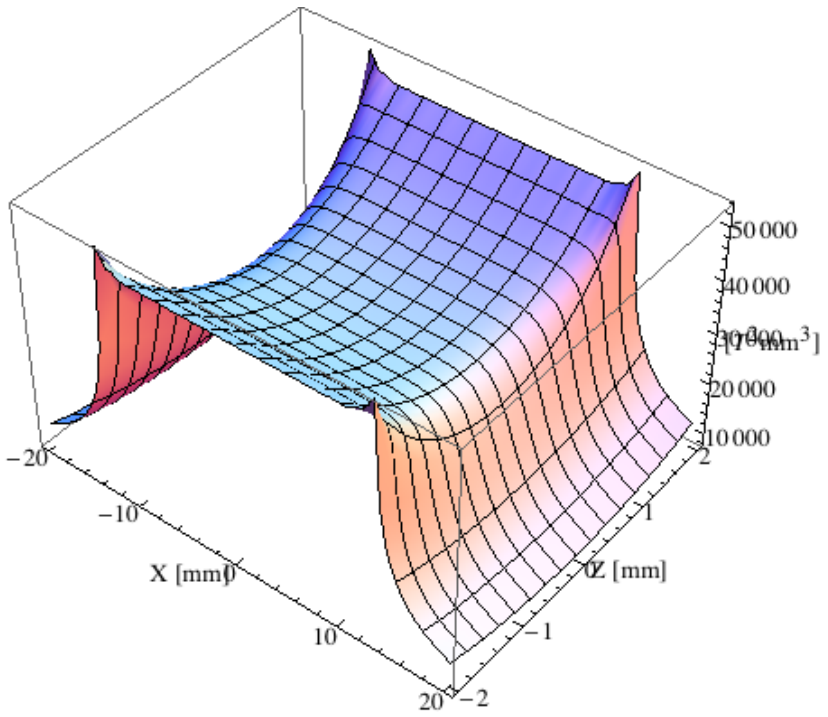

Figure 70: Focusing potential from the pmuC ID over the beam stay clear aparture.

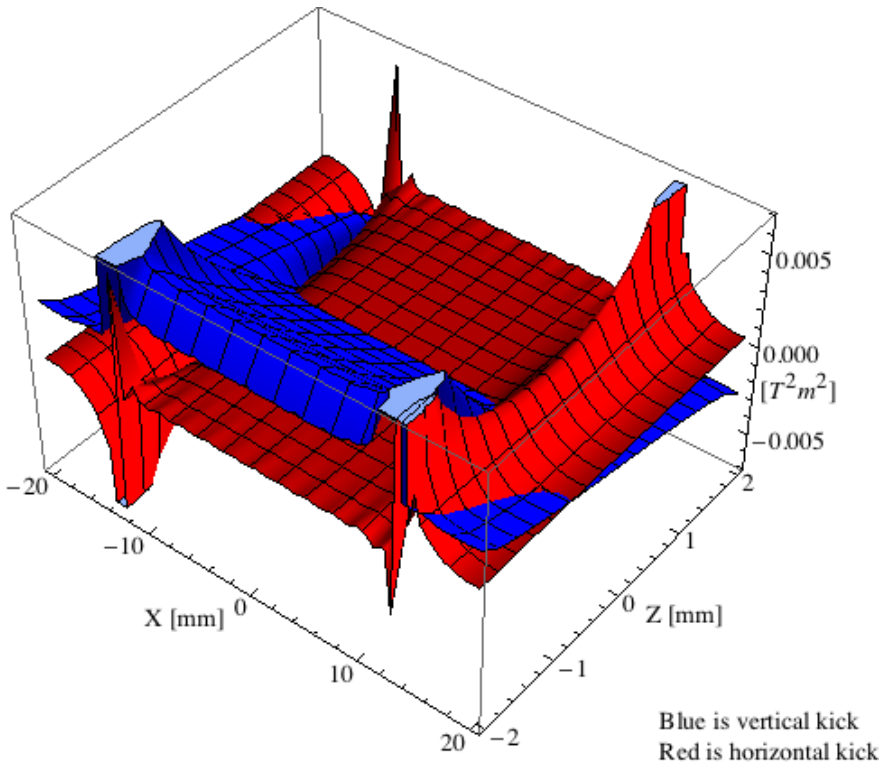

Figure 71: Kick map in the beam energy independant unit T^2m^2 of the kicks induced by the pmuC ID over the beam stay clear aparture.

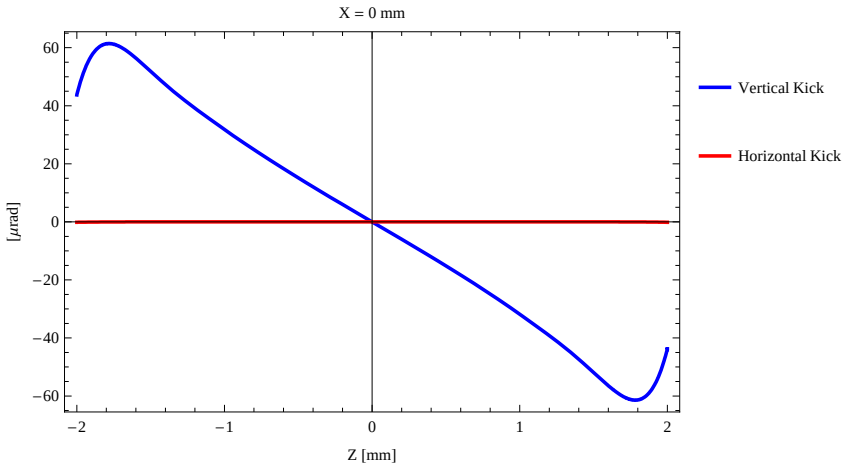

Figure 72: Induced angular kick on the stored beam from the pmuC ID as a function of the vertical distance to the ID axis.

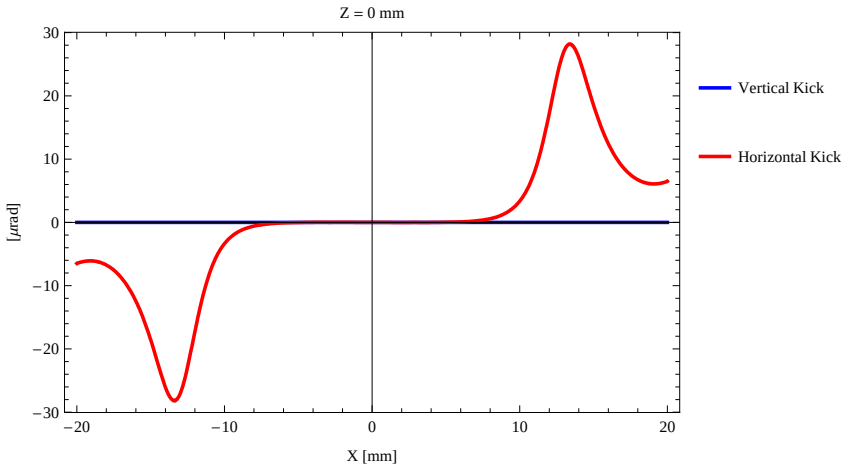

Figure 73: Induced angular kick on the stored beam from the pmuC ID as a function of the horizontal distance to the ID axis.

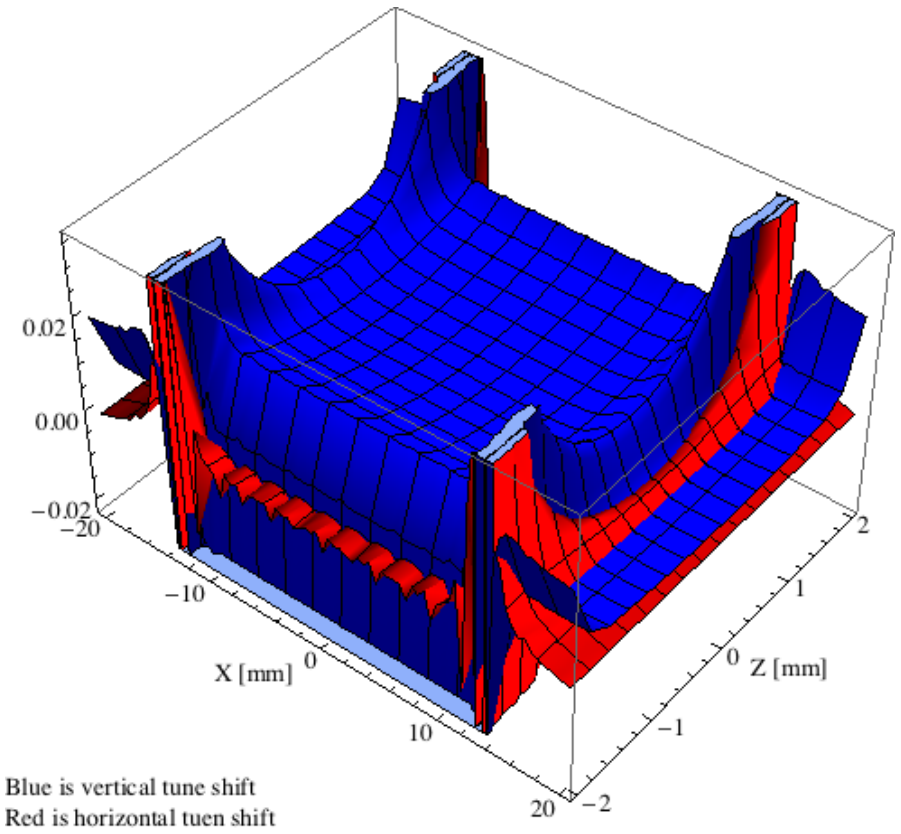

Figure 74: Tune shift induced by the pmuC ID over the beam stay clear aparture.

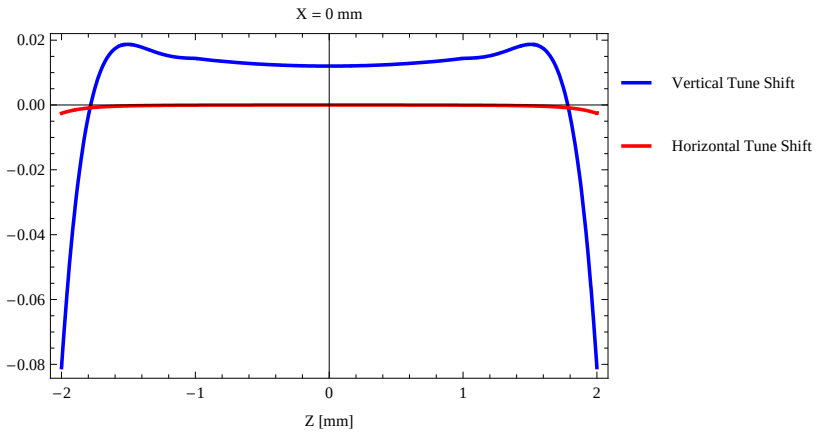

Figure 75: Induced tune shift from the pmuC ID as a function of the vertical distance to the axis of the ID.

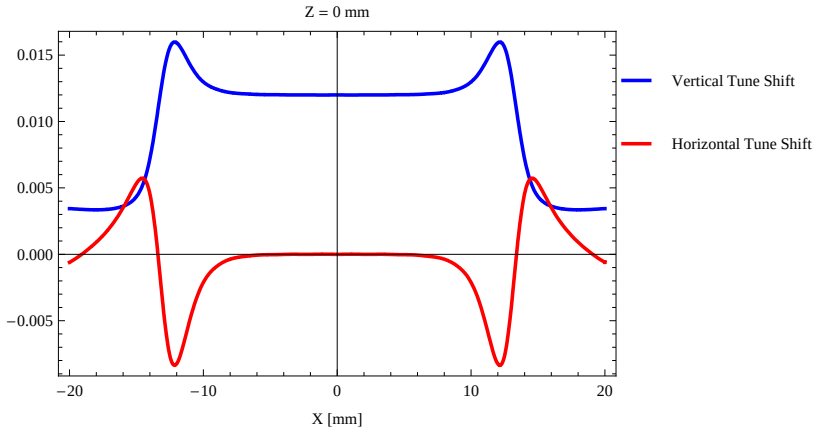

Figure 76: Induced tune shift from the pmuC ID on the stored beam from the ID as a function of the horizontal distance to the axis of the ID.

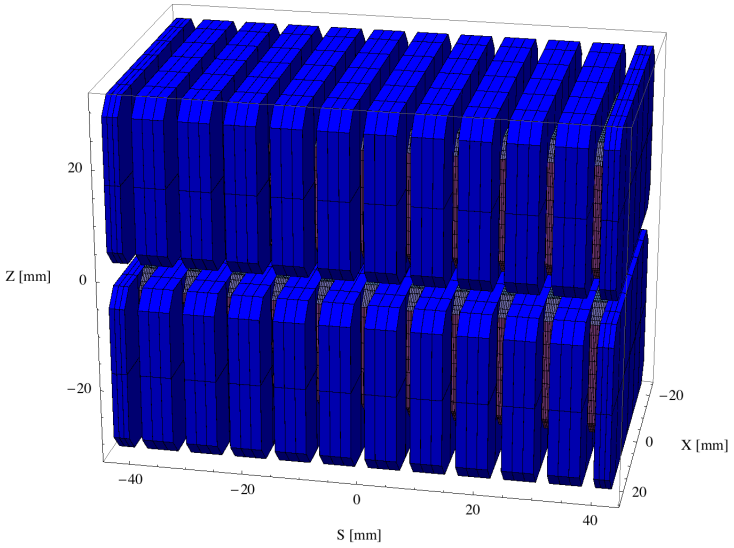

Figure 77: Magnetic model of the cpmuA ID

4.6 The cpmuA ID

4.6.1 Magnet model of the cpmuA ID

The cpmuA is a cryogenicaaly cooled in-vacuum undulator of hybrid type and the magnetic model of the cpmuA is shown in Figure 77. The magnet blocks, which are blue in Figure 77, are made of NdFeB materialwith a magnetic remance of 1.35 T at 140 K. The dimensions of the magnet blocks are 50.00x5.46x30.00x mm^3 and there is a 4 mm chamfer at the corners of the magnet blocks. The poles, which are grey in Figure 77, are made of pure iron. The dimensions of the poles are 32.00x2.34x24.00x mm^3 and there is a 3 mm chamfer at the corners of the poles.

4.6.2 Analysis of the magnetic field of the cpmuA ID

The vertical magnetic field in a central pole of the cpmuA ID along the ID axis, X = Z = 0 is shown in Figure 78. The vertical magnetic field in a central pole of the cpmuA ID in the horizontally transverse direction to the ID axis, S = Z = 0, is shown in Figure 79.

A Fourier anlysis of the magnetic field along the axis of the ID gives the higher harmonic contents in the magnetic field. A non-sinusoidal magnetic field profile along the ID would give a large higher harmonics contribution and it would no longer be possible to calculate the K-value of the ID from the peak field only. Also the higher harmonic contribution must be included to get the correct efficient magnetic field and efficient K-value. The

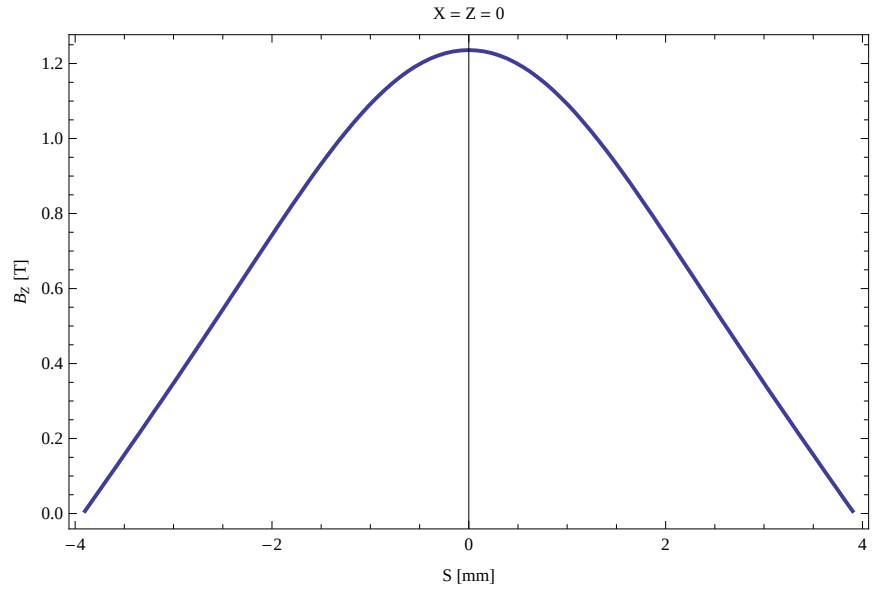

Figure 78: Vertical magnetic field in a central pole of the cpmuA ID along the ID axis, X = Z = 0

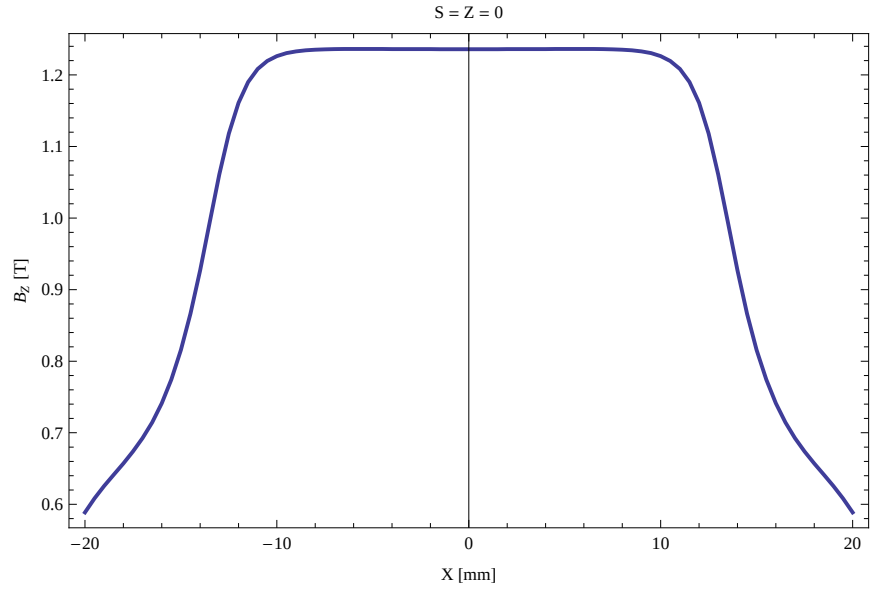

Figure 79: Vertical magnetic field in a central pole of the cpmuA ID along the horizontally transverse direction to the ID axis, S = Z = 0

higher harmonic contribution to the magnetic field is given in in Table 25.

Table 25: Fourier Analysis of the magnetic field of the cpmuA ID

Term	Strength
Harm. Nr. 1	1.148 T
Harm. Nr. 3	0.077 T
Harm. Nr. 5	0.002 T
Harm. Nr. 7	-0.001 T
Harm. Nr. 9	-0.000 T
Harm. Nr. 11	-0.000 T

A tranverse field roll-off may pose a problem to the storage ring since it gives a horizontal tune shift. The transverse field roll-off for the cpmuA for different horizontal positions out from the ID axis is shown in Figure 79 and numbers are given in Table 26.

Table 26: Transverse field roll-off for the cpmuA ID

X-Position	B_Z Field	Roll-off
± 0 mm	1.236 T	
± 5 mm	1.236 T	-0.02 %
± 10 mm	1.226 T	0.78 %
± 15 mm	0.816 T	34.01 %
± 20 mm	0.589 T	52.37 %

The paremeters of the cpmuA are summarised in Table 27.

4.6.3 Synchrotron radiation from the cpmuA ID

The power map of the emitted synchrotron radiation by the cpmuA ID, assuming a 0.5 A filament beam with an energy of 3. GeV and undulator properties of the synchrotron radiation, is shown in Figure 80. The on-axis power density is 119.470 kW/mrad^2

A map of the degree of linear polarisation of the fundamental harmonic of the synchotron radiation emitted by the cpmuA ID over the angle of obsevation is shown in Figure 81.

A map of the degree of 45 degree polarisation of the fundamental harmonic of the synchotron radiation emitted by the cpmuA ID over the angle of obsevation is shown in Figure 82.

A map of the degree of circular polarisation of the fundamental harmonic of the synchotron radiation emitted by the cpmuA ID over the angle of obsevation is shown in

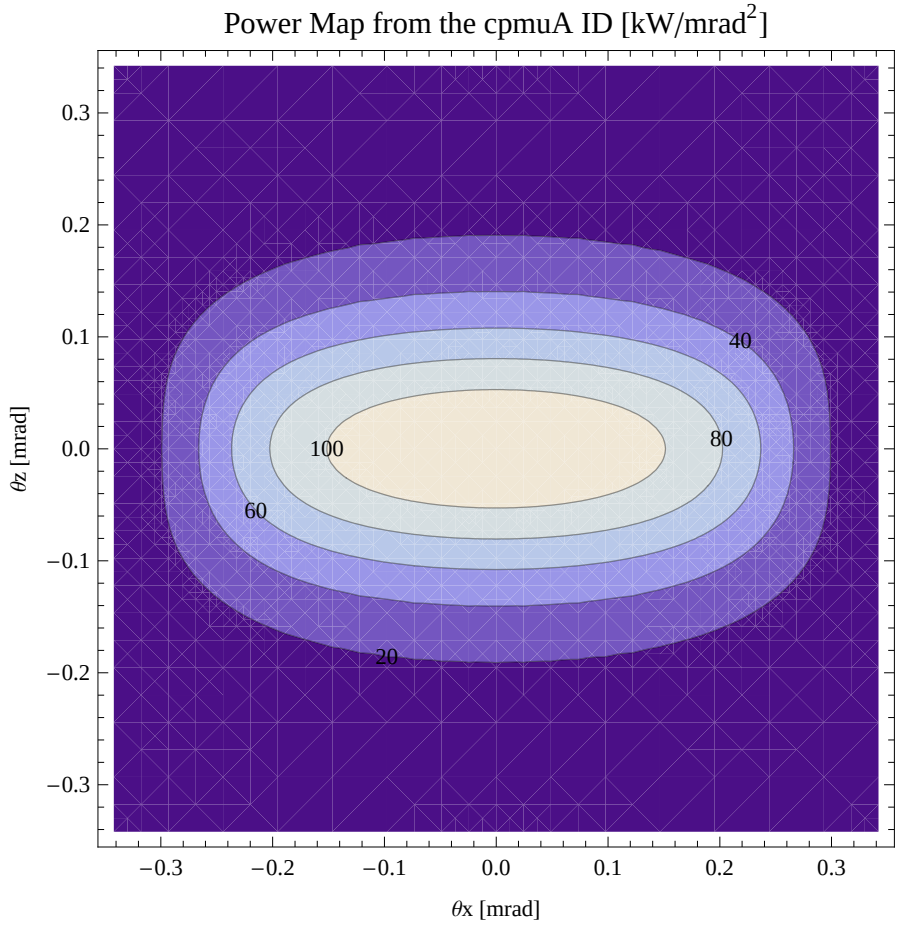

Figure 80: Map of the power distribution of the emitted synchrotron radiation by the cpmuA ID

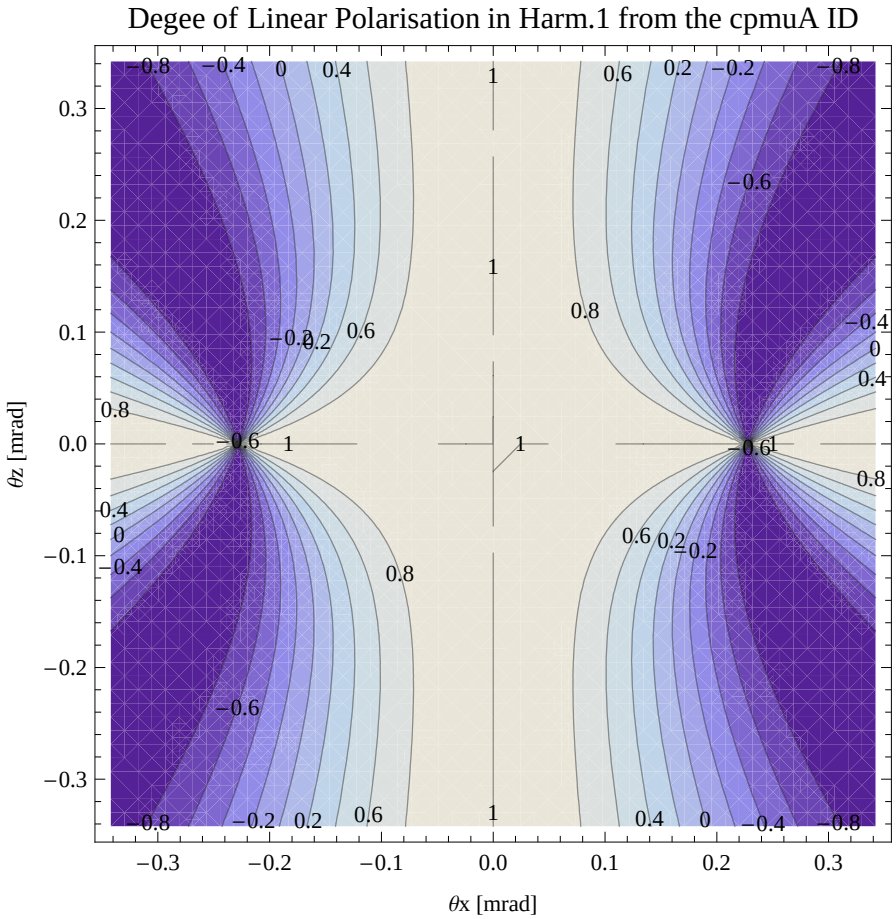

Figure 81: Map of linear polarisation in the fundamental harmonic of the synchotron radiation emitted by the cpmuA ID

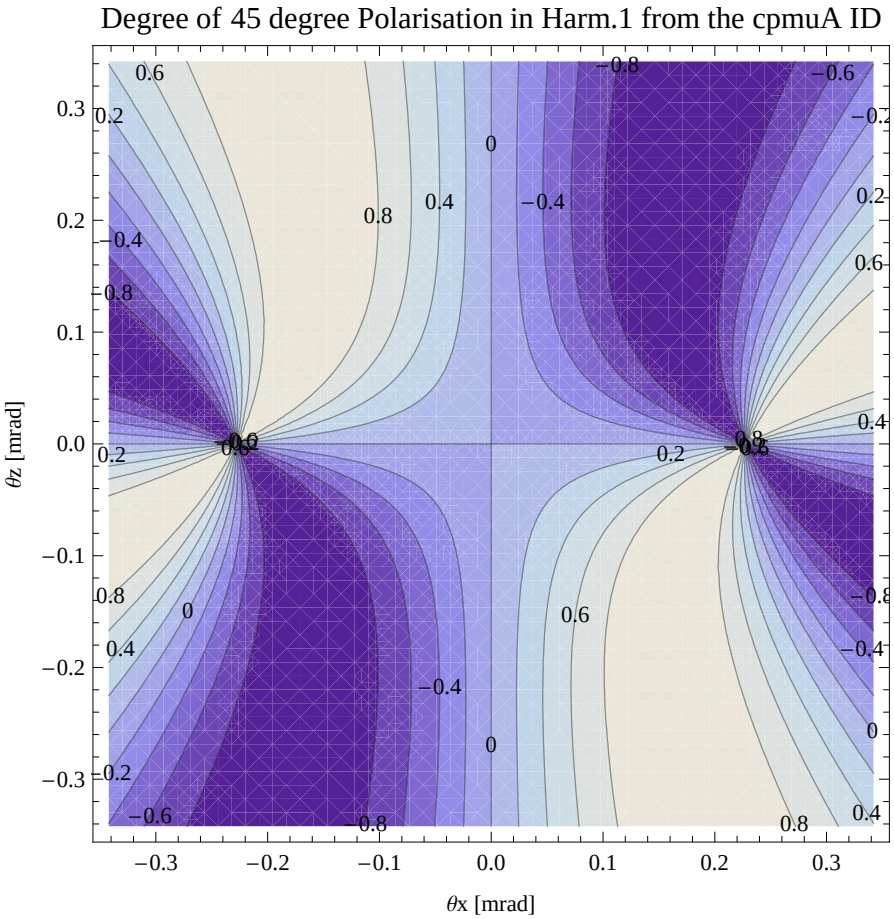

Figure 82: Map of 45 degree polarisation in the fundamental harmonic of the synchotron radiation emitted by the cpmuA ID

Table 27: Summary of the cpmuA ID parameters

Period	15.6	mm
Gap	4.2	mm
Peak Field	1.236	T
Effective Field	1.148	T
Peak k-value	1.801	
Effective k-value	1.673	
Higher Order Contr.	6.73	%
Maximum e-beam deflection	0.28	mrad
Electron Beam Energy	3.0	GeV
Electron Beam Current	500	mA
Max Critical Energy	7.397	keV
Emitted Power	14.261	kW
Photon Energy, n = 1	2.284	keV
Total Length	3798.6	mm

Figure 83.

The on axis brilliance at peak energy the and spectral flux density, also often called angular spectral flux, from the cpmuA ID has been calculated with the given beam parameters, which are 0.5 A of stored current, $\beta_H = 9.$ m, $\varepsilon_H = 0.263$ nmrad, $\beta_V = 4.8$ m, $\varepsilon_V = 8.$ pmrad, and an energy spread of 0.001. Figure 84 shows the brilliance at peak energy and Figure 85 shows the the spectral flux density.

The brilliance at peak energy the and the spectral flux density from the cpmuA ID for different harmonics at maximum K-value (1.673) are given in Table 28 and for minimum K-value (0.400) these values are given in Table 29.

Table 28: The brilliance at peak energy the and the spectral flux density from the cpmuA ID for different harmonics at maximum K-value (1.673)

Harmonic	Photon Energy [keV]	Brilliance [Ph./s/mrad^2/mrad^2/0.1%BW]	Spectral Flux Density [Ph./s/mrad^2/0.1%BW]
1	2.28305	3.39×10^{21}	7.97×10^{18}
3	6.84916	1.91×10^{21}	3.98×10^{18}
5	11.4153	9.74×10^{20}	1.98×10^{18}
7	15.9814	5.01×10^{20}	1.01×10^{18}
9	20.5475	2.59×10^{20}	5.18×10^{17}
11	25.1136	1.35×10^{20}	2.68×10^{17}

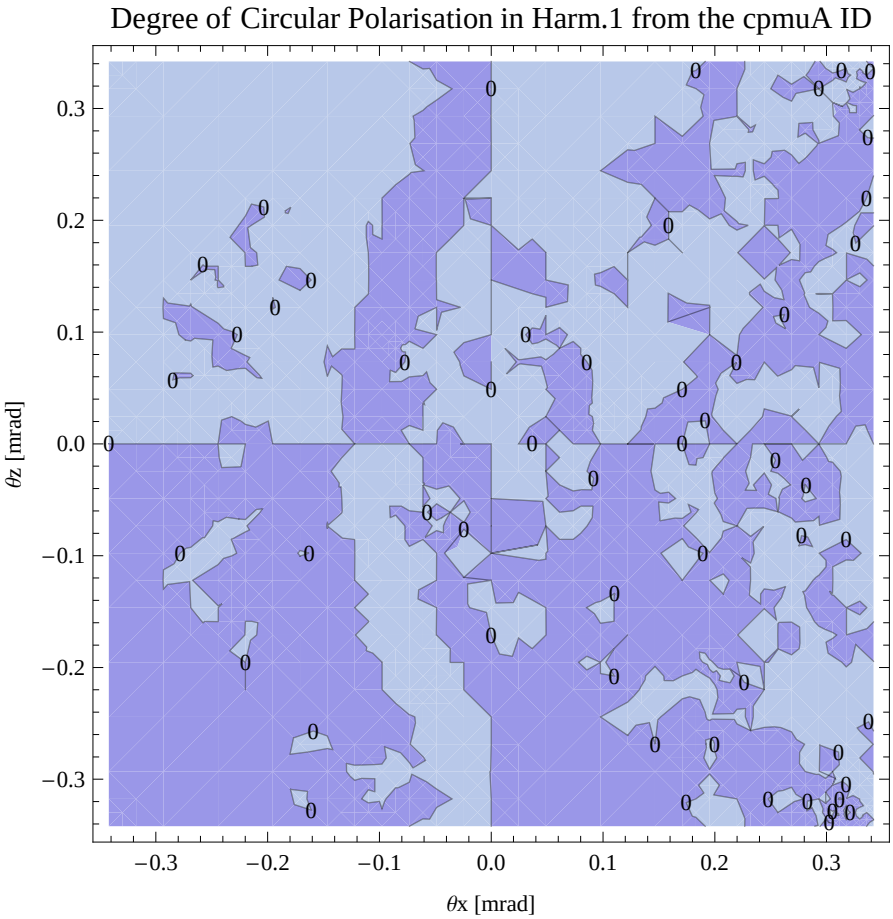

Figure 83: Map of circular polarisation in the fundamental harmonic of the synchotron radiation emitted by the cpmuA ID

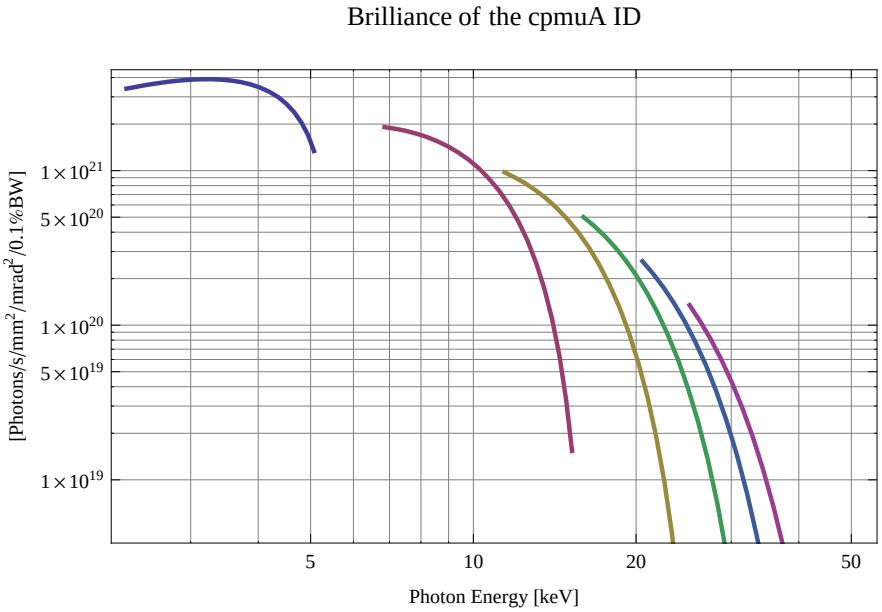

Figure 84: The brilliance at peak energy of the synchotron radiation emitted by the cpmuA ID

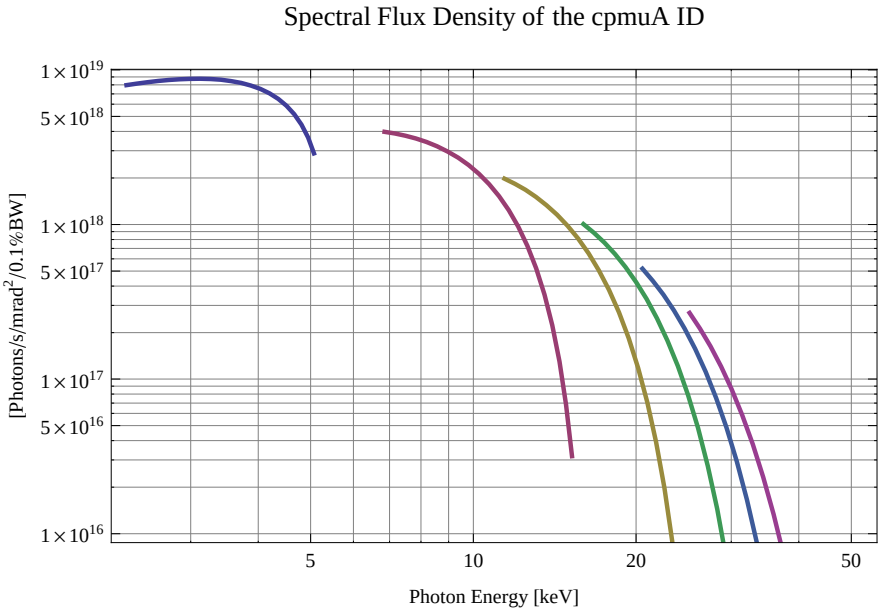

Figure 85: The spectral flux density of the synchotron radiation emitted by the cpmuA ID

The brilliance at peak energy the and the spectral flux density from the cpmuA ID for different harmonics at maximum K-value (1.673) are given in Table 28 and for minimum K-value (0.400) these values are given in Table 29.

Table 29: The brilliance at peak energy the and the spectral flux density from the cpmuA ID for different harmonics at minimum K-value (0.4)

Harmonic	Photon Energy [keV]	Brilliance [Ph./s/mrad^2/mrad^2/0.1%BW]	Spectral Flux Density [Ph./s/mrad^2/0.1%BW]
1	5.07286	1.34×10^{21}	2.89×10^{18}
3	15.2186	1.54×10^{19}	3.17×10^{16}
5	25.3643	1.56×10^{17}	3.21×10^{14}
7	35.51	1.58×10^{15}	3.24×10^{12}
9	45.6558	1.6×10^{13}	3.27×10^{10}
11	55.8015	1.61×10^{11}	3.3×10^{8}

4.6.4 Influence from the cpmuA ID on the optics of the stored beam

Figure 86 shows the focusing potential from the cpmuA over the beam stay clear aperture of the ring aparture.

Figure 87 shows the kick map in the beam energy independant unit T^2m^2 of the kicks induced by the cpmuA ID over the beam stay clear aparture.

Figure 88 shows the induced angular kick on the stored beam from the cpmuA ID as a function of the vertical distance to the axis of the ID.

Figure 89 shows the induced angular kick on the stored beam from the cpmuA ID as a function of the horizontal distance to the axis of the ID.

Figure 90 shows tune shift induced by the cpmuA ID over the beam stay clear aparture. Note that the tune shift depends on the beam size at the ID.

Figure 91 shows the induced tune shift from the cpmuA ID as a function of the vertical distance to the axis of the ID.

Figure 92 shows the induced tune shift from the cpmuA ID as a function of the horizontal distance to the axis of the ID.

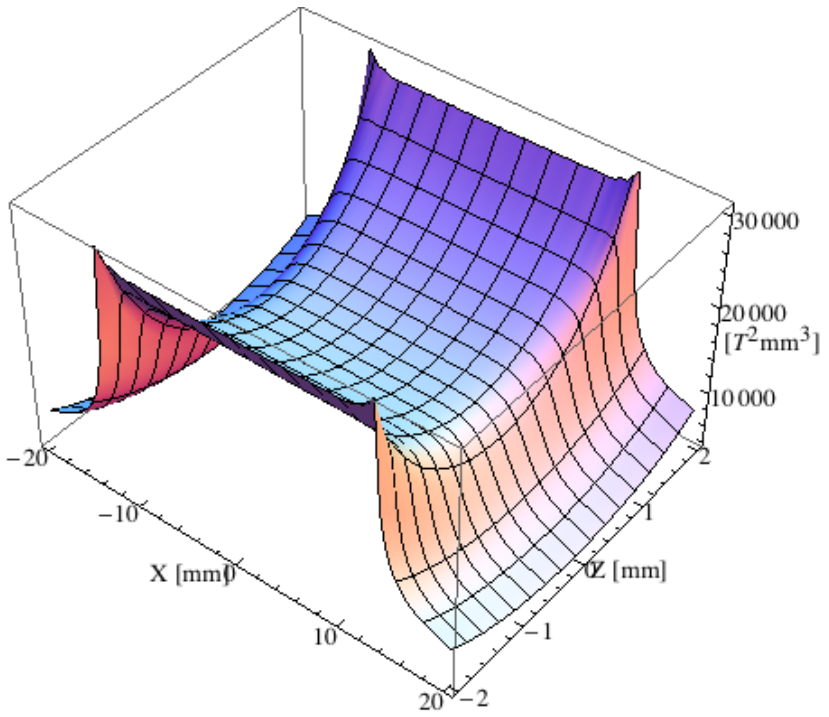

Figure 86: Focusing potential from the cpmuA ID over the beam stay clear aparture.

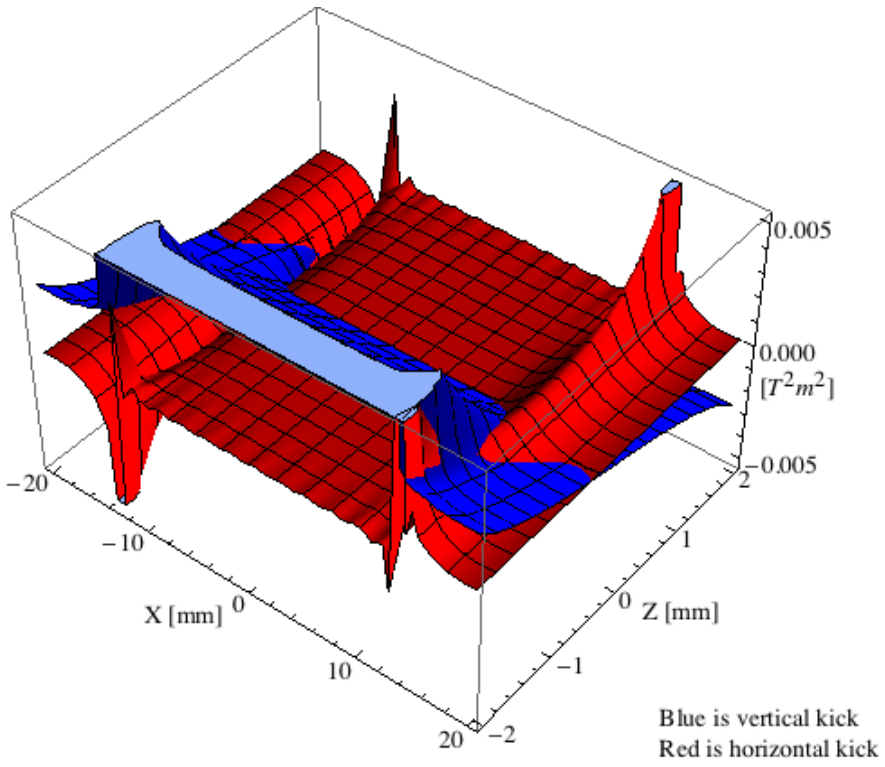

Figure 87: Kick map in the beam energy independant unit T^2m^2 of the kicks induced by the cpmuA ID over the beam stay clear aparture.

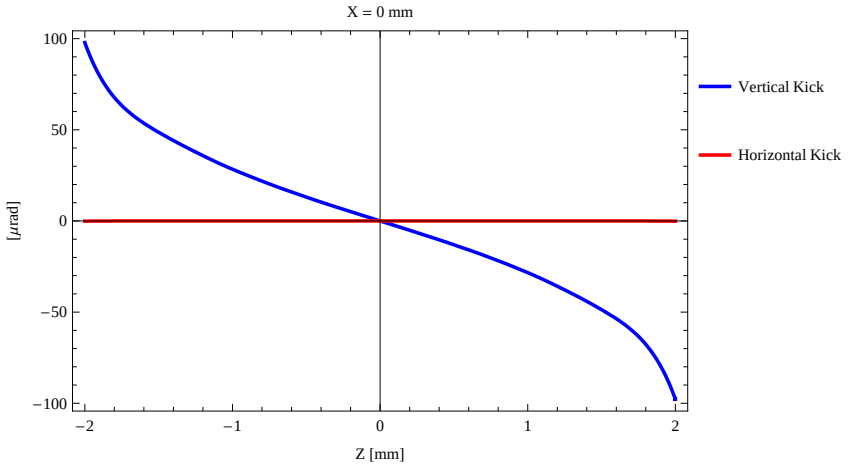

Figure 88: Induced angular kick on the stored beam from the cpmuA ID as a function of the vertical distance to the ID axis.

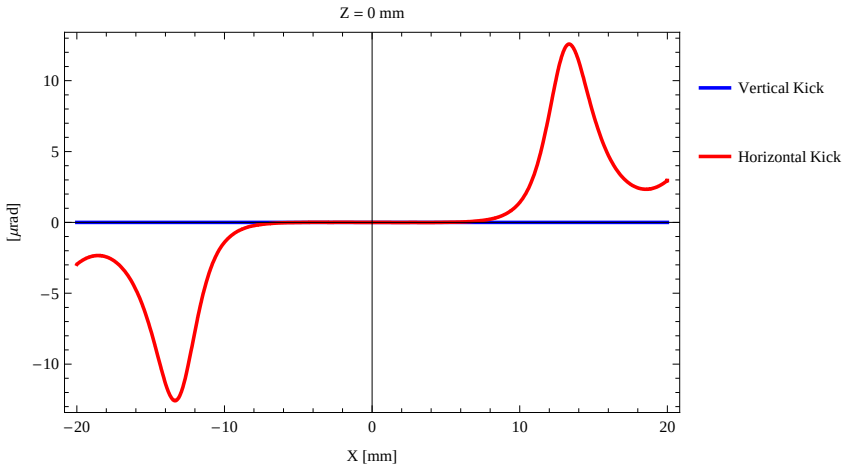

Figure 89: Induced angular kick on the stored beam from the cpmuA ID as a function of the horizontal distance to the ID axis.

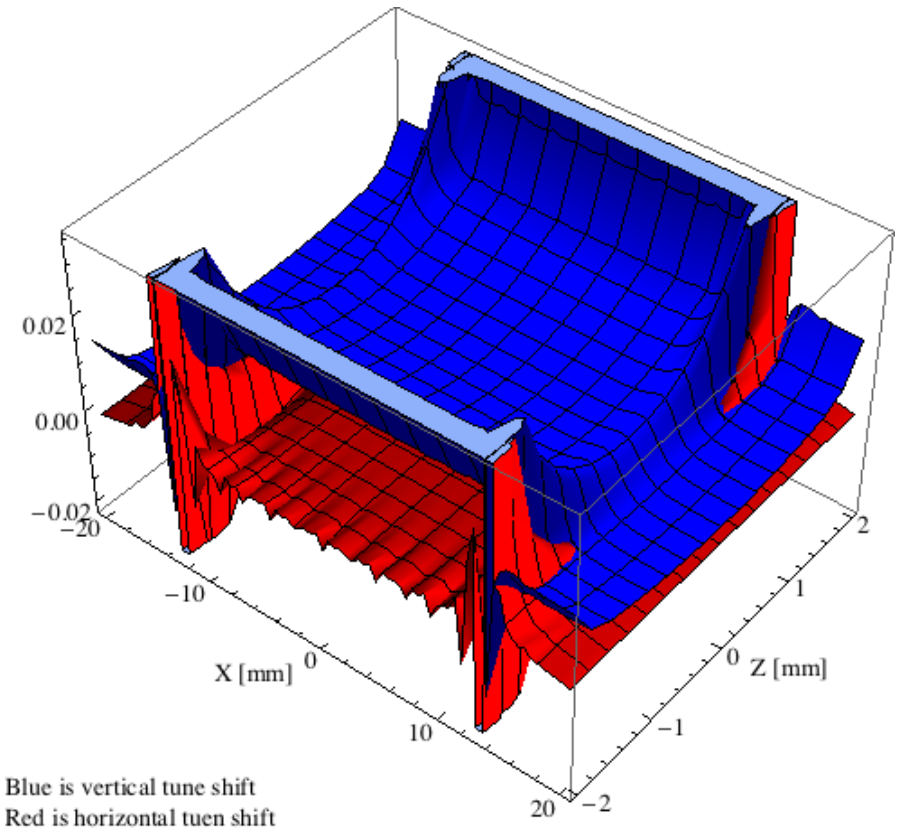

Figure 90: Tune shift induced by the cpmuA ID over the beam stay clear aparture.

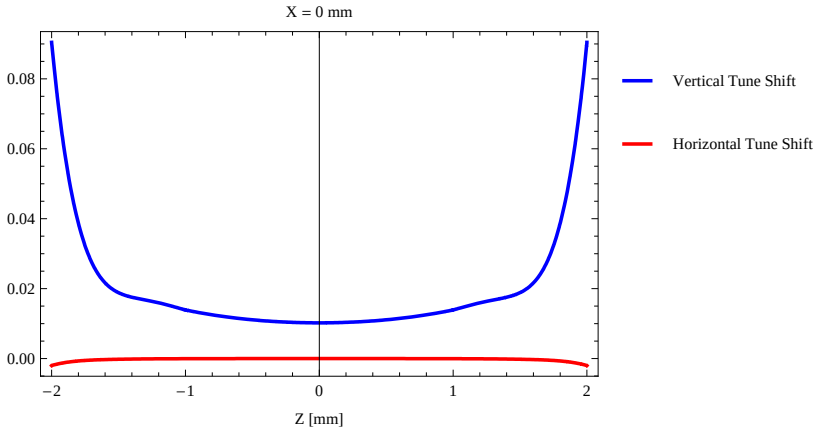

Figure 91: Induced tune shift from the cpmuA ID as a function of the vertical distance to the axis of the ID.

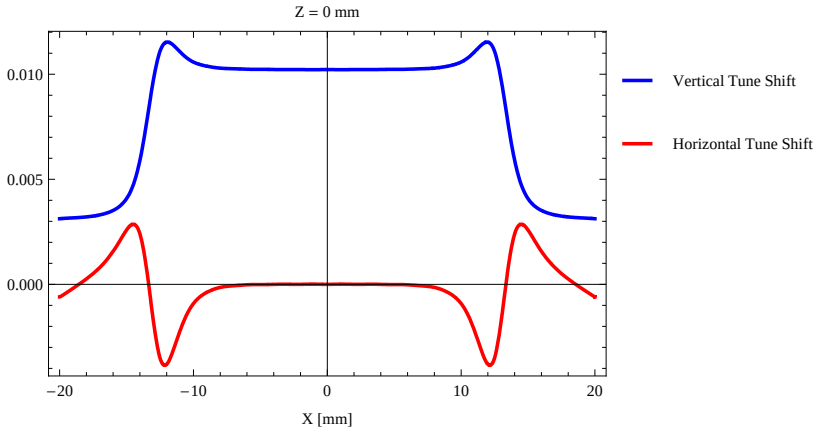

Figure 92: Induced tune shift from the cpmuA ID on the stored beam from the ID as a function of the horizontal distance to the axis of the ID.

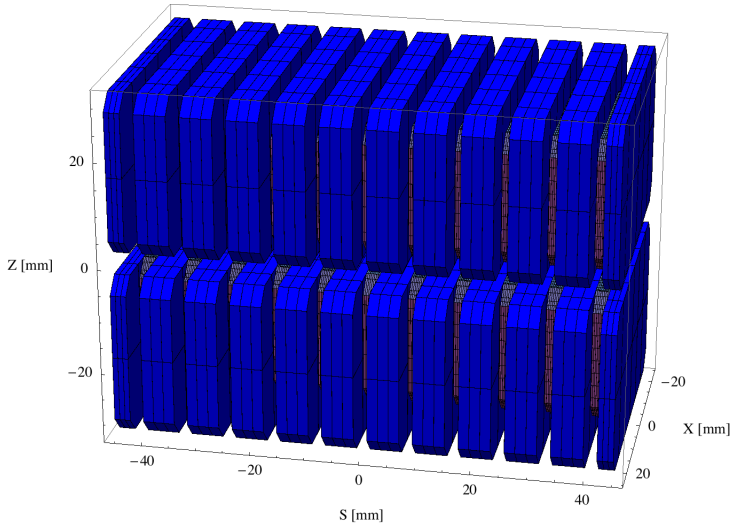

Figure 93: Magnetic model of the cpmuB ID

4.7 The cpmuB ID

4.7.1 Magnet model of the cpmuB ID

The cpmuB is a cryogenicaaly cooled in-vacuum undulator of hybrid type and the magnetic model of the cpmuB is shown in Figure 93. The magnet blocks, which are blue in Figure 93, are made of NdFeB materialwith a magnetic remance of 1.35 T at 140 K. The dimensions of the magnet blocks are 50.00x5.74x30.00x mm^3 and there is a 4 mm chamfer at the corners of the magnet blocks. The poles, which are grey in Figure 93, are made of pure iron. The dimensions of the poles are 32.00x2.46x24.00x mm^3 and there is a 3 mm chamfer at the corners of the poles.

4.7.2 Analysis of the magnetic field of the cpmuB ID

The vertical magnetic field in a central pole of the cpmuB ID along the ID axis, X = Z = 0 is shown in Figure 94. The vertical magnetic field in a central pole of the cpmuB ID in the horizontally transverse direction to the ID axis, S = Z = 0, is shown in Figure 95.

A Fourier anlysis of the magnetic field along the axis of the ID gives the higher harmonic contents in the magnetic field. A non-sinusoidal magnetic field profile along the ID would give a large higher harmonics contribution and it would no longer be possible to calculate the K-value of the ID from the peak field only. Also the higher harmonic contribution must be included to get the correct efficient magnetic field and efficient K-value. The higher harmonic contribution to the magnetic field is given in in Table 30.

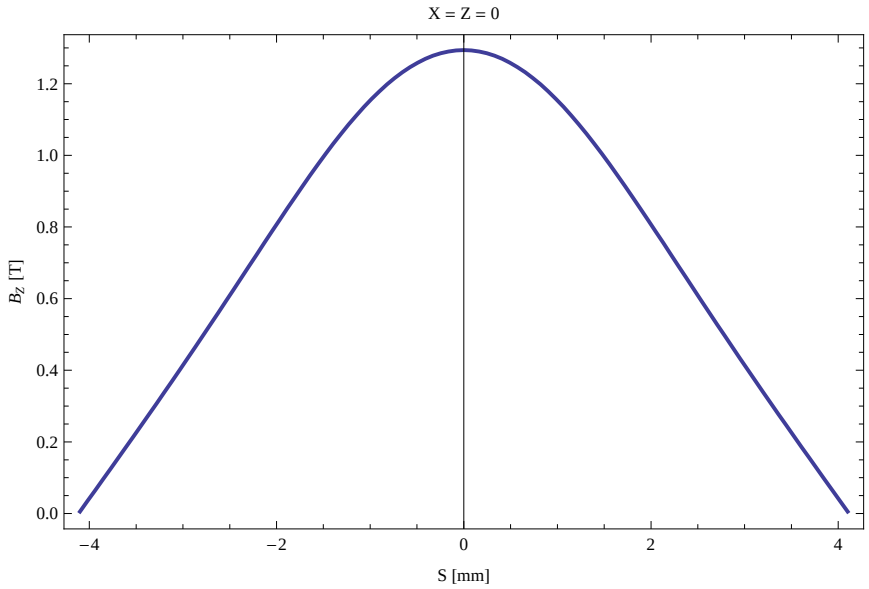

Figure 94: Vertical magnetic field in a central pole of the cpmuB ID along the ID axis, X = Z = 0

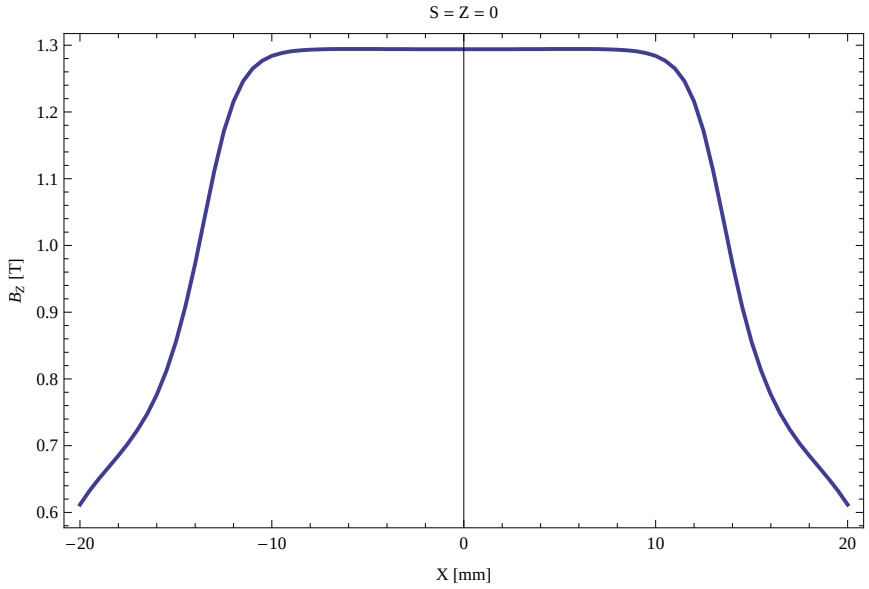

Figure 95: Vertical magnetic field in a central pole of the cpmuB ID along the horizontally transverse direction to the ID axis, S = Z = 0

Table 30: Fourier Analysis of the magnetic field of the cpmuB ID

Term	Strength
Harm. Nr. 1	1.196 T
Harm. Nr. 3	0.087 T
Harm. Nr. 5	0.003 T
Harm. Nr. 7	-0.001 T
Harm. Nr. 9	-0.000 T
Harm. Nr. 11	-0.000 T

A tranverse field roll-off may pose a problem to the storage ring since it gives a horizontal tune shift. The transverse field roll-off for the cpmuB for different horizontal positions out from the ID axis is shown in Figure 95 and numbers are given in Table 31.

Table 31: Transverse field roll-off for the cpmuB ID

X-Position	B_Z Field	Roll-off
± 0 mm	1.294 T	
± 5 mm	1.294 T	-0.03 %
± 10 mm	1.284 T	0.77 %
± 15 mm	0.856 T	33.88 %
± 20 mm	0.612 T	52.73 %

The paremeters of the cpmuB are summarised in Table 32.

4.7.3 Synchrotron radiation from the cpmuB ID

The power map of the emitted synchrotron radiation by the cpmuB ID, assuming a 0.5 A filament beam with an energy of 3. GeV and undulator properties of the synchrotron radiation, is shown in Figure 96. The on-axis power density is 118.750 kW/mrad^2

A map of the degree of linear polarisation of the fundamental harmonic of the synchotron radiation emitted by the cpmuB ID over the angle of obsevation is shown in Figure 97.

A map of the degree of 45 degree polarisation of the fundamental harmonic of the synchotron radiation emitted by the cpmuB ID over the angle of obsevation is shown in Figure 98.

A map of the degree of circular polarisation of the fundamental harmonic of the synchotron radiation emitted by the cpmuB ID over the angle of obsevation is shown in Figure 99.

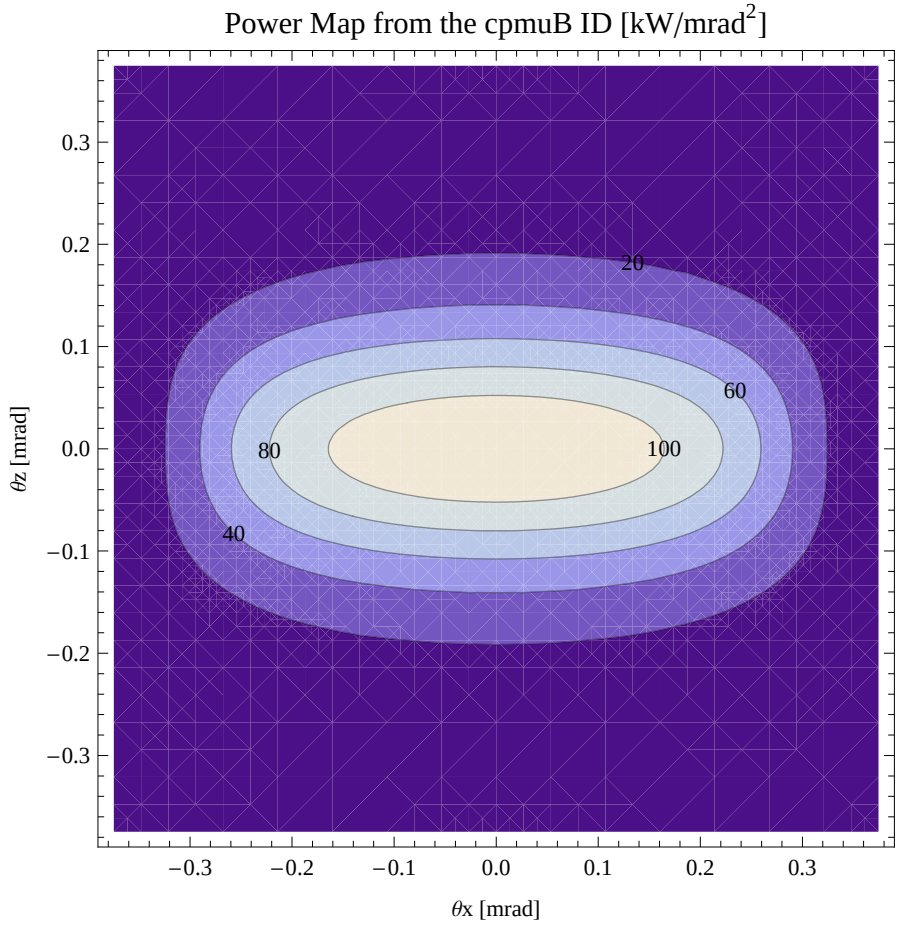

Figure 96: Map of the power distribution of the emitted synchrotron radiation by the cpmuB ID

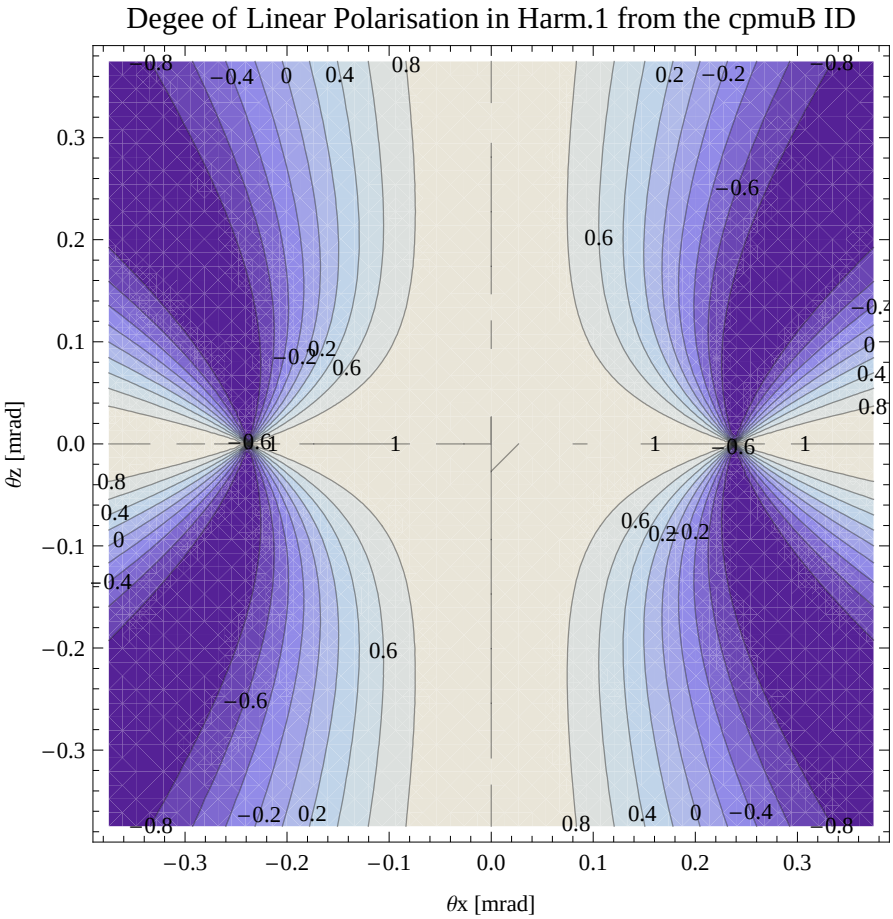

Figure 97: Map of linear polarisation in the fundamental harmonic of the synchotron radiation emitted by the cpmuB ID

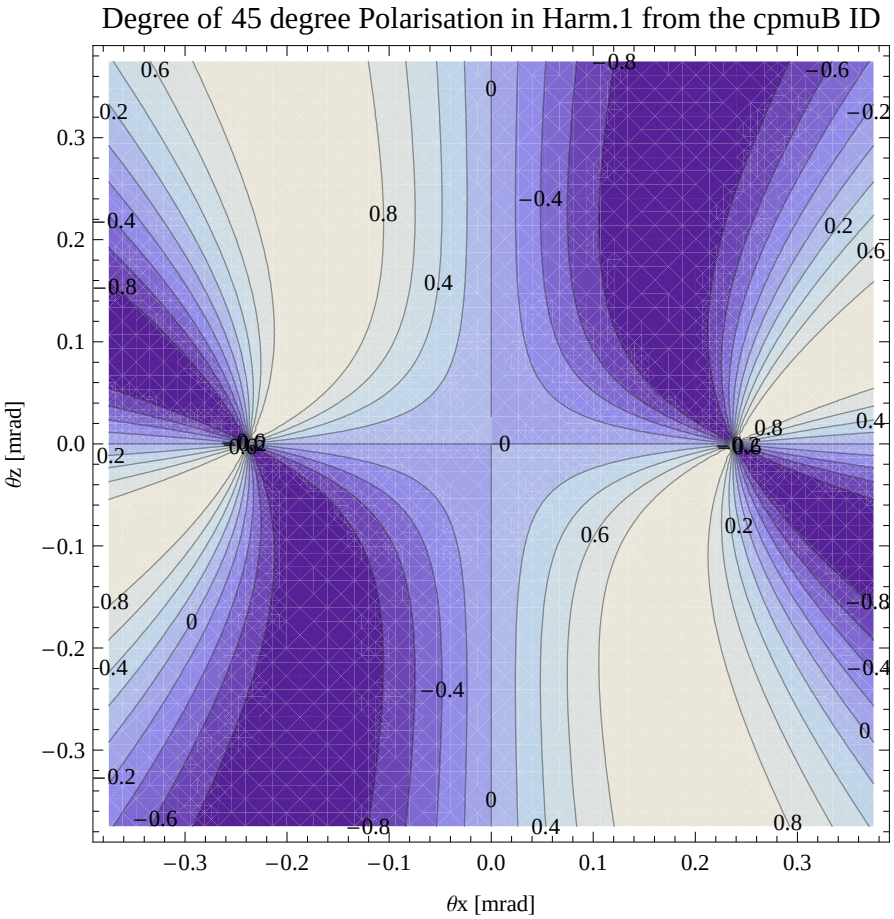

Figure 98: Map of 45 degree polarisation in the fundamental harmonic of the synchotron radiation emitted by the cpmuB ID

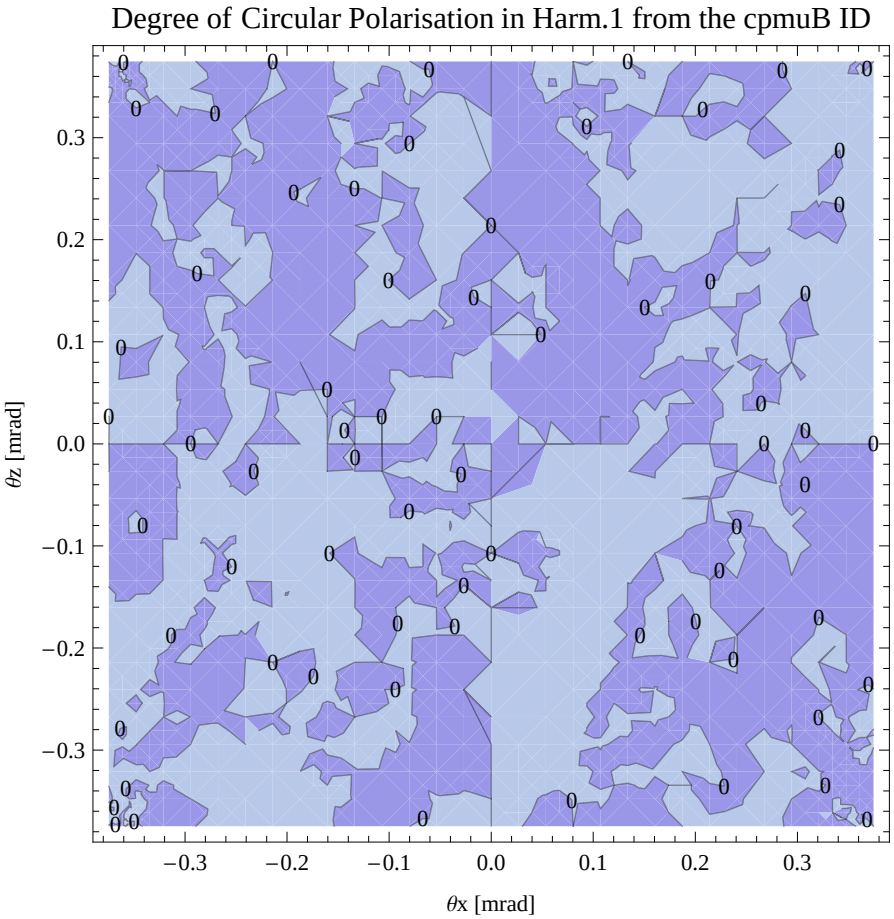

Figure 99: Map of circular polarisation in the fundamental harmonic of the synchotron radiation emitted by the cpmuB ID

Table 32: Summary of the cpmuB ID parameters

Period	16.4	mm
Gap	4.2	mm
Peak Field	1.294	T
Effective Field	1.196	T
Peak k-value	1.982	
Effective k-value	1.833	
Higher Order Contr.	7.31	%
Maximum e-beam deflection	0.30	mrad
Electron Beam Energy	3.0	GeV
Electron Beam Current	500	mA
Max Critical Energy	7.744	keV
Emitted Power	15.472	kW
Photon Energy, n = 1	1.946	keV
Total Length	3796.6	mm

The on axis brilliance at peak energy the and spectral flux density, also often called angular spectral flux, from the cpmuB ID has been calculated with the given beam parameters, which are 0.5 A of stored current, $\beta_H = 9.$ m, $\varepsilon_H = 0.263$ nmrad, $\beta_V = 4.8$ m, $\varepsilon_V = 8.$ pmrad, and an energy spread of 0.001. Figure 100 shows the brilliance at peak energy and Figure 101 shows the the spectral flux density.

The brilliance at peak energy the and the spectral flux density from the cpmuB ID for different harmonics at maximum K-value (1.833) are given in Table 33 and for minimum K-value (0.400) these values are given in Table 34.

Table 33: The brilliance at peak energy the and the spectral flux density from the cpmuB ID for different harmonics at maximum K-value (1.833)

Harmonic	Photon Energy [keV]	Brilliance [Ph./s/mrad^2/mrad^2/0.1%BW]	Spectral Flux Density [Ph./s/mrad^2/0.1%BW]
1	1.94516	2.88×10^{21}	6.97×10^{18}
3	5.83548	1.86×10^{21}	3.9×10^{18}
5	9.7258	1.06×10^{21}	2.17×10^{18}
7	13.6161	6.11×10^{20}	1.23×10^{18}
9	17.5064	3.54×10^{20}	7.08×10^{17}
11	21.3968	2.06×10^{20}	4.1×10^{17}

The brilliance at peak energy the and the spectral flux density from the cpmuB ID for different harmonics at maximum K-value (1.833) are given in Table 33 and for minimum

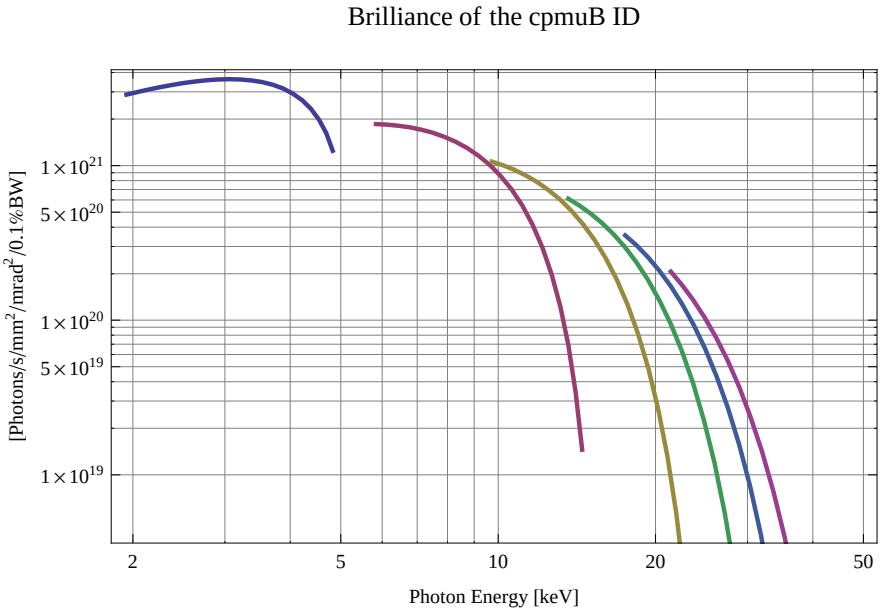

Figure 100: The brilliance at peak energy of the synchotron radiation emitted by the cpmuB ID

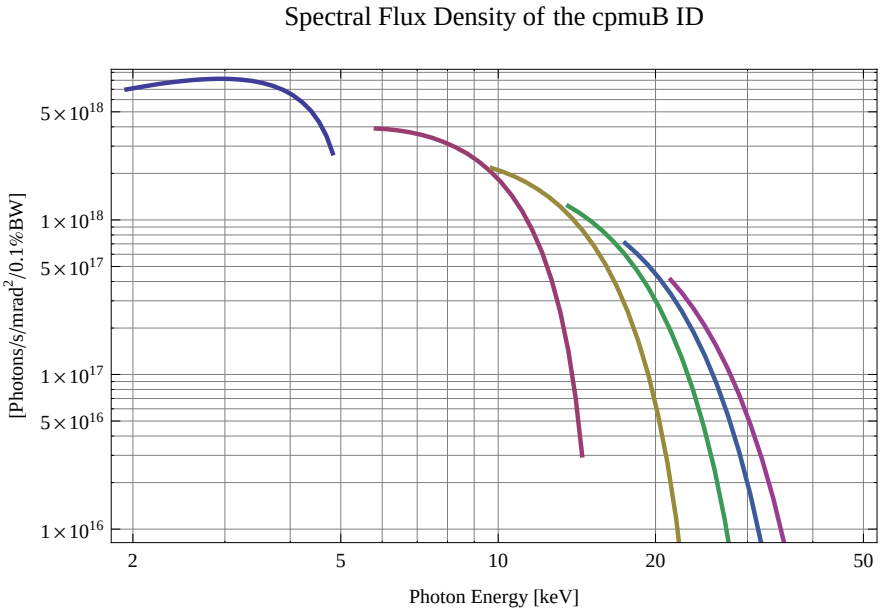

Figure 101: The spectral flux density of the synchotron radiation emitted by the cpmuB ID

K-value (0.400) these values are given in Table 34.

Table 34: The brilliance at peak energy the and the spectral flux density from the cpmuB ID for different harmonics at minimum K-value (0.4)

Harmonic	Photon Energy [keV]	Brilliance [Ph./s/mrad^2/mrad^2/0.1%BW]	Spectral Flux Density [Ph./s/mrad^2/0.1%BW]
1	4.82541	1.25×10^{21}	2.7×10^{18}
3	14.4762	1.46×10^{19}	$3. \times 10^{16}$
5	24.127	1.48×10^{17}	3.05×10^{14}
7	33.7778	1.5×10^{15}	3.08×10^{12}
9	43.4287	1.52×10^{13}	3.11×10^{10}
11	53.0795	1.53×10^{11}	3.14×10^{8}

4.7.4 Influence from the cpmuB ID on the optics of the stored beam

Figure 102 shows the focusing potential from the cpmuB over the beam stay clear aperture of the ring aparture.

Figure 103 shows the kick map in the beam energy independant unit T^2m^2 of the kicks induced by the cpmuB ID over the beam stay clear aparture.

Figure 104 shows the induced angular kick on the stored beam from the cpmuB ID as a function of the vertical distance to the axis of the ID.

Figure 105 shows the induced angular kick on the stored beam from the cpmuB ID as a function of the horizontal distance to the axis of the ID.

Figure 106 shows tune shift induced by the cpmuB ID over the beam stay clear aparture. Note that the tune shift depends on the beam size at the ID.

Figure 107 shows the induced tune shift from the cpmuB ID as a function of the vertical distance to the axis of the ID.

Figure 108 shows the induced tune shift from the cpmuB ID as a function of the horizontal distance to the axis of the ID.

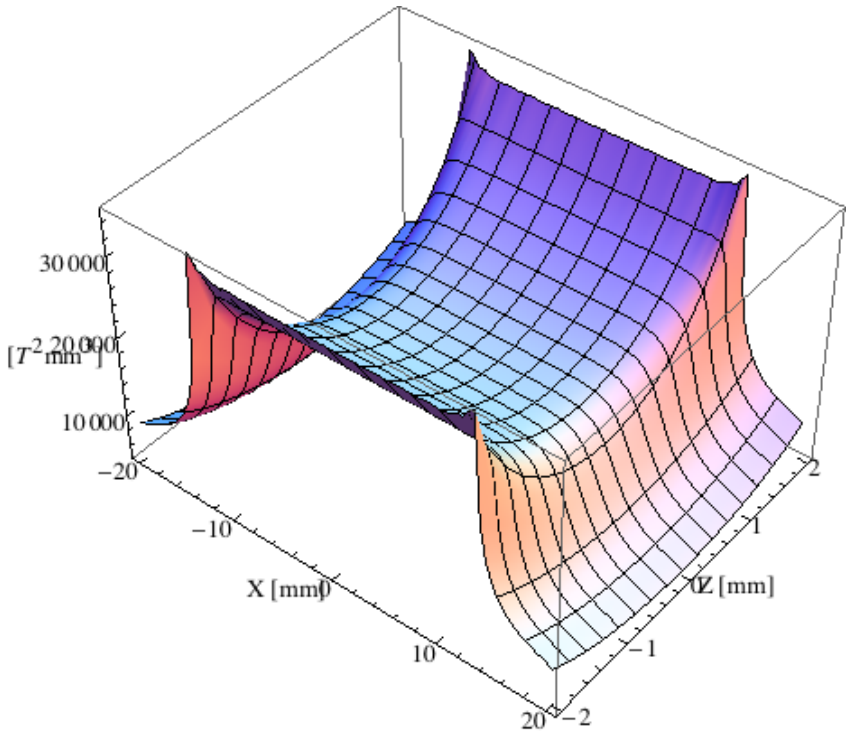

Figure 102: Focusing potential from the cpmuB ID over the beam stay clear aparture.

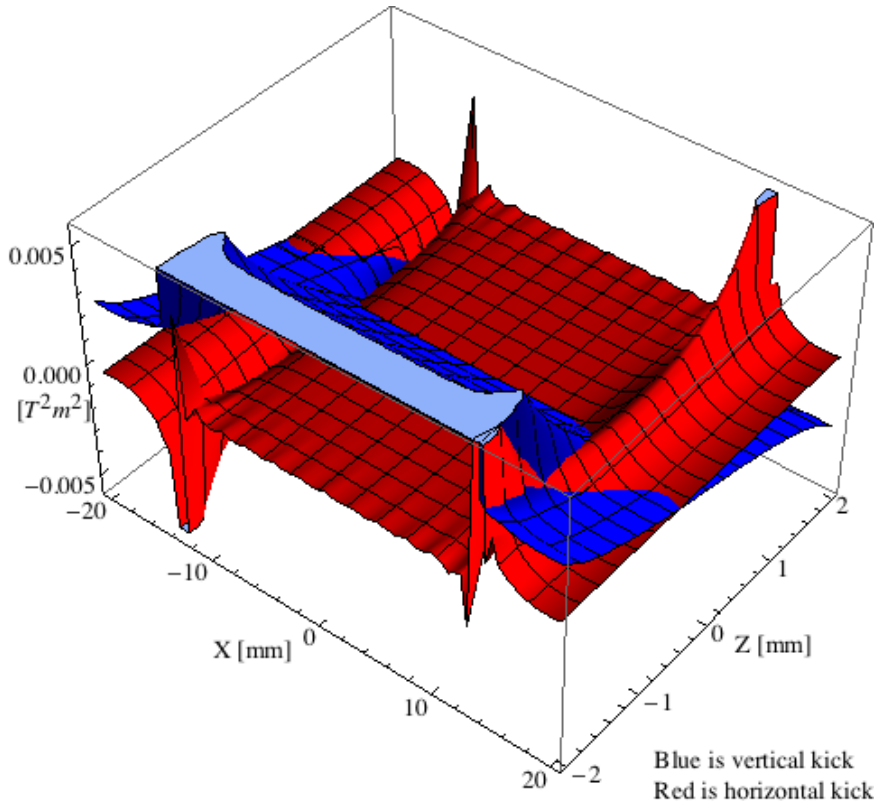

Figure 103: Kick map in the beam energy independant unit T^2m^2 of the kicks induced by the cpmuB ID over the beam stay clear aparture.

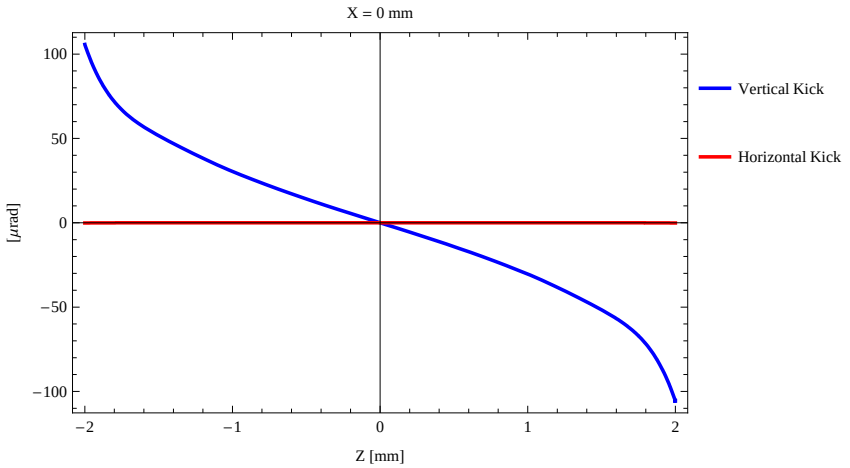

Figure 104: Induced angular kick on the stored beam from the cpmuB ID as a function of the vertical distance to the ID axis.

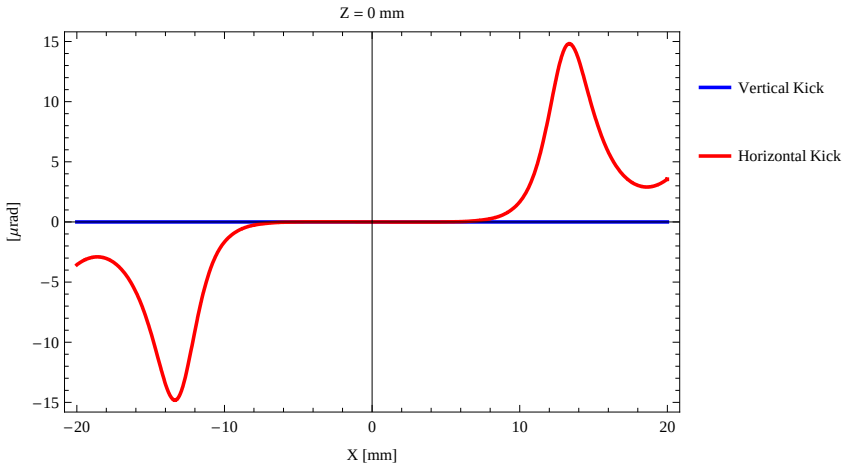

Figure 105: Induced angular kick on the stored beam from the cpmuB ID as a function of the horizontal distance to the ID axis.

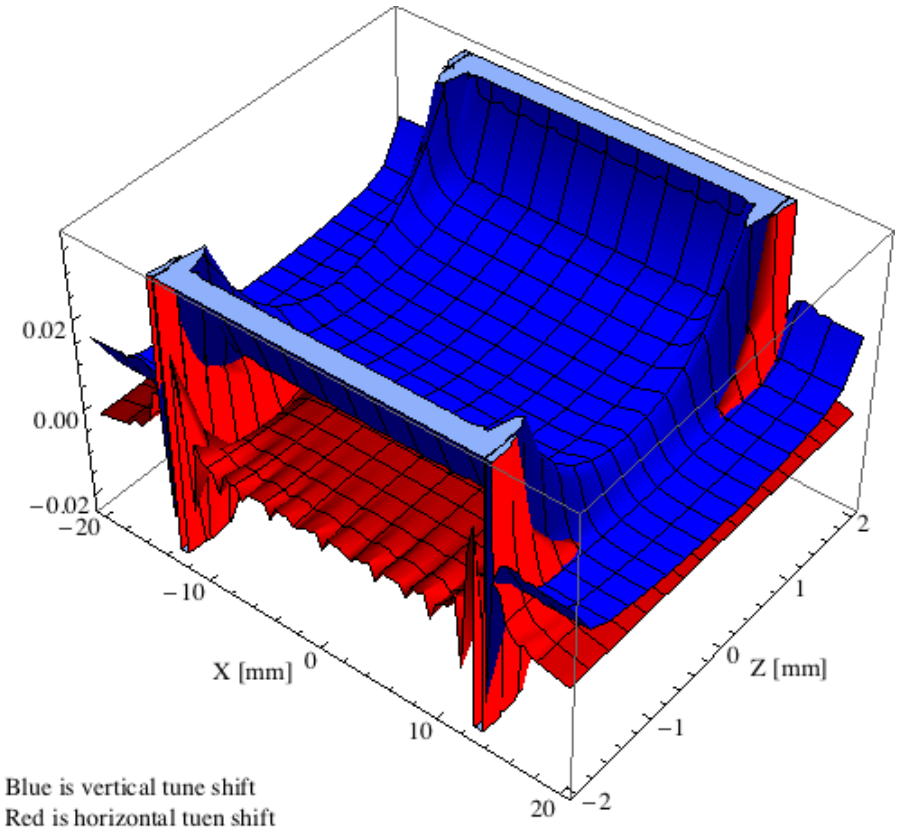

Figure 106: Tune shift induced by the cpmuB ID over the beam stay clear aparture.

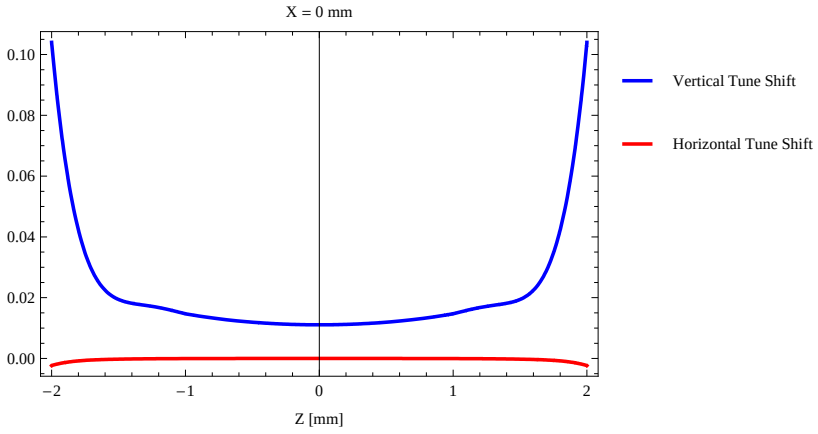

Figure 107: Induced tune shift from the cpmuB ID as a function of the vertical distance to the axis of the ID.

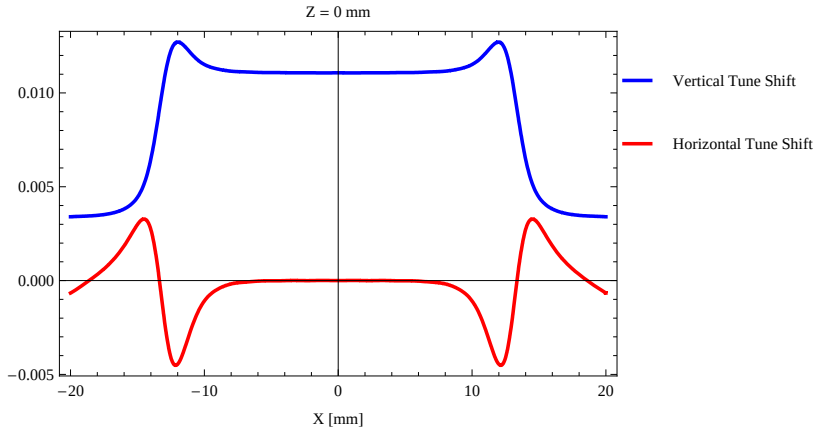

Figure 108: Induced tune shift from the cpmuB ID on the stored beam from the ID as a function of the horizontal distance to the axis of the ID.

4.8 The elliptically polaraising undulator epuA

4.8.1 Modes of operation in the elliptically polaraising undulator epuA

The magnetic structure of an elliptically polarising undulator (EPU) has a different configuration of the magnetic arrays compared to a standard flat field undulator. The upper and lower girders are split in two halves along the vertical plane of the undulator axis giving in total four sub - girders, where the sub - girders can be moved individually to also give a horizontal magnetic field in addition to the vertical magnetic field that is normally found on the undulators axis.

If the horizontal field has an offset along the beam trajectory of a quarter of a period the EPU is running in the helical mode and if the magnetic fields in horizontal and vertical direction have the same magnitude, the EPU is producing synchrotron radiation with circular polarisation. If the sub - girders are moved so that there is no offset between the horizontal and vertical magnetic field along the undulator axis, the EPU is operating in what is called the inclined mode and if the vertical and horizontal magnetic fields have the same magnitude, a state called 45 degree polarisation is obtained.

If the sub - girders are moved so that there is only a horizontal magnetic field component on axis, the EPU is operating is running in what is called the vertical mode. The vertical mode can be reached in bith inclined mode and helical mode with the diffrence that the end sections are longer for the vertical mode and the central section will be one period shorter. The two missing poles are added to the end sections of the EPU.

The horizontal field that could be obtained in an EPU is weaker than the maximum vertical field that could be obtained.

The difference between flat field undulators and EPUs can also be demonstrated by looking at the symmetry planes of the magnetic structures as carried out by [3]. In a planar undulator two symmetry planes can be defined: a horizontal plane Z= 0 in the magnetic mid plane, and a vertical plane X = 0 that cuts the magnet arrays in the middle. The line X = 0, Z = 0 is the magnetic center line or axis of the undulator.

An EPU in helical mode with a phase different from zero also has two symmetry planes X + Z = 0 and X - Z = 0, and the line where the planes cut each other is the axis of the EPU.

An EPU in inclined plane mode has no symmetry planes.

The magnetic field lines must be perpendicular to a symmetry plane, and this requirement means there cannot be any longitudinal field component on the magnetic center line of an EPU in helical mode. In inclined plane mode all three field components will be present.

The movement of the sub-girders are called the phase, ψ, of the EPU and ψ is measured in the same units as the period length λ_0. For the helical mode of operation the vertical

and horizontal fields vary with the EPU phase ψ at constant gap, g, as

$$\begin{aligned} B_Z(g,\psi) &= B_Z(g)\cos\tfrac{\pi\psi}{\lambda_0} \\ B_X(g,\psi) &= B_X(g)\sin\tfrac{\pi\psi}{\lambda_0} \end{aligned} \tag{4}$$

where $B_Z(g)$ and $B_X(g)$ are the efficient vertical and horizontal magnetic fields found at $\psi = 0$ and $\psi = \lambda_0/2$, respectively.

For the inclined plane mode of operation the fields over the central half period varies as

$$\begin{aligned} B_Z(g,\psi) &= B_Z(g)\cos^2\tfrac{\pi\psi}{\lambda_0} \\ B_X(g,\psi) &= B_X(g)\sin^2\tfrac{\pi\psi}{\lambda_0} \end{aligned} \tag{5}$$

The missing magnetic field in the inclined field shows up as a longitudinal field component, which can be seen in the plot below.

For the circular phase in the helical mode and the 45 degree inclined plane phase in the inclined plane mode of operation the horizontal and vertical fields have equal strength. The phases for circular and 45 degree inclined plane as functions of the EPU gap can hence be calculated by using

$$\begin{aligned} \psi_{Circular}(g) &= \tfrac{\lambda_0}{\pi}\arctan\tfrac{B_Z(g)}{B_X(g)} \\ \psi_{45Degree}(g) &= \tfrac{\lambda_0}{\pi}\arctan\sqrt{\tfrac{B_Z(g)}{B_X(g)}} \end{aligned} \tag{6}$$

Circular polarisation is found for a sub-grider movement for two of the four sub-girders of 11.229 mm when the epuA ID (Period=38. mm, Gap=9.mm) is operating in the helical mode. Figure 109 shows the vertical and horizontal magnetic field for the epuA ID when operating in the helical mode for different position for two of the four sub-girders.

45 degree polarisation is found for a sub-grider movement for two of the four sub-girders of 10.3735 mm when the epuA ID (Period=38. mm, Gap=9.mm) is operating in the helical mode. Figure 110 shows the vertical and horizontal magnetic field for the epuA ID when operating in the inclined mode for different position for two of the four sub-girders.

An EPU will give rise to dynamic multipoles due to the strong field gradients out from the undulator axis and these dynamic multipoles may reduce the beam lifetime and injection efficiency in a storage ring dramatically if they are not compensated for. The neutralisation of the induced multipoles from an EPU is not trivial and the method to be chosen for the EPUs at the MAX IV 3 GeV ring requires further studies. The influence from an uncorrected EPU has however been calculated and the results can be found in the following sections where the planar, helical, inclined and vertical modes of operation are described.

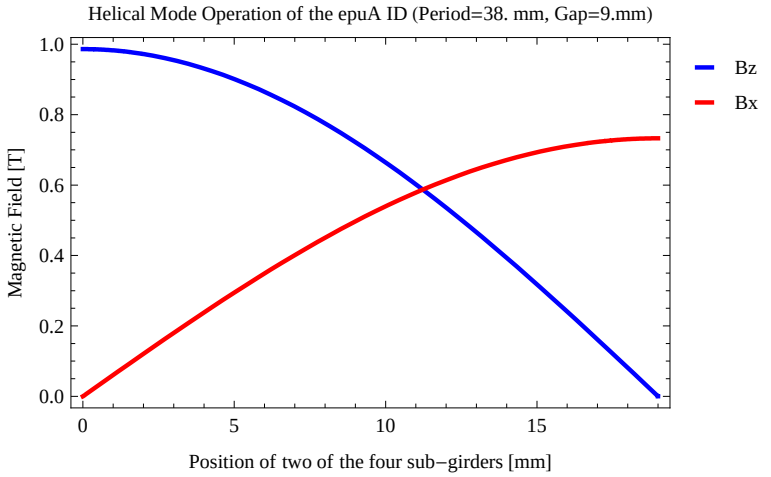

Figure 109: Vertical and horizontal magnetic field for the the epuA ID when operating in the helical mode for different position for two of the four sub-girders

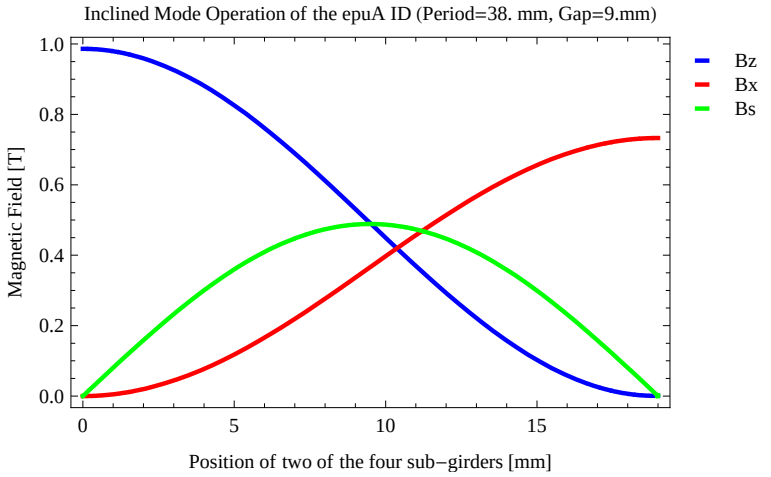

Figure 110: Vertical, horizontal, and longitudinal magnetic field for the the epuA ID when operating in the inclined mode for different position for two of the four sub-girders

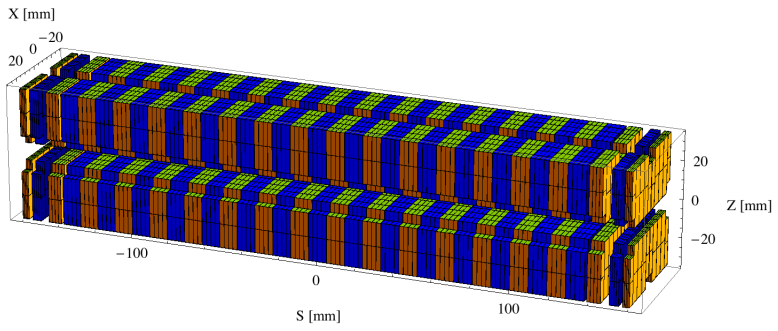

Figure 111: Magnetic model of the epuAPlan ID

The following sub-sections will cover four different situations; the epuA operating in the planar mode (epuAPlan), the epuA operating in the helical mode (epuAHeli),), the epuAoperating in the inclined mode (epuAIncl), and the epuA operating in the vertical mode (epuAIncl).

4.8.2 Magnet model of the elliptically polaraising undulator epuAPlan

The magnet model of the epuAPlan ID is shown in Figure 111. The length of the magnet model is 320.976 mm. The magnetic material in the model is NdFeb with a remanence of 1.28, a meterial similar to Vac776tp from Vacuumschmelze. Blocks with vertical magnetisation are blue and blocks with horizontal magnetisation are yellow. The block size is 30.x30.x9.5 mm^3 and there is a 5. mm cut-out in two of the corners of the blocks. The total length of the epuAPlan ID is 3930.98 mm.

4.8.3 Analysis of the magnetic field of the epuAPlan ID

The effective magnetic fields on axis and the fundamental photon energy of the epuAPlan ID are shown in Table 35. The higher harmonic contents in the magnetic field of an elliptically polarising undulator made of permanent magnets is negigible and the efficient field has about the same strength as the peak field.

4.8.4 Synchrotron radiation from the epuAPlan ID

The power map of the emitted synchrotron radiation by the epuAPlan ID, assuming a 0.5 A filament beam with an energy of 3. GeV and undulator properties of the synchrotron radiation, is shown in Figure 115. The on-axis power density is 43.893 $kW/mrad^2$

Table 35: Effective Fields on axis and Fundamental Photon Energy of the epuAPlan ID

Undulator Period	38.	mm
Undulator Gap	9.	mm
Undulator Mode	Planar	
Undulator Phase	0.000	mm
Vertical Peak Field	0.974	T
Efficient Vertical Field	0.986	T
Kx (from vert. field)	3.500	
Horizontal Peak Field:	0.000	T
Efficient Horizontal Field	0.000	T
Kz (from hor. field)	0.000	
Photon Energy, Harm.1	0.316	keV
Emitted Power	10.881	kW
Total Length	3931.0	mm

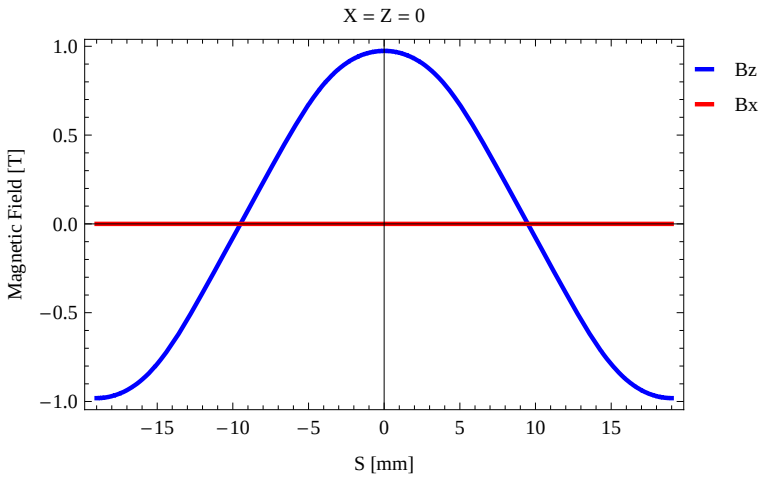

Figure 112: Vertical magnetic field in a central pole of the epuAPlan ID along the ID axis, X = Z = 0

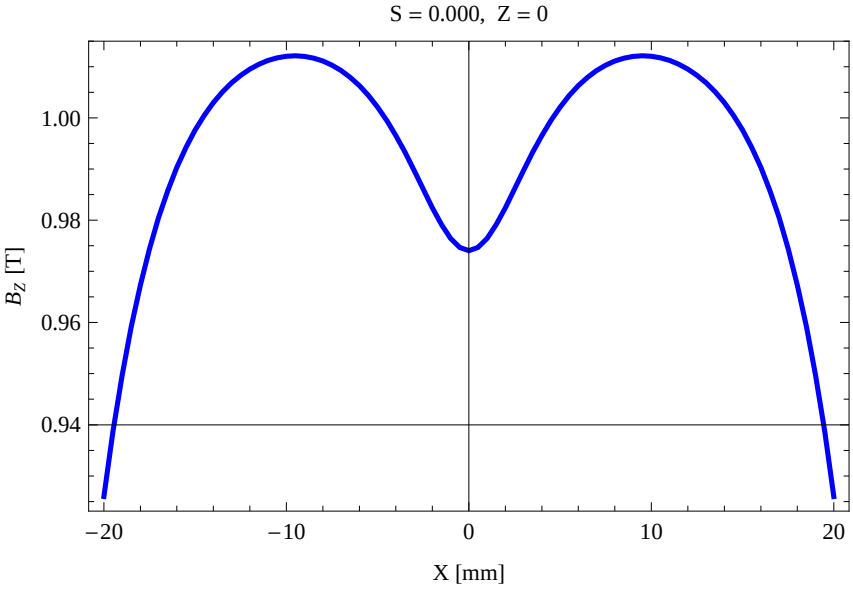

Figure 113: Vertical magnetic field in a central pole of the epuAPlan ID along the horizontally transverse direction to the ID axis, S = 0.000, Z = 0

A map of the degree of linear polarisation of the fundamental harmonic of the synchotron radiation emitted by the epuAPlan ID over the angle of obsevation is shown in Figure 116.

A map of the degree of 45 degree polarisation of the fundamental harmonic of the synchotron radiation emitted by the epuAPlan ID over the angle of obsevation is shown in Figure 117.

A map of the degree of circular polarisation of the fundamental harmonic of the synchotron radiation emitted by the epuAPlan ID over the angle of obsevation is shown in Figure 118.

The on axis brilliance at peak energy the and spectral flux density, also often called angular spectral flux, from the epuAPlan ID has been calculated with the given beam parameters, which are 0.5 A of stored current, $\beta_H = 9.$ m, $\varepsilon_H = 0.263$ nmrad, $\beta_V = 4.8$ m, $\varepsilon_V = 8.$ pmrad, and an energy spread of 0.001. Figure 119 shows the brilliance at peak energy and Figure 120 shows the the spectral flux density.

The brilliance at peak energy the and the spectral flux density from the epuAPlan ID for different harmonics at maximum K-value (3.500) are given in Table 36 and for minimum K-value (0.400) these values are given in Table 37.

The brilliance at peak energy the and the spectral flux density from the epuAPlan ID for different harmonics at maximum K-value (3.500) are given in Table 36 and for minimum K-value (0.400) these values are given in Table 37.

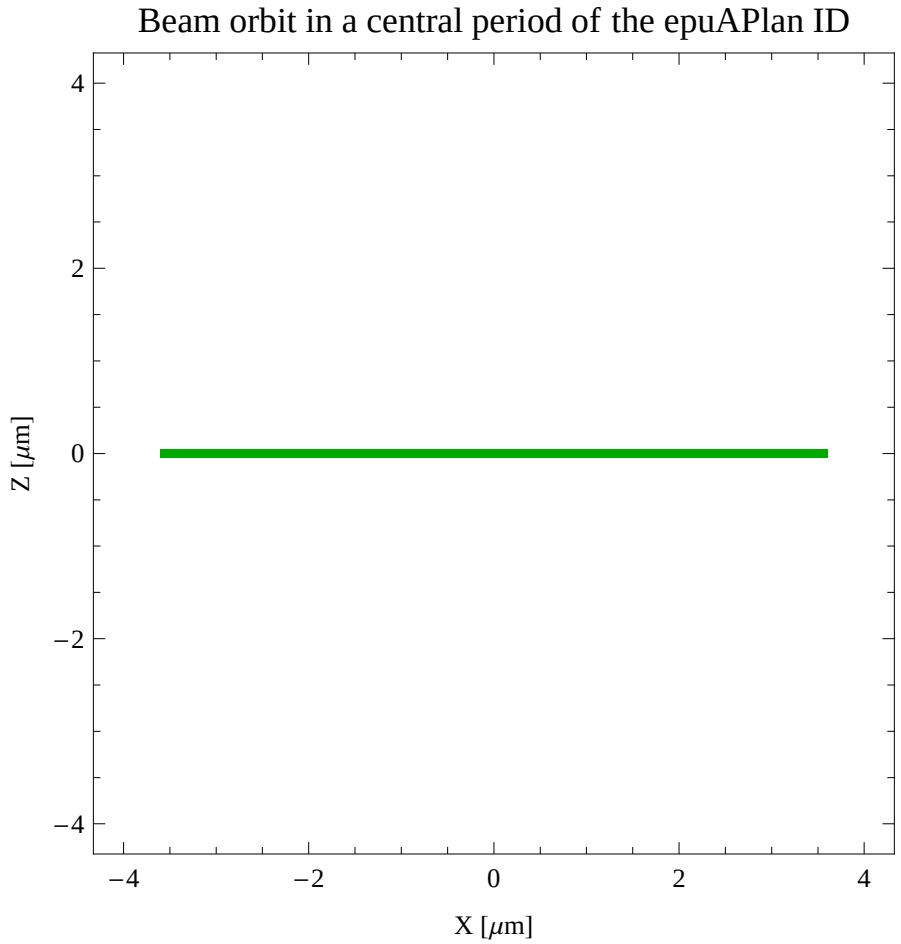

Figure 114: The beam orbit of the electron beam through a central period of the epuAPlan ID

Table 36: The brilliance at peak energy the and the spectral flux density from the epuAPlan ID for different harmonics at maximum K-value (3.500)

Harmonic	Photon Energy [keV]	Brilliance [Ph./s/mrad^2/mrad^2/0.1%BW]	Spectral Flux Density [Ph./s/mrad^2/0.1%BW]
1	0.315746	1.94×10^{20}	8.59×10^{17}
3	0.947237	3.18×10^{20}	9.32×10^{17}
5	1.57873	3.12×10^{20}	7.99×10^{17}
7	2.21022	2.85×10^{20}	6.83×10^{17}
9	2.84171	2.57×10^{20}	5.9×10^{17}
11	3.4732	2.3×10^{20}	5.13×10^{17}

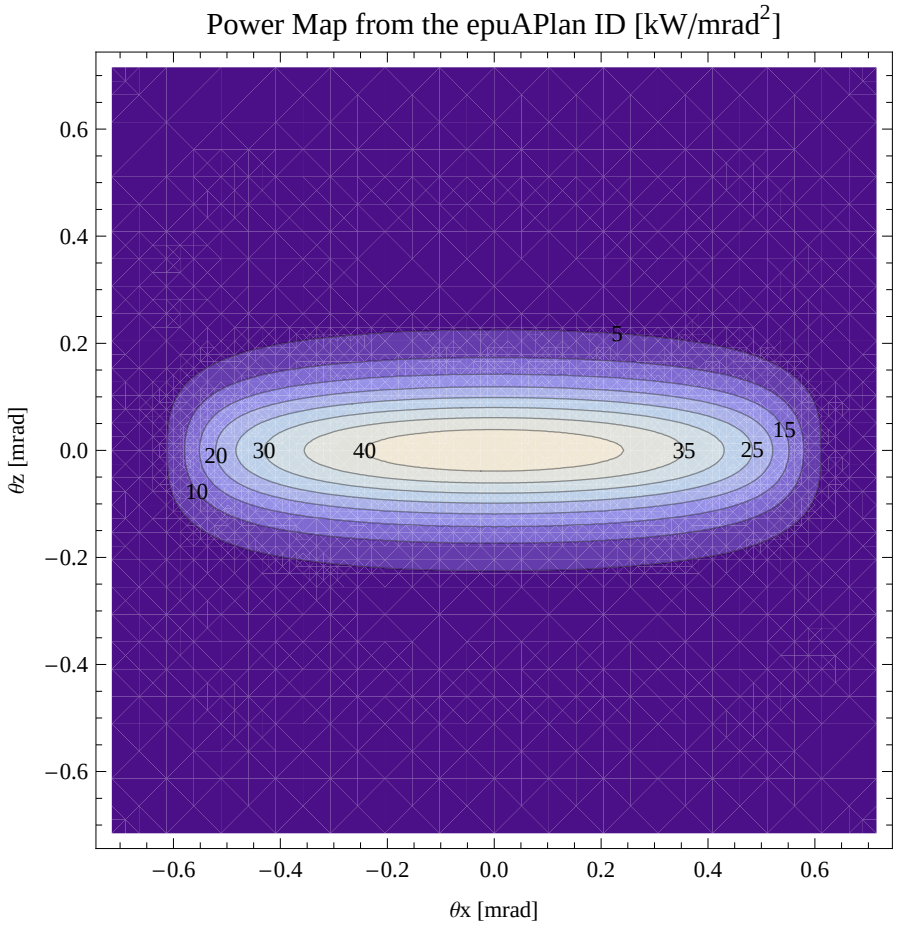

Figure 115: Map of the power distribution of the emitted synchrotron radiation by the epuAPlan ID

Table 37: The brilliance at peak energy the and the spectral flux density from the epuAPlan ID for different harmonics at minimum K-value (0.4)

Harmonic	Photon Energy [keV]	Brilliance [Ph./s/mrad^2/mrad^2/0.1%BW]	Spectral Flux Density [Ph./s/mrad^2/0.1%BW]
1	2.08254	3.23×10^{20}	7.84×10^{17}
3	6.24763	5.54×10^{18}	1.18×10^{16}
5	10.4127	6.1×10^{16}	1.27×10^{14}
7	14.5778	6.35×10^{14}	1.31×10^{12}
9	18.7429	6.5×10^{12}	1.34×10^{10}
11	22.908	6.62×10^{10}	1.36×10^{8}

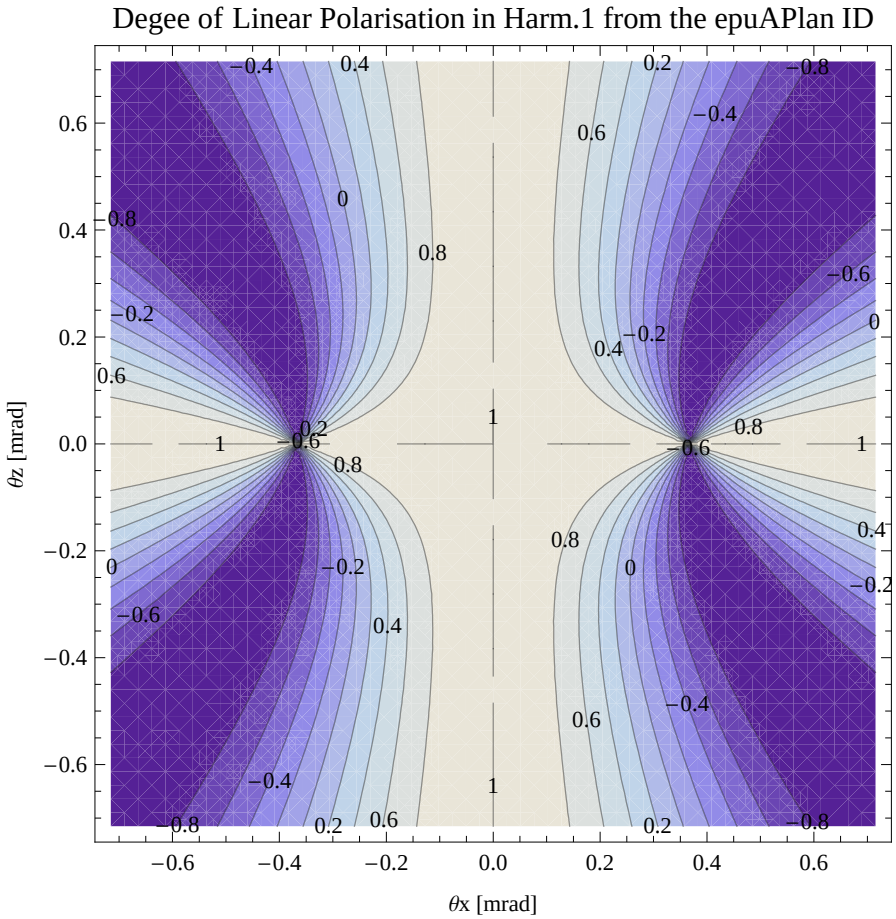

Figure 116: Map of linear polarisation in the fundamental harmonic of the synchotron radiation emitted by the epuAPlan ID

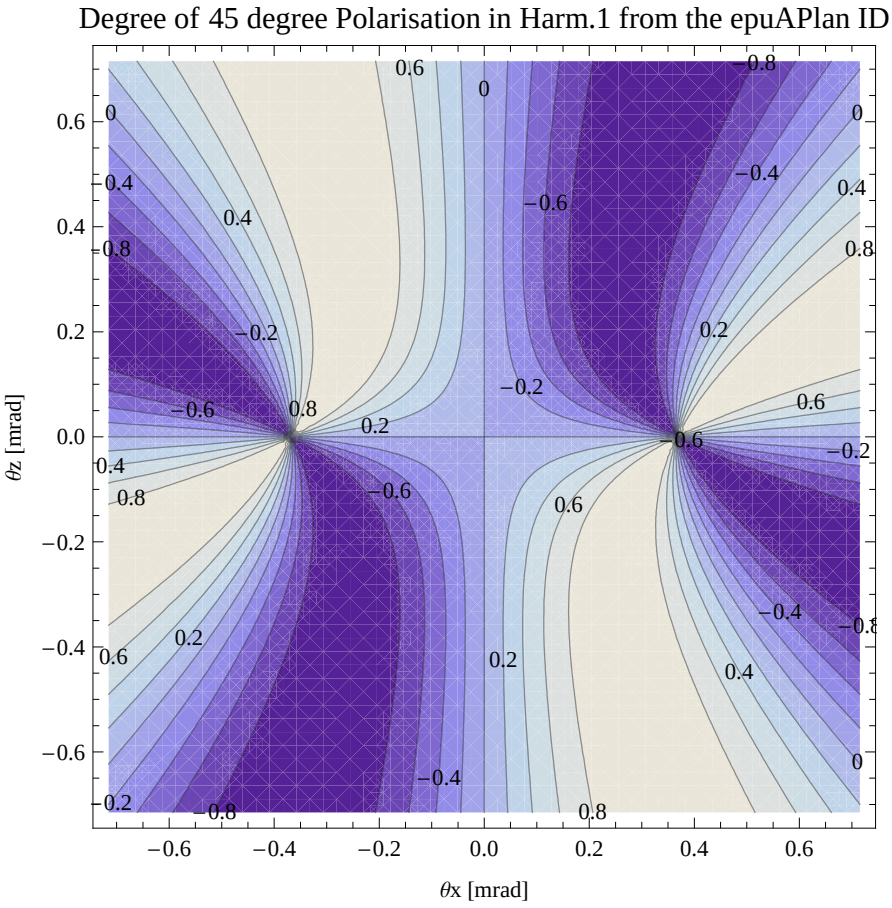

Figure 117: Map of 45 degree polarisation in the fundamental harmonic of the synchotron radiation emitted by the epuAPlan ID

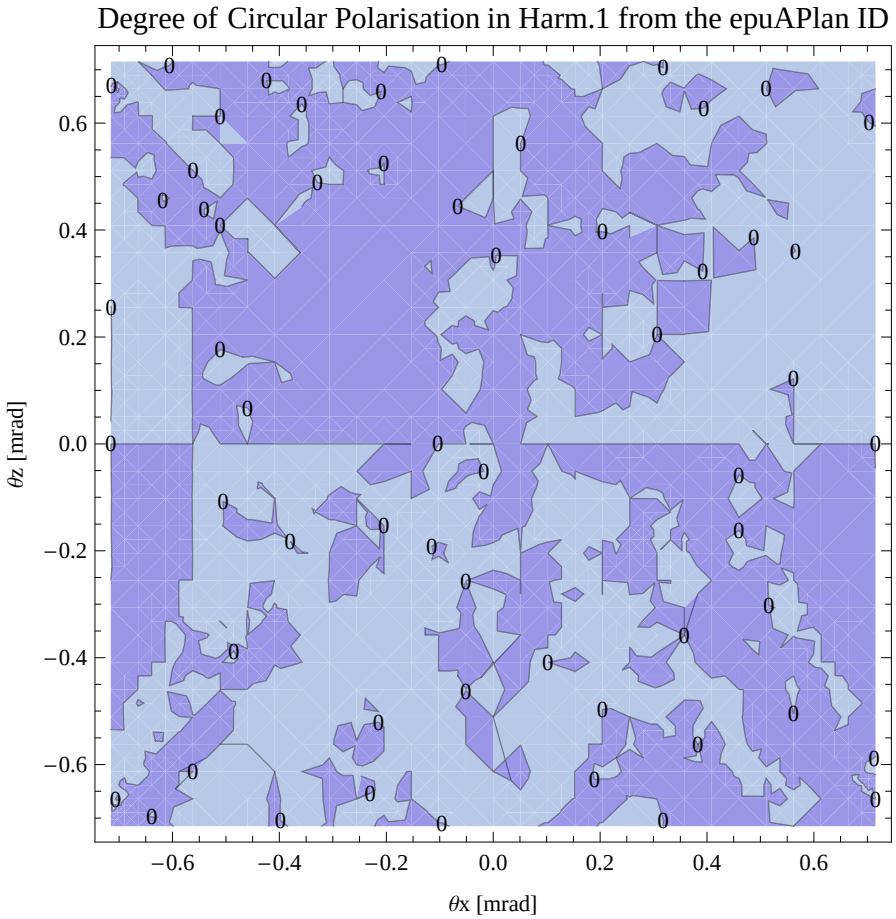

Figure 118: Map of circular polarisation in the fundamental harmonic of the synchotron radiation emitted by the epuAPlan ID

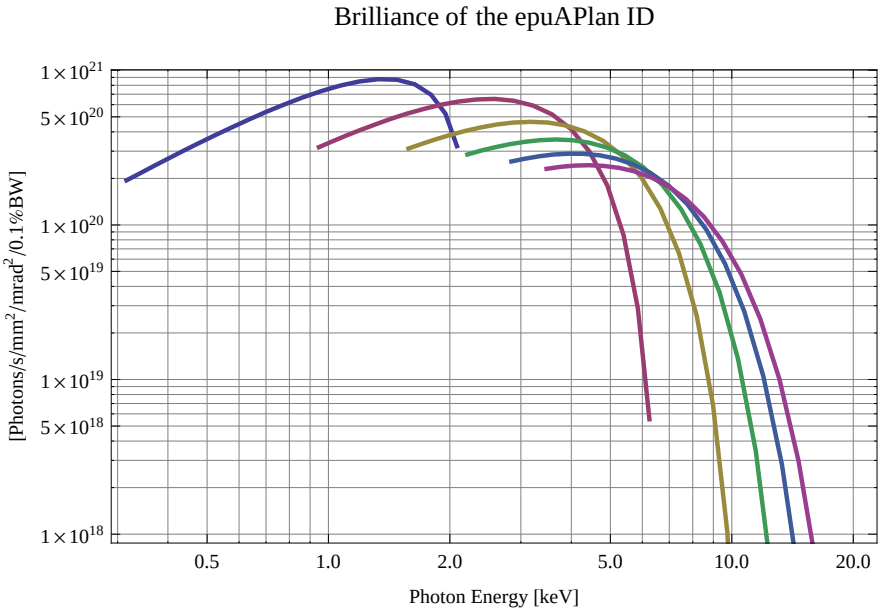

Figure 119: The brilliance at peak energy of the synchotron radiation emitted by the epuAPlan ID

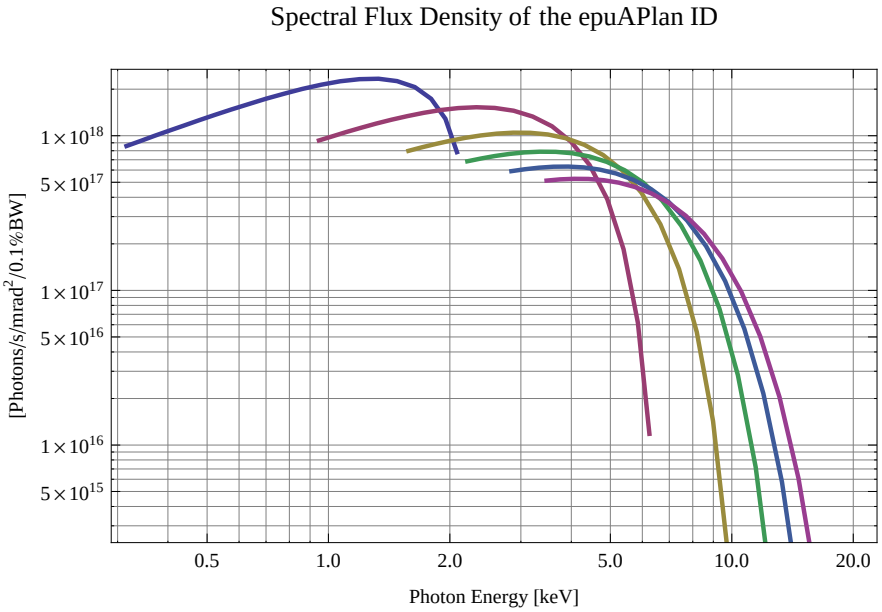

Figure 120: The spectral flux density of the synchotron radiation emitted by the epuA-Plan ID

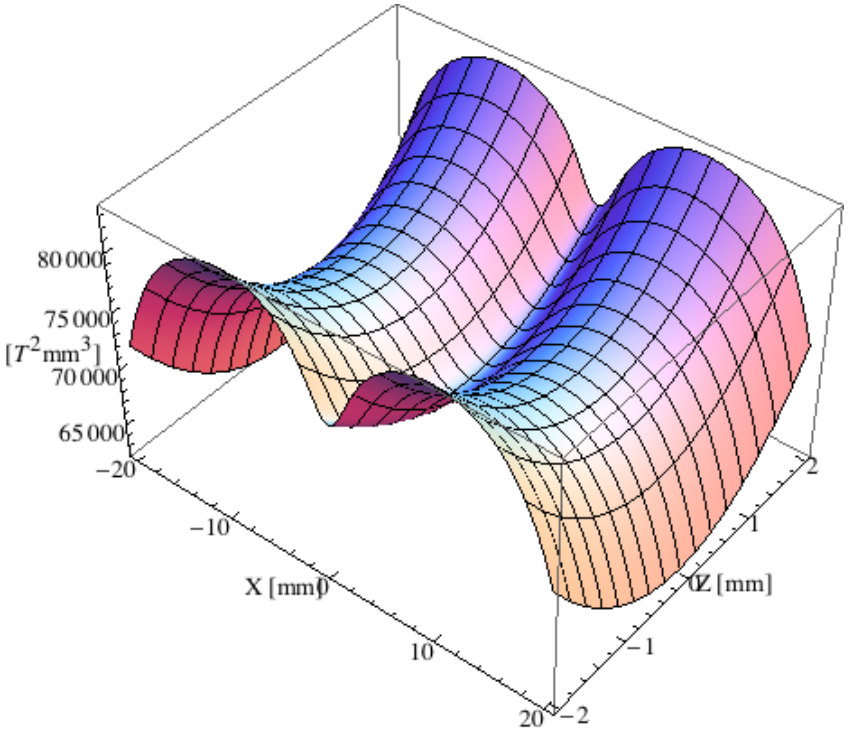

Figure 121: Focusing potential from the epuAPlan ID over the beam stay clear aparture.

4.8.5 Influence from the epuAPlan ID on the optics of the stored beam

Figure 121 shows the focusing potential from the epuAPlan over the beam stay clear aperture of the ring aparture.

Figure 122 shows the kick map in the beam energy independant unit T^2m^2 of the kicks induced by the epuAPlan ID over the beam stay clear aparture.

Figure 123 shows the induced angular kick on the stored beam from the epuAPlan ID as a function of the vertical distance to the axis of the ID.

Figure 124 shows the induced angular kick on the stored beam from the epuAPlan ID as a function of the horizontal distance to the axis of the ID.

Figure 125 shows tune shift induced by the epuAPlan ID over the beam stay clear aparture. Note that the tune shift depends on the beam size at the ID.

Figure 126 shows the induced tune shift from the epuAPlan ID as a function of the vertical distance to the axis of the ID.

Figure 127 shows the induced tune shift from the epuAPlan ID as a function of the horizontal distance to the axis of the ID.

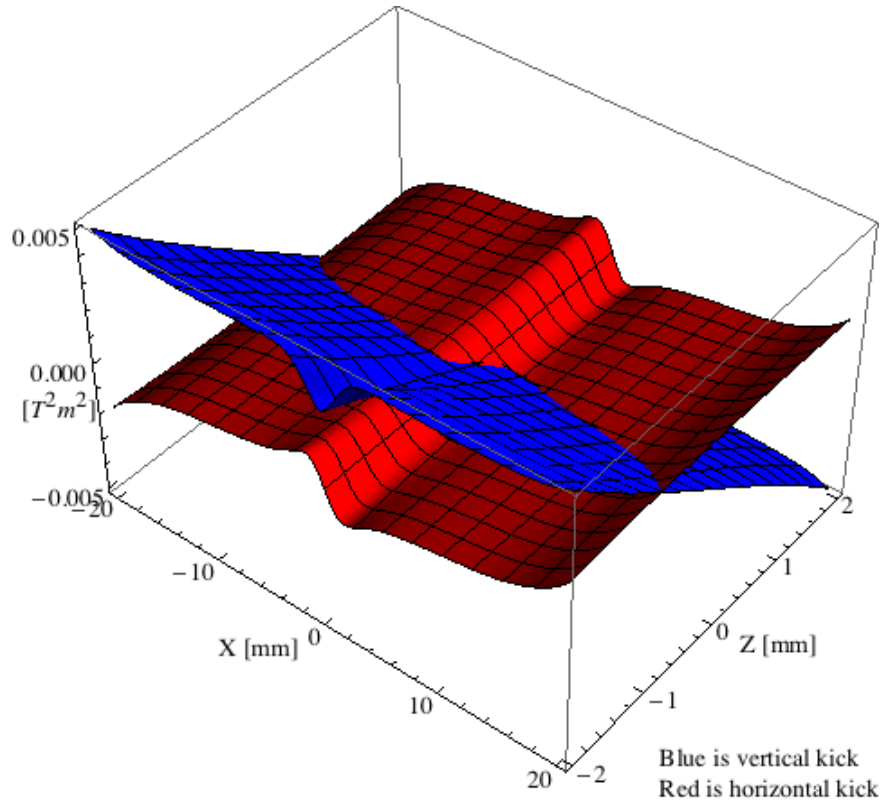

Figure 122: Kick map in the beam energy independant unit T^2m^2 of the kicks induced by the epuAPlan ID over the beam stay clear aparture.

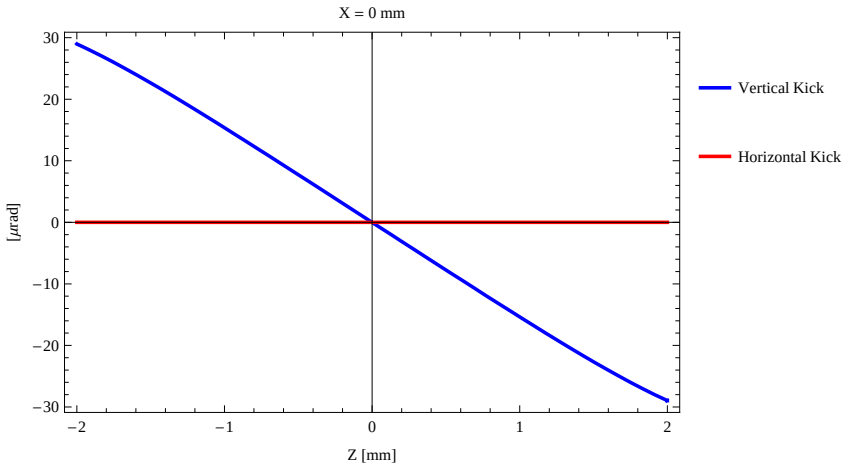

Figure 123: Induced angular kick on the stored beam from the epuAPlan ID as a function of the vertical distance to the ID axis.

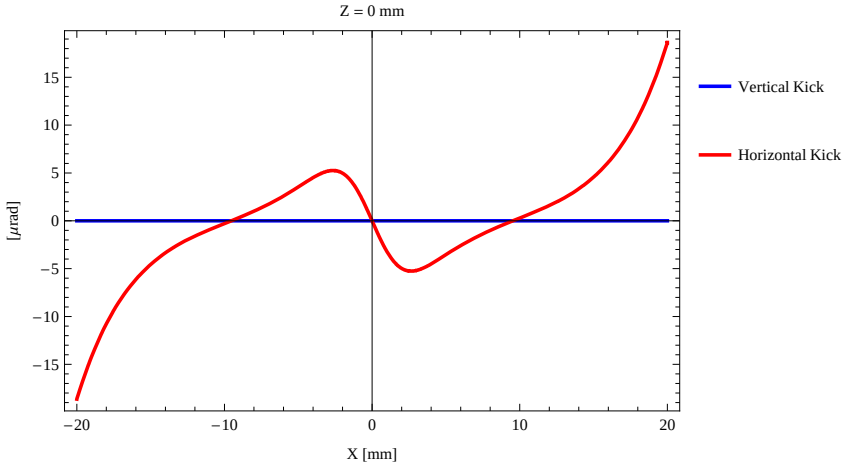

Figure 124: Induced angular kick on the stored beam from the epuAPlan ID as a function of the horizontal distance to the ID axis.

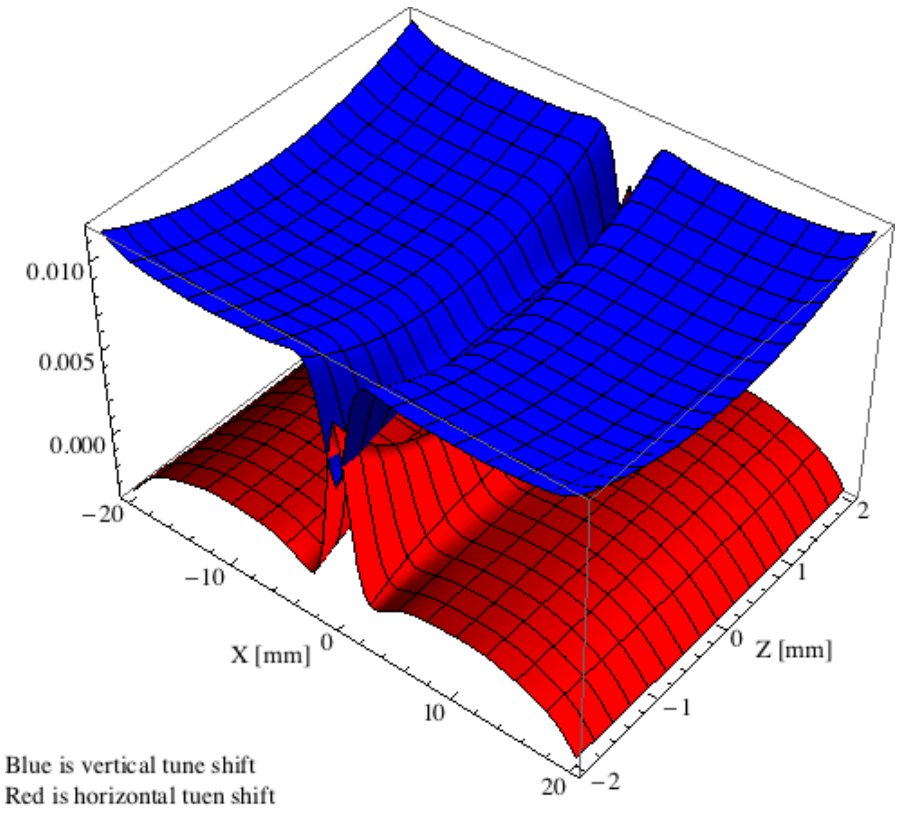

Figure 125: Tune shift induced by the epuAPlan ID over the beam stay clear aparture.

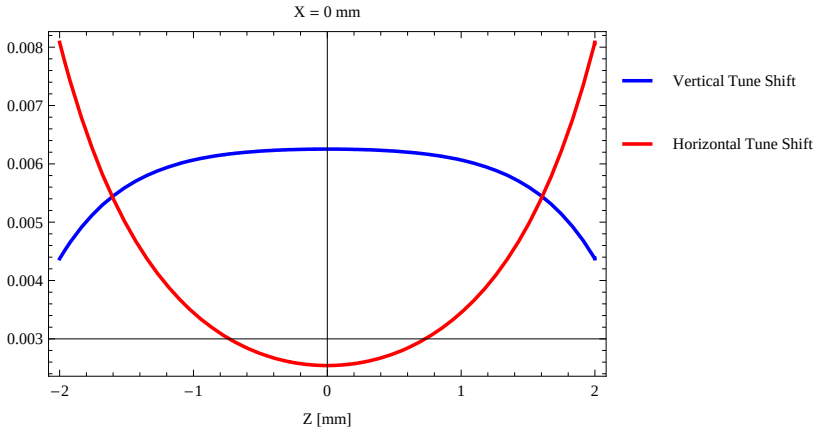

Figure 126: Induced tune shift from the epuAPlan ID as a function of the vertical distance to the axis of the ID.

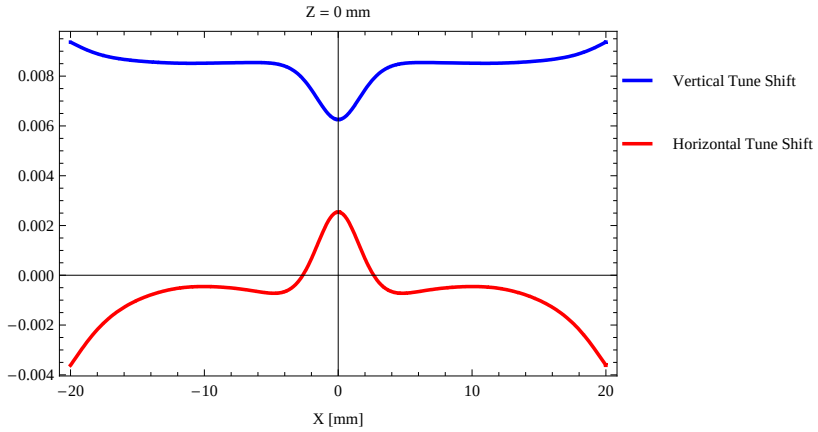

Figure 127: Induced tune shift from the epuAPlan ID on the stored beam from the ID as a function of the horizontal distance to the axis of the ID.

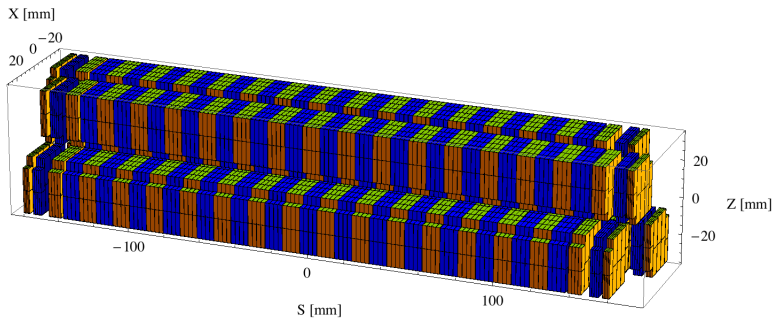

Figure 128: Magnetic model of the epuAHeli ID

4.8.6 Magnet model of the elliptically polaraising undulator epuAHeli

The magnet model of the epuAHeli ID is shown in Figure 128. The length of the magnet model is 320.976 mm. The magnetic material in the model is NdFeb with a remanence of 1.28, a meterial similar to Vac776tp from Vacuumschmelze. Blocks with vertical magnetisation are blue and blocks with horizontal magnetisation are yellow. The block size is 30.x30.x9.5 mm^3 and there is a 5. mm cut-out in two of the corners of the blocks. The total length of the epuAHeli ID is 3930.98 mm.

4.8.7 Analysis of the magnetic field of the epuAHeli ID

The effective magnetic fields on axis and the fundamental photon energy of the epuAHeli ID are shown in Table 38. The higher harmonic contents in the magnetic field of an elliptically polarising undulator made of permanent magnets is negigible and the efficient field has about the same strength as the peak field.

4.8.8 Synchrotron radiation from the epuAHeli ID

The power map of the emitted synchrotron radiation by the epuAHeli ID, assuming a 0.5 A filament beam with an energy of 3. GeV and undulator properties of the synchrotron radiation, is shown in Figure 133. The on-axis power density is 1.644 $kW/mrad^2$

A map of the degree of linear polarisation of the fundamental harmonic of the synchotron radiation emitted by the epuAHeli ID over the angle of obsevation is shown in Figure 134.

A map of the degree of 45 degree polarisation of the fundamental harmonic of the synchotron radiation emitted by the epuAHeli ID over the angle of obsevation is shown in Figure 135.

Table 38: Effective Fields on axis and Fundamental Photon Energy of the epuAHeli ID

Undulator Period	38.	mm
Undulator Gap	9.	mm
Undulator Mode	Helical	
Undulator Phase	11.229	mm
Vertical Peak Field	0.585	T
Efficient Vertical Field	0.587	T
Kx (from vert. field)	2.083	
Horizontal Peak Field:	0.590	T
Efficient Horizontal Field	0.587	T
Kz (from hor. field)	2.083	
Photon Energy, Harm.1	0.421	keV
Emitted Power	7.713	kW
Total Length	3931.0	mm

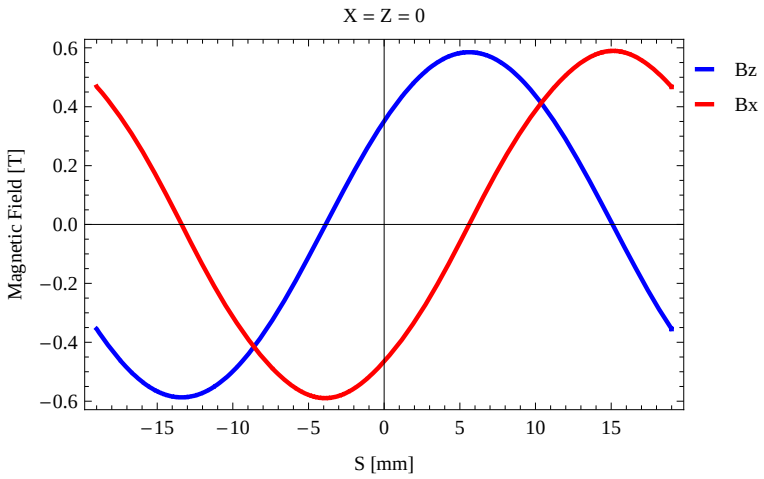

Figure 129: Vertical magnetic field in a central pole of the epuAHeli ID along the ID axis, X = Z = 0

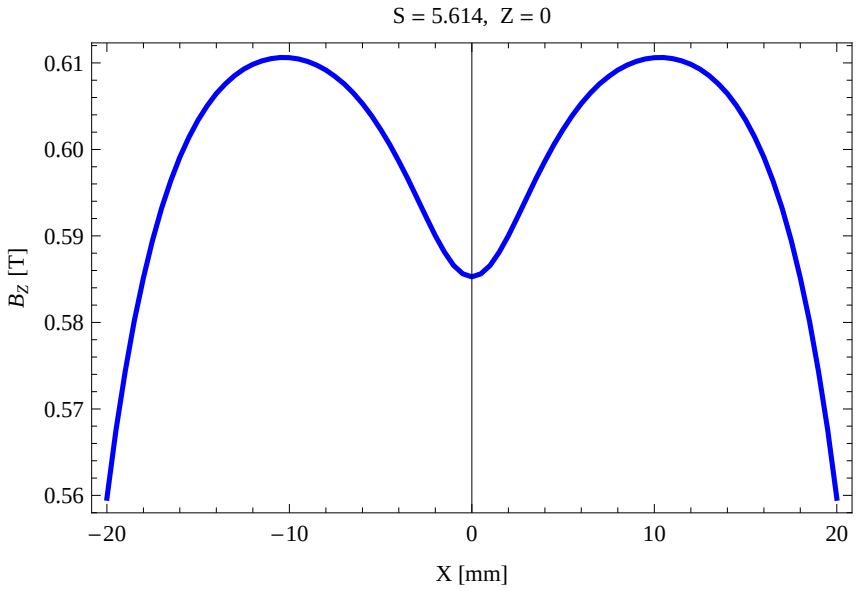

Figure 130: Vertical magnetic field in a central pole of the epuAHeli ID along the horizontally transverse direction to the ID axis, S = 5.614, Z = 0

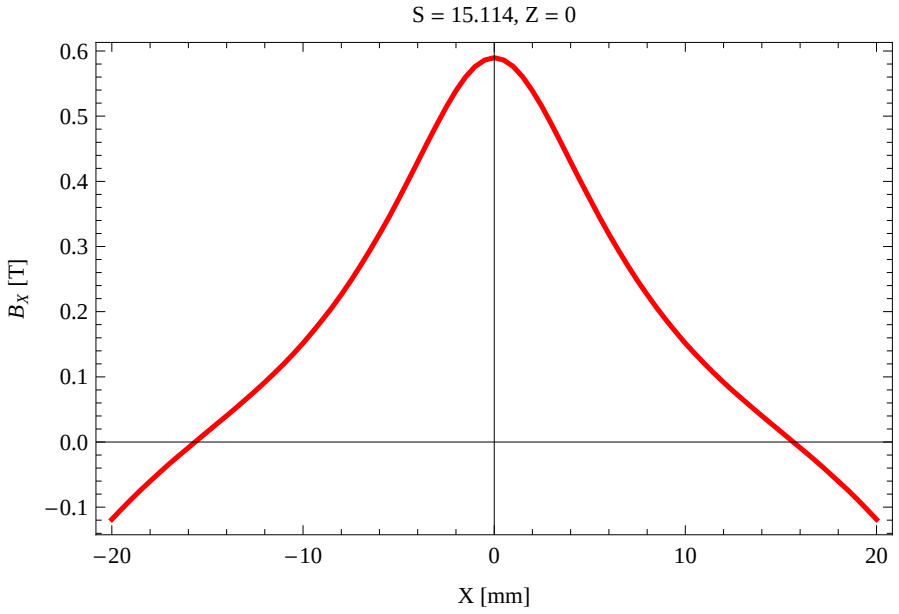

Figure 131: Horizontal magnetic field in a central pole of the epuAHeli ID along the horizontally transverse direction to the ID axis, S = 15.114, Z = 0

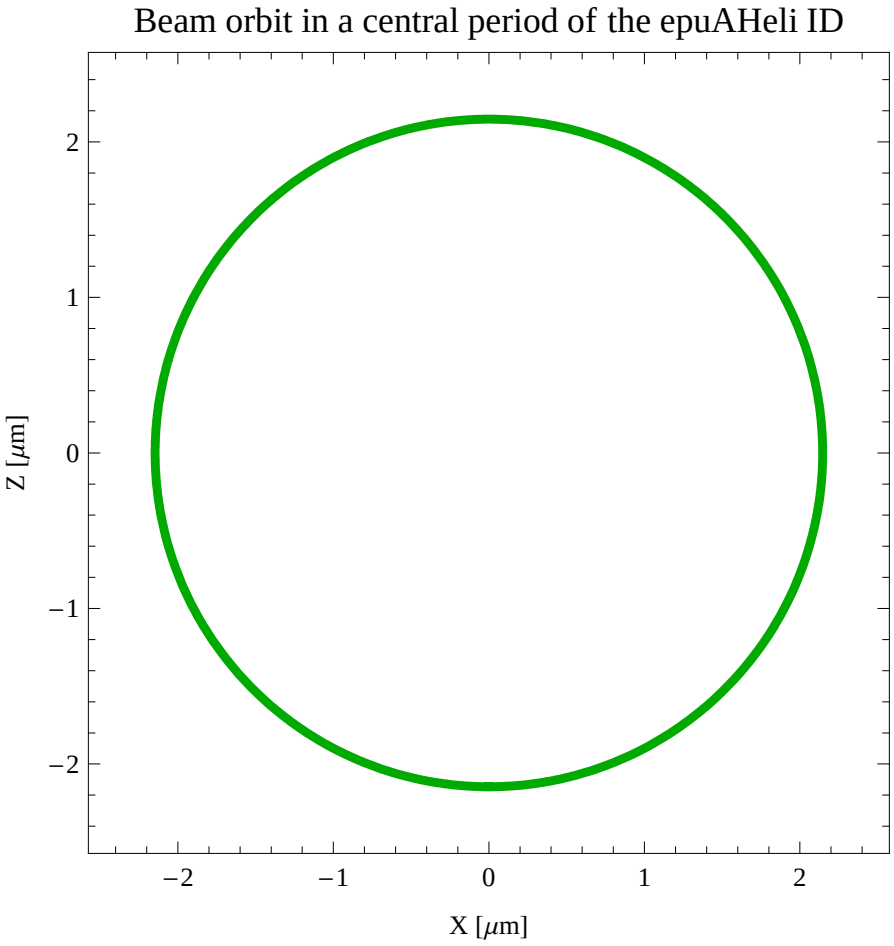

Figure 132: The beam orbit of the electron beam through a central period of the epuA-Heli ID

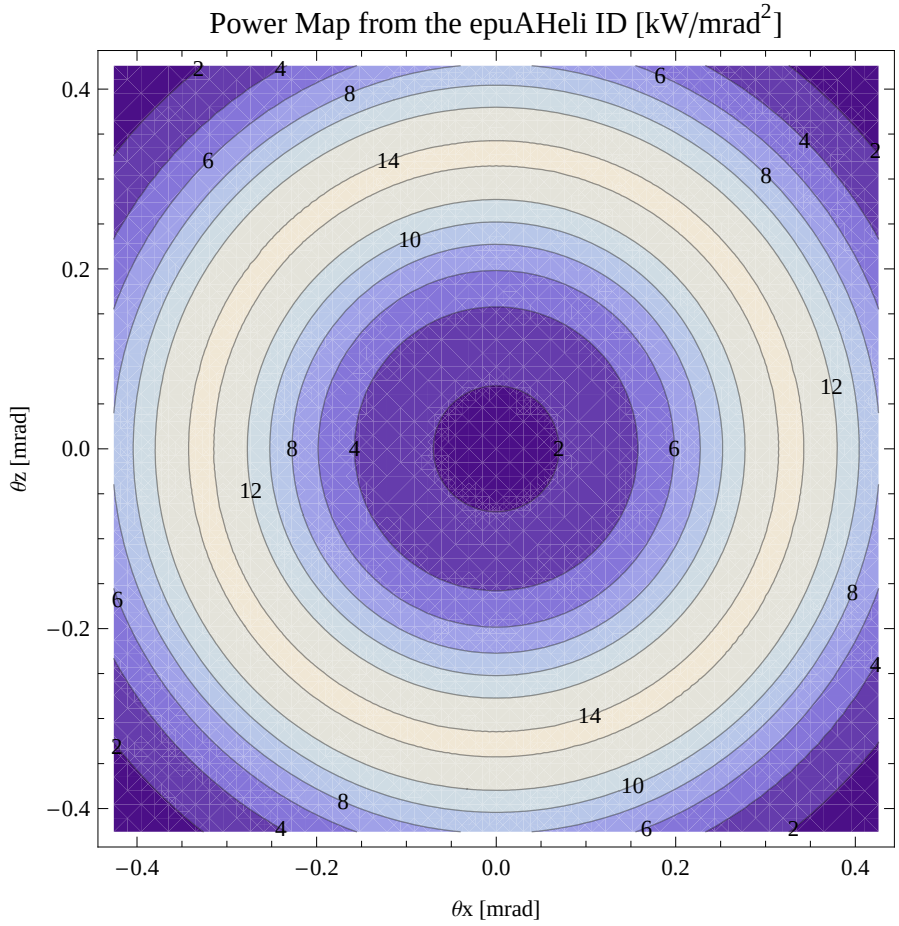

Figure 133: Map of the power distribution of the emitted synchrotron radiation by the epuAHeli ID

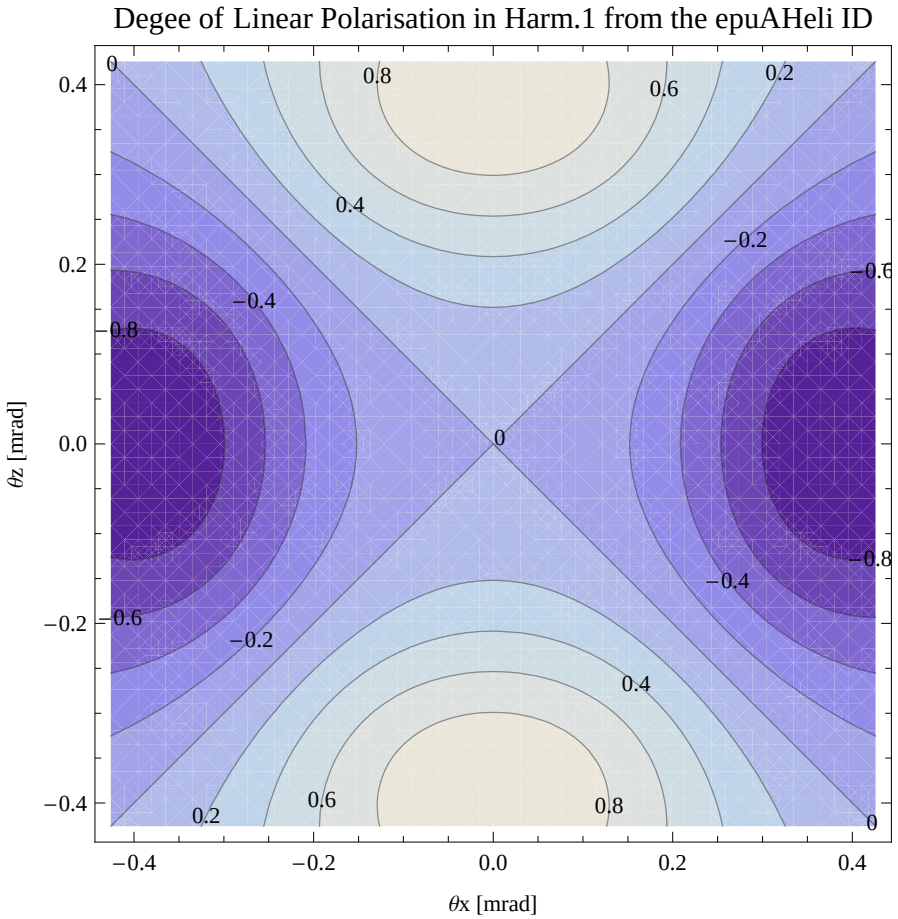

Figure 134: Map of linear polarisation in the fundamental harmonic of the synchotron radiation emitted by the epuAHeli ID

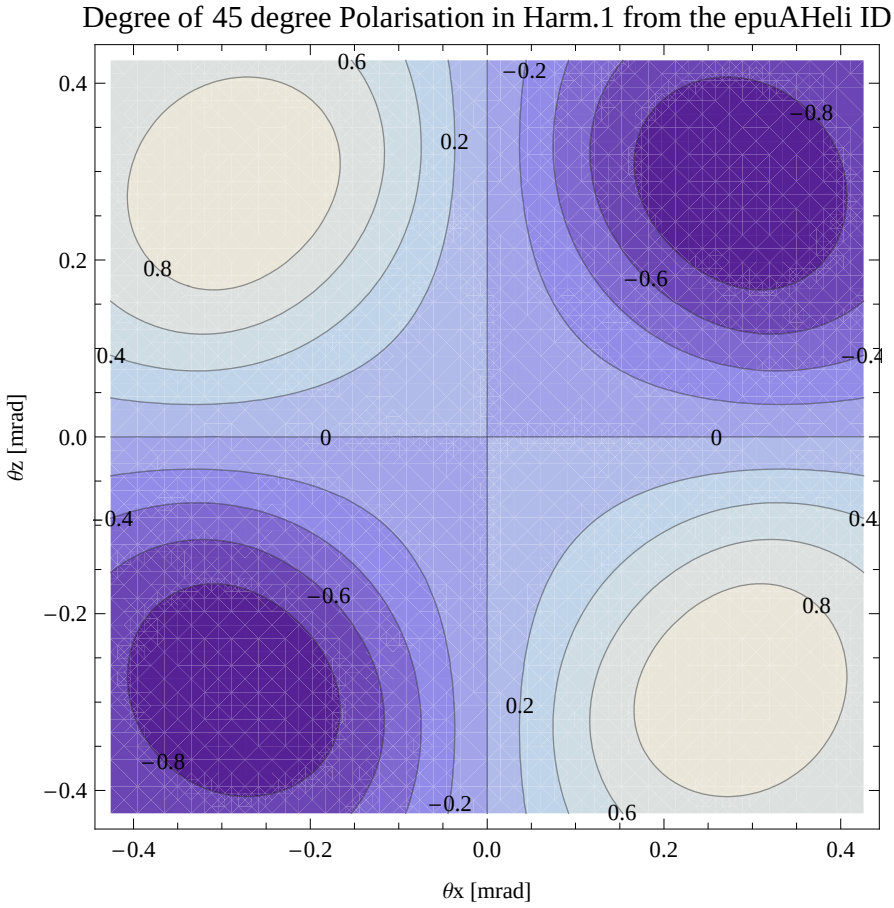

Figure 135: Map of 45 degree polarisation in the fundamental harmonic of the synchotron radiation emitted by the epuAHeli ID

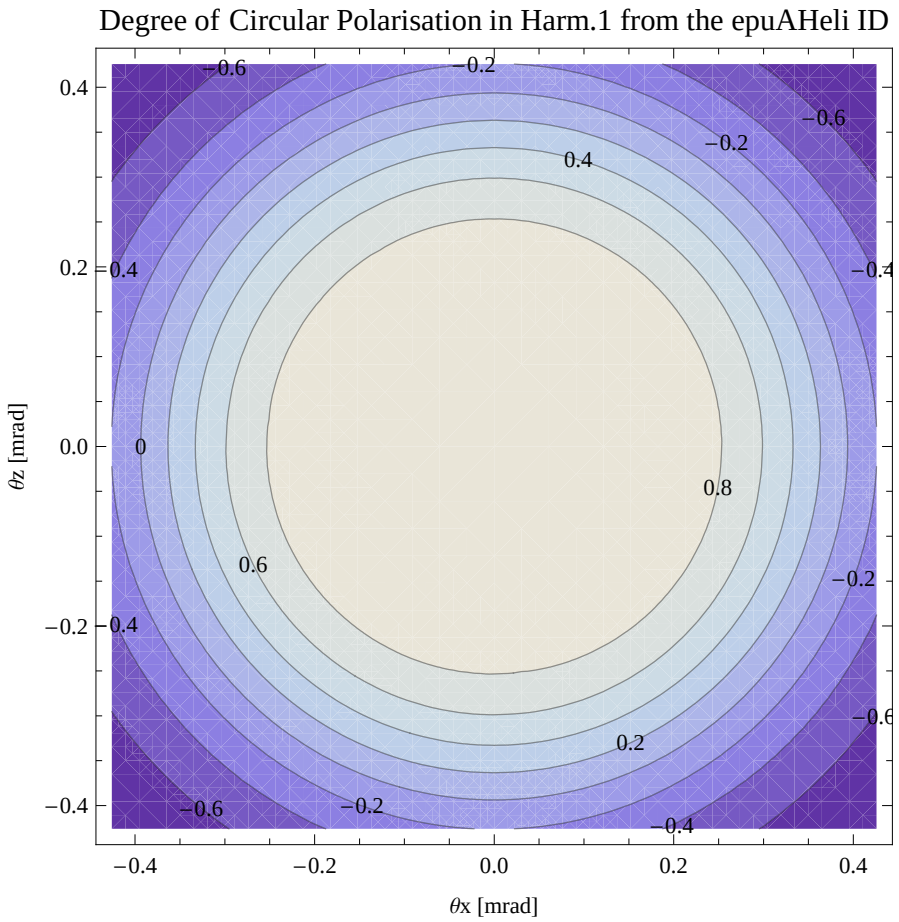

Figure 136: Map of circular polarisation in the fundamental harmonic of the synchotron radiation emitted by the epuAHeli ID

A map of the degree of circular polarisation of the fundamental harmonic of the synchotron radiation emitted by the epuAHeli ID over the angle of obsevation is shown in Figure 136.

The on axis brilliance at peak energy the and spectral flux density, also often called angular spectral flux, from the epuAHeli ID has been calculated with the given beam parameters, which are 0.5 A of stored current, $\beta_H = 9.$ m, $\varepsilon_H = 0.263$ nmrad, $\beta_V = 4.8$ m, $\varepsilon_V = 8.$ pmrad, and an energy spread of 0.001. Figure 137 shows the brilliance at peak energy and Figure 138 shows the the spectral flux density.

The brilliance at peak energy the and the spectral flux density from the epuAHeli ID for different harmonics at maximum K-value (2.946) are given in Table 39 and for minimum K-value (0.400) these values are given in Table 40.

The brilliance at peak energy the and the spectral flux density from the epuAHeli ID for

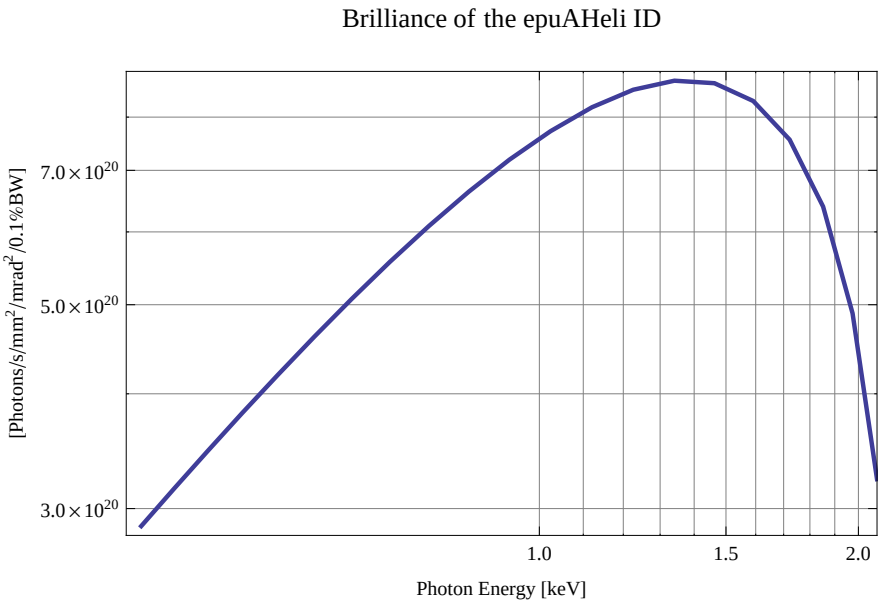

Figure 137: The brilliance at peak energy of the synchotron radiation emitted by the epuAHeli ID

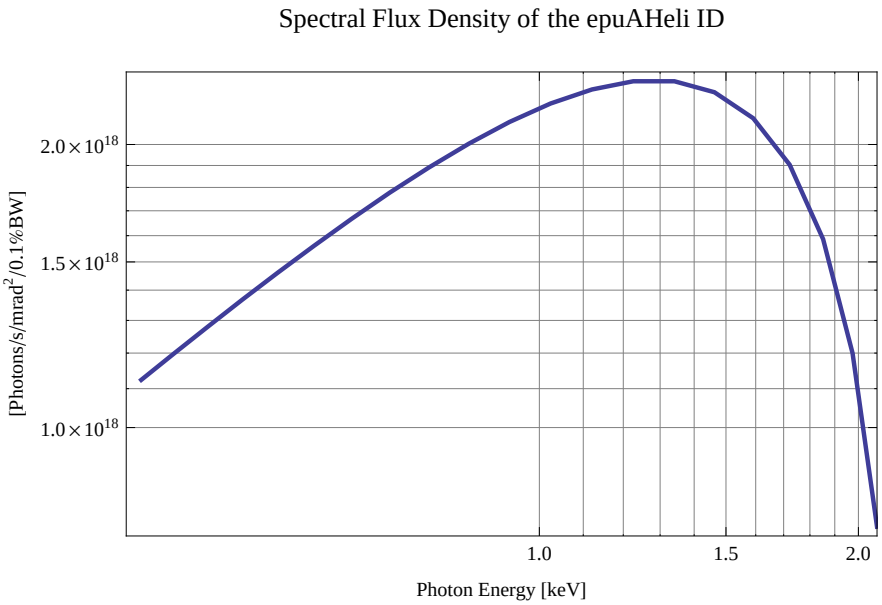

Figure 138: The spectral flux density of the synchotron radiation emitted by the epuA-Heli ID

Table 39: The brilliance at peak energy the and the spectral flux density from the epuAHeli ID for different harmonics at maximum K-value (2.946)

Harmonic	Photon Energy [keV]	Brilliance [Ph./s/mrad^2/mrad^2/0.1%BW]	Spectral Flux Density [Ph./s/mrad^2/0.1%BW]
1	0.421151	2.87×10^{20}	1.12×10^{18}

different harmonics at maximum K-value (2.946) are given in Table 39 and for minimum K-value (0.400) these values are given in Table 40.

Table 40: The brilliance at peak energy the and the spectral flux density from the epuAHeli ID for different harmonics at minimum K-value (0.4)

Harmonic	Photon Energy [keV]	Brilliance [Ph./s/mrad^2/mrad^2/0.1%BW]	Spectral Flux Density [Ph./s/mrad^2/0.1%BW]
1	2.08254	3.23×10^{20}	7.84×10^{17}

4.8.9 Influence from the epuAHeli ID on the optics of the stored beam

Figure 139 shows the focusing potential from the epuAHeli over the beam stay clear aperture of the ring aparture.

Figure 140 shows the kick map in the beam energy independant unit T^2m^2 of the kicks induced by the epuAHeli ID over the beam stay clear aparture.

Figure 141 shows the induced angular kick on the stored beam from the epuAHeli ID as a function of the vertical distance to the axis of the ID.

Figure 142 shows the induced angular kick on the stored beam from the epuAHeli ID as a function of the horizontal distance to the axis of the ID.

Figure 143 shows tune shift induced by the epuAHeli ID over the beam stay clear aparture. Note that the tune shift depends on the beam size at the ID.

Figure 144 shows the induced tune shift from the epuAHeli ID as a function of the vertical distance to the axis of the ID.

Figure 145 shows the induced tune shift from the epuAHeli ID as a function of the horizontal distance to the axis of the ID.

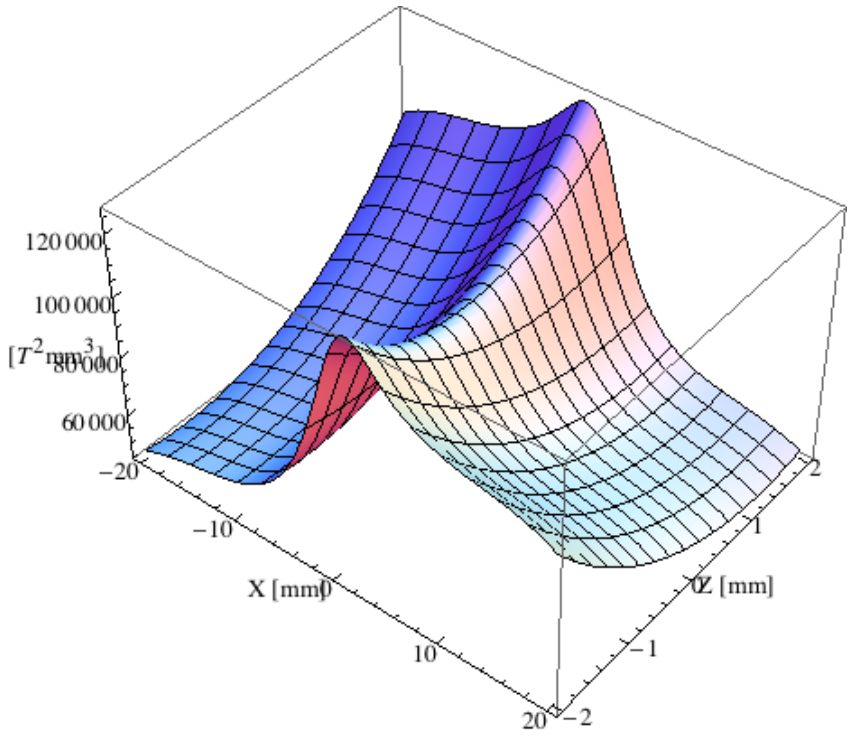

Figure 139: Focusing potential from the epuAHeli ID over the beam stay clear aparture.

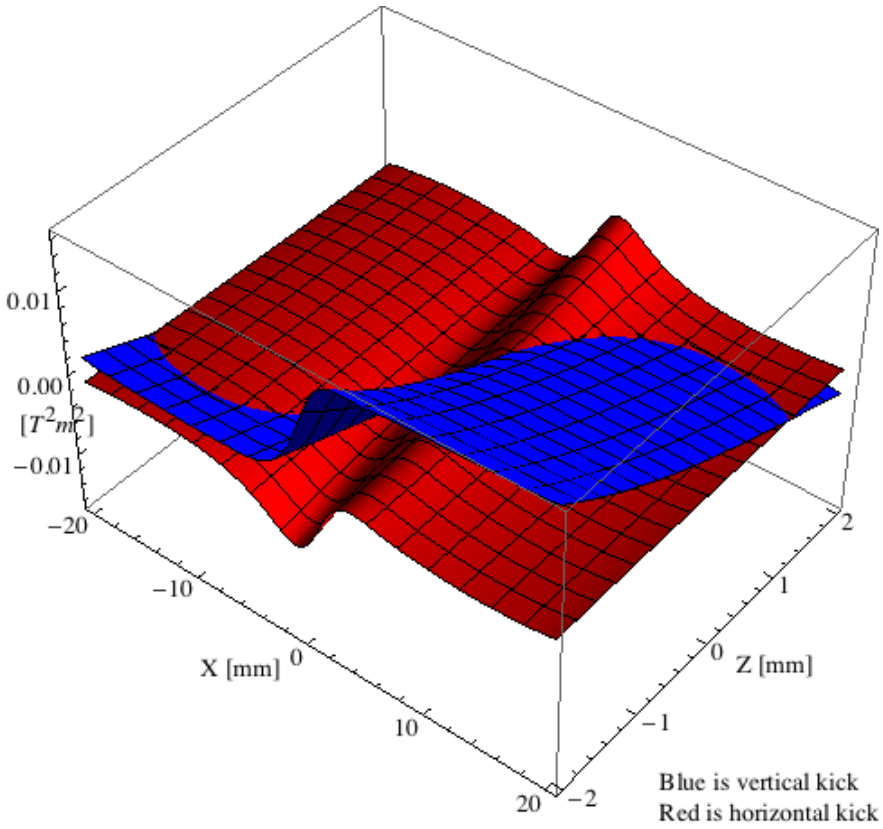

Figure 140: Kick map in the beam energy independant unit T^2m^2 of the kicks induced by the epuAHeli ID over the beam stay clear aparture.

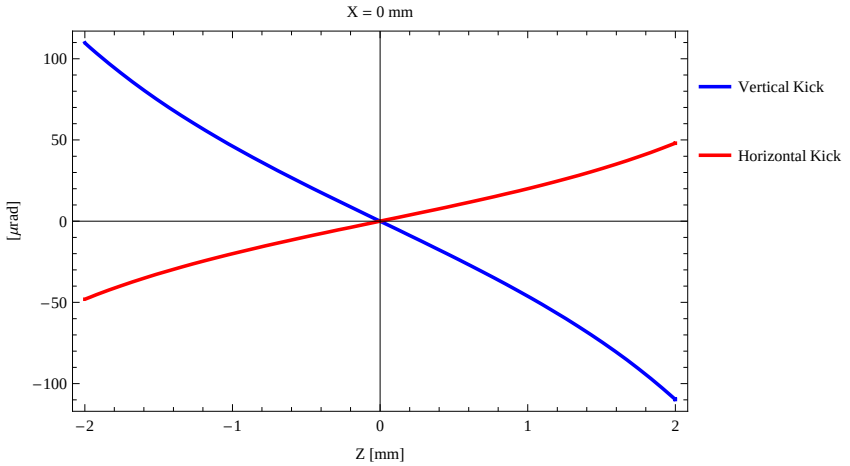

Figure 141: Induced angular kick on the stored beam from the epuAHeli ID as a function of the vertical distance to the ID axis.

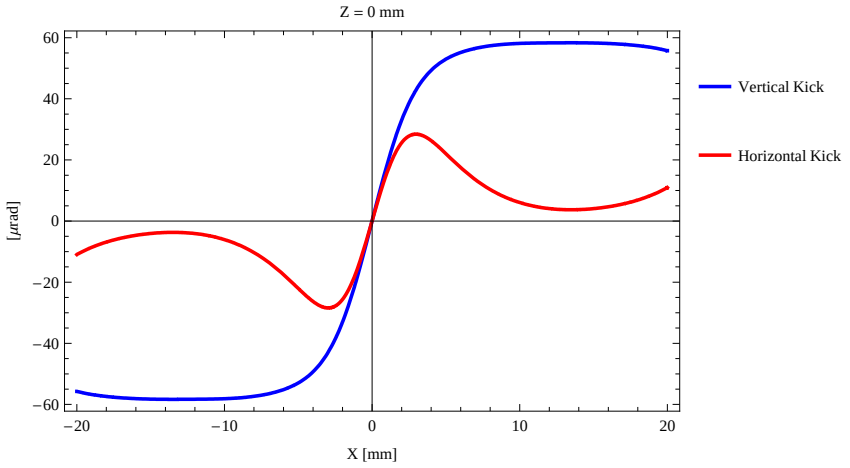

Figure 142: Induced angular kick on the stored beam from the epuAHeli ID as a function of the horizontal distance to the ID axis.

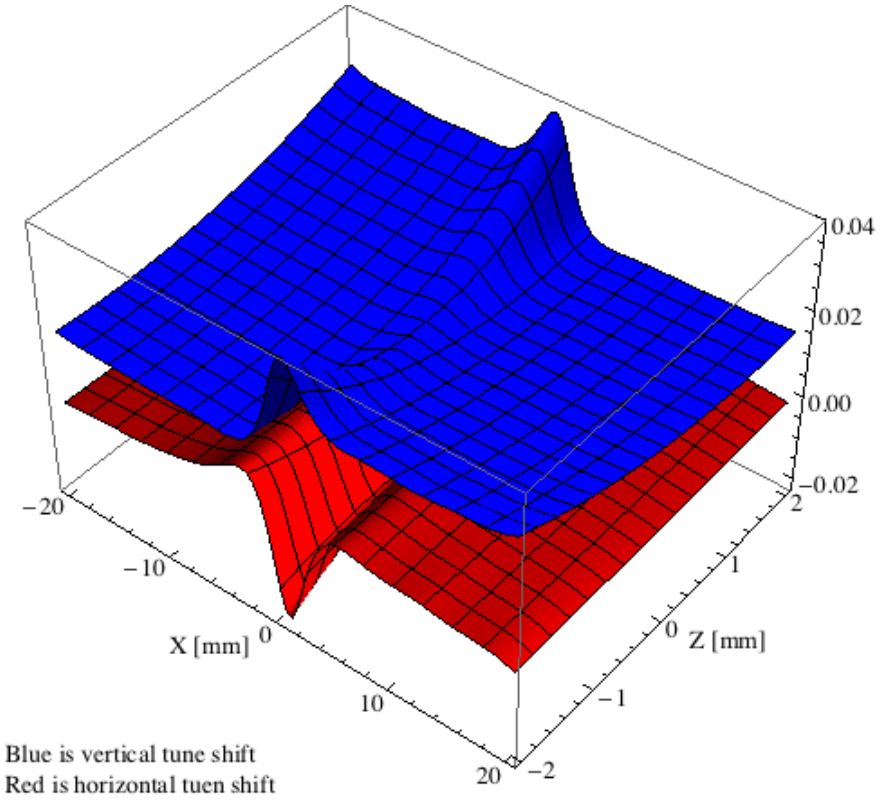

Figure 143: Tune shift induced by the epuAHeli ID over the beam stay clear aparture.

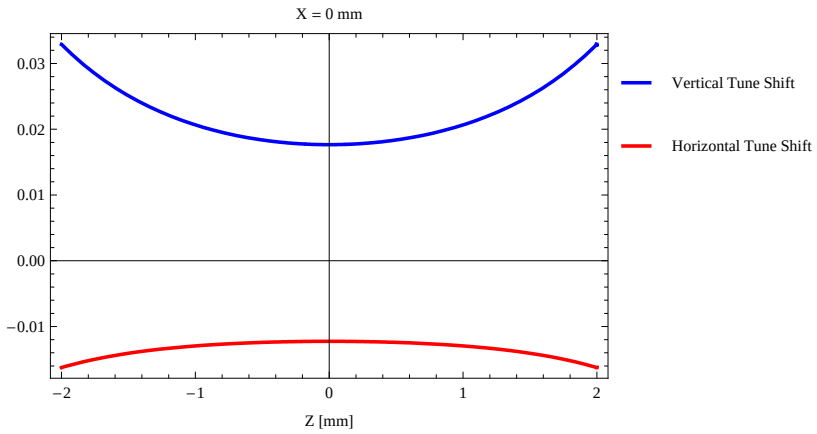

Figure 144: Induced tune shift from the epuAHeli ID as a function of the vertical distance to the axis of the ID.

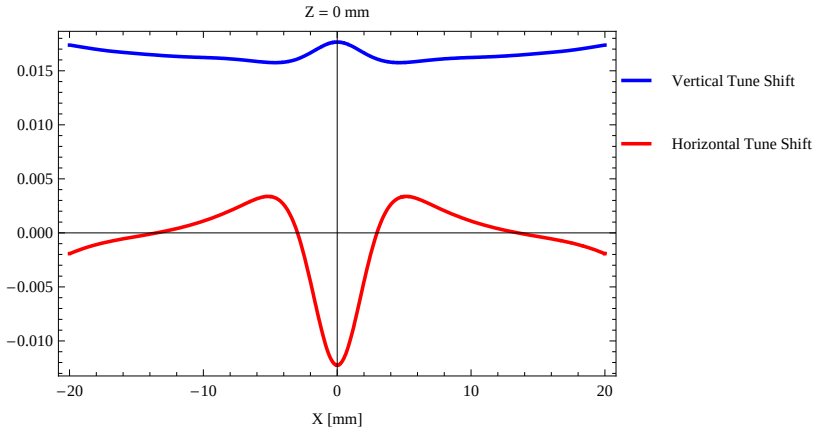

Figure 145: Induced tune shift from the epuAHeli ID on the stored beam from the ID as a function of the horizontal distance to the axis of the ID.

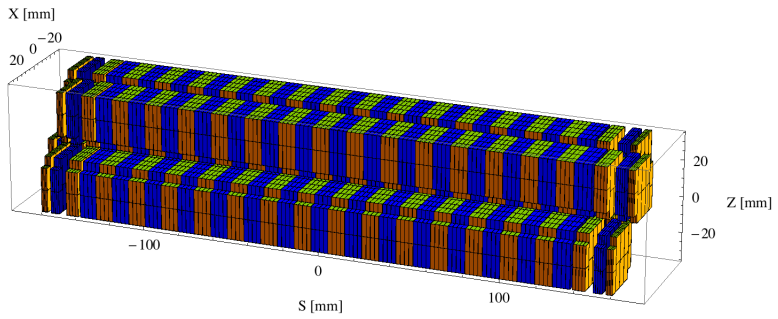

Figure 146: Magnetic model of the epuAIncl ID

4.8.10 Magnet model of the elliptically polaraising undulator epuAIncl

The magnet model of the epuAIncl ID is shown in Figure 146. The length of the magnet model is 320.976 mm. The magnetic material in the model is NdFeb with a remanence of 1.28, a meterial similar to Vac776tp from Vacuumschmelze. Blocks with vertical magnetisation are blue and blocks with horizontal magnetisation are yellow. The block size is 30.x30.x9.5 mm^3 and there is a 5. mm cut-out in two of the corners of the blocks. The total length of the epuAIncl ID is 3930.98 mm.

4.8.11 Analysis of the magnetic field of the epuAIncl ID

The effective magnetic fields on axis and the fundamental photon energy of the epuAIncl ID are shown in Table 41. The higher harmonic contents in the magnetic field of an elliptically polarising undulator made of permanent magnets is negigible and the efficient field has about the same strength as the peak field.

4.8.12 Synchrotron radiation from the epuAIncl ID

The power map of the emitted synchrotron radiation by the epuAIncl ID, assuming a 0.5 A filament beam with an energy of 3. GeV and undulator properties of the synchrotron radiation, is shown in Figure 151. The on-axis power density is 26.124 $kW/mrad^2$

A map of the degree of linear polarisation of the fundamental harmonic of the synchotron radiation emitted by the epuAIncl ID over the angle of obsevation is shown in Figure 152.

A map of the degree of 45 degree polarisation of the fundamental harmonic of the synchotron radiation emitted by the epuAIncl ID over the angle of obsevation is shown in Figure 153.

Table 41: Effective Fields on axis and Fundamental Photon Energy of the epuAIncl ID

Undulator Period	38.	mm
Undulator Gap	9.	mm
Undulator Mode	Inclined	
Undulator Phase	10.373	mm
Vertical Peak Field	0.417	T
Efficient Vertical Field	0.419	T
Kx (from vert. field)	1.487	
Horizontal Peak Field:	−0.416	T
Efficient Horizontal Field	0.420	T
Kz (from hor. field)	1.491	
Photon Energy, Harm.1	0.699	keV
Emitted Power	3.939	kW
Total Length	3931.0	mm

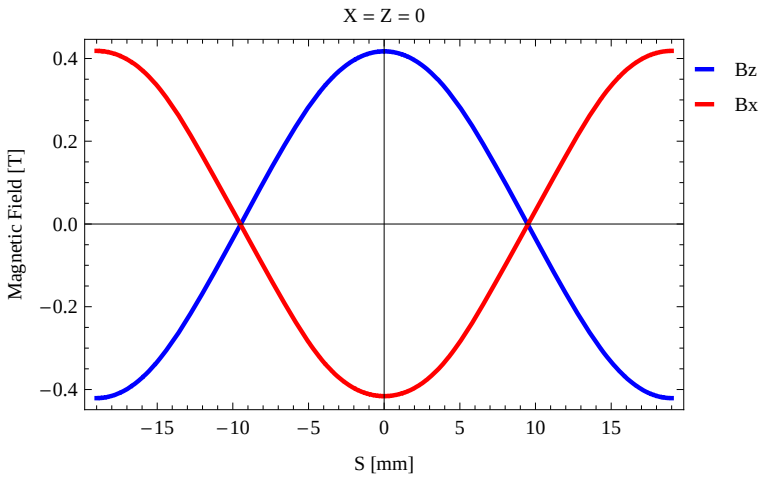

Figure 147: Vertical magnetic field in a central pole of the epuAIncl ID along the ID axis, X = Z = 0

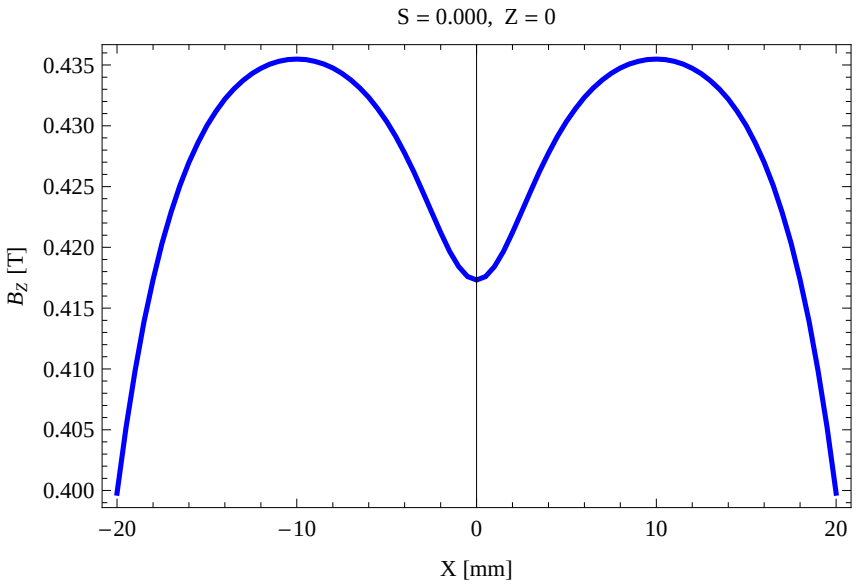

Figure 148: Vertical magnetic field in a central pole of the epuAIncl ID along the horizontally transverse direction to the ID axis, S = 0.000, Z = 0

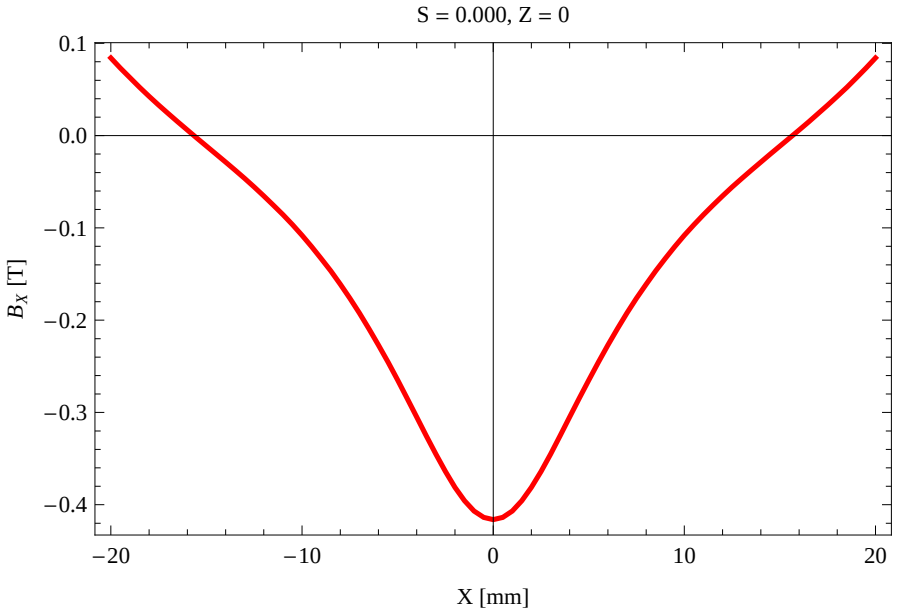

Figure 149: Horizontal magnetic field in a central pole of the epuAIncl ID along the horizontally transverse direction to the ID axis, S = 0.000, Z = 0

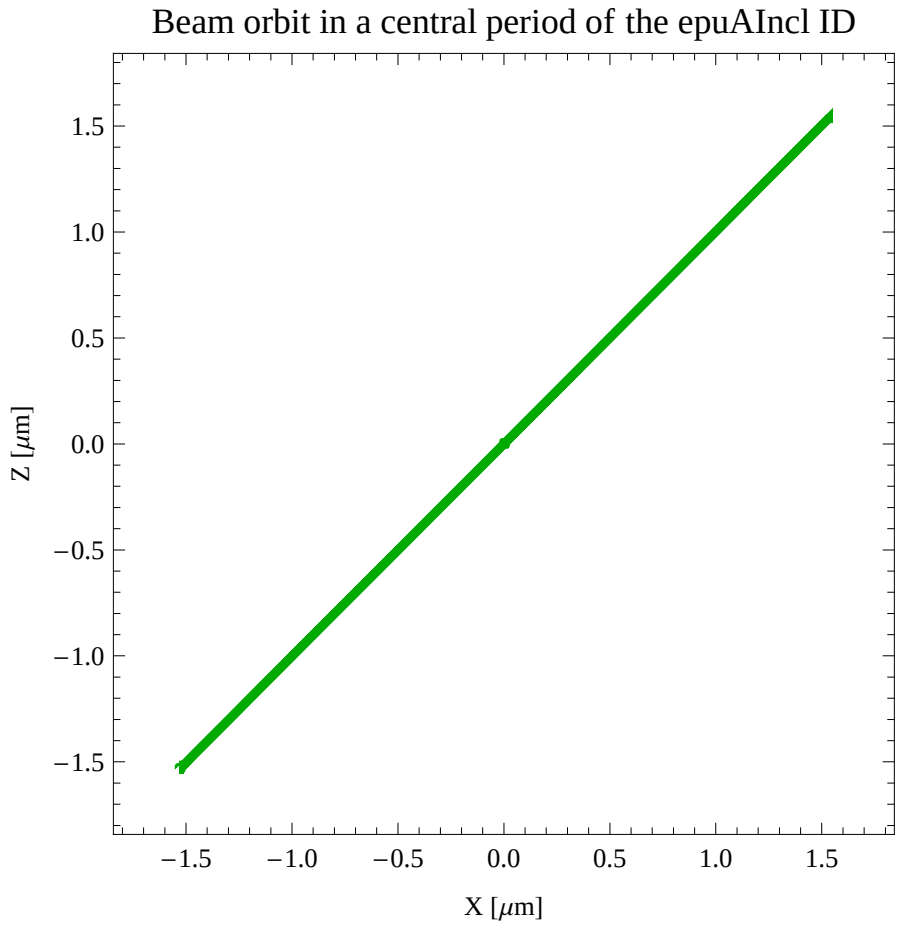

Figure 150: The beam orbit of the electron beam through a central period of the epuAIncl ID

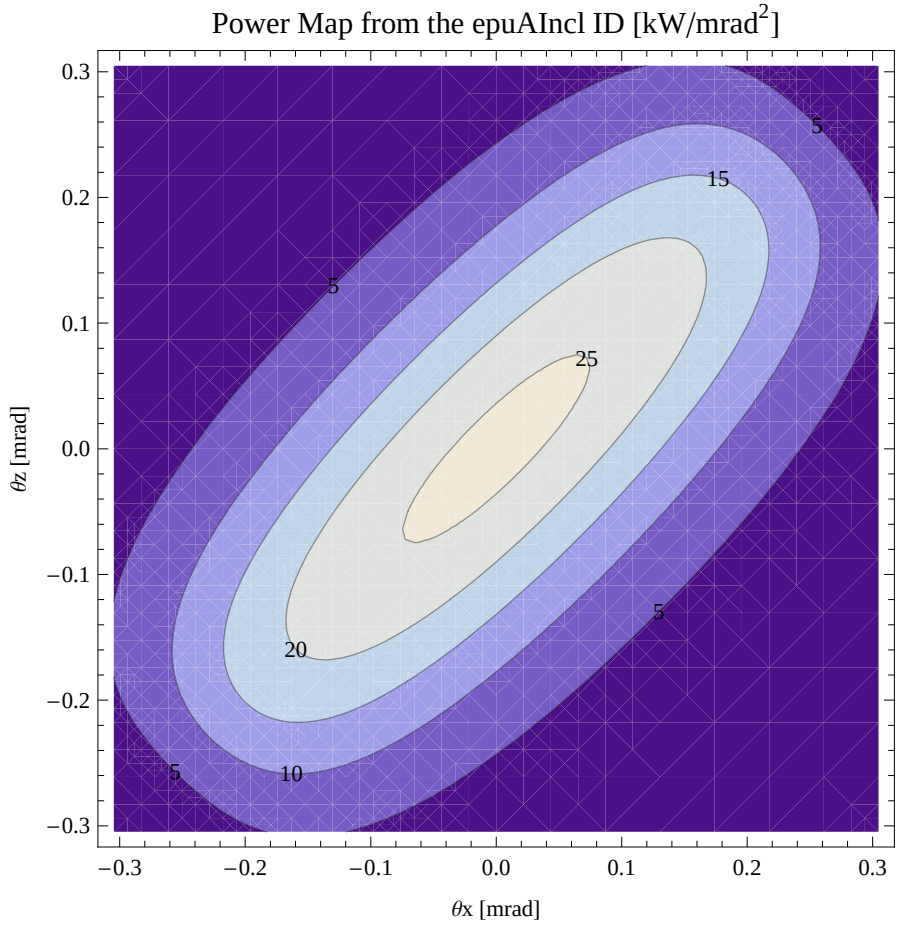

Figure 151: Map of the power distribution of the emitted synchrotron radiation by the epuAIncl ID

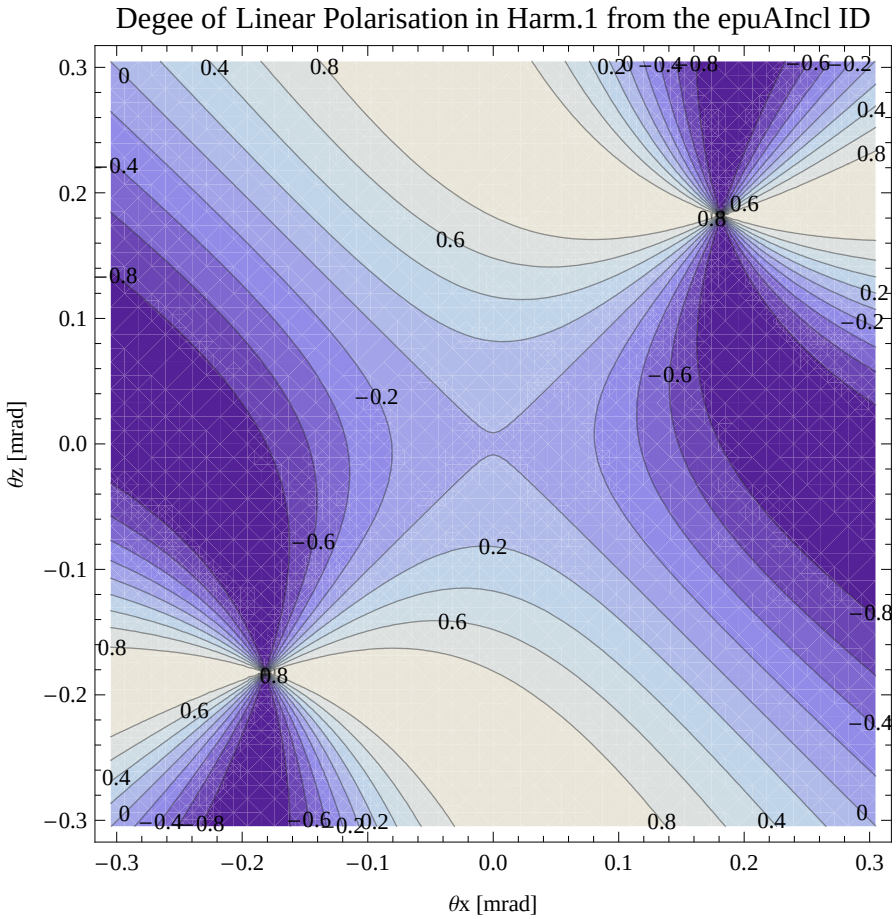

Figure 152: Map of linear polarisation in the fundamental harmonic of the synchotron radiation emitted by the epuAIncl ID

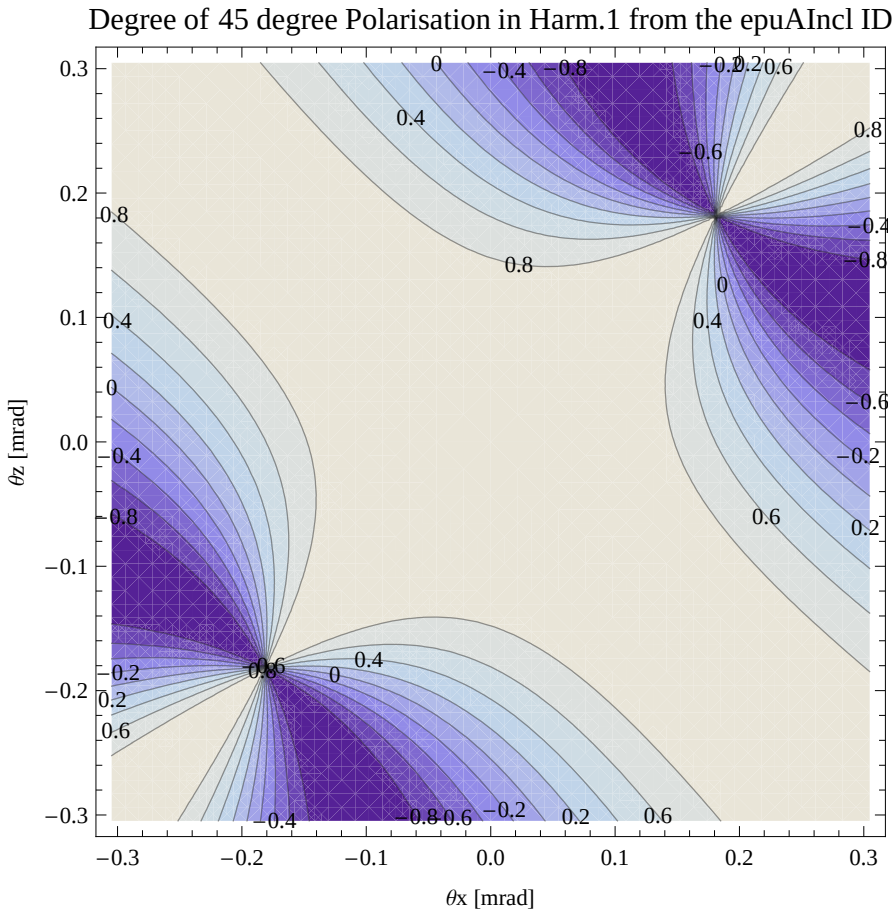

Figure 153: Map of 45 degree polarisation in the fundamental harmonic of the synchotron radiation emitted by the epuAIncl ID

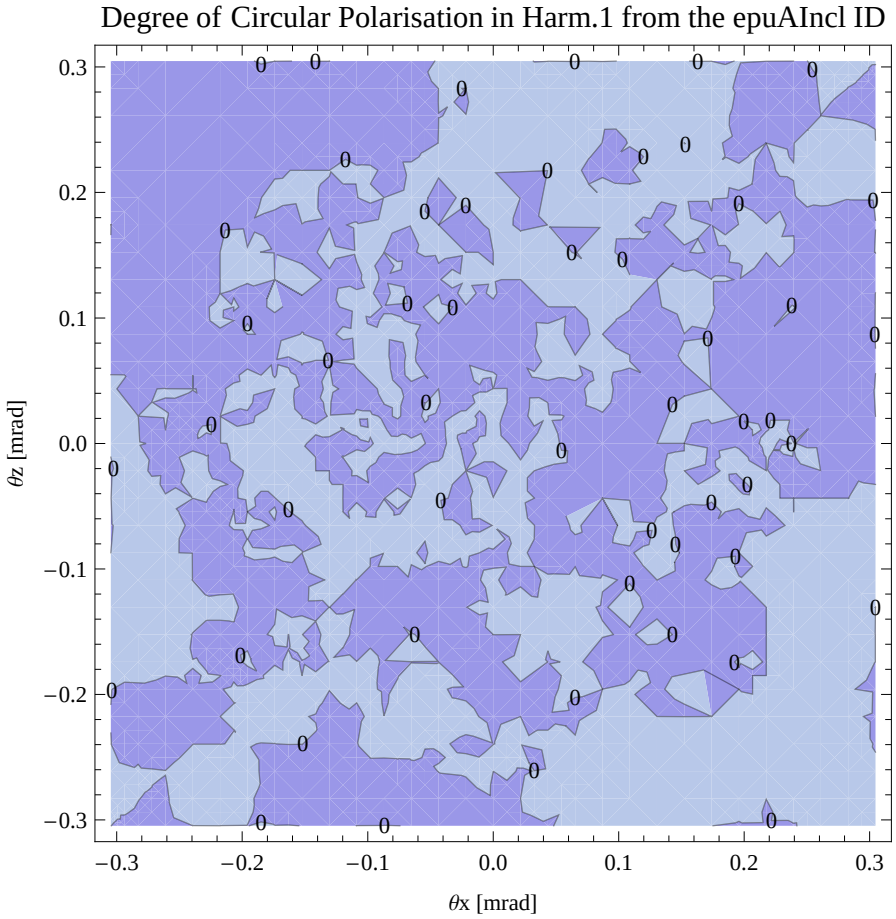

Figure 154: Map of circular polarisation in the fundamental harmonic of the synchotron radiation emitted by the epuAIncl ID

A map of the degree of circular polarisation of the fundamental harmonic of the synchotron radiation emitted by the epuAIncl ID over the angle of obsevation is shown in Figure 154.

The on axis brilliance at peak energy the and spectral flux density, also often called angular spectral flux, from the epuAIncl ID has been calculated with the given beam parameters, which are 0.5 A of stored current, $\beta_H = 9.$ m, $\varepsilon_H = 0.263$ nmrad, $\beta_V = 4.8$ m, $\varepsilon_V = 8.$ pmrad, and an energy spread of 0.001. Figure 155 shows the brilliance at peak energy and Figure 156 shows the the spectral flux density.

The brilliance at peak energy the and the spectral flux density from the epuAIncl ID for different harmonics at maximum K-value (2.106) are given in Table 42 and for minimum K-value (0.400) these values are given in Table 43.

The brilliance at peak energy the and the spectral flux density from the epuAIncl ID for

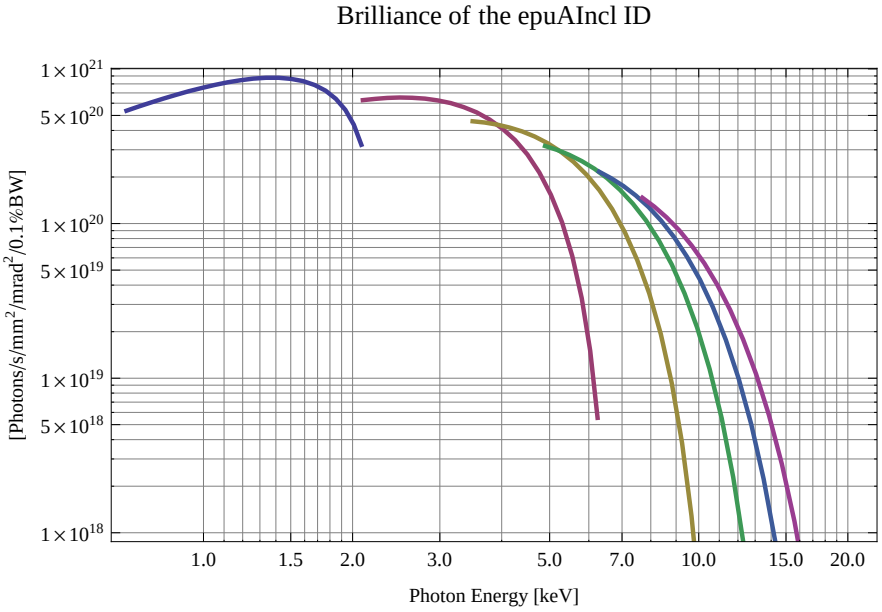

Figure 155: The brilliance at peak energy of the synchotron radiation emitted by the epuAIncl ID

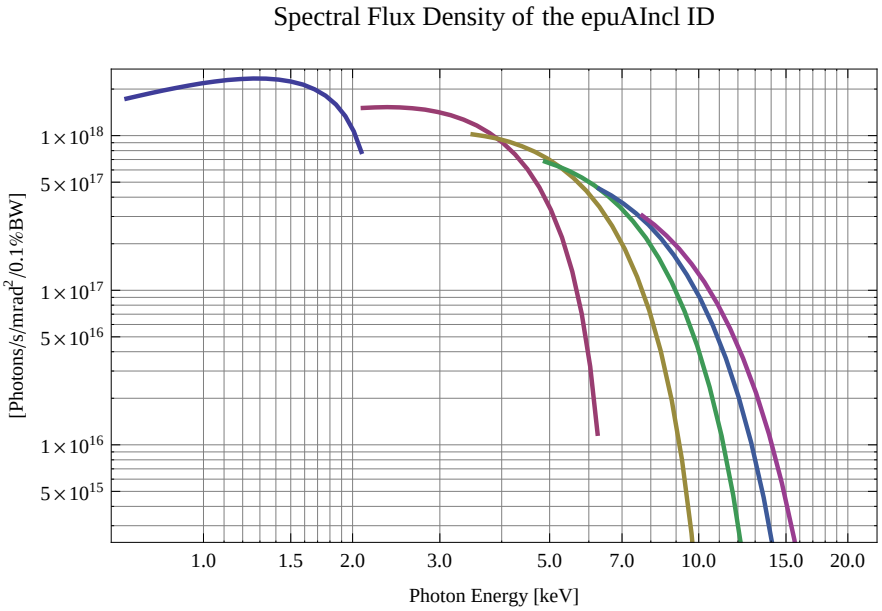

Figure 156: The spectral flux density of the synchotron radiation emitted by the epuAIncl ID

Table 42: The brilliance at peak energy the and the spectral flux density from the epuAIncl ID for different harmonics at maximum K-value (2.106)

Harmonic	Photon Energy [keV]	Brilliance [Ph./s/mrad^2/mrad^2/0.1%BW]	Spectral Flux Density [Ph./s/mrad^2/0.1%BW]
1	0.699189	5.37×10^{20}	1.73×10^{18}
3	2.09757	6.28×10^{20}	1.51×10^{18}
5	3.49594	4.59×10^{20}	1.02×10^{18}
7	4.89432	3.17×10^{20}	6.79×10^{17}
9	6.2927	2.16×10^{20}	4.53×10^{17}
11	7.69108	1.47×10^{20}	3.04×10^{17}

different harmonics at maximum K-value (2.106) are given in Table 42 and for minimum K-value (0.400) these values are given in Table 43.

Table 43: The brilliance at peak energy the and the spectral flux density from the epuAIncl ID for different harmonics at minimum K-value (0.4)

Harmonic	Photon Energy [keV]	Brilliance [Ph./s/mrad^2/mrad^2/0.1%BW]	Spectral Flux Density [Ph./s/mrad^2/0.1%BW]
1	2.08254	3.23×10^{20}	7.84×10^{17}
3	6.24763	5.54×10^{18}	1.18×10^{16}
5	10.4127	6.1×10^{16}	1.27×10^{14}
7	14.5778	6.35×10^{14}	1.31×10^{12}
9	18.7429	6.5×10^{12}	1.34×10^{10}
11	22.908	6.62×10^{10}	1.36×10^{8}

4.8.13 Influence from the epuAIncl ID on the optics of the stored beam

Figure 157 shows the focusing potential from the epuAIncl over the beam stay clear aperture of the ring aparture.

Figure 158 shows the kick map in the beam energy independant unit T^2m^2 of the kicks induced by the epuAIncl ID over the beam stay clear aparture.

Figure 159 shows the induced angular kick on the stored beam from the epuAIncl ID as a function of the vertical distance to the axis of the ID.

Figure 160 shows the induced angular kick on the stored beam from the epuAIncl ID as a function of the horizontal distance to the axis of the ID.

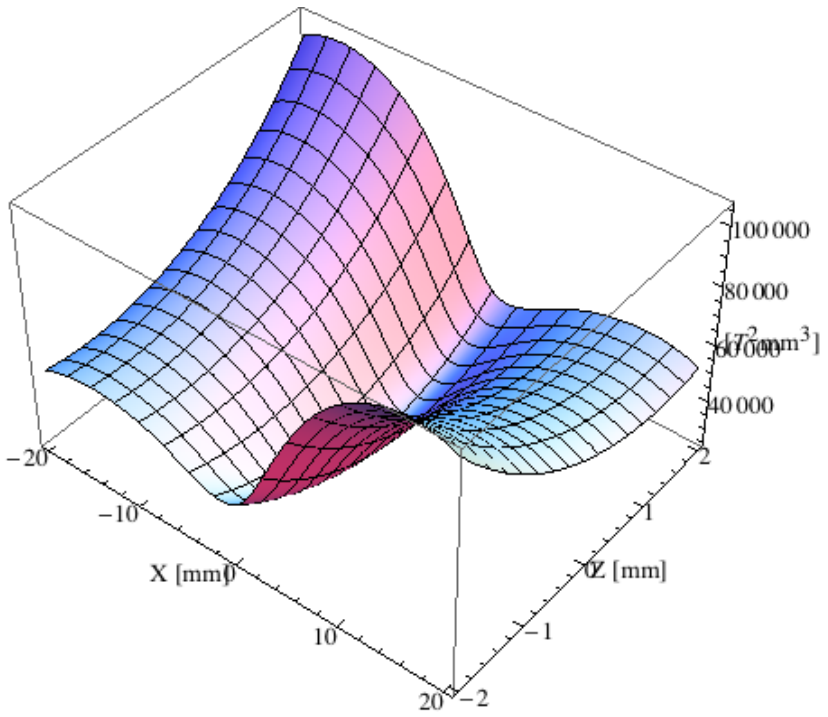

Figure 157: Focusing potential from the epuAIncl ID over the beam stay clear aparture.

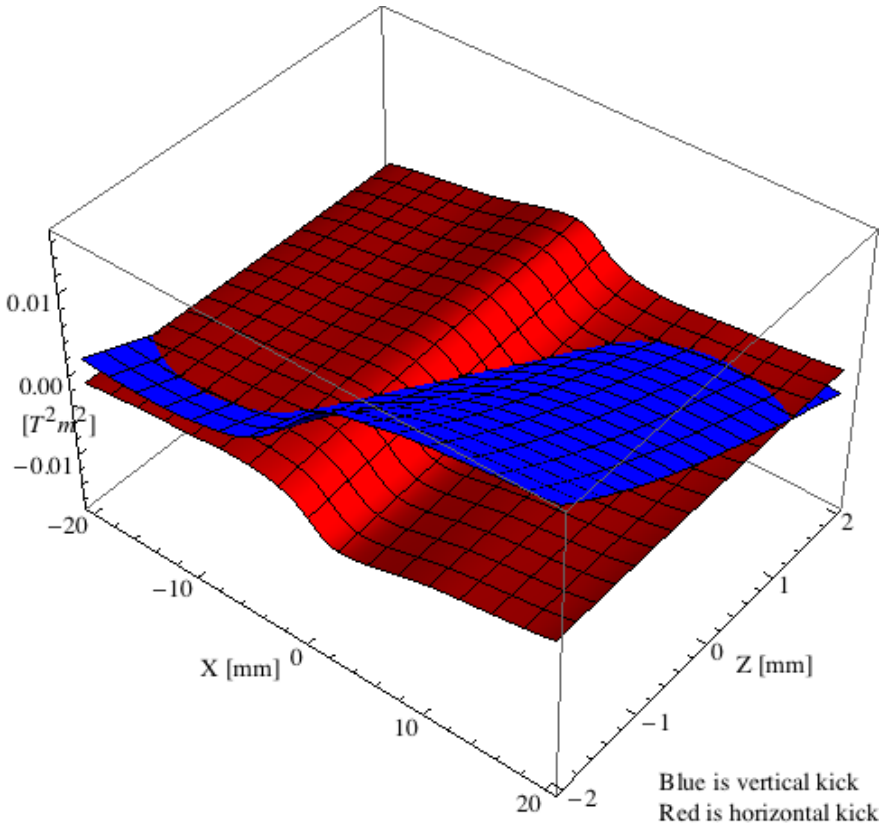

Figure 158: Kick map in the beam energy independant unit T^2m^2 of the kicks induced by the epuAIncl ID over the beam stay clear aparture.

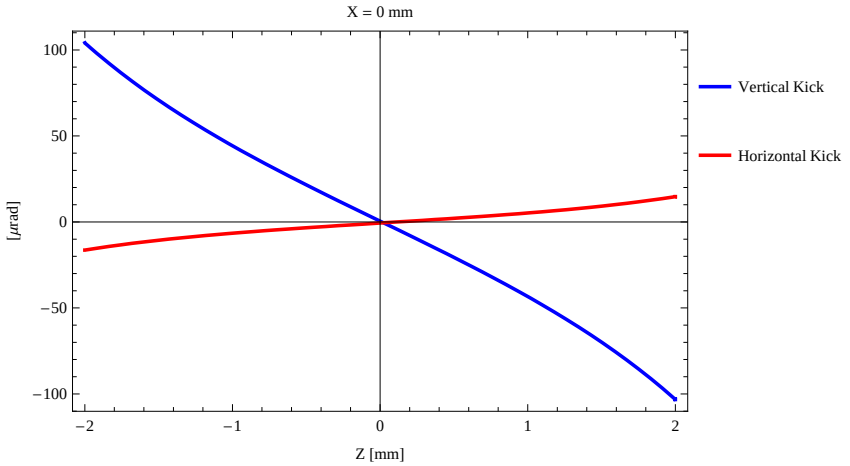

Figure 159: Induced angular kick on the stored beam from the epuAIncl ID as a function of the vertical distance to the ID axis.

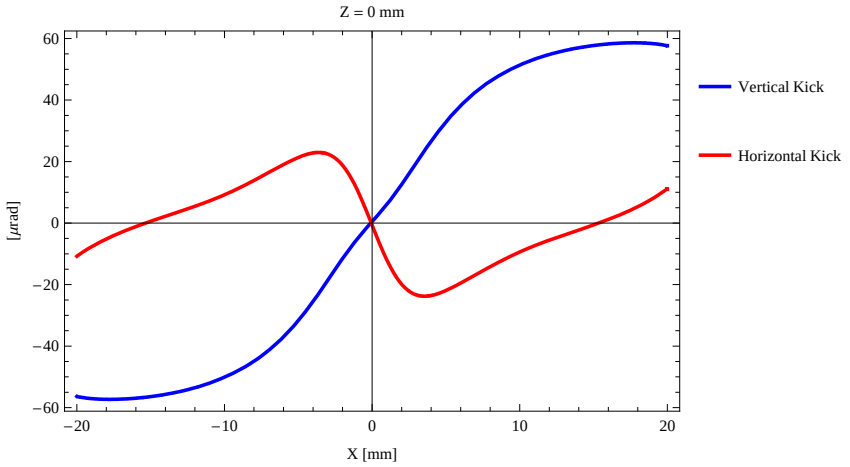

Figure 160: Induced angular kick on the stored beam from the epuAIncl ID as a function of the horizontal distance to the ID axis.

Figure 161 shows tune shift induced by the epuAIncl ID over the beam stay clear aparture. Note that the tune shift depends on the beam size at the ID.

Figure 162 shows the induced tune shift from the epuAIncl ID as a function of the vertical distance to the axis of the ID.

Figure 163 shows the induced tune shift from the epuAIncl ID as a function of the horizontal distance to the axis of the ID.

4.8.14 Magnet model of the elliptically polaraising undulator epuAVert

The magnet model of the epuAVert ID is shown in Figure 164. The length of the magnet model is 320.976 mm. The magnetic material in the model is NdFeb with a remanence of 1.28, a meterial similar to Vac776tp from Vacuumschmelze. Blocks with vertical magnetisation are blue and blocks with horizontal magnetisation are yellow. The block size is 30.x30.x9.5 mm^3 and there is a 5. mm cut-out in two of the corners of the blocks. The total length of the epuAVert ID is 3930.98 mm.

4.8.15 Analysis of the magnetic field of the epuAVert ID

The effective magnetic fields on axis and the fundamental photon energy of the epuAVert ID are shown in Table 44. The higher harmonic contents in the magnetic field of an elliptically polarising undulator made of permanent magnets is negigible and the efficient field has about the same strength as the peak field.

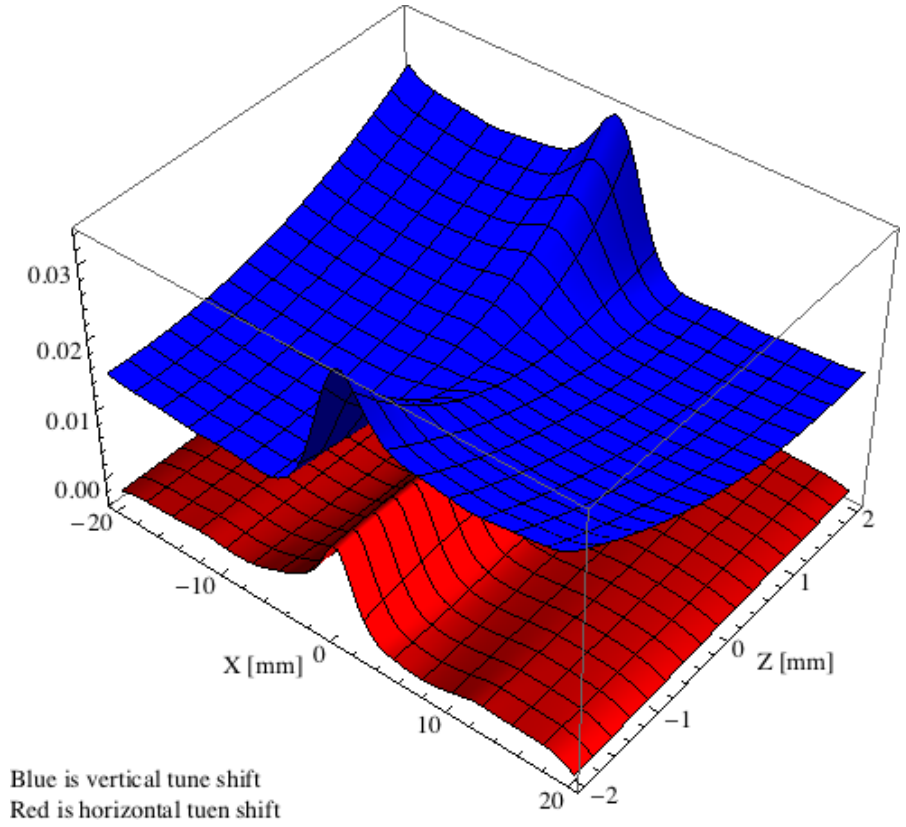

Figure 161: Tune shift induced by the epuAIncl ID over the beam stay clear aparture.

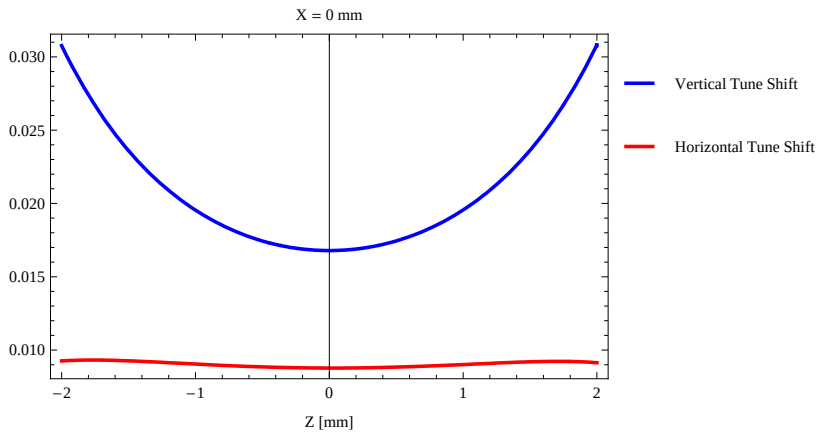

Figure 162: Induced tune shift from the epuAIncl ID as a function of the vertical distance to the axis of the ID.

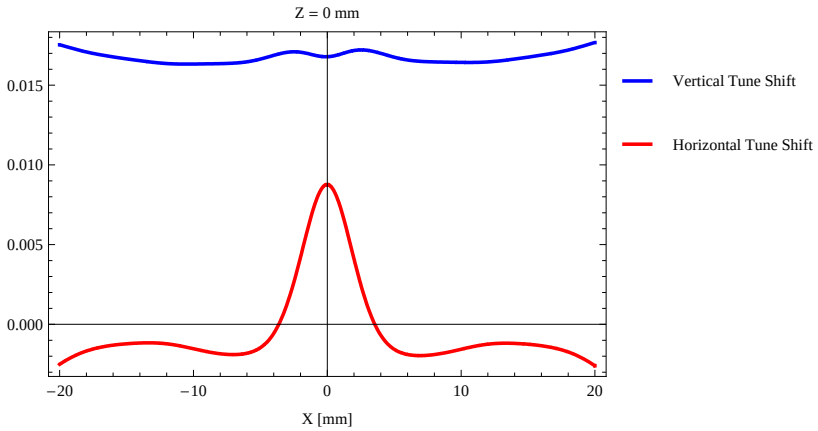

Figure 163: Induced tune shift from the epuAIncl ID on the stored beam from the ID as a function of the horizontal distance to the axis of the ID.

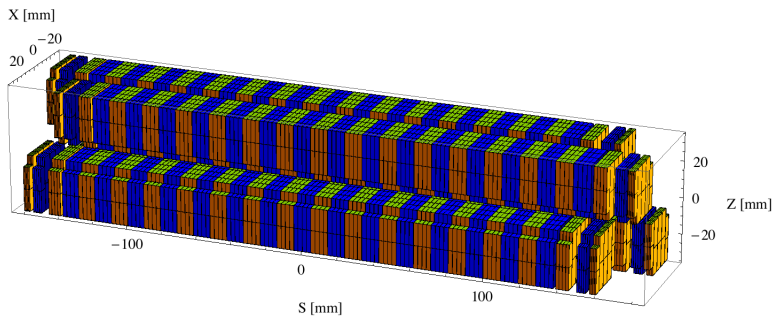

Figure 164: Magnetic model of the epuAVert ID

Table 44: Effective Fields on axis and Fundamental Photon Energy of the epuAVert ID

Undulator Period	38.	mm
Undulator Gap	9.	mm
Undulator Mode	Vertical	
Undulator Phase	19.000	mm
Vertical Peak Field	−0.001	T
Efficient Vertical Field	0.000	T
Kx (from vert. field)	0.000	
Horizontal Peak Field:	0.732	T
Efficient Horizontal Field	0.733	T
Kz (from hor. field)	2.602	
Photon Energy, Harm.1	0.513	keV
Emitted Power	6.013	kW
Total Length	3931.0	mm

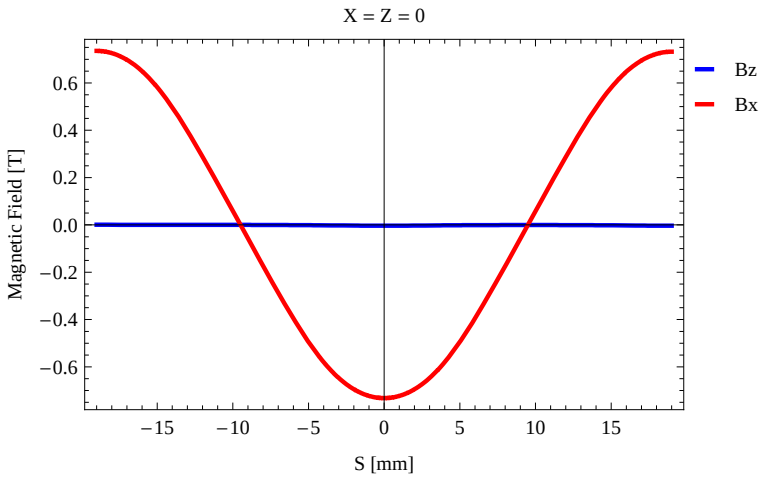

Figure 165: Vertical magnetic field in a central pole of the epuAVert ID along the ID axis, X = Z = 0

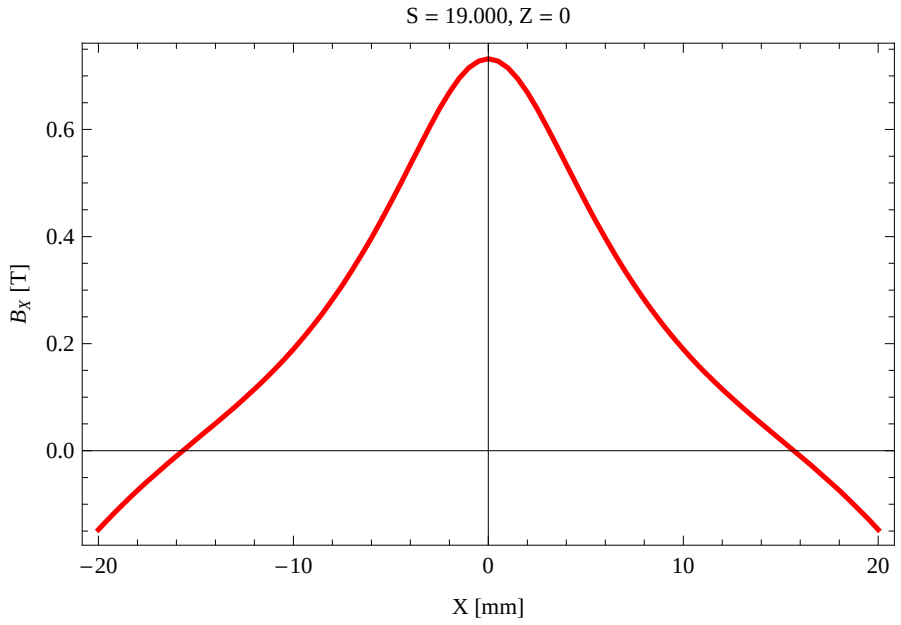

Figure 166: Horizontal magnetic field in a central pole of the epuAVert ID along the horizontally transverse direction to the ID axis, S = 19.000, Z = 0

4.8.16 Synchrotron radiation from the epuAVert ID

The power map of the emitted synchrotron radiation by the epuAVert ID, assuming a 0.5 A filament beam with an energy of 3. GeV and undulator properties of the synchrotron radiation, is shown in Figure 168. The on-axis power density is 32.461 kW/mrad^2

A map of the degree of linear polarisation of the fundamental harmonic of the synchotron radiation emitted by the epuAVert ID over the angle of obsevation is shown in Figure 169.

A map of the degree of 45 degree polarisation of the fundamental harmonic of the synchotron radiation emitted by the epuAVert ID over the angle of obsevation is shown in Figure 170.

A map of the degree of circular polarisation of the fundamental harmonic of the synchotron radiation emitted by the epuAVert ID over the angle of obsevation is shown in Figure 171.

The on axis brilliance at peak energy the and spectral flux density, also often called angular spectral flux, from the epuAVert ID has been calculated with the given beam parameters, which are 0.5 A of stored current, $\beta_H = 9.$ m, $\varepsilon_H = 0.263$ nmrad, $\beta_V = 4.8$ m, $\varepsilon_V = 8.$ pmrad, and an energy spread of 0.001. Figure 172 shows the brilliance at peak energy and Figure 173 shows the the spectral flux density.

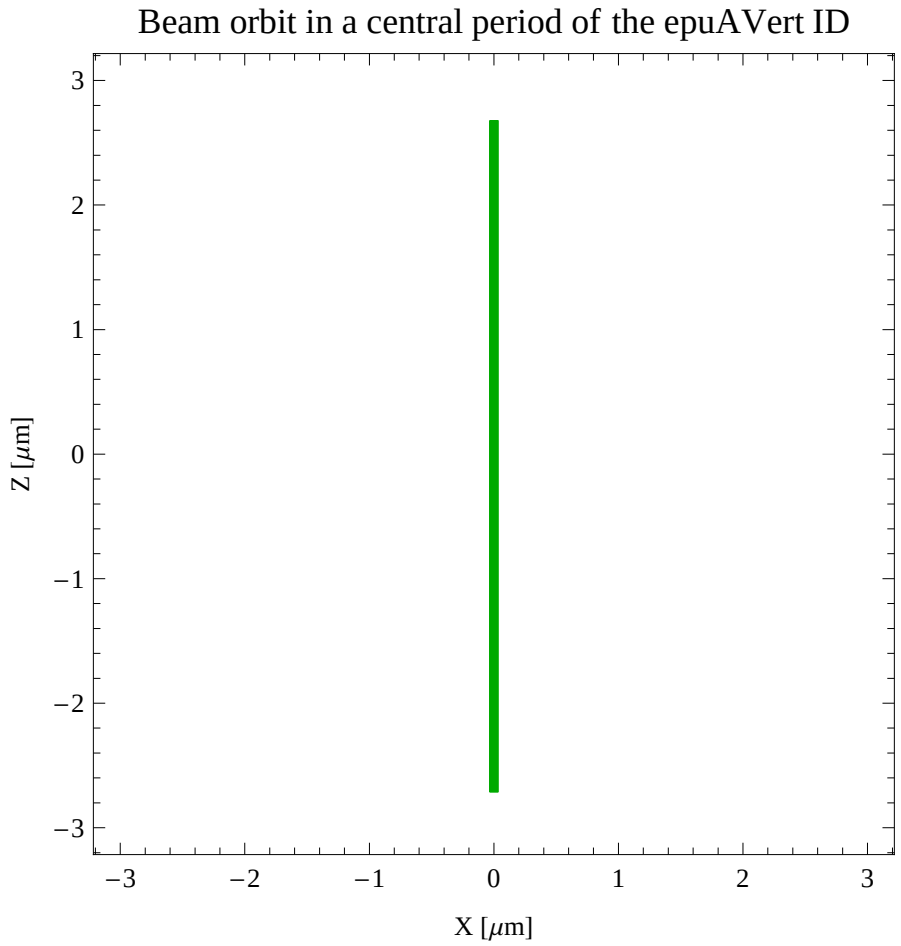

Figure 167: The beam orbit of the electron beam through a central period of the epuAVert ID

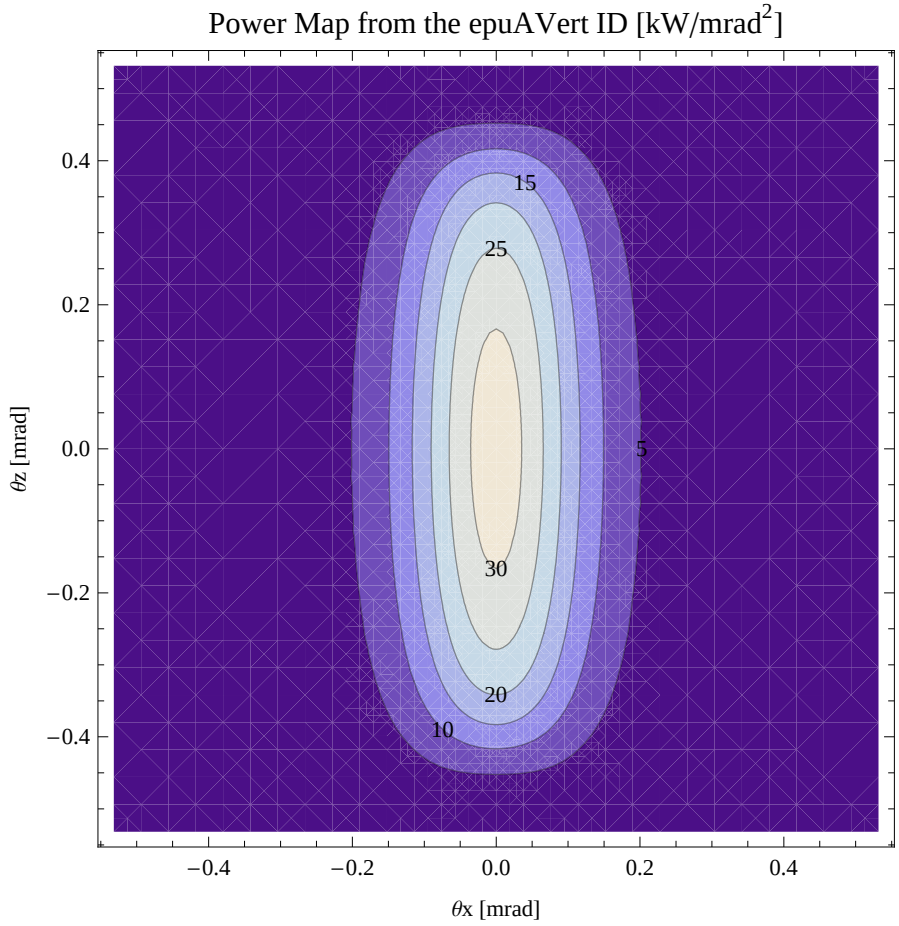

Figure 168: Map of the power distribution of the emitted synchrotron radiation by the epuAVert ID

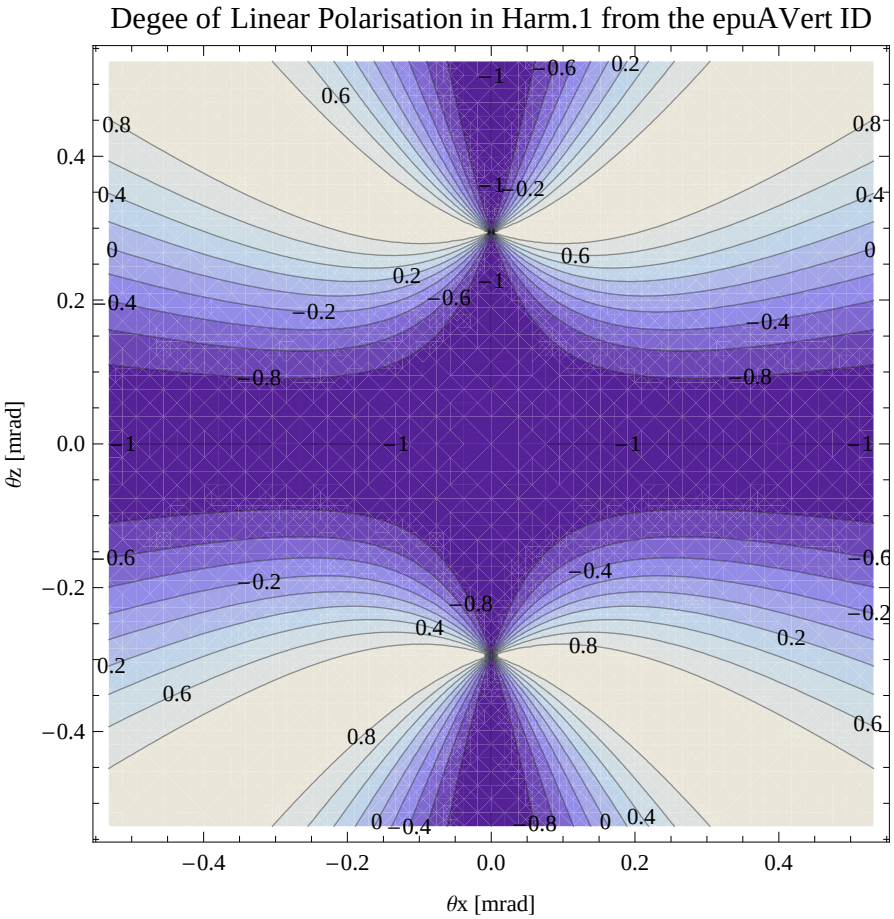

Figure 169: Map of linear polarisation in the fundamental harmonic of the synchotron radiation emitted by the epuAVert ID

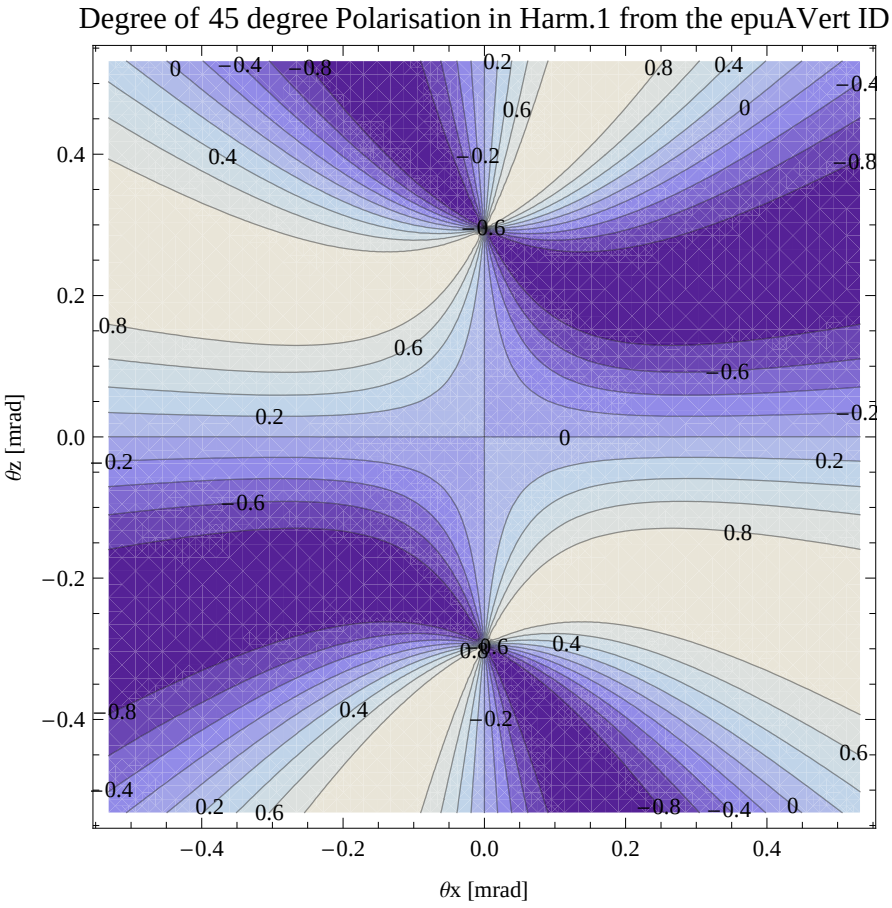

Figure 170: Map of 45 degree polarisation in the fundamental harmonic of the synchotron radiation emitted by the epuAVert ID

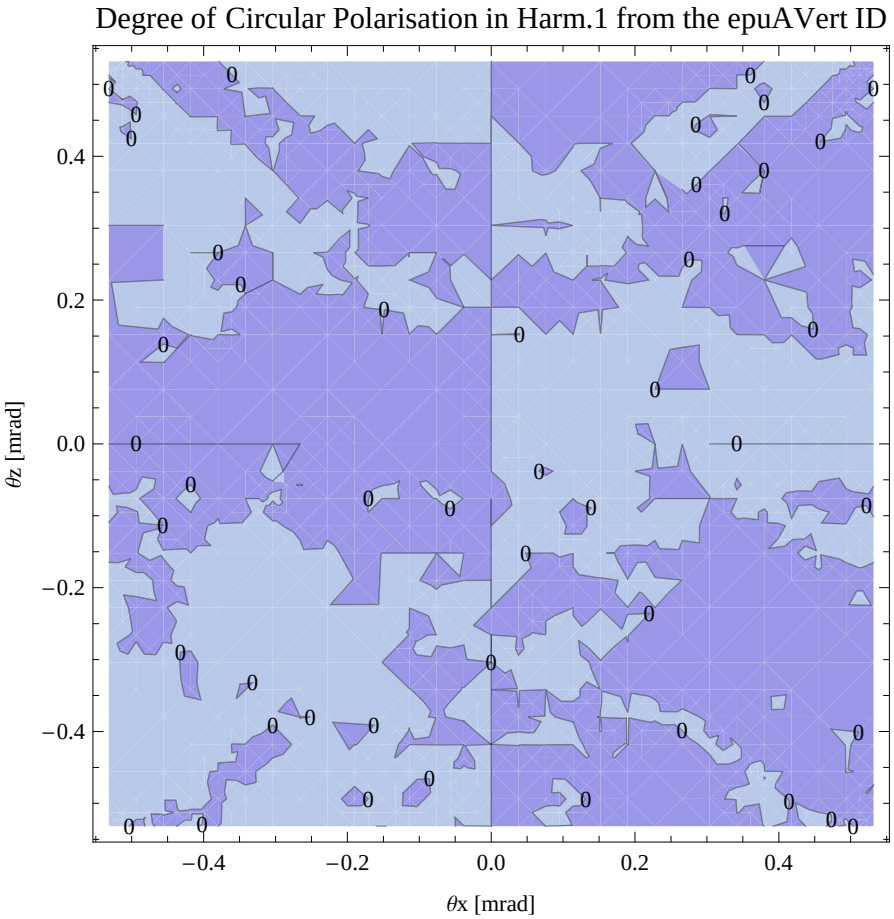

Figure 171: Map of circular polarisation in the fundamental harmonic of the synchotron radiation emitted by the epuAVert ID

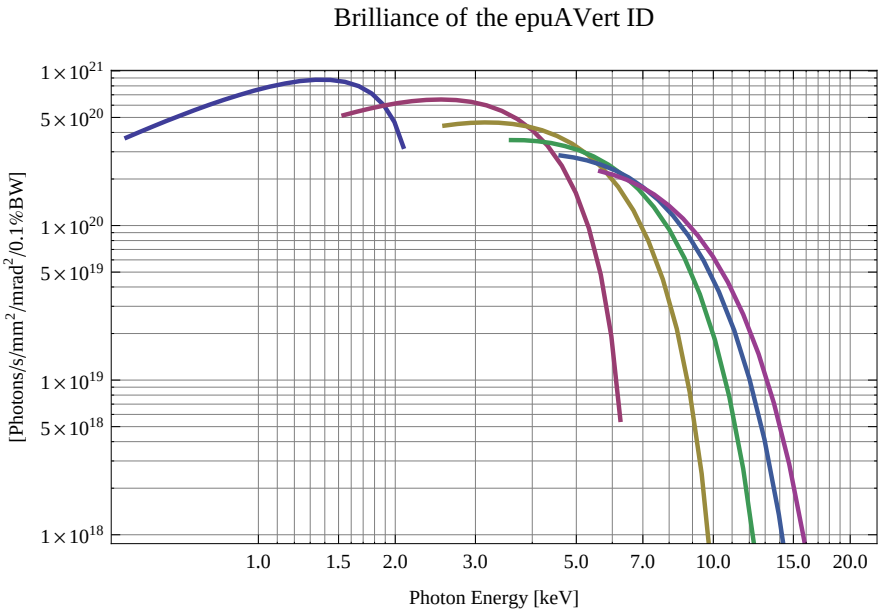

Figure 172: The brilliance at peak energy of the synchotron radiation emitted by the epuAVert ID

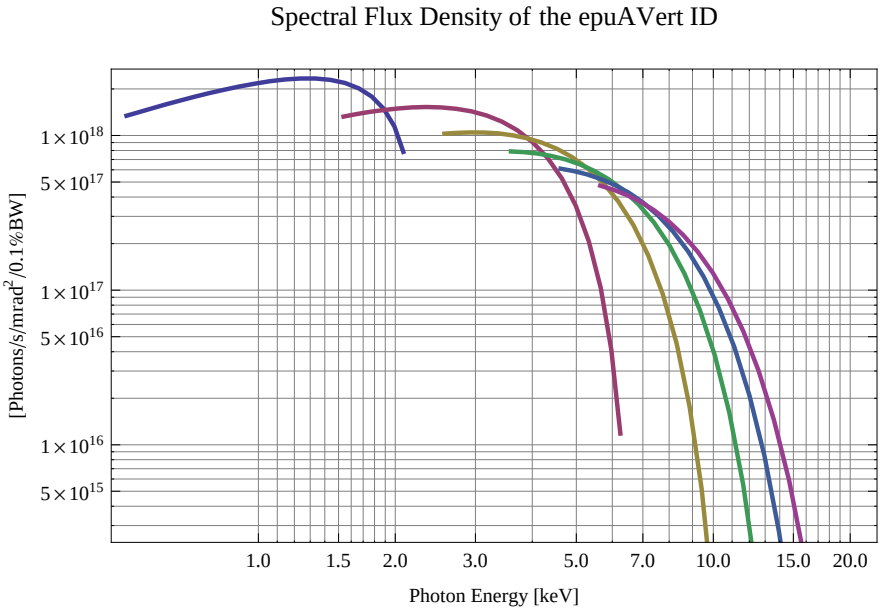

Figure 173: The spectral flux density of the synchotron radiation emitted by the epuAVert ID

The brilliance at peak energy the and the spectral flux density from the epuAVert ID for different harmonics at maximum K-value (2.602) are given in Table 45 and for minimum K-value (0.400) these values are given in Table 46.

Table 45: The brilliance at peak energy the and the spectral flux density from the epuAVert ID for different harmonics at maximum K-value (2.602)

Harmonic	Photon Energy [keV]	Brilliance [Ph./s/mrad^2/mrad^2/0.1%BW]	Spectral Flux Density [Ph./s/mrad^2/0.1%BW]
1	0.513028	3.71×10^{20}	1.34×10^{18}
3	1.53908	5.17×10^{20}	1.33×10^{18}
5	2.56514	4.42×10^{20}	1.03×10^{18}
7	3.59119	3.57×10^{20}	7.89×10^{17}
9	4.61725	2.83×10^{20}	6.1×10^{17}
11	5.6433	2.24×10^{20}	4.74×10^{17}

The brilliance at peak energy the and the spectral flux density from the epuAVert ID for different harmonics at maximum K-value (2.602) are given in Table 45 and for minimum K-value (0.400) these values are given in Table 46.

Table 46: The brilliance at peak energy the and the spectral flux density from the epuAVert ID for different harmonics at minimum K-value (0.4)

Harmonic	Photon Energy [keV]	Brilliance [Ph./s/mrad^2/mrad^2/0.1%BW]	Spectral Flux Density [Ph./s/mrad^2/0.1%BW]
1	2.08254	3.23×10^{20}	7.84×10^{17}
3	6.24763	5.54×10^{18}	1.18×10^{16}
5	10.4127	6.1×10^{16}	1.27×10^{14}
7	14.5778	6.35×10^{14}	1.31×10^{12}
9	18.7429	6.5×10^{12}	1.34×10^{10}
11	22.908	6.62×10^{10}	1.36×10^{8}

4.8.17 Influence from the epuAVert ID on the optics of the stored beam

Figure 174 shows the focusing potential from the epuAVert over the beam stay clear aperture of the ring aparture.

Figure 175 shows the kick map in the beam energy independant unit T^2m^2 of the kicks induced by the epuAVert ID over the beam stay clear aparture.

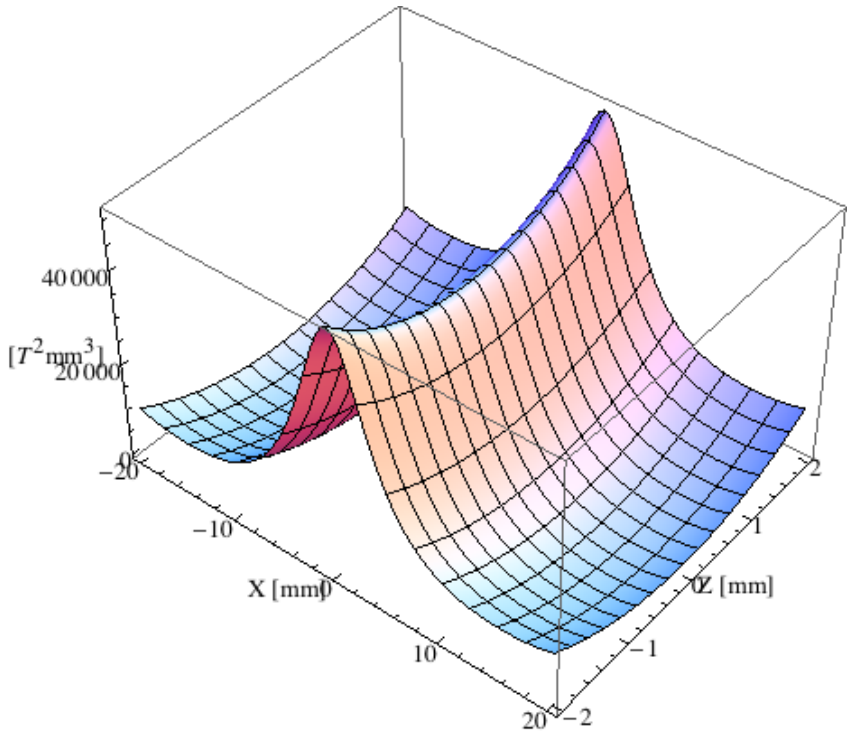

Figure 174: Focusing potential from the epuAVert ID over the beam stay clear aparture.

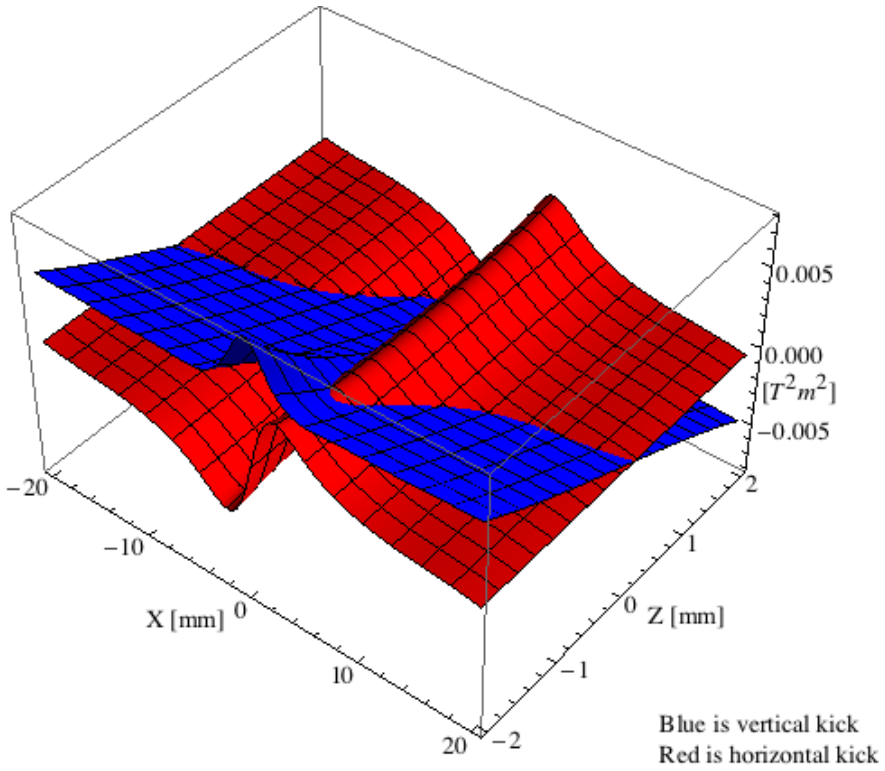

Figure 175: Kick map in the beam energy independant unit T^2m^2 of the kicks induced by the epuAVert ID over the beam stay clear aparture.

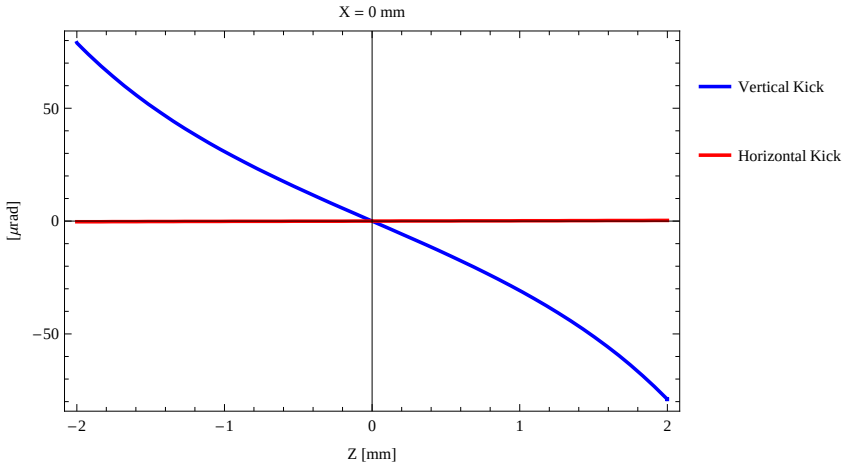

Figure 176: Induced angular kick on the stored beam from the epuAVert ID as a function of the vertical distance to the ID axis.

Figure 176 shows the induced angular kick on the stored beam from the epuAVert ID as a function of the vertical distance to the axis of the ID.

Figure 177 shows the induced angular kick on the stored beam from the epuAVert ID as a function of the horizontal distance to the axis of the ID.

Figure 178 shows tune shift induced by the epuAVert ID over the beam stay clear aparture. Note that the tune shift depends on the beam size at the ID.

Figure 179 shows the induced tune shift from the epuAVert ID as a function of the vertical distance to the axis of the ID.

Figure 180 shows the induced tune shift from the epuAVert ID as a function of the horizontal distance to the axis of the ID.

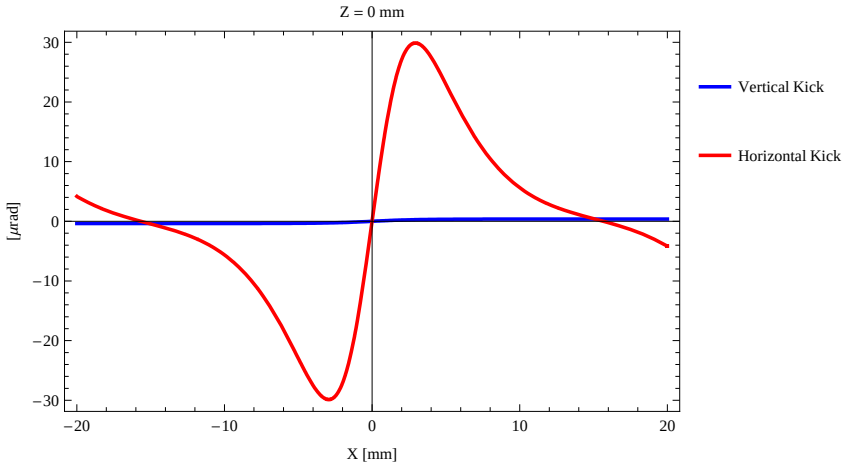

Figure 177: Induced angular kick on the stored beam from the epuAVert ID as a function of the horizontal distance to the ID axis.

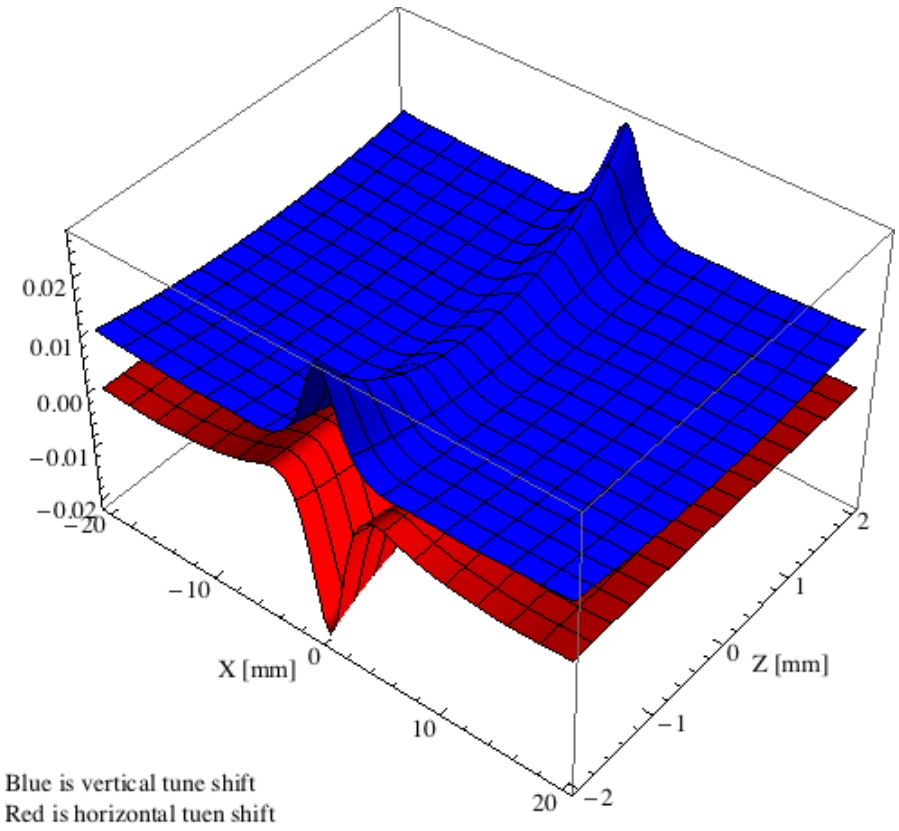

Figure 178: Tune shift induced by the epuAVert ID over the beam stay clear aparture.

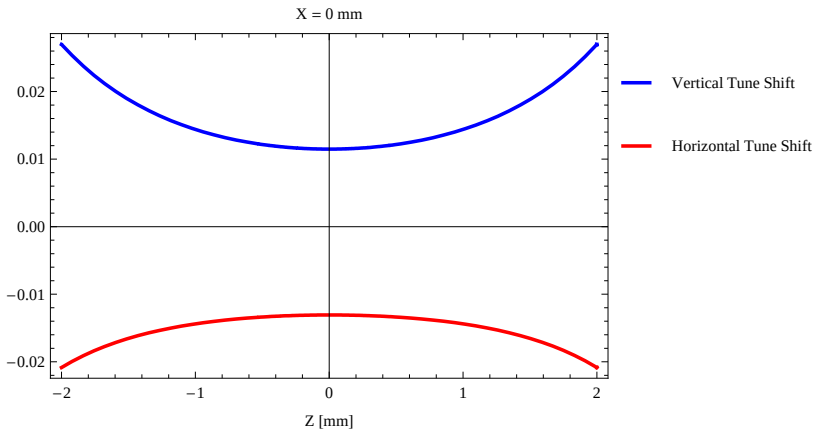

Figure 179: Induced tune shift from the epuAVert ID as a function of the vertical distance to the axis of the ID.

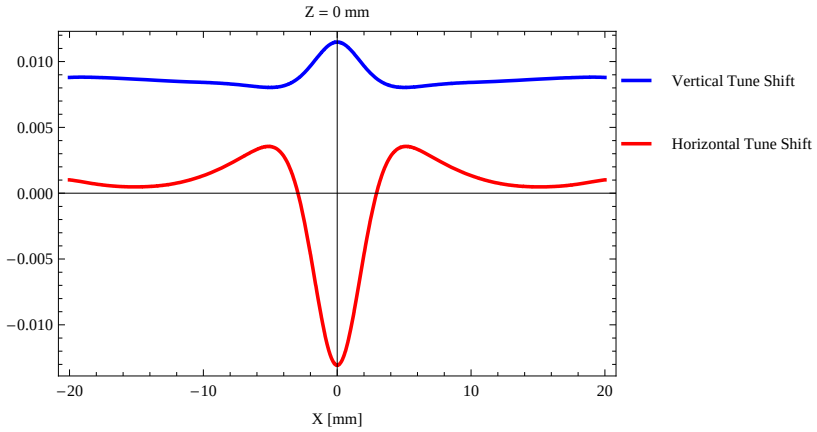

Figure 180: Induced tune shift from the epuAVert ID on the stored beam from the ID as a function of the horizontal distance to the axis of the ID.

4.9 Summary of the magnet model calculations

In total 8 different IDs have been modelled. The wigS is a wiggler of hybrid type that will produces synchrotron radiation for the MSC and TOM beamlines and there will be 2 IDs of this type installed in the middle of a straight sections. The wigD is a wiggler of hybrid type that will produces synchrotron radiation for the SXB and MAG beamlines and there will be 2 IDs of this type installed in the middle of a straight sections. The pmuA is an in-vacuum undulator of hybrid type that will produces synchrotron radiation for the PX1,NF1, and NF2 beamlines and there will be 3 IDs of this type installed in the middle of a straight sections. The pmuB is an in-vacuum undulator of hybrid type that will produces synchrotron radiation for the MUS and HIK beamlines and there will be 2 IDs of this type installed in the middle of a straight sections. The pmuC is an in-vacuum undulator of hybrid type that will produces synchrotron radiation for the ENV beamlines and there will be 1 IDs of this type installed in the middle of a straight sections. The cpmuA is a cryogenically cooled in-vacuum undulator of hybrid type that will produces synchrotron radiation for the PX2 beamlines and there will be 1 IDs of this type installed in the middle of a straight sections. The cpmuB is a cryogenically cooled in-vacuum undulator of hybrid type that will produces synchrotron radiation for the SXM beamlines and there will be 1 IDs of this type installed in the middle of a straight sections. The epuA is an elliptically polarising undulator that will produces synchrotron radiation for the HRS and MAG beamlines and there will be 2 IDs of this type installed in the middle of a straight sections. The served beamlines, length, magnetic gap and period lengths of the modelled IDs are given in Table 47. The magnetic peak field and efficient field and the Kx-value of the modelled IDs are given in Table 48. The emitted synchrotron radiation power and on-axis power density of the modelled IDs are given in Table 49. The vertical and horizontal tune shifts of the modelled IDs for the IDs are given in Table 50.

Table 47: The served beamlines, length, magnetic gap and period lengths of the modelled IDs

Name	Beamline	Length [mm]	Gap [mm]	Period Length [mm]
wigS	MSC and TOM	950.7	12.	80.
wigD	SXB and MAG	3990.7	9.	80.
pmuA	PX1,NF1, and NF2	3783.25	4.2	18.5
pmuB	MUS and HIK	3790.	4.2	20.
pmuC	ENV	3795.	4.2	22.
cpmuA	PX2	3798.6	4.2	15.6
cpmuB	SXM	3796.6	4.2	16.4
epuA	HRS and MAG	3930.98	9.	38.

Table 48: The magnetic peak field and efficient field and the Kx-value of the modelled IDs

Name	Peak Field [T]	Efficient Field [T]	Efficient Kx-value
wigS	1.86948	1.64048	12.2577
wigD	2.22307	1.88646	14.0956
pmuA	1.24131	1.11146	1.92049
pmuB	1.3244	1.17294	2.19105
pmuC	1.4239	1.24384	2.55585
cpmuA	1.23594	1.14832	1.67315
cpmuB	1.29392	1.19639	1.83258
epuA	0.974	0.986	3.49951

Table 49: The emitted synchrotron radiation power and on-axis power density of the modelled IDs

Name	SR Power [kW]	On-axis power density [kW/mrad^2]
wigS	7.28436	8.9332
wigD	40.4341	47.7514
pmuA	13.3062	97.1077
pmuB	14.8454	95.8185
pmuC	16.7166	92.3083
cpmuA	14.2612	119.474
cpmuB	15.472	118.746
epuA	10.8807	43.8925

Table 50: The vertical and horizontal tune shifts of the modelled IDs

Name	Vertical Tune Shift	Horizontal Tune Shift
wigS	0.005010	−0.000078
wigD	0.029504	−0.000302
pmuA	0.009544	−0.000003
pmuB	0.010649	−0.000003
pmuC	0.012000	−0.000002
cpmuA	0.010219	−0.000002
cpmuB	0.011073	−0.000001
epuA	0.006253	0.002542

5 Infuence from the insertion devices on the RF-system the emittance and energy spread of the stored electron beam

The insertion devices in this report can be combined in 2592 different ways, which naturally is too long to include in this report. The influence on the RF-system and the emittance and energy spread of the stored beam for 50 different combinations, including situations with 0 and all insertion devices installed, of insertion devices are given in Table 51, where a-h represents the different insertion devices, P_g is the generator power, P_b is the beam loading, P_r is the reflected power, and the last three columns are the momentum acceptance of the RF-system, the change of emittance, and the change of energy spread compared to the bare lattice when installing insertion devices.

Table 51: The influence on the RF-system and the emittance and energy spread of the stored beam

a	b	c	d	e	f	g	h	P_g	P_b	P_r	$\delta_{\mathrm{rf}}[\%]$	$\frac{\Delta\epsilon_{ID}}{\epsilon_0}[\%]$	$\frac{\Delta\sigma_{eID}}{\sigma_{\mathrm{e0}}}[\%]$
0	0	0	0	0	0	0	0	299	180	12	6.2	100.	100.
1	1	3	1	1	0	0	2	428	321	0	4.98	86.7	159.6
0	2	3	0	0	0	1	2	445	338	0	4.83	85.8	170.6
0	0	0	2	1	0	0	2	358	248	3	5.62	93.1	127.
1	1	1	1	0	1	1	1	404	296	0	5.19	89.2	153.
0	1	0	2	1	1	1	1	415	307	0	5.1	88.	155.8
1	2	3	2	1	1	1	1	505	395	3	4.31	80.1	187.1
2	0	3	0	1	0	1	1	386	278	1	5.36	90.3	139.7
1	2	1	0	0	0	1	2	426	319	0	5.	87.8	166.6
2	1	2	1	0	0	0	0	385	276	1	5.37	91.3	148.2
0	2	1	1	0	1	0	1	421	314	0	5.04	88.2	164.7
0	2	0	2	1	0	0	0	415	307	0	5.1	88.9	163.9
1	0	2	0	1	1	0	1	365	256	3	5.55	92.4	131.
1	0	2	1	0	1	1	1	378	269	2	5.43	91.	135.5
0	1	1	1	1	1	1	2	424	317	0	5.02	87.	157.8
1	1	3	1	0	1	1	2	441	334	0	4.86	85.4	163.1
1	0	2	1	0	0	0	2	361	251	3	5.6	92.9	128.2
2	2	1	1	1	0	0	0	427	320	0	4.98	87.7	169.3
2	0	1	1	1	0	0	1	360	250	3	5.6	93.1	130.7
2	0	2	2	0	1	1	0	389	281	1	5.33	90.	141.2
2	1	0	2	0	1	1	1	413	305	0	5.12	88.4	156.9
1	1	2	0	1	0	1	1	405	297	0	5.19	89.1	153.5
2	0	1	0	1	0	1	2	371	262	2	5.5	91.9	134.2
2	1	1	2	1	1	1	1	443	335	0	4.85	85.3	165.7
2	1	3	1	0	1	1	2	449	341	0	4.8	84.7	166.1
0	0	3	1	1	0	0	0	361	251	3	5.59	92.8	128.8

Table 51: The influence on the RF-system and the emittance and energy spread of the stored beam

a	b	c	d	e	f	g	h	P_g	P_b	P_r	$\delta_{\mathrm{rf}}[\%]$	$\frac{\Delta\epsilon_{ID}}{\epsilon_0}[\%]$	$\frac{\Delta\sigma_{eID}}{\sigma_{\mathrm{e0}}}[\%]$
0	2	1	0	0	1	1	1	422	315	0	5.03	88.1	165.
2	0	1	0	0	0	0	0	323	208	8	5.96	97.4	114.8
1	0	3	2	1	1	1	2	432	325	0	4.94	85.4	153.1
2	1	0	2	1	0	0	1	400	292	0	5.23	89.7	153.3
0	0	1	2	0	1	1	1	373	264	2	5.48	91.5	132.6
2	2	1	2	0	1	1	2	478	370	1	4.54	82.7	181.2
0	2	1	0	1	1	0	0	412	305	0	5.12	89.1	163.
1	2	1	1	0	1	0	0	418	311	0	5.07	88.6	165.2
0	1	2	2	0	1	1	1	425	317	0	5.01	87.	158.
1	2	3	0	0	0	1	0	431	324	0	4.96	87.3	168.6
2	2	2	2	1	1	1	2	511	400	4	4.26	79.7	188.9
2	2	0	1	1	1	1	1	455	348	0	4.74	85.	176.4
2	2	0	1	0	0	1	0	413	306	0	5.11	89.2	165.2
2	1	0	1	0	1	0	2	394	286	1	5.29	90.3	150.3
0	0	1	2	1	0	0	2	371	261	2	5.5	91.8	131.6
2	0	1	0	0	1	1	2	369	259	2	5.52	92.1	132.8
1	0	2	1	0	0	0	0	341	229	5	5.78	95.1	121.4
1	1	3	0	1	0	0	1	403	295	0	5.21	89.3	152.5
1	2	0	1	0	0	1	1	417	309	0	5.08	88.8	164.7
2	2	2	2	1	1	1	0	487	378	2	4.46	81.9	184.4
1	0	2	2	1	1	1	2	419	312	0	5.06	86.7	149.2
2	0	0	0	1	0	0	1	335	222	6	5.84	95.9	120.5
2	0	2	1	1	1	1	1	401	293	0	5.22	88.7	145.1
2	2	3	2	1	1	1	2	525	413	5	4.14	78.3	192.

An explanation of the naming of the insertion devices in Table 51 is found in Table 52.

Table 52: Explanation of the naming of the insertion devices in Table 51

a	wigS
b	wigD
c	pmuA
d	pmuB
e	pmuC
f	cpmuA
g	cpmuB
h	epuA

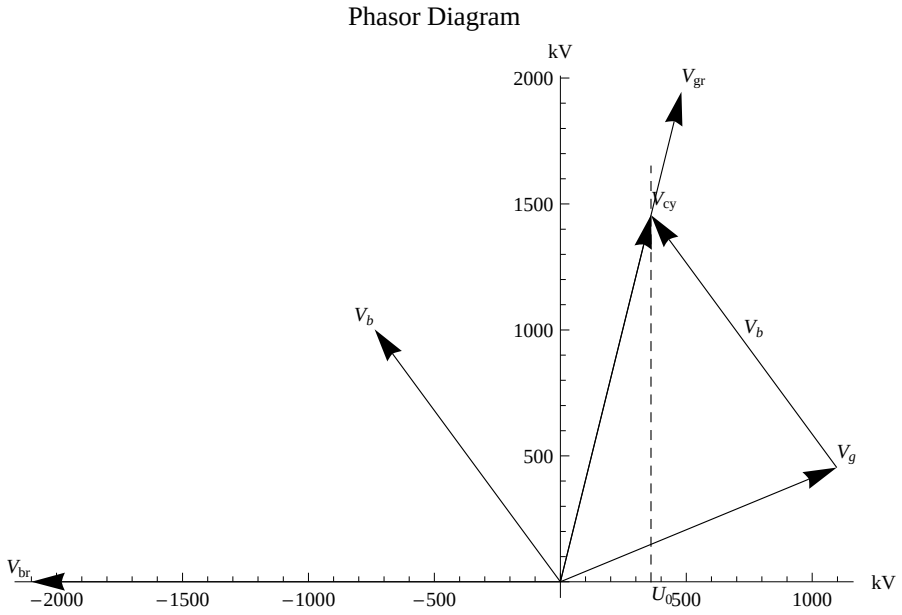

Figure 181: Phasor diagram with 0 insertion devices installed

The RF-system parameters with 0 insertion devices installed are given in Table 53 and Figure 181 shows the phasor diagram with 0 insertion devices installed.

Table 53: RF-system parameters with 0 insertion devices installed

P_g =	298.81	kW
P_{cy}=	107.14	kW
P_b =	180.00	kW
P_r=	11.67	kW
|Vcy| =	1500.00	kV
|Vb| =	1244.60	kV
|Vg| =	1187.70	kV
|Vgr| =	2004.00	kV
ψ =	0.94	
β =	4	

The RF-system parameters with all insertion devices installed are given in Table 54 and Figure 182 shows the phasor diagram with all insertion devices installed.

Table 54: RF-system system parameters with all insertion devices installed

$P_g =$	525.32	kW
$P_{\mathrm{cy}} =$	107.14	kW
$P_b =$	413.26	kW
$P_r =$	4.92	kW
$\lvert \mathrm{Vcy} \rvert =$	1500.00	kV
$\lvert \mathrm{Vb} \rvert =$	1365.60	kV
$\lvert \mathrm{Vg} \rvert =$	1727.80	kV
$\lvert \mathrm{Vgr} \rvert =$	2657.10	kV
$\psi =$	0.86	
$\beta =$	4	

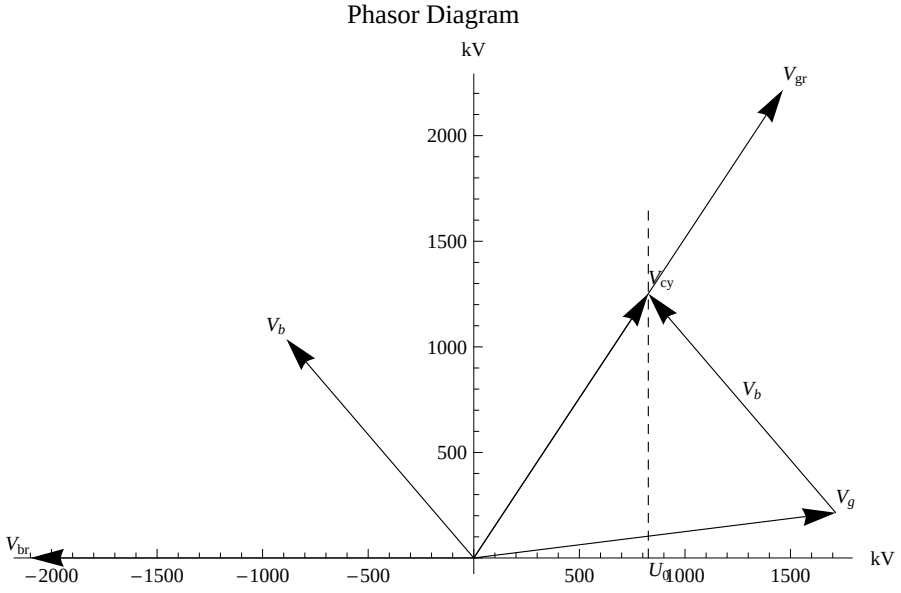

Figure 182: Phasor diagram with all insertion devices installed

6 Appendix 1: Influence from the insertion devices on the magnetic optics of the storage ring

6.1 Beam deflection

The insertion devices will be equipped with a set of air coils for each insertion device that will will compensate for varying field integrals, which will deflect the beam, with gap of the insertion device. Feed forward tables for the air coils will be established during measurements with stored beam in the storage ring.

6.2 Simple approximations for focusing effect from planar field insertion devices

The main effect on the stored beam of flat field insertion devices is a vertical focusing effect. This focusing effect is inversely proportional to the square of the energy of the stored beam and is hence more pronounced in low energy storage rings.

The strength of the vertical focusing K_z is [6]

$$K_z = \frac{1}{2\rho^2} \tag{7}$$

where ρ is the radius of curvature in the field B_0, which is given by the relation $\rho = E/(ce\mathrm{B}_0) \approx E\,[\mathrm{GeV}]\,/(0.3\ \mathrm{B}_0\,[\mathrm{T}])$.The focusing effect is independent of the period length λ_0. The vertical focusing acts like a lens with the focal length F_z given by

$$\frac{1}{F_z} = LK_z = \frac{L}{2\rho^2} \tag{8}$$

where L is the total length of the insertion device. The (linear) vertical tune shifts induced is given by

$$\Delta\nu_z = \frac{\langle\beta_z\rangle L}{8\pi\rho^2} \tag{9}$$

The tune shift is directly proportional to the average vertical beta function, $\langle\beta_z\rangle$, at the wiggler. Hence the tune shift can be limited by providing a small β_z at the wiggler. The vertical focusing will, if it is not compensated for, distort the vertical beta function like

$$\left[\frac{\Delta\beta_z}{\beta_z}\right] = \frac{\langle\beta_z\rangle L}{4\rho^2\sin(2\pi\nu_z)} \tag{10}$$

The vertical focusing varies with the vertical aperture, i.e. it is nonlinear, and this gives rise to an amplitude dependent tune shift which might reduce the dynamic aperture of the storage ring. The tune shift with amplitude, which depends on the period length, is given by

$$\frac{d\Delta\nu_z}{dJ_z} = \frac{\pi\langle\beta_z^2\rangle L}{4\lambda_0^2\rho^2} \tag{11}$$

where J_z is the vertical action angle variable. Also in this case the effect of the nonlinear vertical focusing is reduced by reducing the beta function.

An undulator also has a transverse field roll-off varying with the horizontal position out from the undulator axis. This transverse field roll gives rise to a horizontal defocusing of the stored electron beam and give a change of the horizontal tune of the storage ring. The horizontal defocusing effect is in general low compared to the vertical focusing effect of the undulator.

The simple approximation described above is a somewhat poor approximation of the effect on the stored beam, especially for other insertion devices than flat field insertion devices with a negligible field roll off.

6.3 Focusing potential and kick maps for arbitrary types of periodic insertion devices

A better way to estimate the effect of an insertion device on the beam optics and dynamic aperture of a storage ring is to use the concept with kick-maps in the tracking calculations [7]. The kick-map describes the kick an electron would get when passing the undulator and the kick-map covers the full horizontal and vertical aperture of the insertion device.

The kick map is calculated from the potential function $U(x,z)$, which for a periodic insertion device with length L aligned to the longitudinal axis $\hat{s}$ is given by

$$U(x,z) = L \int\limits_{1\ period} \left[\int\limits_{-\infty}^{s} B_x(x,s',z)ds'\right]^2 + \left[\int\limits_{-\infty}^{s} B_z(x,s',z)ds'\right]^2 ds \tag{12}$$

In principle this an integration of the square of the angular deviation of the beam path over one undulator period.

The horizontal $\Delta x'$ and the vertical $\Delta z'$ angular kicks the electrons will get when the beam is passing through the undulator is then given by

$$\Delta x' = -\left(\frac{e}{\gamma m_e c}\right)^2 \frac{1}{2}\frac{\partial U}{\partial x} \qquad (13)$$
$$\Delta z' = -\left(\frac{e}{\gamma m_e c}\right)^2 \frac{1}{2}\frac{\partial U}{\partial z}$$

For tracking studies it is convenient to use kick maps where the energy dependent factor $(e/(\gamma m_e c))^2$ has been omitted. A useful approximation is $e/(\gamma m_e c) \approx 0.3/E\,[\mathrm{GeV}]$.

The kick maps with the unit $\mathrm{T}^2\mathrm{m}^2$ can then be included in the line of elements in the tracking lattice and be used as a drift-kick-drift element.

The vertical and horizontal focusing/defocusing effects make the undulator works like a magnetic lens for the stored beam and the focal lengths of the insertion device is given by

$$\frac{1}{F_x} = -\frac{\partial \Delta x'}{\partial x} = \left(\frac{e}{\gamma m_e c}\right)^2 \frac{1}{2}\frac{\partial^2 U}{\partial x^2} \qquad (14)$$
$$\frac{1}{F_z} = -\frac{\partial \Delta z'}{\partial z} = \left(\frac{e}{\gamma m_e c}\right)^2 \frac{1}{2}\frac{\partial^2 U}{\partial z^2}$$

The tune shifts of the storage ring can be calculated from the focusing potential by using

$$\Delta\nu_x = \frac{1}{4\pi}\frac{\langle\beta_x\rangle}{F_x} \qquad (15)$$
$$\Delta\nu_z = \frac{1}{4\pi}\frac{\langle\beta_z\rangle}{F_z}$$

6.4 Other methods

Instead of kick maps it is also possible to describe the influence from the insertion devices in a sympletic way with generating functions and include the generating function in the tracking calculations, as described in [8]. It is also possible to model the insertion device as a hamiltonian and use symplectic integration at the tracking calculations, as described in [9].

7 Appendix 2: Influence from the insertion devices on the emittance and energy spread of the stored beam

The distribution of the electrons in an electron storage and the emittance will be determined by an equilibrium determined by the excitation, given by quantum excitation and intrabeam scattering (IBS), and the damping given by the emitted synchrotron radiation. The electron beam injected into the storage will after a damping time of typically 10-15 ms reach the equilibrium distribution.

7.1 Synchrotron radiation integrals, momentum compaction, emittance, and energy spread

The synchrotron radiation integrals , $I_1 - I_5$, determine the damping and quantum excitation. In the MAX IV 3 GeV ring the vertical emittance will be put by artificial means, e.g. a skew quadrupole, to a fixed value of 8 pmrad [11] and we are here only interested in the horizontal emittance and the energy spread and we can neglect the vertical part of the synchrotron radiation integrals. The synchrotron integrals, neglecting the vertical part, are [4]

$$I_1 = \int_0^C \frac{D_x}{\rho} ds \tag{16}$$

$$I_2 = \int_0^C \frac{1}{\rho^2} ds \tag{17}$$

$$I_3 = \int_0^C \frac{1}{|\rho^3|} ds \tag{18}$$

$$I_{4,x} = \int_0^C \frac{D_x(1+2\rho^2 k)}{\rho^3} ds \tag{19}$$

$$I_{5,x} = \int_0^C \frac{\mathcal{H}_x}{|\rho^3|} ds \tag{20}$$

where C is the circumference of the ring, k is the quadrupole strength in the magnets, and $\mathcal{H}_x$ is given by

$$\mathcal{H}_x = \frac{1}{\beta_x}(D_x^2 + (\beta_x D_x' - \frac{1}{2}\beta_x' D_x)^2) \tag{21}$$

The radiation integrals for the lattice of the 528 m circumference 3 GeV storage ring without insertion devices are computed by the software packages used for designing the storage ring and they are [12]:

$$\begin{aligned} I_{1,0} &= 0.1621534257 \\ I_{2,0} &= 0.3157347208 \\ I_{3,0} &= 0.01613875828 \\ I_{4,x0} &= -0.2719069455 \\ I_{5,x0} &= 1.448995144 \times 10^{-5} \end{aligned} \tag{22}$$

The momentum compaction α is given by

$$\alpha = \frac{I_1}{C} \tag{23}$$

The energy loss per turn U_0 is given by

$$U_0 = \frac{2}{3} r_e \frac{E^4}{(mc^2)^3} I_2 \tag{24}$$

where r_e is the classical electron radius, m is the elctron mass, and E is the energy of the stored beam.

The horizontal electron beam emittance neglecting IBS, ϵ_x, is given by

$$\varepsilon_x = C_q \gamma^2 \frac{I_{5,x}}{I_2 - I_{4,x}} \tag{25}$$

where C_q is the quantum excitation constant defined by

$$C_q = \frac{55}{32\sqrt{3}} \frac{\hbar c}{m_e c^2} = 3.8319 \times 10^{-13}\text{m} \tag{26}$$

The energy spread neglecting IBS, σ_e is given by

$$\sigma_e^2 = C_q \gamma^2 \frac{I_3}{2I_2 + I_{4,x}} \tag{27}$$

7.2 Influence from insertion devices on the synchrotron radiation integrals, momentum compaction, emittance, and energy spread

What we are interested in here is the change of the horizontal emittance and the energy spread that is introduced by the insertion devices. The change of emittance and energy spread from the insertion devices are given by the relative change of the radiation integrals $\Delta I_2, \Delta I_3, \Delta I_{4,x}, \Delta I_{5,x}$ by the relations [10]

$$\varepsilon_{xID} = \varepsilon_{x,0} \frac{1 + \Delta I_{5,x}/I_{5,x0}}{1 + (\Delta I_2 - \Delta I_{4,x})/(I_{2,0} - I_{4,x0})} \tag{28}$$

$$\sigma^2_{eID} = \sigma^2_{e0} \frac{1 + \Delta I_3/I_{3,0}}{1 + (2\Delta I_2 + \Delta 4, x)/(2I_{2,0} + I_{4,x0})} \tag{29}$$

The insertion devices are assumed to be installed in dispersion free straight sections and to have a sinusoidal field. The $1/\rho$ factor for a sinusoidal field is

$$\frac{1}{\rho} = \frac{1}{\rho_0} \sin(\frac{2\pi s}{\lambda_0}) \tag{30}$$

where ρ_0 is the bending radius at the undulator peak field, which is 8 m for a 1.25 T peak field in a 3 GeV storage ring, and λ_0 is the undulator period length. D_x and D'_x in the undulator are the given by

$$D_x(s) = \frac{\lambda_0^2}{4\pi^2 \rho_0} \sin(\frac{2\pi s}{\lambda_0}) \tag{31}$$

$$D'_x(s) = \frac{\lambda_0}{2\pi \rho_0} \cos(\frac{2\pi s}{\lambda_0}) \tag{32}$$

The integral $I_{1,x}$ along the undulator length L, which will change the momentum compaction factor of the machine, is given by

$$\Delta I_{1,x} = \frac{L\lambda_0^2}{8\pi^2 \rho_0^2} \tag{33}$$

The integral $I_{2,x}$ along the undulator length L, which will change the amount of emitted synchrotron radiation, is given by

$$\Delta I_{2,x} = \frac{L}{2\rho_0^2} \tag{34}$$

The integral $I_{3,x}$ along the undulator length L, which affects the energy spread, is given by

$$\Delta I_{3,x} = \frac{4L}{3\pi \rho_0^3} \tag{35}$$

The integral $I_{4,x}$ along the undulator length will be a very small number compared to I_2 along the undulator and the influence from $I_{4,x}$ on the emittance, energy spread, and damping time change from IDs can be neglected.

Since $\mathcal{H}_x$ in the $I_{5,x}$ integral is dominated by the term $\beta_x D'_x$ over the length L of the insertion device, $\Delta I_{5,x}$ may be approximated by

$$\Delta I_{5,x} \approx \int_{-L/2}^{L/2} \beta_x \frac{D'_x(s)^2}{|\rho^3|} ds \approx \hat{\beta}_x \int_{-L/2}^{L/2} \frac{D'_x(s)^2}{|\rho^3|} \tag{36}$$

where $\hat{\beta}_x$ is the average horizontal beta function in the insertion device. The relation

$$\frac{D'_x(s)^2}{|\rho^3|} = \frac{\lambda_0^2}{4\pi^2\rho_0^5} cos^2(\frac{2\pi s}{\lambda_0})|\sin^3(\frac{2\pi s}{\lambda_0})| \tag{37}$$

makes it possible to get a finite number for $\Delta I_{5,x}$, which is

$$\Delta I_{5,x} \approx \hat{\beta}_x \frac{L\lambda_0^2}{15\pi^3\rho_0^5} \tag{38}$$

The beam is also excited by intrabeam scattering (IBS) as explained elsewhere in the MAX IV detatiled design report, where also the bare lattice emittance and energy spread including IBS are given. A review of ways of calculating IBS can be found in [13]. From studying [13], it seems like the excitation due to IBS in the longitudinal and transverse directions follows the same scaling laws when installing IDs as the quantum excitation disregarding IBS. The exact relations for the IBS excitation requires further studies, which will be carried out in future versions of this report.

The influence from the installed IDs on the momentum compaction α_0, emittance $\varepsilon_{x,0}$, and energy spread σ_{e0}, calculated with or without an IBS contribution, of the lattice without insertion devices are hence given by

$$\frac{\alpha_{ID}}{\alpha_0} = 1 + \frac{L\frac{\lambda_0^2}{8\pi^2\rho_0^2}}{I_{1,0}} \tag{39}$$

$$\frac{\varepsilon_{xID}}{\varepsilon_{x,0}} \approx \frac{1 + (\hat{\beta}_x \frac{L\lambda_0^2}{15\pi^3\rho_0^5})/I_{5,x0}}{1 + (\frac{L}{2\rho_0^2})/(I_{2,0} - I_{4,x0})} \tag{40}$$

$$\frac{\sigma_{eID}}{\sigma_{e0}} \approx \sqrt{\frac{1 + (\frac{4L}{3\pi\rho_0^3})/I_{3,0}}{1 + (\frac{L}{\rho_0^2})/(2I_{2,0} + I_{4,x0})}} \tag{41}$$

Figure 183: The newtork model of an accelerator cavity and the RF-generator

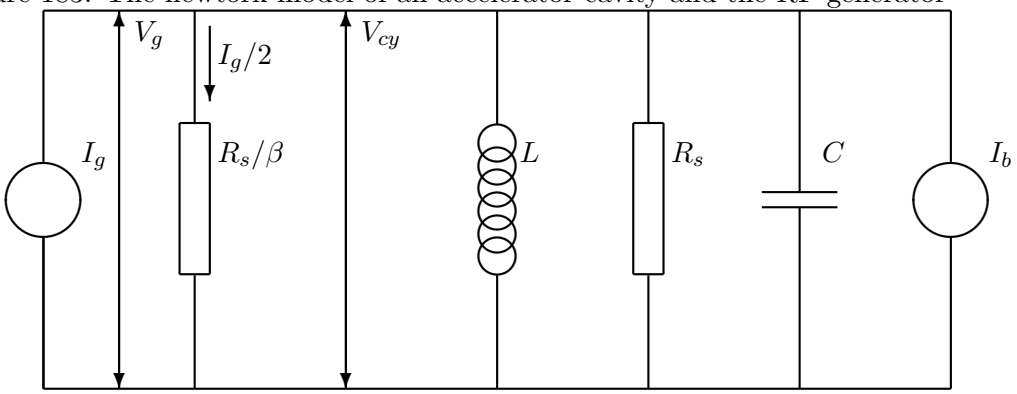

8 Appendix 3: Beam loading of the radio frequency system from insertion devices

8.1 The network model of an RF system

The interaction between the radio frequency (RF) generator, cavity and beam is well described in [14] and this text is a short summary of the relations found in [14].

The accelerating cavity in an accelerator can be described by a parallel resonant circuit network model which is driven by an external rf-current current source I_g from a generator and the currents of the particle beam I_b. Figure 183 shows the network model. β is the coupling factor between the generator and cavity.

The resonance frequency ω_r of the system is given the inductance L and capacitance C.

$$\omega_r = \frac{1}{\sqrt{LC}} \tag{42}$$

The losses in the cavity P_{cy}, the cavity peak field V_{cy} and the shunt impedance of the cavity R_S are related like

$$P_{cy} = \frac{V_{cy}^2}{2R_S} \tag{43}$$

The beam induced voltage at the cavity V_{br} at resonance by a beam with current I_b is given by

$$V_{br} = \frac{2I_b R_S}{1+\beta} \tag{44}$$

The generator induced voltage at the cavity V_{gr} at resonance is given by

$$V_{gr} = \frac{2\sqrt{2\beta}}{1+\beta}\sqrt{R_S P_g} \tag{45}$$

The losses U_0, measured in volts, during one turn of the electrons in the storage ring, gives the synchronous phase ψ_s

$$\psi_s = \arcsin \frac{U_0}{V_{cy}} \tag{46}$$

The cavity is in normal operation not at resonance but it is side tuned to a slightly lower frequency than the resonance frequency, which gives a capacitance loaded system. Off resonance, the generator voltage and current are no more in phase. The phase difference can be derived from the complex impedance Z of the network,which is the same seen from the generator as seen from the beam

$$\frac{1}{Z} = \frac{1+\beta}{R_s} + i\omega C + \frac{1}{i\omega L} \tag{47}$$

The cavity detuning angle ψ and the generator angle $\psi_g =$ at perfect phase matching, i.e. when the cavity and generator are in phase are given by

$$\psi = \arctan(\frac{V_{br}}{V_{cy}} \cos\psi_s) \tag{48}$$

$$\psi_g = \frac{\pi}{2} - \psi_s \tag{49}$$

The generator induced voltage V_g and the beam induced voltage V_b at the cavity are given by

$$V_g = V_{gr} \cos(\psi) e^{i\psi} \tag{50}$$

$$V_b = -V_{br} \cos(\psi) e^{i\psi} \tag{51}$$

The required power from the generator P_g is given by

$$P_g = \frac{(1+\beta)^2}{8\beta R_S} |V_{gr}|^2 \tag{52}$$

The coupling factor β gives optimum coupling between the generator and the cavity for one specific beam loading situation only and in other situations there will be a reflected power P_r from the cavity given by.

$$P_r = P_g - P_{cy} - U_0 I_b \tag{53}$$

8.2 The phasor diagram for the RF system of the MAX IV 3 GeV ring a typical running situation

The complex vectors of V_b, V_g, and V_{cy} can be shown in a phasor diagram. Figure 184 shows the phasor diagram for typical running situation for the MAX IV 3 GeV storage

Figure 184: Phasor diagram for the beam-cavity-generator interaction in a typical running situation at the MAX IV 3 GeV storage ring

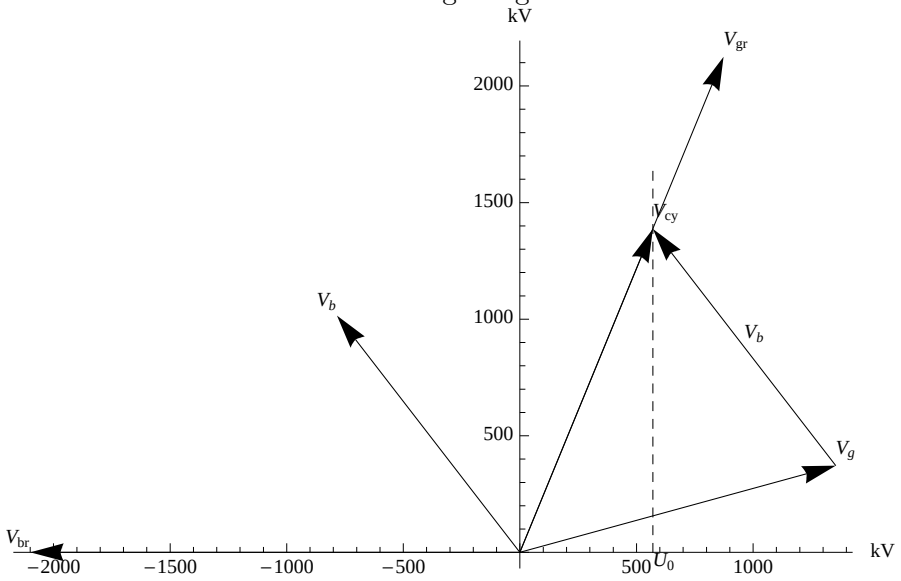

ring. The RF power levels for the same situation are given in Table 55. At the MAX IV 3 GeV storage ring, the coupling factor β will be fixed to 4 and there will be 6 cavities giving a total R_S of 10.5 MOhm and a total V_{cy} of 1.5 MV [15]. The energy loss per turn for the electrons with 4 wigglers installed is typically 570 keV.

Table 55: RF power distribution at a typical running situation

P_g	392.92	kW
P_{cy}	107.14	kW
P_b	285.00	kW
P_r	0.77	kW

8.3 RF acceptance

The RF momentum acceptance δ_{rf} of the system, which gives the maximum energy deviation for the electrons to stay within the RF-bucket, is given by

$$\delta_{rf} = \sqrt{\frac{V_{cy}\cos\psi_s}{\pi h|\gamma^{-2} - \alpha_c|E_0}}\sqrt{2 - (\pi - 2\psi_s)\tan\psi_s} \tag{54}$$

where γ is the relativistic factor of the beam with beam energy E_0, α_c is the momentum compaction, and h is the harmonic number of the ring. For the MAX IV 3 GeV storage

ring h=176, $\gamma = 5871$, $E_0 = 3 \times 10^9$ eV, and α_c is varying with the number of IDs but it is in the region of 3.07×10^{-4}.

9 Appendix 4: Synchrotron radiation relations

In this appendix some fundamental relations of synchrotron radiation are explained and expressions for the synchrotron radiation produced by an ultra-relativistic electron beam passing through a sinusoidally periodic field with a large number of periods are given.

9.1 Synchrotron radiation from a single electron moving along an arbitrary trajectory

The scalar and vector potentials generated by an electron moving along an arbitrary trajectory (Liénard-Wiechert potential, SI-units) are given by [16, 17, 19]

$$\phi(\mathbf{r}, t) = \frac{e}{4\pi\varepsilon_0 \left[R - \mathbf{v} \cdot \mathbf{R}/c\right]_{ret}} \tag{55}$$

$$\mathbf{A}(\mathbf{r}, t) = \frac{e\mathbf{v}}{4\pi\varepsilon_0 c^2 \left[R - \mathbf{v} \cdot \mathbf{R}/c\right]_{ret}} \tag{56}$$

with

$$\mathbf{R} = \mathbf{r} - \mathbf{r}' \tag{57}$$

where $\mathbf{r}$ is the vector from the origin to the observer, $\mathbf{r}'$ is the vector from the origin to the electron, $\mathbf{v}$ is the velocity of the electron, e is the electron charge, c is the speed of light, and ε_0 is the permittivity of vacuum. The subscript 'ret' denotes that the values in in the square brackets should be calculated at the retarded time t' determined by

$$t' + R(t')/c = t \tag{58}$$

The electric $\mathbf{E}(t)$ and magnetic $\mathbf{B}(\mathbf{t})$ fields are given from the scalar and vector potential by

$$\mathbf{E}(t) = -\nabla\phi - \frac{\partial \mathbf{A}}{\partial t} \tag{59}$$

$$\mathbf{B}(t) = \nabla \times \mathbf{A} \tag{60}$$

The power density, or radiated power $\mathrm{d}P$ per unit area $\mathrm{d}S$ can be written as

$$\frac{\mathrm{d}P}{\mathrm{d}S} = \varepsilon_0 c \int_{-\infty}^{\infty} |\mathbf{E}(t)|^2 dt =$$
$$= \frac{e^2\gamma^4}{2\pi^2\varepsilon_0^2 c^2} \int_{-\infty}^{\infty} \left[\frac{(\gamma\dot{\beta}_x)^2 + (\gamma\dot{\beta}_z)^2}{R^2 D^3} - \frac{4(\xi\gamma\dot{\beta}_x + \psi\gamma\dot{\beta}_z)^2}{R^2 D^5} + \frac{4c^2(\xi^2+\psi^2)}{R^4 D^5} \right] dt \qquad (61)$$

with

$$\begin{aligned} D &= 1 + \xi^2 + \psi^2 \\ \xi &= \gamma n_x - \gamma\beta_x \\ \psi &= \gamma n_z - \gamma\beta_z \\ \mathbf{n} &= \mathbf{R}/R \end{aligned} \qquad (62)$$

where γ is the Lorentz factor, $\beta = v/c$ is relative velocity of the moving electron, and and $\mathbf{n}$ is a direction.

When calculating the spectral flux density of synchrotron radiation it is more convenient to be in the frequency domain and use the Fourier transform $\mathbf{E}_\omega$ of the electric field [18]

$$\mathbf{E}_\omega = -\nabla\phi_\omega + i\omega\mathbf{A} \qquad (63)$$

Using the retarded time (58), the following expression are obtained

$$\phi_\omega = \frac{e}{4\pi\varepsilon_0} \int_{-\infty}^{\infty} \frac{1}{R(t')} \exp[i\omega t(t')] dt' \qquad (64)$$

$$\mathbf{A} = \frac{e}{4\pi\varepsilon_0 c} \int_{-\infty}^{\infty} \frac{\mathbf{v}(t')/c}{R(t')} \exp[i\omega t(t')] dt' \qquad (65)$$

and by substitution of (64) and (65) into (63), we get

$$\mathbf{E}_\omega = \frac{e}{4\pi\varepsilon_0}\mathbf{H} \qquad (66)$$

where

$$\mathbf{H} = i\omega \int_{-\infty}^{\infty} \frac{1}{R(t')} \left[\mathbf{v}(t')/c - \left(1 + \frac{ic}{\omega R(t')}\right) \mathbf{n}(t') \right] \exp[i\omega t(t')] dt' \tag{67}$$

The spectral flux density from the single electron, also often called angular spectral flux, is calculated as

$$\frac{\mathrm{d}\Phi}{\mathrm{d}\Omega} = \frac{\mathrm{d}^2 P}{\hbar \mathrm{d}S \mathrm{d}\omega} = \frac{\varepsilon_0 c}{\hbar \pi} \left| \mathbf{E}_\omega^2 \right| = \frac{\alpha}{4\pi^2} \left| \mathbf{H} \right|^2 \tag{68}$$

The degree of polarization of the emitted synchrotron radiation are determined by the Stokes paremeters

$$\begin{aligned} S_0 &= |H_x|^2 + |H_z|^2 \\ S_1 &= |H_x|^2 - |H_z|^2 \\ S_2 &= 2Re(H_x H_{\omega z}^*) \\ S_3 &= 2Im(H_x H_z^*) \end{aligned} \tag{69}$$

There are 3 types of degree of polarization : linear (PL), circular (PC) and 45 - degree linear (PL45) polarization.

$$\begin{aligned} PL &= S_1/S_0 \\ PL45 &= S_2/S_0 \\ PC &= S_3/S_0 \end{aligned} \tag{70}$$

PL = +1 (-1) means that the electric vector of the photon beam lies on the horizontal (vertical) plane.

PL45 = +1 (-1) means that the electric vector lies on the plane tilted by 45 (135) degree from the horizontal plane.

PC = +1 (-1) means that the electric vector rotates counterclockwise (clockwise). Note counterclockwise polarization = right hand polarization = positive circular polarization and clockwise polarization = left hand polarization = negative circular polarization.

9.2 Angular spectral flux from periodic undulators with sinusoidal field and a filament current

Under the assumptions that the periodic field of the undulator is sinusoidal and the number of periods in the undulator is large a number of approximations can can be done, as described in e.g. [19], and rather compact expressions for the angular spectral flux density can be derived.

The K-value is a fundamental parameter of an undulator and it is a unit-less parameter denoting the maximum deflection that the beam does in a period of the undulator in units of $1/\gamma$. The K-value for an undulator with a sinusoidal field with peak field B_0 and period length λ_0 is given by the relation (SI-units)

$$K = \frac{\lambda_0 \mathrm{B}_0 e}{2\pi m_e c} \tag{71}$$

which in practical units is given by

$$K = 93.3737 \lambda_0[\mathrm{m}] \mathrm{B}_0[\mathrm{T}] \tag{72}$$

A vertical periodical field in the undulator gives a horizontal K_x-value and a horizontal periodical field gives a vertical K_z-value. The motion of an electron in the filament along the undulator in the s-direction is given by

$$\begin{array}{l} X(s) = \frac{K_x \lambda_0}{2\pi\gamma} sin(2\pi s/\lambda_0) \\ Z(s) = \frac{K_z \lambda_0}{2\pi\gamma} sin(2\pi s/\lambda_0 + \varphi) \end{array} \tag{73}$$

The oscillating electrons in the beam will emit synchrotron radiation at the fundamental frequency of the oscillation and also at higher harmonics of the fundamental oscillation frequency. The wavelength of fundamental harmonic is given by

$$\lambda_1 = \frac{\lambda_0}{2\gamma^2} \left(1 + K_x^2/2 + K_z^2/2 + \gamma^2\theta_x^2 + \gamma^2\theta_z^2\right) \tag{74}$$

where θ_x and θ_z are the horizontal and vertical angle out from the undulator axis in the s-direction. The emitted radiation can in the frequency domain be described by the lobe function

$$\mathbf{H_n} = \begin{bmatrix} H_{nx} \\ H_{nz} \end{bmatrix} = \frac{n}{\lambda_1} \int_0^{\lambda_0} \begin{bmatrix} \frac{K_x}{\gamma} cos(2\pi s/\lambda_0) - \theta_x \\ \frac{K_z}{\gamma} cos(2\pi s/\lambda_0 + \varphi) - \theta_z \end{bmatrix} e^{In\Psi} ds \tag{75}$$

where

$$\begin{aligned} \Psi = & \frac{2\pi s}{\lambda_0} + \\ & + \frac{-2\gamma\theta_x K_x sin(\frac{2\pi s}{\lambda_0}) - 2\gamma\theta_z K_z sin(\frac{2\pi s}{\lambda_0} + \varphi) + \frac{K_x^2}{4} sin(\frac{4\pi s}{\lambda_0}) + \frac{K_z^2}{4} sin(\frac{4\pi s}{\lambda_0} + 2\varphi)}{1 + K_x^2/2 + K_z^2/2 + \gamma^2\theta_x^2 + \gamma^2\theta_z^2} \end{aligned} \tag{76}$$

The angular spectral flux, also often called spectral flux density, at the photon energy ϵ from the harmonic n on axis for a filament current with zero energy spread and zero emittance is given by the expression

$$\frac{\mathrm{d}\Phi_n}{\mathrm{d}\Omega} = \alpha\frac{I}{e}N^2(|H_{nx}|^2 + |H_{nz}|^2)sinc\left[\pi N\left(\frac{\epsilon}{hc}\lambda_1 - n\right)\right]^2 \tag{77}$$

where α is the fine structure constant, N is the number of periods in the undulator, I is the beam current,and $sinc(x) = sin(x)/x$. The lobe function has in this expression been multiplied with the the interference factor with the $sinc^2$ function. The interference factor has a sharper peak in the forward direction than the lobe function.

The angular spectral flux at a specific photon energy is given by the summation over all harmonics

$$\frac{\mathrm{d}\Phi}{\mathrm{d}\Omega} = \sum_{n=1}^{\infty}\frac{\mathrm{d}\Phi_n}{\mathrm{d}\Omega} \tag{78}$$

9.3 On axis angular spectral flux and brilliance from a planar undulator and a filament current

When the observer of the synchrotron radiation is on the undulator axis even shorter expression may be derived for the angular spectral flux and the brilliance. The brilliance is the angular spectral flux divided by the source size and it is a quality measure of the emitted radiation.

The angular spectral flux, also often called spectral flux density, at the harmonic n on axis for a filament current with zero energy spread and zero emittance is given by the expression [19]

$$\frac{\mathrm{d}\Phi_n}{\mathrm{d}\Omega} = \alpha\frac{I}{e}N^2\gamma^2F_n \tag{79}$$

F_n is function that involves Bessel functions of the first kind, $J_n(z)$.

$$\begin{array}{ll} F_n = \frac{n^2K^2}{(1+K^2/2)^2}\left(J_{(n-1)/2}\left[\frac{nK^2}{4+2K^2}\right] - J_{(n+1)/2}\left[\frac{nK^2}{4+2K^2}\right]\right)^2 & \text{for } n = 1,3,5,.. \\ F_n = 0 & \text{for } n = 2,4,6,.. \end{array} \tag{80}$$

where K is the K-value of the undulator.

The on axis brilliance $\mathfrak{B}_n$ at the peak energy at harmonic n for a filament current is given by the expression

$$\mathfrak{B}_n = \frac{4}{(\lambda_1/n)^2}\frac{\pi}{2}\alpha\frac{I}{e}NQ_n \tag{81}$$

where Q_n is given by

$$\begin{array}{ll} Q_n = \frac{nK^2}{1+K^2/2}\left(J_{(n-1)/2}\left[\frac{nK^2}{4+2K^2}\right] - J_{(n+1)/2}\left[\frac{nK^2}{4+2K^2}\right]\right)^2 & \text{for } n = 1,3,5,.. \\ Q_n = 0 & \text{for } n = 2,4,6,.. \end{array} \tag{82}$$

and λ_1 is the wavelength of the fundamental harmonic on axis

$$\lambda_1 = \frac{\lambda_0}{2\gamma^2}\left(1 + \frac{K^2}{2}\right) \tag{83}$$

The maximum brilliance for a filament beam is a factor of 2 larger than the brilliance at peak energy as explained in e.g.[19] and the maximum brilliance is found at a slightly lower photon energy than the peak energy of the harmonic.

9.4 Approximative expressions including the finite emittance and energy spread of the beam

For rapid calculations it may be useful to have approximative expressions for the angular spectral flux and brilliance. Below expressions that gives the a numerical output within $\pm$ 10% of the numerical output of Spectra [17] up to harmonic 13 are given.

It is assumed that the undulator is installed in the middle of a straight section and that the beam size has its minimum in the centre of the undulator. The finite beam emittance, i.e. the beam size and divergence in the centre of the undulator, and the energy spread is described by the variables:

σ_γ	energy spread
σ_x	horizontal rms electron beam size [m]
$\sigma_{x'}$	horizontal rms electron beam divergence [rad]
σ_z	vertical rms electron beam size [m]
$\sigma_{z'}$	vertical rms electron beam divergence [rad]

The wavelength spread σ_ω of the undulator peak from a filament beam is given by [20]

$$\sigma_\omega \;=\; \frac{0.360}{nN} \tag{84}$$

The energy spread σ_γ of a real beam will also give rise to a wavelength spread of the undulator peak and the induced wavelength spread is a factor 2 larger than the energy spread since the beam energy has a quadratic influence on the wavelength of the emitted synchrotron radiation. The total wavelength spread $\left(\frac{\Delta\lambda}{\lambda}\right)_{tot}$ is obtained by quadratic addition

$$\left(\frac{\Delta\lambda}{\lambda}\right)^2_{tot} = (2\sigma_\gamma)^2 + \left(\frac{0.360}{nN}\right)^2 = \mu_\lambda^2\sigma_\omega^2 \tag{85}$$

where μ_λ is introduced as the broadening factor

$$\mu_\lambda = \sqrt{1 + \left(\frac{2\sigma_\gamma nN}{0.36}\right)^2} \tag{86}$$

To describe the source size including the broadening factor, the following total rms values are used

$$\begin{aligned}
\sigma_{tx} &= \sqrt{\sigma_x^2 + (\lambda_1/n\ N\lambda_0)/(8\pi^2)} \\
\sigma_{tx'} &= \sqrt{\sigma_{x'}^2 + \mu_\lambda(\lambda_1/n)/(2N\lambda_0)} \\
\sigma_{tz} &= \sqrt{\sigma_z^2 + (\lambda_1/n\ N\lambda_0)/(8\pi^2)} \\
\sigma_{tz'} &= \sqrt{\sigma_{z'}^2 + \mu_\lambda(\lambda_1/n)/(2N\lambda_0)}
\end{aligned} \tag{87}$$

An approximative value for the angular spectral flux $\frac{\mathrm{d}\Phi_n}{\mathrm{d}\Omega}_{Real}$ at the peak energy at harmonic n for a real beam including finite beam emittance and energy spread is given by the expression

$$\frac{\mathrm{d}\Phi_n}{\mathrm{d}\Omega}_{Real} = \mathfrak{C}_n\ \alpha\frac{I}{e}N^2\gamma^2F_n \tag{88}$$

where $\mathfrak{C}_n$ is a convolution over the energy spread and the angular divergence of the real beam

$$\begin{aligned}
\mathfrak{C}_n = \frac{1.6}{(2\pi)^{3/2}\sigma_{tx'}\sigma_{tz'}\sigma_\gamma} \int_{-\infty}^{\infty}\int_{-\infty}^{\infty}\int_{-\infty}^{\infty} \exp\left[-\left(\frac{\theta_x^2}{2\sigma_{tx'}^2} + \frac{\theta_z^2}{2\sigma_{tz'}^2} + \frac{\xi^2}{2\sigma_\gamma^2}\right)\right]\times \\
\times\ sinc\left[\pi nN\left(-2\xi - \frac{\gamma^2\left(\theta_x^2+\theta_z^2\right)}{1+\frac{K^2}{2}}\right)\right]^2 d\xi d\theta_x d\theta_z
\end{aligned} \tag{89}$$

The factor 1.6 in $\mathfrak{C}_n$ is empirical and is found by comparing the numerical value of $\frac{\mathrm{d}\Phi_n}{\mathrm{d}\Omega}_{Real}$ and the numerical output of Spectra.

An approximate value for the on axis brilliance $\mathfrak{B}_{nReal}$ at the peak energy at harmonic n for a real beam including finite beam emittance and energy spread is given by the expression

$$\mathfrak{B}_{nReal} = \frac{1}{(2\pi)^2} \frac{1}{\sigma_{tx}\sigma_{tx'}\sigma_{tz}\sigma_{tz'}} \frac{\pi}{2} \alpha \frac{I}{e} N Q_n \tag{90}$$

The choice of calculating the brilliance at peak energy and not the maximum brilliance that is found at a slightly lower photon energy than the peak energy is that it is believed that in light sources with extremely low emittance it is of higher priority to use the narrow cone at the peak energy than the circular cone of synchrotron radiation at the peak brilliance.

9.5 Numerical calculation of synchrotron radiation

The numerical calculation of the properties of synchrotron radiation is better carried out with dedicated software packages for synchrotron radiation calculations. Two excellent such software packages are Spectra [17] from Spring 8 in Japan or SRW [21] from the ESRF in France.

References

[1] E. Wallén, J. Chavanne and P. Elleaume, Nucl. Instr. And Meth. A. 541 (2005) pp. 630-650.

[2] O. Chubar, P. Elleaume and J. Chavanne, Journal of Synchrotron Radiation, 1998, vol. 5, p. 481.

[3] K. Ingvar Blomqvist, Magnetic Design of Two Elliptically Polarizing Undulators for the APRES Beam Line at the Canadian Light Source., October 15, 2006.

[4] A. Chao, and M. Tigner, *Handbook of accelerator physics and engineering*, World Scintific Publishing Co. Pte. Ltd. second primting 2002, ISBN 9180238584, pp. 187-190.

[5] H. Widemann, *An ultra-low emittance mode for PEP using damping wigglers*, NIM A 266 (1988) pp. 24-31.

[6] A. Ropert, CAS 98-04, p.116.

[7] P. Elleaume, *A New Approach to the Electron Beam Dynamics in Undulators and Wigglers*, Proceedings of EPAC 92, Berlin 1992, pp. 661-663.

[8] L. Bhardt, M. Scheer, and G. Wustefeldt, *Beam dynamics simulation tools for insertion devices at BESSY II*, Wiggle 2005 mini-workshop, LNF Frascati, Italy 2005.

[9] Y. Wu, V. N. Litvinenko, and J. M. J. Madey, *Lattice and and dynamic aperture of the Duke FEL storage ring*, Proceedings of PAC 1993, pp. 218-220.

[10] James A. Clarke, *The science and technology of undulators and wigglers*, Oxford publishing, ISBN13: 9780198508557.

[11] Mikael Eriksson, Private Commnuication August 2009.

[12] Simulation of the MAX IV 3 GeV storage ring lattice without insertion devices carried out by Simon Leemann, September 2009.

[13] Kiyoshi Kubo, Sekazi K. Mtingwa, and Andrzej Wolski4, *Intrabeam scattering formulas for high energy beams*, PHYSICAL REVIEW SPECIAL TOPICS - ACCELERATORS AND BEAMS 8, 081001 (2005)

[14] Helmut Widemann, *Particle Accelerator Physics*, Third Edition, ISBN-13 978-3-540-49043-2 3rd ed. Springer Berlin Heidelberg New York, Chapter 16, pp.577-598.

[15] Private communication with A. Andersson September 14, 2009.

[16] J. D. Jackson, *Classical Electron Dynamics*, ISBN 0-471-30932-X.

[17] T. Tanaka and H. Kitamura, *SPECTRA: a synchrotron radiation calculation code*, J. Synchrotron Rad. (2001). 8, 1221-1228.

[18] O. ,V. Chubar, Rev. Sci. Instr. 66, 1872-1874 (1995)

[19] H. Onuki and P.Elleaume, *Undulators, Wiggler and Their Applications*, ISBN 0-415-28040-0.

[20] W. Joho, *Radiation properties of an undulator*, SLS-Note 4/95 (July 1995, rev. April 1996)

[21] O. Chubar and P. Elleaume, *Accurate and efficient computation of synchrotron radiation in the near field region*,Proceedings of EPAC 1998, pp. 1177-1179.